

¹ **Searches for Supersymmetric signatures in
2 all hadronic final states with the α_T
3 variable.**

⁴ Darren Burton

⁵ Imperial College London
⁶ Department of Physics

⁷ A thesis submitted to Imperial College London
⁸ for the degree of Doctor of Philosophy

Abstract

A search for supersymmetric particles in events with high p_T jets and a large missing energy signature, is conducted using 11.7 fb^{-1} of data, collected with a center-of-mass collision energy of 8 TeV by the CMS detector. The dimensionless kinematic variable α_T is used to select events with genuine missing energy signatures. Standard Model backgrounds are estimated through the use of data driven control samples. No excess over Standard Model expectations is found. Exclusion limits are set at the 95% confidence level in the parameter space of a range of supersymmetric simplified model topologies. Emphasis is placed on the interpretations of model topologies typical of ‘natural’ SUSY signatures.

Results of benchmarking the Level-1 single jet and H_T trigger efficiencies, before and after the implementation of a change to the Level-1 jet clustering algorithm are presented. Similar performance is observed for all L1 quantities. This change was introduced to negate an increase in trigger cross-section, which can be attributed to soft jets from secondary interactions.

Furthermore, a templated fit method to estimate the b-tagged jet distribution of Standard Model backgrounds at a high number of reconstructed b-tagged jets, is validated in data and simulation. Applicable to supersymmetric searches which are sensitive to gluino induced third-generation signatures, this technique is utilised as a crosscheck to the results of the α_T analysis. Standard Model background predictions from the template fits are compared to those from the α_T search in the hadronic signal region, where good agreement between the two methods is observed.

37

Declaration

38

I, the author of this thesis, declare that the work presented within this
39 document to be my own. The work presented in Chapters 4, 5, 6 and Section
40 3.4, is a result of the author's own work, or that of which I have been a major
41 contributor unless explicitly stated otherwise, and is carried out within the
42 context of the Imperial College London and CERN SUSY groups, itself a
43 subsection of the greater CMS collaboration. All figures and studies taken
44 from external sources are referenced appropriately throughout this document.

45

Darren Burton

46

Acknowledgements

47 I would like to thank the many people whom I have had the pleasure of working with
48 during the course of the last three and a half years. The opportunity to work as part
49 of the largest scientific collaboration during one of the most exciting times in particle
50 physics for decades, has been a real privilege to be a part of. I could not have achieved
51 the results presented in this thesis without the help of my colleagues who were part of the
52 RA1 team, Edward Laird, Chris Lucas, Henning Flaecher, Yossof Eshaq, Bryn Mathais,
53 Sam Rogerson, Zhaoxia Meng and Georgia Karapostoli whom I worked with on L1 jets. I
54 also thank my supervisor Oliver Buchmuller for his guidance in getting me to this point.

55 I also feel it important to single out thanks to the postdocs that I have worked with during
56 my PhD. Jad Marrouche from whom I have learnt a great deal and Robert Bainbridge
57 who has been like a second supervisor to me, helping me during my time at Imperial and
58 CERN, especially during those most stressful of times approaching conference deadlines!

59 My fellow PhD students who I live with and have seen on an almost daily basis for the
60 last few years, Andrew Gilbert, Patrick Owen, Indrek Sepp, Matthew Kenzie and my
61 wonderful girlfriend Hannah. Thanks for putting up with the whining, complaining and
62 clomping.

63 Finally my largest thanks go to my Mum and Dad whose patience, encouragement and
64 considerable financial support have allowed me to take the many steps that led me here
65 today.

66 Contents

67	List of Figures	viii
68	List of Tables	xiv
69	1. Introduction	2
70	2. A Theoretical Overview	5
71	2.1. The Standard Model	5
72	2.1.1. Gauge Symmetries of the SM	7
73	2.1.2. The Electroweak Sector and Electroweak Symmetry Breaking	9
74	2.2. Motivation for Physics beyond the Standard Model	13
75	2.3. Supersymmetry Overview	14
76	2.3.1. R-Parity	16
77	2.4. Experimental Signatures of SUSY at the LHC	16
78	2.4.1. Simplified Models	18
79	3. The LHC and the CMS Detector	20
80	3.1. The LHC	20
81	3.2. The CMS Detector	23
82	3.2.1. Detector Subsystems	23
83	3.2.2. Tracker	24
84	3.2.3. Electromagnetic Calorimeter	25
85	3.2.4. Hadronic Calorimeter	26
86	3.2.5. Muon Systems	27
87	3.3. Event Reconstruction and Object Definition	28
88	3.3.1. Jets	28
89	3.3.2. B-tagging	30
90	3.4. Triggering System	33
91	3.4.1. The Level-1 Trigger	34

92	3.4.2. The L1 Trigger Jet Algorithm	36
93	3.4.3. Measuring L1 Jet Trigger Efficiencies	38
94	3.4.4. Effects of the L1 Jet Seed	40
95	3.4.5. Robustness of L1 Jet Performance against Pile-up	43
96	3.4.6. Summary	45
97	4. SUSY Searches in Hadronic Final States	47
98	4.1. An Introduction to the α_T Search	48
99	4.1.1. The α_T Variable	50
100	4.2. Search Strategy	52
101	4.2.1. Physics Objects	55
102	4.2.2. Event Selection	58
103	4.2.3. Control Sample Definition and Background Estimation	61
104	4.2.4. Estimating the QCD Multi-jet Background	68
105	4.3. Trigger Strategy	70
106	4.4. Measuring Standard Model Process Normalisation Factors via H_T Sidebands	71
107	4.5. Determining Monte Carlo Simulation Yields with Higher Statistical Precision	73
108	4.5.1. The Formula Method	73
109	4.5.2. Establishing Proof of Principle	75
110	4.5.3. Correcting Measured Efficiencies in Simulation to Data	76
111	4.6. Systematic Uncertainties on Transfer Factors	78
112	4.6.1. Determining Systematic Uncertainties from Closure Tests	82
113	4.7. Simplified Models, Efficiencies and Systematic Uncertainties	84
114	4.7.1. Signal Efficiency	85
115	4.7.2. Applying B-tagging Scale Factor Corrections in Signal Samples . .	86
116	4.7.3. Experimental Uncertainties	87
117	4.8. Statistical Interpretation	90
118	4.8.1. Hadronic Sample	90
119	4.8.2. H_T Evolution Model	91
120	4.8.3. Electroweak Sector (EWK) Control Samples	92
121	4.8.4. Contributions from Signal	94
122	4.8.5. Total Likelihood	95
123	5. Results and Interpretation	97
124	5.1. Compatibility with the Standard Model Hypothesis	97
125	5.2. SUSY	106
126	5.2.1. The CL_s Method	106

127	5.2.2. Interpretation in Simplified Signal Models	107
128	6. SUSY Searches with B-tag Templates	111
129	6.1. Concept	112
130	6.2. Application to the α_T Search	115
131	6.2.1. Proof of Principle in Simulation	116
132	6.2.2. Results in a Data Control Sample	119
133	6.2.3. Application to the α_T Hadronic Search Region	121
134	6.3. Summary	123
135	7. Conclusions	125
136	A. Miscellaneous	127
137	A.1. Jet Identification Criteria	127
138	A.2. Primary Vertices	128
139	B. L1 Jets	129
140	B.1. Jet Matching Efficiencies	129
141	B.2. Leading Jet Energy Resolution	130
142	B.3. Resolution for Energy Sum Quantities	133
143	C. Additional Material on Background Estimation Methods	135
144	C.1. Determination of k_{QCD}	135
145	C.2. Effect of Varying Background Cross-sections on Closure Tests	136
146	D. Additional Material For B-tag Template Method	138
147	D.1. Templates Fits in Simulation	138
148	D.2. Pull Distributions for Template Fits	141
149	D.3. Templates Fits in Data Control Sample	142
150	D.4. Templates Fits in Data Signal Region	144
151	Bibliography	147

¹⁵² List of Figures

¹⁵³ 2.1.	One loop quantum corrections to the Higgs squared mass parameter m_h^2 due to a fermion.	¹⁴
¹⁵⁵ 2.2.	Two example simplified model decay chains.	¹⁹
¹⁵⁶ 3.1.	A top-down layout of the LHC, with the position of the four main detectors labelled.	²¹
¹⁵⁸ 3.2.	The total integrated luminosity delivered to and collected by Compact Muon Solenoid (CMS) during the 2012 8 TeV pp runs	²²
¹⁶⁰ 3.3.	A pictorial depiction of the CMS detector.	²⁴
¹⁶¹ 3.4.	Illustration of the CMS Electromagnetic CALorimeter (ECAL).	²⁶
¹⁶² 3.5.	Schematic of the CMS Hadronic CALorimeter (HCAL).	²⁷
¹⁶³ 3.6.	Combined Secondary Vertex (CSV) algorithm discriminator values in enriched ttbar and inclusive multi-jet samples	³¹
¹⁶⁵ 3.7.	Data/MC b-tag scale factors derived using the Combined Secondary Vertex Medium Working Point (CSVM) tagger.	³²
¹⁶⁷ 3.8.	Data/MC mis-tag scale factors derived using the CSVM tagger.	³³
¹⁶⁸ 3.9.	The CMS Level 1 Trigger (L1) Trigger system.	³⁴
¹⁶⁹ 3.10.	Illustration of the Level-1 jet finding algorithm.	³⁷
¹⁷⁰ 3.11.	L1 jet efficiency turn-on curves as a function of the offline CaloJet and PFJet E_T	³⁹
¹⁷² 3.12.	L1 jet efficiency turn-on curves as a function of the offline CaloJet E_T for the 2012 run period B and C.	⁴¹

174	3.13. L1 H_T efficiency turn-on curves as a function of the offline CaloJet H_T	41
175	3.14. Trigger cross section for the L1HTT150 trigger path.	42
176	3.15. L1 jet efficiency turn-on curves as a function of the leading offline E_T Calo	
177	(left) and PF (right) jet, for low, medium and high pile-up conditions.	43
178	3.16. Fit values from an Exponentially Modified Gaussian (EMG) function fitted	
179	to the resolution plots of leading Calo jet E_T measured as a function of	
180	$\frac{(L1\ E_T - \text{Offline}\ E_T)}{\text{Offline}\ E_T}$ for low, medium and high pile-up conditions.	45
181	3.17. Fit values from an EMG function fitted to the resolution plots of leading	
182	PF jet E_T measured as a function of $\frac{(L1\ E_T - \text{Offline}\ E_T)}{\text{Offline}\ E_T}$ for low, medium and	
183	high pile-up conditions.	45
184	4.1. Reconstructed offline H_T distribution in the hadronic signal selection, from	
185	11.7fb^{-1} of data, in which no α_T requirement is made.	49
186	4.2. The event topologies of background QCD dijet events (right) and a generic	
187	SUSY signature with genuine Z_T (left).	50
188	4.3. The α_T distributions for the low 2-3 (left) and high ≥ 4 (right) jet	
189	multiplicities after a full analysis selection and $H_T > 375$ requirement.	52
190	4.4. Pictorial depiction of the analysis strategy employed by the α_T search to	
191	increase sensitivity to a wide spectra of SUSY models.	55
192	4.5. Data/MC comparisons of key variables for the hadronic signal region.	61
193	4.6. Data/MC comparisons of key variables for the $\mu +$ jets selection.	64
194	4.7. Data/MC comparisons of key variables for the $\mu\mu +$ jets selection.	66
195	4.8. Data/MC comparisons of key variables for the $\gamma +$ jets selection.	67
196	4.9. QCD sideband regions, used for determination of k_{QCD}	69
197	4.10. Tagging efficiencies of (a) b-jets, (b) c-jets, and (c) light-jets determined	
198	from all jets within each H_T category.	76
199	4.11. Sets of closure tests overlaid on top of the systematic uncertainty used for	
200	each of the five H_T regions.	83

201	4.12. Signal efficiencies fo the Simplified Model Spectra (SMS) models (a) T1	
202	and (b) T2.	85
203	5.1. Comparison of the observed yields and Standard Model (SM) expectations	
204	given by the simultaneous fit in bins of H_T for the (a) hadronic, (b) $\mu +$	
205	jets, (c) $\mu\mu +$ jets and (d) $\gamma +$ jets samples when requiring $n_b^{reco} = 0$ and	
206	$n_{jet} \leq 3$	99
207	5.2. Comparison of the observed yields and SM expectations given by the	
208	simultaneous fit in bins of H_T for the (a) hadronic, (b) $\mu +$ jets, (c) $\mu\mu +$	
209	jets and (d) $\gamma +$ jets samples when requiring $n_b^{reco} = 1$ and $n_{jet} \leq 3$	100
210	5.3. Comparison of the observed yields and SM expectations given by the	
211	simultaneous fit in bins of H_T for the (a) hadronic, (b) $\mu +$ jets, (c) $\mu\mu +$	
212	jets and (d) $\gamma +$ jets samples when requiring $n_b^{reco} = 2$ and $n_{jet} \leq 3$	101
213	5.4. Comparison of the observed yields and SM expectations given by the	
214	simultaneous fit in bins of H_T for the (a) hadronic, (b) $\mu +$ jets, (c) $\mu\mu +$	
215	jets and (d) $\gamma +$ jets samples when requiring $n_b^{reco} = 0$ and $n_{jet} \geq 4$	102
216	5.5. Comparison of the observed yields and SM expectations given by the	
217	simultaneous fit in bins of H_T for the (a) hadronic, (b) $\mu +$ jets, (c) $\mu\mu +$	
218	jets and (d) $\gamma +$ jets samples when requiring $n_b^{reco} = 1$ and $n_{jet} \geq 4$	103
219	5.6. Comparison of the observed yields and SM expectations given by the	
220	simultaneous fit in bins of H_T for the (a) hadronic, (b) $\mu +$ jets, (c) $\mu\mu +$	
221	jets and (d) $\gamma +$ jets samples when requiring $n_b^{reco} = 2$ and $n_{jet} \geq 4$	104
222	5.7. Comparison of the observed yields and SM expectations given by the	
223	simultaneous fit in bins of H_T for the (a) hadronic, (b) $\mu +$ jets, (c) $\mu\mu +$	
224	jets and (d) $\gamma +$ jets samples when requiring $n_b^{reco} = 3$ and $n_{jet} \geq 4$	104
225	5.8. Comparison of the observed yields and SM expectations given by the	
226	simultaneous fit in bins of H_T for the (a) hadronic, (b) $\mu +$ jets, (c) $\mu\mu +$	
227	jets and (d) $\gamma +$ jets samples when requiring $n_b^{reco} \geq 4$ and $n_{jet} \geq 4$	105
228	5.9. Production and decay modes for the various SMS models interpreted	
229	within the analysis.	109
230	5.10. Upper limit of cross section at 95% CL as a function of $m_{\tilde{q}/\tilde{g}}$ and m_{LSP}	
231	for various SMS models.	110

232	6.1. The b-tagging (a), c-quark mis-tagging (b), and light-quark mis-tagging rate (c) as a function of jet p_T , measured in simulation after the application of the α_T analysis $\mu + \text{jets}$ control sample selection, in the region $H_T > 375.114$	
235	6.2. An example of a template fit with the defined Z0 (blue) and Z2 (red) templates to data within the low n_b^{reco} control region (left).	115
237	6.3. The results of fitting the $Z = 0$ and $Z = 2$ templates in the $n_b^{\text{reco}} = 0, 1, 2$ control region to yields from simulation in the $\mu + \text{jets}$ control sample for the $H_T > 375 \text{ GeV}$, $n_{\text{jet}} \geq 5$ category for all CSV working points.	118
240	6.4. The results of fitting the $Z = 0$ and $Z = 2$ templates in the $n_b^{\text{reco}} = 0, 1, 2$ control region to data from the $\mu + \text{jets}$ control sample, for the CSV medium working point, with a jet multiplicity $n_{\text{jet}} \geq 5$, in all three H_T categories.	120
244	6.5. The results of fitting the $Z = 0$ and $Z = 2$ templates in the $n_b^{\text{reco}} = 0, 1, 2$ control region to data from the hadronic signal selection, in the $n_{\text{jet}} \geq 5$ and $H_T > 375$ category for all CSV working points.	122
247	B.1. Leading jet matching efficiency as a function of the offline CaloJet E_T	129
248	B.2. Resolution plots of the leading offline Calo E_T measured as a function of $\frac{(L1 E_T - \text{Offline } E_T)}{\text{Offline } E_T}$ for (a) low, (b) medium, and (c) high pile-up conditions.	131
250	B.3. Resolution plots of the leading off-line PF E_T measured as a function of $\frac{(L1 E_T - \text{Offline } E_T)}{\text{Offline } E_T}$ for (a) low, (b) medium, and (c) high pile-up conditions.	133
252	B.4. H_T resolution parameters in bins of Calo H_T measured in the defined low, medium and high pile up conditions.	133
254	B.5. H_T resolution parameters in bins of PF H_T measured in the defined low, medium and high pile up conditions.	134
256	B.6. \mathcal{H}_T resolution parameters in bins of Calo \mathcal{H}_T measured in the defined low, medium and high pile up conditions.	134
258	B.7. \mathcal{H}_T resolution parameters in bins of PF \mathcal{H}_T measured in the defined low, medium and high pile up conditions.	134

260	C.1. $R_{\alpha_T}(H_T)$ and exponential fits for each of the data sideband regions. Fit is conducted between the H_T region $275 < H_T < 575$	135
261		
262	C.2. Sets of closure tests overlaid on top of the systematic uncertainty used for each of the five H_T regions in the $2 \leq n_{jet} \leq 3$ jet multiplicity category for nominal and varied cross-sections.	136
263		
264		
265	C.3. Sets of closure tests overlaid on top of the systematic uncertainty used for each of the five H_T regions in the $n_{jet} \geq 4$ jet multiplicity category for nominal and varied cross-sections.	136
266		
267		
268	D.1. The results of fitting the $Z = 0$ and $Z = 2$ templates in the $n_b^{reco} = 0, 1, 2$ control region to yields from simulation in the $\mu +$ jets control sample for the $H_T > 375$ GeV, $n_{jet} = 3$ category.	139
269		
270		
271	D.2. The results of fitting the $Z = 0$ and $Z = 2$ templates in the $n_b^{reco} = 0, 1, 2$ control region to yields from simulation in the $\mu +$ jets control sample for the $H_T > 375$ GeV, $n_{jet} = 4$ category.	140
272		
273		
274	D.3. Pull distributions of the normalisation parameter of each template, $\frac{(\theta - \hat{\theta})}{\sigma}$. Distributions are constructed from 10^4 pseudo-experiments generated by a gaussian distribution with width σ , centred on the nominal template value of each point within the low n_b^{reco} control region.	141
275		
276		
277		
278	D.4. The results of fitting the $Z = 0$ and $Z = 2$ templates in the $n_b^{reco} = 0, 1, 2$ control region to data from the $\mu +$ jets control sample, for the CSV medium working point, with a jet multiplicity $n_{jet} = 3$, in all three H_T categories.	142
279		
280		
281		
282	D.5. The results of fitting the $Z = 0$ and $Z = 2$ templates in the $n_b^{reco} = 0, 1, 2$ control region to data from the $\mu +$ jets control sample, for the CSV medium working point, with a jet multiplicity $n_{jet} = 4$, in all three H_T categories.	143
283		
284		
285		
286	D.6. The results of fitting the $Z = 0$ and $Z = 2$ templates in the $n_b^{reco} = 0, 1, 2$ control region to data from the hadronic signal selection, in the $n_{jet} = 3$ and $H_T > 375$ category for all CSV working points.	144
287		
288		

289	D.7. The results of fitting the $Z = 0$ and $Z = 2$ templates in the $n_b^{reco} = 0, 1, 2$ control region to data from the hadronic signal selection, in the $n_{jet} = 4$ and $H_T > 375$ category for all CSV working points.	145
290		
291		

List of Tables

293	2.1. The fundamental particles of the SM, with spin, charge and mass displayed.	6
294	3.1. Results of a cumulative EMG function fit to the turn-on curves for L1	
295	single jet triggers in 2012 Run Period C.	39
296	3.2. Results of a cumulative EMG function fit to the turn-on curves for L1	
297	single jet triggers in the 2012 run period B and C.	41
298	3.3. Results of a cumulative EMG function fit to the turn-on curves for H_T in	
299	2012 run period B and C.	42
300	3.4. Results of a cumulative EMG function fit to the efficiency turn-on curves	
301	for L1 single jet triggers in the 2012 run period C, for low,medium and	
302	high pile-up conditions.	43
303	3.5. Results of a cumulative EMG function fit to the efficiency turn-on curves	
304	for Level-1 single jet triggers in the 2012 run period C, for low,medium	
305	and high pile-up conditions.	44
306	4.1. A summary of the SMS models interpreted in this analysis, involving both	
307	direct (D) and gluino-induced (G) production of squarks and their decays.	48
308	4.2. Muon identification criteria used within the analysis for selection/veto	
309	purposes in the muon control/signal selections.	56
310	4.3. Photon identification criteria used within the analysis for selection/veto	
311	purposes in the $\gamma +$ jets control/signal selections.	57
312	4.4. Electron identification criteria used within the analysis for veto purposes.	57
313	4.5. Noise filters that are applied to remove spurious and non-physical \cancel{E}_T	
314	signatures within the CMS detector.	58

315	4.6. Jet thresholds used in the three H_T regions of the analysis.	59
316	4.7. Best fit values for the parameters k_{QCD} obtained from sideband regions	
317	B,C ₁ ,C ₂ ,C ₃	70
318	4.8. Measured efficiencies of the H_T and α_T legs of the HT and HT_alphaT	
319	triggers in independent analysis bins.	71
320	4.9. k-factors calculated for different EWK processes.	72
321	4.10. Comparing yields in simulation within the $\mu + \text{jets}$ selection determined	
322	from the formula method described in Equation (4.11), and that taken	
323	directly from simulation.	75
324	4.11. The absolute change in the Transfer Factor (TF)s used to predict the	
325	entire signal region SM background, using the $\mu + \text{jets}$ control sample	
326	when the systematic uncertainties of the data to simulation scale factors	
327	are varied by $\pm 1\sigma$	77
328	4.12. A summary of the results obtained from zeroeth order polynomial (i.e.	
329	a constant) and linear fits to five sets of closure tests performed in the	
330	$2 \geq n_{\text{jet}} \geq 3$ category.	80
331	4.13. A summary of the results obtained from zeroeth order polynomial (i.e.	
332	a constant) and linear fits to five sets of closure tests performed in the	
333	$n_{\text{jet}} \geq 4$ category.	81
334	4.14. A summary of the results obtained from zeroeth order polynomial (i.e. a	
335	constant) and linear fits to three sets of closure tests performed between	
336	the $2 \leq n_{\text{jet}} \leq 3$ and $n_{\text{jet}} \geq 4$ categories.	81
337	4.15. Calculated systematic uncertainties for the five H_T regions, determined	
338	from the closure tests.	82
339	4.16. Estimates of systematic uncertainties on the signal efficiency (%) for	
340	various SMS models when considering points in the region near to the	
341	diagonal	90
342	4.17. Estimates of systematic uncertainties on the signal efficiency (%) for	
343	various SMS models when considering points in the region near to the	
344	diagonal	90

345	4.18. The systematic parameters used in H_T bins.	94
346	4.19. Nuisance parameters used within the different hadronic signal bins of the	
347	analysis	96
348	5.1. Summary of control samples used by each fit results, and the Figures in	
349	which they are displayed.	98
350	5.2. Comparison of the measured yields in each H_T , n_{jet} and n_b^{reco} jet multiplicity bins for the hadronic sample with the SM expectations and combined	
351	statistical and systematic uncertainties given by the simultaneous fit. . .	98
352		
353	5.3. A table representing the SMS models interpreted within the analysis. . .	108
354	6.1. Typical underlying b-quark content of different SM processes which are	
355	common to many SUSY searches.	112
356	6.2. Summary of the fit predictions in the n_b^{reco} signal region after combination	
357	of the $n_{jet} = 3, = 4, \geq 5$ categories compared against yields taken directly	
358	from simulation. The predictions are extrapolated from a $n_b^{reco} = 0, 1,$	
359	2 control region and simulation yields are normalised to an integrated	
360	luminosity of 10 fb^{-1}	117
361	6.3. Summary of the fit predictions in the n_b^{reco} signal region of the $\mu + \text{jets}$	
362	control sample, after combination of the $n_{jet} = 3, = 4, \geq 5$ categories.. The	
363	predictions are extrapolated from a $n_b^{reco} = 0, 1, 2$ control region using	
364	11.4 fb^{-1} of $\sqrt{s} = 8\text{TeV}$ data.	121
365	6.4. Summary of the fit predictions in the n_b^{reco} signal region of the α_T hadronic	
366	signal selection, after combination of the $n_{jet} = 3, = 4, \geq 5$ categories. The	
367	predictions are extrapolated from a $n_b^{reco} = 0, 1, 2$ control region using	
368	11.7 fb^{-1} of $\sqrt{s} = 8\text{TeV}$ data.	123
369	A.1. Criteria for a reconstructed jet to pass the loose calorimeter jet id.	127
370	A.2. Criteria for a reconstructed jet to pass the loose PF jet id.	128
371	A.3. Criteria for a vertex in an event to be classified as a 'good' reconstructed	
372	primary vertex.	128

373	B.1. Results of a cumulative EMG function fit to the turn-on curves for the	
374	matching efficiency of the leading jet in an event to a Level-1 jet in run	
375	2012C and 2012B data.	130
376	C.1. Translation factors constructed from the $\mu + \text{jets}$ control sample and signal	
377	selection MC, to predict yields for the $W + \text{jets}$ and $t\bar{t}$ back-grounds in	
378	the signal region.	137
379		

Chapter 1.

³⁸⁰ Introduction

³⁸¹ During the 20th century, great advances were made in the human understanding of
³⁸² the universe, its origins, its future and its composition. The Standard Model (**SM**)
³⁸³ first formulated in the 1960s is one of the crowning achievements in science's quest to
³⁸⁴ explain the most fundamental processes and interactions that make up our universe. It
³⁸⁵ has provided a highly successful explanation for a wide range of phenomena in Particle
³⁸⁶ Physics and has stood up to extensive experimental scrutiny [1].

³⁸⁷ Despite its success it is not a complete theory, with significant questions remaining
³⁸⁸ unanswered. It describes only three of the four known forces with gravity not incorporated
³⁸⁹ within the framework of the **SM**. Cosmological experiments infer that just $\sim 4\%$ of the
³⁹⁰ observable universe exists as matter, with elusive "Dark Matter" accounting for a further
³⁹¹ $\sim 23\%$ [2]. However no particle predicted by the **SM** is able to account for it. At higher
³⁹² energy scales, the (non-)unification of the fundamental forces point to problems with the
³⁹³ **SM** at least at higher energies not yet probed experimentally.

³⁹⁴ Many theories exist as extensions to the **SM**, predicting a range of observables that can
³⁹⁵ be detected at the Large Hadron Collider (**LHC**) of which SUperSYmmetry (**SUSY**) is
³⁹⁶ one such example. It predicts a new symmetry of nature in which all current particles
³⁹⁷ in the **SM** would have a corresponding supersymmetric partner. Common to most
³⁹⁸ Supersymmetric theories is a stable, weakly interacting Lightest Supersymmetric Partner
³⁹⁹ (**LSP**), which has the properties of a possible dark matter candidate. The **SM** and the
⁴⁰⁰ main principles of Supersymmetric theories are outlined in Chapter 2, with emphasis
⁴⁰¹ placed on how experimental signatures of **SUSY** may reveal themselves in proton collisions
⁴⁰² at the **LHC**.

403 The experimental goal of the **LHC** is to further test the framework of the **SM**, exploring the
404 TeV mass scale for the first time, and to seek a connection between the particles produced
405 in proton collisions and dark matter. The first new discovery by this extraordinary
406 machine was announced on the 4th of July 2012. The long-awaited discovery was the
407 culmination of decades of experimental endeavours in the search for the Higgs boson,
408 which provided an answer to the mechanism of electroweak symmetry breaking within
409 the **SM** [3][4].

410 This discovery was made possible through the combination of data taken by the Compact
411 Muon Solenoid (**CMS**) and A Toroidal LHC ApparatuS (**ATLAS**), two multipurpose
412 detectors located on the **LHC** ring. An experimental description of the **CMS** detector
413 and the **LHC** is described in Chapter 3, including some of the object reconstruction used
414 by **CMS** in searches for **SUSY** signatures.

415 The performance of the **CMS** Level-1 single jet and energy sum triggers is also bench-
416 marked within this chapter. The Level-1 triggers are of paramount importance to the
417 collection of physics events at **CMS**, and to which a change in the jet clustering algorithm
418 was introduced approximately half way through the data taking period. The aim of this
419 change, was to reduce the rate at which data events not of interest to physics analysis
420 were recorded, whilst avoiding impact to the overall performance of the triggers.

421 Chapter 4, contains a description of the search for evidence of the production of Supersym-
422 metric particles at the **LHC**. The main basis of the search centres around the kinematic
423 dimensionless α_T variable; which provides a strong rejection of backgrounds with fake
424 missing energy signatures, whilst maintaining good sensitivity to a variety of **SUSY**
425 topologies. The author’s work (as an integral part of the analysis group) is documented
426 in detail, and has culminated in numerous publications over the past two years, the latest
427 results having been published in the European Physical Journal C (**EPJC**) [5].

428 The author in particular has played a major role in the extension of the α_T analysis into
429 the additional b-tagged and jet multiplicity dimensions, increasing the sensitivity of the
430 analysis to a range of **SUSY** topologies. Additionally, the author has worked extensively
431 on increasing the statistical precision of the data driven electroweak predictions, through
432 analytical techniques. This included work on developing the derivation of data driven
433 systematic uncertainties through the establishment of closure tests within the control
434 samples of the analysis.

435 The compatibility of the data collected for the α_T search with a **SM** only hypothesis is
436 documented in Chapter 5. In the absence of an observed excess, interpretations of the

437 data within the framework of a variety of Simplified Model Spectra (**SMS**), describing an
438 array of possible **SUSY** event topologies are made.

439 Finally, a method to search for gluino mediated **SUSY** signatures rich in top and bottom
440 flavoured jet final states, is introduced in Chapter 6. These particular **SUSY** topologies
441 are increasingly of interest to physicists in light of the discovery of the Higgs boson.
442 A parametrisation of the b-tagging distribution for different electroweak processes is
443 used to establish template shapes, which are then fitted at low b-tagged jet multiplicity
444 (0-2), to estimate the expected **SM** background of 3 and 4 b-tagged jet events within an
445 event sample. The α_T control and hadronic signal event selections are used to validate
446 the functionality of this template method in both data and simulation. Background
447 predictions within the hadronic signal region are compared to those presented in Chapter 5,
448 with the intention of serving as a independent crosscheck of the estimated **SM** backgrounds
449 from the α_T search.

450 Natural units are used throughout this thesis in which $\hbar = c = 1$.

Chapter 2.

⁴⁵¹ A Theoretical Overview

⁴⁵² Within this chapter, a brief introduction and background to the **SM** is given. Its success
⁴⁵³ as a rigorously tested and widely accepted theory is discussed as are its deficiencies which
⁴⁵⁴ lead to the argument that this theory is not a complete description of our universe. The
⁴⁵⁵ motivations for new physics at the TeV scale and in particular Supersymmetric theories
⁴⁵⁶ are outlined within Section (2.3). The chapter concludes with how an experimental
⁴⁵⁷ signature of such theories can be produced and observed at the **LHC** in Section (2.4).

⁴⁵⁸ 2.1. The Standard Model

⁴⁵⁹ The **SM** is the name given to the relativistic Quantum Field Theory (**QFT**), where
⁴⁶⁰ particles are represented as excitations of fields, which describe the interactions and
⁴⁶¹ properties of all the known elementary particles [6][7][8][9]. It is a renormalisable field
⁴⁶² theory which contains three symmetries: $SU(3)$ for colour charge; $SU(2)$ for weak isospin
⁴⁶³ and; $U(1)$ relating to weak hyper charge, which requires its Lagrangian \mathcal{L}_{SM} to be
⁴⁶⁴ invariant under local gauge transformation.

⁴⁶⁵ Within the **SM** theory, matter is composed of spin $\frac{1}{2}$ fermions that interact with each
⁴⁶⁶ other via the exchange of spin-1 gauge bosons. A summary of the known fundamental
⁴⁶⁷ fermions and bosons is given in Table 2.1.

⁴⁶⁸ Fermions are separated into quarks and leptons of which only quarks interact with the
⁴⁶⁹ strong nuclear force. Quarks unlike leptons are not seen as free particles in nature, but
⁴⁷⁰ rather exist only within baryons, which are composed of three quarks with an overall
⁴⁷¹ integer charge, and quark-anti-quark pairs called mesons. Both leptons and quarks are

Particle	Symbol	Spin	Charge	Mass (GeV)
First Generation Fermions				
Electron Neutrino	ν_e	$\frac{1}{2}$	0	$< 2.2 \times 10^{-6}$
Electron	e	$\frac{1}{2}$	-1	0.51×10^{-3}
Up Quark	u	$\frac{1}{2}$	$\frac{2}{3}$	$2.3^{+0.7}_{-0.5} \times 10^{-3}$
Down Quark	d	$\frac{1}{2}$	$-\frac{1}{3}$	$4.8^{+0.7}_{-0.3} \times 10^{-3}$
Second Generation Fermions				
Muon Neutrino	ν_μ	$\frac{1}{2}$	0	-
Muon	μ	$\frac{1}{2}$	-1	1.05×10^{-3}
Charm Quark	c	$\frac{1}{2}$	$\frac{2}{3}$	1.275 ± 0.025
Strange Quark	s	$\frac{1}{2}$	$-\frac{1}{3}$	$95 \pm 5 \times 10^{-3}$
Third Generation Fermions				
Tau Neutrino	ν_τ	$\frac{1}{2}$	0	-
Tau	τ	$\frac{1}{2}$	-1	1.77
Top Quark	t	$\frac{1}{2}$	$\frac{2}{3}$	173.5 ± 0.8
Bottom Quark	b	$\frac{1}{2}$	$-\frac{1}{3}$	4.65 ± 0.03
Gauge Bosons				
Photon	γ	1	0	0
W Boson	W^\pm	1	± 1	80.385 ± 0.015
Z Boson	Z	1	0	91.187 ± 0.002
Gluons	g	1	0	0
Higgs Boson	H	0	0	125.3 ± 0.5 [4]

Table 2.1: The fundamental particles of the SM, with spin, charge and mass displayed. Latest mass measurements taken from [1].

⁴⁷² grouped into three generations which have the same properties, but with ascending mass
⁴⁷³ in each subsequent generation.

⁴⁷⁴ The gauge bosons mediate the interactions between fermions. The field theories of
⁴⁷⁵ Quantum Electro-Dynamics (QED) and Quantum Chromo-Dynamics (QCD), yield
⁴⁷⁶ massless mediator bosons, the photon and eight coloured gluons which are consequences
⁴⁷⁷ of the gauge invariance of those theories (detailed in Section (2.1.1)).

⁴⁷⁸ The unification of the electromagnetic and weak-nuclear forces into the current Elec-
⁴⁷⁹ troweak theory yield the weak gauge bosons W^\pm and Z through the mixing of the asso-
⁴⁸⁰ ciated gauge fields. The force carriers of this theory were experimentally detected by the
⁴⁸¹ observation of weak neutral current. This was first discovered in 1973 by the Gargamelle
⁴⁸² bubble chamber located at European Organisation for Nuclear Research (CERN) [10].
⁴⁸³ The masses of the weak gauge bosons were measured by the UA1 and U2 experiments at
⁴⁸⁴ the Super Proton Synchrotron (SPS) collider in 1983 [11][12].

⁴⁸⁵ 2.1.1. Gauge Symmetries of the SM

- ⁴⁸⁶ Symmetries are of fundamental importance in the description of physical phenomena.
⁴⁸⁷ Noether's theorem states that for a dynamical system, the consequence of any symmetry
⁴⁸⁸ is an associated conserved quantity [13]. Invariance under translations, rotations, and
⁴⁸⁹ Lorentz transformations in physical systems lead to the conservation of momentum,
⁴⁹⁰ energy and angular momentum.
- ⁴⁹¹ In the **SM**, a quantum theory described by Lagrangian formalism, the weak, strong and
⁴⁹² electromagnetic interactions are described in terms of “gauge theories”. A gauge theory
⁴⁹³ possesses invariance under a set of “local transformations”, which are transformations
⁴⁹⁴ whose parameters are space-time dependent. The requirement of gauge invariance within
⁴⁹⁵ the **SM** necessitates the introduction of force-mediating gauge bosons, and interactions
⁴⁹⁶ between fermions and the bosons themselves. Given the nature of the topics covered by
⁴⁹⁷ this thesis, the formulation of Electroweak Sector (**EWK**) within the **SM** Lagrangian is
⁴⁹⁸ reviewed within this section.
- ⁴⁹⁹ The simplest example of the application of the principle of local gauge invariance within
⁵⁰⁰ the **SM** is in Quantum Electro-Dynamics (**QED**), the consequences of which require a
⁵⁰¹ massless photon field [14][15].
- ⁵⁰² The free Dirac Lagrangian can be first written as

$$\mathcal{L} = \bar{\psi}(i\gamma^\mu \partial_\mu - m)\psi, \quad (2.1)$$

- ⁵⁰³ where ψ represents a free non interacting fermionic field, with the matrices γ^μ , $\mu \in 0, 1, 2, 3$
⁵⁰⁴ defined by the anti commutator relationship $\gamma^\mu \gamma^\nu + \gamma^\nu \gamma^\mu = 2\eta^{\mu\nu} I_4$, with $\eta^{\mu\nu}$ being the
⁵⁰⁵ flat space-time metric $(+, -, -, -)$, and I_4 the 4×4 identity matrix.
- ⁵⁰⁶ Under a local U(1) abelian gauge transformation, in which ψ transforms as

$$\psi(x) \rightarrow \psi'(x) = e^{i\theta(x)}\psi(x) \quad \bar{\psi}(x) \rightarrow \bar{\psi}'(x) = e^{i\theta(x)}\bar{\psi}(x) \quad (2.2)$$

- ⁵⁰⁷ the kinetic term of the Lagrangian will not remain invariant, due to the partial derivative
⁵⁰⁸ interposed between the $\bar{\psi}$ and ψ yielding

$$\partial_\mu \psi \rightarrow e^{i\theta(x)} \partial_\mu \psi + ie^{i\theta(x)} \psi \partial_\mu \theta. \quad (2.3)$$

To ensure that \mathcal{L} remains invariant, a modified derivative, D_μ , that transforms covariantly under phase transformations is introduced. In doing this, a vector field A_μ with transformation properties that cancel out the unwanted term in (2.3) must also be included,

$$D_\mu \equiv \partial_\mu - ieA_\mu, \quad A_\mu \rightarrow A_\mu + \frac{1}{e} \partial_\mu \theta. \quad (2.4)$$

Invariance of the Lagrangian is then achieved by replacing ∂_μ by D_μ :

$$\begin{aligned} \mathcal{L} &= i\bar{\psi}\gamma^\mu D_\mu \psi - m\bar{\psi}\psi \\ &= \bar{\psi}(i\gamma^\mu \partial_\mu - m)\psi + e\bar{\psi}\gamma^\mu \psi A_\mu \end{aligned} \quad (2.5)$$

An additional interaction term is now present in the Lagrangian, coupling the Dirac particle to this vector field, which is interpreted as the photon in QED. To regard this new field as the physical photon field, a term corresponding to its kinetic energy must be added to the Lagrangian from Equation (2.5). Since this term must also be invariant under the conditions of Equation (2.4), it is defined in the form $F_{\mu\nu} = \partial^\mu A^\nu - \partial^\nu A^\mu$.

This then leads to the Lagrangian of QED,

$$\mathcal{L}_{QED} = \underbrace{i\bar{\psi}\gamma^\mu \partial_\mu \psi - \frac{1}{4}F_{\mu\nu}F^{\mu\nu}}_{\text{kinetic term}} + \underbrace{m\bar{\psi}\psi}_{\text{mass term}} + \underbrace{e\bar{\psi}\gamma^\mu \psi A_\mu}_{\text{interaction term}}. \quad (2.6)$$

Within the Lagrangian there remains no mass term of the form $m^2 A_\mu A^\mu$, which is prohibited by gauge invariance. This implies that the gauge particle, the photon, must be massless.

523 2.1.2. The Electroweak Sector and Electroweak Symmetry

524 Breaking

525 The same application of gauge symmetry and the requirement of local gauge invariance
 526 can be used to unify QED and the Weak force in the Electroweak Sector (EWK).

527 The nature of EWK interactions is encompassed within a Lagrangian invariant under
 528 transformations of the group $SU(2)_L \times U(1)_Y$.

529 The weak interactions from experimental observation [16] are known to violate parity
 530 and are therefore not symmetric under interchange of left and right helicity fermions.

531 Thus, within the SM the left- and right-handed parts of these fermion fields are treated
 532 separately. A fermion field is then split into two left and right handed chiral components,
 533 $\psi = \psi_L + \psi_R$, where $\psi_{L/R} = (1 \pm \gamma^5)\psi$.

534 The $SU(2)_L$ group is the special unitary group of 2×2 matrices, U , satisfying $UU^\dagger = I$
 535 and $\det(U) = 1$. It may be written in the form $U = e^{-i\omega_i T_i}$, with the generators of the
 536 group written as $T_i = \frac{1}{2}\tau_i$ where τ_i , $i \in 1,2,3$ are the 2×2 Pauli matrices

$$\tau_1 = \begin{pmatrix} 0 & 1 \\ 1 & 0 \end{pmatrix} \quad \tau_2 = \begin{pmatrix} 0 & -i \\ i & 0 \end{pmatrix} \quad \tau_3 = \begin{pmatrix} 1 & 0 \\ 0 & -1 \end{pmatrix}. \quad (2.7)$$

537 The generators of the group form a non Abelian group obeying the commutation relation
 538 $[T^a, T^b] \equiv if^{abc}T^c \neq 0$. The gauge fields that accompany this group are represented by
 539 $\hat{W}_\mu = (\hat{W}_\mu^1, \hat{W}_\mu^2, \hat{W}_\mu^3)$ and act only on the left handed component of the fermion field ψ_L .

540 One additional generator, Y , which represents the hypercharge of the particle under
 541 consideration is introduced through the $U(1)_Y$ group acting on both components of the
 542 fermion field, with an associated vector boson field \hat{B}_μ .

543 The $SU(2)_L \times U(1)_Y$ transformations of the left- and right-handed components of ψ are
 544 summarised by,

$$\begin{aligned} \chi_L &\rightarrow \chi'_L = e^{i\theta(x) \cdot T + i\theta(x)Y} \chi_L, \\ \psi_R &\rightarrow \psi'_R = e^{i\theta(x)Y} \psi_R, \end{aligned} \quad (2.8)$$

545 where the left-handed fermions form isospin doubles χ_L and the right handed fermions
 546 are isosinglets ψ_R . For the first generation of leptons and quarks this represents

$$\chi_L = \begin{pmatrix} \nu_e \\ e \end{pmatrix}_L, \quad \begin{pmatrix} u \\ d \end{pmatrix}_L, \\ \psi_R = e_R, \quad u_R, d_R. \quad (2.9)$$

547 Local gauge invariance within \mathcal{L}_{EWK} is once again imposed by modifying the covariant
 548 derivative

$$D_\mu = \partial_\mu - \frac{ig}{2}\tau^i W_\mu^i - \frac{ig'}{2}YB_\mu, \quad (2.10)$$

549 where g and g' are the coupling constant of the $SU(2)_L$ and $U(1)_Y$ groups respectively.
 550 Taking the example of the first generation of fermions defined in Equation (2.9), with input
 551 hypercharge values of -1 and -2 for χ_L and e_R respectively, would lead to a Lagrangian
 552 \mathcal{L}_1 of the form,

$$\mathcal{L}_1 = \bar{\chi}_L \gamma^\mu [i\partial_\mu - g \frac{1}{2} \tau \cdot W_\mu - g' (-\frac{1}{2}) B_\mu] \chi_L \\ + \bar{e}_R \gamma^\mu [i\partial_\mu - g' (-1) B_\mu] e_R - \frac{1}{4} W_{\mu\nu} \cdot W^{\mu\nu} - \frac{1}{4} B_{\mu\nu} B^{\mu\nu}. \quad (2.11)$$

553 As in QED, these additional gauge fields introduce field strength tensors $B_{\mu\nu}$ and $W_{\mu\nu}$,

$$\hat{B}_{\mu\nu} = \partial_\mu \hat{B}_\nu - \partial_\nu \hat{B}_\mu \quad (2.12)$$

$$\hat{W}_{\mu\nu} = \partial_\mu \hat{W}_\nu - \partial_\nu \hat{W}_\mu - g \hat{W}_\mu \times \hat{W}_\mu \quad (2.13)$$

554 corresponding to the kinetic energy and self coupling of the W_μ fields and the kinetic
 555 energy term of the B_μ field.

556 None of these gauge bosons are physical particles, and instead linear combinations of
 557 these gauge bosons make up γ and the W and Z bosons, defined as

$$W^\pm = \frac{1}{\sqrt{2}} (W_\mu^1 \mp iW_\mu^2), \quad \begin{pmatrix} Z_\mu \\ A_\mu \end{pmatrix} = \begin{pmatrix} \cos\theta_W & -\sin\theta_W \\ \sin\theta_W & \cos\theta_W \end{pmatrix} \begin{pmatrix} W_\mu^3 \\ B_\mu \end{pmatrix}, \quad (2.14)$$

558 where the mixing angle, $\theta_w = \tan^{-1} \frac{g'}{g}$, relates the coupling of the neutral weak and
 559 electromagnetic interactions.

560 As in the case of the formulation of the QED Lagrangian there remains no mass term
 561 for the photon. However contrary to experimental measurement, this is also the case
 562 for the W, Z and fermions in the Lagrangian. Any explicit introduction of mass terms
 563 would break the symmetry of the Lagrangian, and instead mass terms can be introduced
 564 through spontaneous breaking of the EWK symmetry via the Higgs mechanism.

565 The Higgs mechanism induces spontaneous symmetry breaking through the introduction
 566 of a complex scalar SU(2) doublet field ϕ , which attains a non-zero Vacuum Expectation
 567 Value (VEV) [17][18][19][20].

$$\phi = \begin{pmatrix} \phi^+ \\ \phi^0 \end{pmatrix} \quad \text{with} \quad \begin{aligned} \phi^+ &\equiv (\phi_1 + i\phi_2)/\sqrt{2} \\ \phi^0 &\equiv (\phi_3 + i\phi_4)/\sqrt{2} \end{aligned} \quad (2.15)$$

568 The Lagrangian defined in Equation (2.11) attains an additional term \mathcal{L}_{Higgs} of the form

$$\mathcal{L}_{Higgs} = \overbrace{(D_\mu\phi)^\dagger(D^\mu\phi)}^{\text{kinetic}} - \overbrace{\mu^2\phi^\dagger\phi - \lambda(\phi^\dagger\phi)^2}^{\text{potential } V(\phi)} \quad (\mu^2, \lambda) > 0 \in \mathbb{R},$$

$$\mathcal{L}_{SM} = \mathcal{L}_{EWK} + \mathcal{L}_{Higgs}, \quad (2.16)$$

569 where the covariant derivative D_μ is that defined in Equation (2.10). The last two terms
 570 of \mathcal{L}_{Higgs} correspond to the Higgs potential, in which real positive values of μ^2 and λ are
 571 required to ensure the generation of masses for the bosons and leptons. The minimum of

572 this potential is found at $\phi^\dagger \phi = \frac{1}{2}(\phi_1^2 + \phi_2^2 + \phi_3^2 + \phi_4^2) = \mu^2/\lambda = v^2$, where v represents
573 the **VEV**.

574 The ground state of the ϕ field is defined to be consistent with the $V(\phi)$ minimum. By
575 then expanding around a ground state chosen to maintain an unbroken electromagnetic
576 symmetry. This preserves a zero photon mass [21] and leads to

$$\phi_0 = \sqrt{\frac{1}{2}} \begin{pmatrix} 0 \\ v \end{pmatrix}, \quad \phi(x) = e^{i\tau \cdot \theta(x)/v} \sqrt{\frac{1}{2}} \begin{pmatrix} 0 \\ v + h(x) \end{pmatrix}, \quad (2.17)$$

577 where the fluctuations from the vacuum ϕ_0 are parametrized in terms of four real fields,
578 $\theta_1, \theta_2, \theta_3$ and $h(x)$.

579 Choosing to gauge away the three massless Goldstone boson fields by setting $\theta(x)$ to
580 zero and substituting $\phi(x)$ back into kinetic term of \mathcal{L}_{Higgs} from Equation (2.16) leads
581 to mass terms for the W^\pm and Z bosons

$$(D_\mu \phi)^\dagger (D^\mu \phi) = \frac{1}{2} (\partial_\mu h)^2 + \frac{g^2 v^2}{2} W_\mu^+ W^{-\mu} + \frac{v^2 g^2}{8 \cos^2 \theta_w} Z_\mu Z^\mu + 0 A_\mu A^\mu, \quad (2.18)$$

582 where the relations between the physical and electroweak gauge fields from Equation
583 (2.14) are used. The W^\pm and Z boson masses can then be determined to be

$$M_W = \frac{1}{2} g v \quad M_Z = \frac{1}{2} \frac{g v}{\cos \theta_w}. \quad (2.19)$$

584 This mechanism is also used to generate fermion masses by introducing a Yukawa coupling
585 between the fermions and the ϕ field [22], with the coupling strength of a particle to the
586 ϕ field governing its mass. Additionally, a scalar boson h with mass $m_h = v \sqrt{\frac{\lambda}{2}}$, is also
587 predicted as a result of this spontaneous symmetry breaking. This became known as
588 the Higgs boson. Its discovery by the CMS and ATLAS experiments in 2012 is the first
589 direct evidence to support this method of mass generation within the SM.

590 2.2. Motivation for Physics beyond the Standard 591 Model

592 As has been described, the **SM** has proven to be a very successful theory, predicting the
593 existence of the W^\pm and Z bosons and the top quark long before they were experimentally
594 observed. However, the theory does not accurately describe all observed phenomena and
595 has some fundamental theoretical flaws that hint at the need for additional extensions to
596 the current theory.

597 On a theoretical level, the **SM** is unable to incorporate the gravitational interactions of
598 fundamental particles within the theory. Whilst at the electroweak energy scales the
599 relative strength of gravity is negligible compared to the other three fundamental forces,
600 at much higher energy scales, $M_{\text{planck}} \sim 10^{18} \text{GeV}$, quantum gravitational effects become
601 increasingly dominant. The failure to reconcile gravity within the **SM**, demonstrates that
602 the **SM** must become invalid at some higher energy scale.

603 Other deficiencies with the **SM** include the fact that the predicted rate of Charge-Parity
604 violation does not account for the matter dominated universe which we inhabit, and
605 that the **SM** prediction of a massless neutrino conflicts with the observation of neutrino
606 flavour mixing, attributed to mixing between neutrino mass eigenstates [23][24].

607 Perhaps one of the most glaring gaps in the predictive power of the **SM** is that there
608 exists no candidate to explain the cosmic dark matter observed in galactic structures
609 through indirect techniques; including gravitational lensing and measurement of the
610 orbital velocity of stars at galactic edges. Any such candidate must be very weakly
611 interacting but must also be stable, owing to the lack of direct detection of the decay
612 products of such a process. Therefore, a predicted stable dark matter candidate is one of
613 the main obstacles to address for any Beyond Standard Model (**BSM**) physics model.

614 The recent discovery of the Higgs boson, whilst a significant victory for the predictive
615 power of the **SM**, brings with it still unresolved questions. This issue is commonly
616 described as the “hierarchy problem”.

617 In the absence of new physics between the TeV and Planck scale, calculating beyond
618 tree-level contributions to the Higgs mass term given by its self interaction, results in
619 divergent terms that push the Higgs mass up to the planck mass M_{planck} .

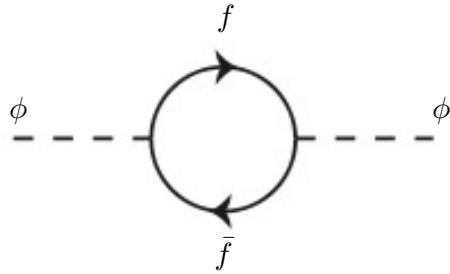


Figure 2.1: One loop quantum corrections to the Higgs squared mass parameter m_h^2 due to a fermion.

620 This can be demonstrated by considering the one loop quantum correction to the Higgs
 621 mass with a fermion f , shown in Figure 2.1 with mass m_f . The Higgs field couples to f
 622 with a term in the Lagrangian $-\lambda_f h \bar{f} f$, yielding a correction of the form [25],

$$\delta m_h^2 = -\frac{|\lambda_f|^2}{8\pi^2} \Lambda^2 + \dots, \quad (2.20)$$

623 where λ_f represents the coupling strength for each type of fermion $\propto m_f$, and Λ the
 624 cutoff energy scale at which the **SM** ceases to be a valid theory.

625 To recover the mass of the now discovered Higgs boson would require a fine-tuning of
 626 the parameters to cancel out these mass corrections of the Higgs mass, to the scale of
 627 30 orders of magnitude. This appears as an unnatural solution to physicists and it is
 628 this hierarchy problem that provides one of the strongest motivations for the theory of
 629 SUperSYmmetry (**SUSY**).

630 2.3. Supersymmetry Overview

631 Supersymmetry provides potential solutions to many of the issues raised in the previous
 632 section. It provides a dark matter candidate, can explain baryogenesis in the early
 633 universe and also provides an elegant solution to the hierarchy problem [26][27][28][29].
 634 At its heart it represents a new space-time symmetry that relates fermions and bosons.
 635 This symmetry converts bosonic states into fermionic states, and vice versa, see Equation
 636 (2.21),

$$Q|\text{Boson}\rangle = |\text{Fermion}\rangle \quad Q|\text{Fermion}\rangle = |\text{Boson}\rangle, \quad (2.21)$$

637 where the operator Q is the generator of these transformations. Quantum field theories
 638 which are invariant under such transformations are called supersymmetric.

639 This symmetry operator therefore acts upon a particle's spin altering it by a half integer
 640 value. The consequences of the application of this additional space-time symmetry
 641 introduce a new rich phenomenology. For example, in supersymmetric theories both
 642 the left handed $SU(2)$ doublet and right handed singlet of fermions will have a spin-0
 643 superpartner containing the same electric charge, weak isospin, and colour as its **SM**
 644 partner. In the case of leptons $(\nu_l, l)_L$, they will have two superpartners, a sneutrino $\tilde{\nu}_l{}_L$
 645 and a slepton \tilde{l}_L , whilst the singlet l_R also has a superpartner slepton \tilde{l}_R .

646 Each particle in a supersymmetric theory is paired together with their superpartners as a
 647 result of these supersymmetric transformations in what is called a supermultiplet. These
 648 superpartners will then consequently also contribute to the corrections to the Higgs mass.
 649 Bosonic and fermionic loops contributing to the correction appear with opposite signs,
 650 and therefore cancellation of these divergent terms will stabilise the Higgs mass, solving
 651 the hierarchy problem [30][31].

652 One of the simplest forms of **SUSY**, is to simply have a set of **SM** supersymmetric partners
 653 with the same mass and interactions as their counterparts. However, the current lack
 654 of any experimental evidence for that predicted sparticle spectrum implies **SUSY** must
 655 be a broken symmetry in which any sparticle masses must be greater than their **SM**
 656 counterparts.

657 There exists many techniques which can induce supersymmetric breaking [32][33][34]. Of
 658 particular interest to experimental physicists are those at which the breaking scale is
 659 of an order that is experimentally accessible to the **LHC** i.e. \sim TeV scale. Whilst
 660 there is no requirement for supersymmetric breaking to occur at this energy scale, for
 661 supersymmetry to provide a solution to the hierarchy problem, it is necessary for this
 662 scale to not differ too drastically from the **EWK** scale [35][36].

⁶⁶³ 2.3.1. R-Parity

⁶⁶⁴ Supersymmetric theories can also present a solution to the dark matter problem. These
⁶⁶⁵ theories contain a stable Lightest Supersymmetric Partner (**LSP**), which match the
⁶⁶⁶ criteria of a Weakly Interacting Massive Particle (**WIMP**) required by cosmological
⁶⁶⁷ observation when R-parity is conserved.

⁶⁶⁸ Baryon (B) and Lepton (L) number conservation is forbidden in the **SM** by renormal-
⁶⁶⁹ isability requirements. The violation of Baryon or Lepton number results in a proton
⁶⁷⁰ lifetime much shorter than those set by experimental limits [37]. Another symmetry
⁶⁷¹ called R-parity is then often introduced to **SUSY** theories to maintain baryon and lepton
⁶⁷² conservation.

⁶⁷³ R-parity is described by the equation

$$R_P = (-1)^{3(B-L)+2s}, \quad (2.22)$$

⁶⁷⁴ where s represents the spin of the particles. $B = \pm \frac{1}{3}$ for quarks/antiquarks and $B = 0$
⁶⁷⁵ for all others, $L = \pm 1$ for leptons/antileptons, $L = 0$ for all others.

⁶⁷⁶ R-parity ensures the stability of the proton in **SUSY** models, and also has other conse-
⁶⁷⁷ quences for the production and decay of supersymmetric particles. In particle colliders
⁶⁷⁸ supersymmetric particles can then only be pair produced. Similarly the decay of any
⁶⁷⁹ produced supersymmetric particle is restricted to a **SM** particle and a lighter supersym-
⁶⁸⁰ metric particle, as allowed by conservation laws. A further implication of R-parity is
⁶⁸¹ that once a supersymmetric particle has decayed to the **LSP** it remains stable, unable to
⁶⁸² decay into a **SM** particle.

⁶⁸³ A **LSP** will not interact in a detector at a particle collider, leaving behind a missing
⁶⁸⁴ energy \cancel{E}_T signature. The assumption of R-parity and its consequences are used to
⁶⁸⁵ determine the physical motivation and search strategies for **SUSY** at the **LHC**.

⁶⁸⁶ 2.4. Experimental Signatures of **SUSY** at the **LHC**

⁶⁸⁷ Should strongly interacting sparticles be within the experimental reach of the **LHC**, then
⁶⁸⁸ it is expected that they can be produced in a variety of ways:

- 689 • squark/anti-squark and gluino pairs can be produced via both gluon fusion and
690 quark/anti-quark scattering,
691 • a gluino and squark produced together via quark-gluon scattering,
692 • squark pairs produced via quark-quark scattering.

693 Whilst most **SUSY** searches invoke the requirement of R-parity to explore parameter
694 phase space, there still exist a whole plethora of possible **SUSY** model topologies, which
695 could yet be discovered at the **LHC**.

696 During the 2011 run period at $\sqrt{s} = 7$ TeV, particular models were used to benchmark
697 performance and experimental reach of both **CMS** searches and previous experiments.
698 The Compressed Minimal SuperSymmetric Model (**CMSSM**) was initially chosen for a
699 number of reasons [38]. One of the most compelling being the reduction of the up to 105
700 new parameters that can be introduced by **SUSY** (in addition to the existing 19 of the
701 **SM**), to just 5 extra free parameters. It was this simplicity, combined with the theory
702 not requiring any fine tuning of particle masses to produce experimentally verified **SM**
703 observables, that made it an attractive model to interpret physics results.

704 However, recent results from the **LHC** now strongly disfavour large swathes of **CMSSM**
705 parameter space [39][40][41]. In the face of such results a more pragmatic model indepen-
706 dent search strategy is now applied across most **SUSY** searches at the **LHC**, see Section
707 (2.4.1).

708 As previously stated, a stable **LSP** that exhibits the properties of a dark matter candidate
709 would be weakly interacting and therefore will not be directly detected in a detector
710 environment. Additionally, the cascade decays of supersymmetric particles to this **LSP**
711 state would also result in significant hadronic activity. These signatures will then be
712 characterised through large amounts of hadronic jets (see Section (3.3.1)), leptons and
713 a significant amount of missing energy dependent upon the size of the mass splitting
714 between the **LSP** and the supersymmetric particle it has decayed from.

715 The **SM** contains processes which can exhibit a similar event topology to that described
716 above, with the largest contribution coming from the general QCD multi-jet environ-
717 ment of a hadron collider. A multitude of different analytical techniques are used by
718 experimental physicists to reduce or estimate any reducible or irreducible backgrounds,
719 allowing a possible **SUSY** signature to be extracted. The techniques employed within
720 this thesis are described in great detail within Section (4.1).

721 2.4.1. Simplified Models

722 With such a variety of different ways for a **SUSY** signal to manifest itself, it is necessary
723 to be able to interpret experimental reach through the masses of gluinos and squarks
724 which can be excluded by experimental searches, rather than on a model specific basis.

725 This is accomplished through **SMS** models, which are defined by a set of hypothetical
726 particles and a sequence of their production and decay modes [42][43]. In the **SMS** models
727 considered within this thesis, only the production process for the two primary particles
728 are considered. Each primary particle can undergo a direct or a cascade decay through
729 an intermediate new particle. At the end of each decay chain there remains a neutral,
730 undetected **LSP** particle, denoted $\tilde{\chi}_{LSP}$ which can represent a neutralino or gravitino.
731 Essentially it is easier to consider each **SMS** with branching ratios set to 100%. The
732 masses of the primary particle and the **LSP** remain as free parameters, in which the
733 absolute value and relative difference between the primary and **LSP** particle alter the
734 kinematics of the event.

735 Different **SMS** models are denoted with a T-prefix, with a summary of the types interpreted
736 within this thesis listed below [44].

- 737 • **T1,T1xxxx**, models represent a simplified version of gluino pair production, with
738 each gluino (superpartner to the gluon) undergoing a three-body decay to a quark-
739 antiquark pair and the **LSP** (i.e. $\tilde{g} \rightarrow q\bar{q}\tilde{\chi}_{LSP}$). The resultant final state from this
740 decay is typically 4 jets + \cancel{E}_T in the absence of initial/final state radiation and
741 detector effects. xxxx denotes models in which the quarks are of a specific flavour,
742 typically t or b quark-antiquarks.
- 743 • **T2,T2xx**, models represent a simplified version of squark anti-squark production
744 with each squark undergoing a two-body decay into a light-flavour quark and **LSP**
745 (i.e. $\tilde{q} \rightarrow q\tilde{\chi}_{LSP}$). This results in final states with less jets than gluino mediated
746 production, typically 2 jets + \cancel{E}_T when again ignoring the effect of initial/final state
747 radiation and detector effects. xx models represent decays in which both the quark
748 and the squark within the decay is of a specific flavour, which in this thesis are
749 again \tilde{t}/t or \tilde{b}/b .

750 Models rich in b and t quarks are interpreted within this thesis as they remain of
751 particular interest within “Natural **SUSY**” scenarios [45][46]. The largest contribution
752 to the quadratic divergence in the Higgs mass parameter comes from a loop of top
753 quarks via the Yukawa coupling. Cancellation of these divergences can be achieved in

⁷⁵⁴ supersymmetric theories by requiring a light right-handed top squark, \tilde{t}_R , and left-handed
⁷⁵⁵ double $SU(2)_L$ doublet containing top and bottom squarks, $(\tilde{t}, \tilde{b})_L$ [47].

⁷⁵⁶ These theories therefore solve the hierarchy problem by predicting light \sim EWK scale third
⁷⁵⁷ generation sleptons, accessible at the LHC. Search strategies involving the requirement
⁷⁵⁸ of b-tagging (see Section (3.3.2)) are used to give sensitivity to these type of SUSY
⁷⁵⁹ scenarios and are discussed in greater detail within Chapter 4.

⁷⁶⁰ Two example decay chains are shown in Figure 2.2; the pair production of gluinos (T1)
⁷⁶¹ and the pair production of squarks (T2) decaying into SM particles and LSPs.

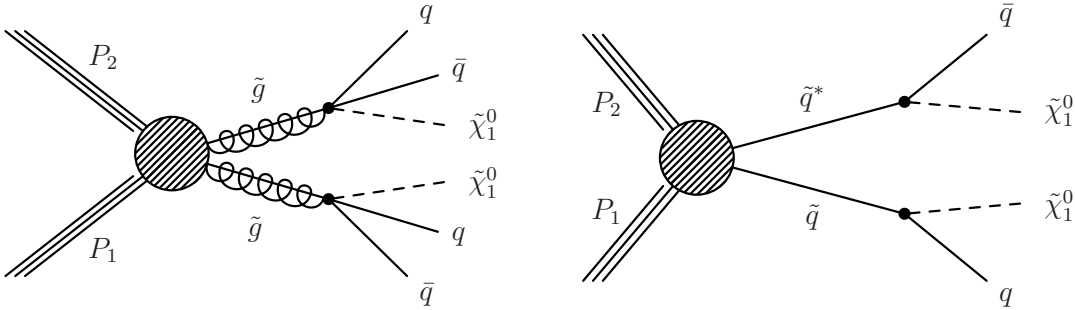


Figure 2.2: Two example SMS model decays (T1 (left), T2 (right)), which are used in interpretations of physics reach by CMS.

Chapter 3.

⁷⁶² The LHC and the CMS Detector

⁷⁶³ Probing the SM for signs of new physics would not be possible without the immensely
⁷⁶⁴ complex electronics and machinery that has made the TeV energy scale accessible to
⁷⁶⁵ physicists for the first time. This chapter will introduce both the LHC based at European
⁷⁶⁶ Organisation for Nuclear Research (CERN) and the Compact Muon Solenoid (CMS)
⁷⁶⁷ detector (of which the author is a member). Section (3.2) serves to present an overview of
⁷⁶⁸ the different components of the CMS detector, with specific components relevant to the
⁷⁶⁹ search for supersymmetric particles described in greater detail. Section (3.3) will focus
⁷⁷⁰ on event and object reconstruction, again, with more emphasis on jet level quantities
⁷⁷¹ which are most relevant to the author's analysis research. Finally, Section (3.4) will
⁷⁷² describe and detail the service work for the CMS Collaboration performed by the author,
⁷⁷³ in measuring the performance of L1 single jet and energy sum triggers in the Global
⁷⁷⁴ Calorimeter Trigger (GCT) during the 2012-2013 run period.

⁷⁷⁵ 3.1. The LHC

⁷⁷⁶ The LHC is a storage ring, accelerator, and collider of circulating beams of protons or ions.
⁷⁷⁷ Housed in the tunnel dug for Large Electron-Positron Collidor (LEP), it is approximately
⁷⁷⁸ 27km in circumference, 100m underground, and straddles the border between France and
⁷⁷⁹ Switzerland, outside of Geneva. It is currently the only collider in operation that is able
⁷⁸⁰ to study physics at the TeV scale. A double-ring circular synchrotron, it was designed
⁷⁸¹ to collide both proton-proton (pp) and heavy ion (PbPb) with a centre of mass energy
⁷⁸² $\sqrt{s} = 14$ TeV at a final design luminosity of $10^{34}\text{cm}^{-2}\text{s}^{-1}$.

⁷⁸³

These counter-circulating beams of protons or Pb ions are merged in four sections around the ring to enable collisions of the beams, with each interaction point being home to one of the four major experiments; A Large Ion Collider Experiment (**ALICE**) [48], A Toroidal LHC ApparatuS (**ATLAS**) [49], Compact Muon Solenoid (**CMS**) [50] and Large Hadron Collider Beauty (**LHCb**) [51] which record the resultant collisions. The layout of the **LHC** ring is shown in Figure 3.1. The remaining four sections contain acceleration, collimation and beam dump systems. In the eight arc sections, the beams are steered by magnetic fields of up to 8 T provided by super conduction dipole magnets, which are maintained at temperatures of 2 K using superfluid helium. Additional magnets for focusing and corrections are also present in straight sections within the arcs and near the interaction regions where the detectors are situated.

795

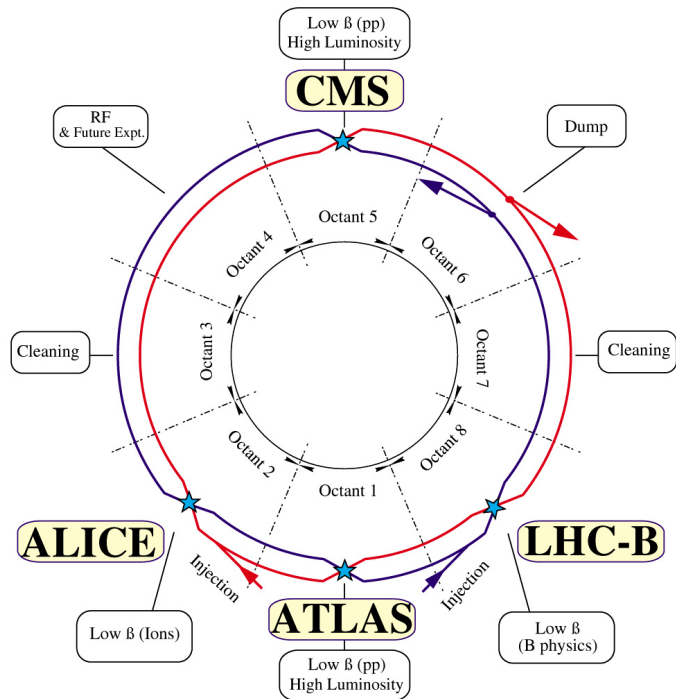


Figure 3.1: A top down layout of the LHC. [52], with the position of the four main detectors labelled.

Proton beams are formed inside the Proton Synchrotron (**PS**) from bunches of protons 50 ns apart with an energy of 26 GeV. The protons are then accelerated in the Super Proton Synchrotron (**SPS**) to 450 GeV before being injected into the **LHC**. These **LHC** proton beams consists of many “bunches” (i.e. approximately 1.1×10^{11} protons localised into less than 1 ns in the direction of motion). Before collision, the beams are ramped to

801 4 TeV (2012) per beam, in a process involving increasing the current passing through
 802 the dipole magnets. Once the desired \sqrt{s} energy is reached then the beams are allowed
 803 to collide at the interaction points. The luminosity falls regularly as the run progresses;
 804 protons are lost in collisions, and eventually the beam is dumped before repeating the
 805 process again.

806 Colliding the beams produced an instantaneous luminosity of approximately 5×10^{33}
 807 $\text{cm}^{-2}\text{s}^{-1}$ during the 2012 run. The high number of protons in each bunch increases
 808 the likelihood of multiple interactions with each crossing of the counter-circulating
 809 beams. This leads to isotropic energy depositions within the detectors positioned at these
 810 interaction points, increasing the energy scale of the underlying event. This is known
 811 as *pile-up* and the counteracting of its effects are important to the many measurements
 812 performed at the [LHC](#).

813 In the early phase of prolonged operation, after the initial shutdown, the machine operated
 814 in 2010-2011 at 3.5 TeV per beam, $\sqrt{s} = 7$ TeV, delivering 6.13 fb^{-1} of data [53]. During
 815 the 2012-2013 run period, data was collected at an increased $\sqrt{s} = 8$ TeV improving the
 816 sensitivity of searches for new physics. Over the whole run period 23.3 fb^{-1} of data was
 817 delivered, of which 21.8 fb^{-1} was recorded by the [CMS](#) detector as shown in Figure 3.2
 818 [53]. A total of 12 fb^{-1} of 8 TeV certified data was collected by October 2012, and it is
 819 this data which forms the basis of the results presented within this thesis.

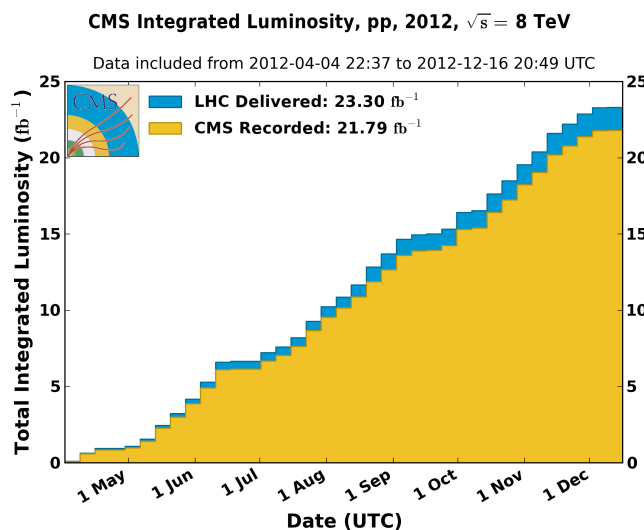


Figure 3.2: The total integrated luminosity delivered to and collected by [CMS](#) during the 2012 8 TeV *pp* runs.

820 3.2. The CMS Detector

821 The Compact Muon Solenoid (**CMS**) detector is one of two general purpose detectors
 822 at the **LHC** designed to search for new physics. The detector is designed to provide
 823 efficient identification and measurement of many physics objects including photons,
 824 electrons, muons, taus, and hadronic showers over wide ranges of transverse momentum
 825 and direction. Its nearly 4π coverage in solid angle allows for accurate measurement of
 826 global transverse momentum imbalance. These design factors give **CMS** the ability to
 827 search for direct production of **SUSY** particles at the TeV scale, making the search for
 828 Supersymmetric particles one of the highest priorities among the wide range of physics
 829 programmes at **CMS**.

830 **CMS** uses a right-handed Cartesian coordinate system with the origin at the interaction
 831 point and the z-axis pointing along the beam axis. The x-axis points radially inwards to
 832 the centre of the collider ring, with the y-axis points vertically upward. The azimuthal
 833 angle ϕ , ranging between $[-\pi, \pi]$, is defined in the x-y plane starting from the x-axis. The
 834 polar angle θ is measured from the z axis. The common convention in particle physics is
 835 to express an out-going particle in terms of ϕ and its pseudorapidity defined as

$$\eta = -\log \tan \left(\frac{\theta}{2} \right). \quad (3.1)$$

836 The variable $\Delta R = \sqrt{\Delta\phi^2 + \Delta\eta^2}$ is commonly used to define angular distance between
 837 objects within the detector. Additionally, energy and momentum is typically measured in
 838 the transverse plane perpendicular to the beam line. These values are calculated from the
 839 x and y components of the object and are denoted as $E_T = E \sin \theta$ and $p_T = \sqrt{p_x^2 + p_y^2}$.

840 3.2.1. Detector Subsystems

841 As the range of particles produced from pp collisions interact in different ways with
 842 matter, **CMS** is divided into sub-detector systems, which perform complementary roles
 843 to identify the identity, the mass, and the momentum of different physics objects present
 844 in each event. These detector sub-systems contained within **CMS** are wrapped in layers
 845 around a central 13m long 4 T super conducting solenoid, as shown in Figure 3.3. With
 846 the endcaps closed, **CMS** is a cylinder of length 22m, diameter 15m, and mass 12.5

847 kilotons. A more detailed complete description of the detector can be found elsewhere [50].

848

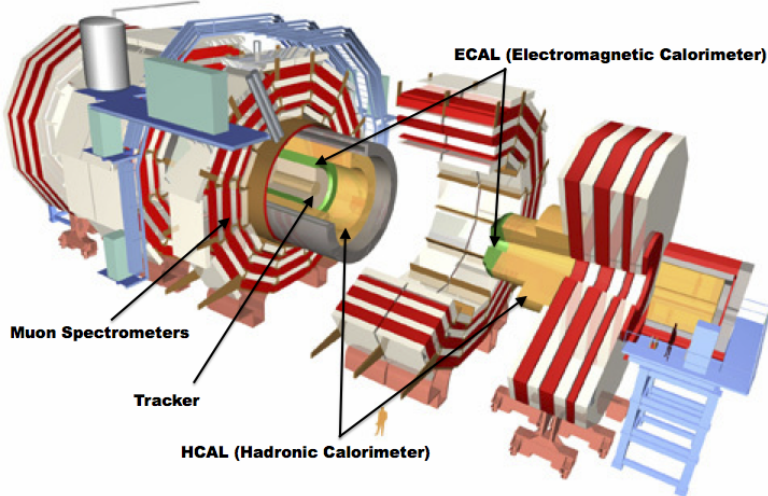


Figure 3.3: A pictorial depiction of the CMS detector with the main detector subsystems labelled [54].

849 3.2.2. Tracker

850 The inner-most sub-detector of the barrel is the multi-layer silicon tracker, formed of a
 851 pixel detector component encased by layers of silicon strip detectors. The pixel detector
 852 consists of three layers of silicon pixel sensors providing measurements of the momentum,
 853 position coordinates of the charged particles as they pass, and the location of primary
 854 and secondary vertices between 4 cm and 10 cm transverse to the beam. Outside the
 855 pixel detector, ten cylindrical layers of silicon strip detectors extend the tracking system
 856 out to a radius of 1.20m from the beam line. The tracking system provides efficient
 857 and precise determination of the charges, momenta, and impact parameters of charged
 858 particles, with the geometry of the tracker extending to cover a rapidity range up to $|\eta| <$
 859 2.5.

860

861 The tracking system also plays a crucial part in the identification of jets that originate
 862 from b-quarks through the measurement of displaced secondary vertices. The methods
 863 in which these b-flavoured jets are identified are discussed within Section (3.3.2). The
 864 identification of b-jets is important in many searches for natural SUSY models and forms
 865 an important part of the inclusive search strategy described within Section (4.2).

⁸⁶⁶ **3.2.3. Electromagnetic Calorimeter**

⁸⁶⁷ Immediately outside of the tracker, but still within the magnet core, sits the Electromagnetic CALorimeter (**ECAL**). Covering a pseudorapidity up to $|\eta| < 3$ and comprising ⁸⁶⁸ ⁸⁶⁹ of over 75×10^3 PbWO₄ (lead tungstate) crystals that scintillate as particles deposit ⁸⁷⁰ energy, the **ECAL** provides high resolution measurements of the electromagnetic showers ⁸⁷¹ from photons and electrons in the detector.

⁸⁷²

⁸⁷³ Lead tungstate is used because of its short radiation length ($X_0 \sim 0.9$ cm) and small ⁸⁷⁴ Molieré radius (~ 2.1 cm) leading to high granularity and resolution. Its fast scintillation ⁸⁷⁵ time (~ 25 ns) reduces the effects of pile-up, which occurs when energy from previous ⁸⁷⁶ collisions are still being read out, and its radiation hardness gives it longevity. The ⁸⁷⁷ crystals are arranged in modules which surround the beam line in a non-projective ⁸⁷⁸ geometry, angled at 3° , with respect to the interaction point to minimise the risk of ⁸⁷⁹ particles escaping down the cracks between the crystals.

⁸⁸⁰

⁸⁸¹ The **ECAL** is primarily composed of two sections, the Electromagnetic CALorimeter ⁸⁸² Barrel (**EB**) which extends in pseudo-rapidity to $|\eta| < 1.479$ with a crystal front cross section of 22×22 mm and a length of 230 mm corresponding to 25.8 radiation lengths. The ⁸⁸³ ⁸⁸⁴ Electromagnetic CALorimeter Endcap (**EE**) covers a rapidity range of $1.479 < |\eta| < 3.0$, ⁸⁸⁵ which consists of two identical detectors on either side of the **EB**. A lead-silicon sampling ⁸⁸⁶ ‘pre-shower’ detector Electromagnetic CALorimeter pre-Shower (**ES**) is placed before ⁸⁸⁷ the endcaps to aid in the identification of neutral pions. Their arrangement is shown in ⁸⁸⁸ Figure 3.4.

⁸⁸⁹

⁸⁹⁰ Scintillation photons from the lead tungstate crystals are instrumented with Avalanche ⁸⁹¹ Photo-Diodes (**APD**) and Vacuum Photo-Triodes (**VPT**), located in the **EB** and **EE** ⁸⁹² respectively. They convert the scintillating light into an electric signal which is conse- ⁸⁹³ quently used to determine the amount of energy deposited within the crystal. These ⁸⁹⁴ instruments are chosen for their resistance under operation to the strong magnetic field ⁸⁹⁵ of **CMS**. The scintillation of the **ECAL** crystals, as well as the response of the **APDs**, ⁸⁹⁶ vary as a function of temperature; and so cooling systems continually maintain an overall ⁸⁹⁷ constant **ECAL** temperature $\pm 0.05^\circ C$.

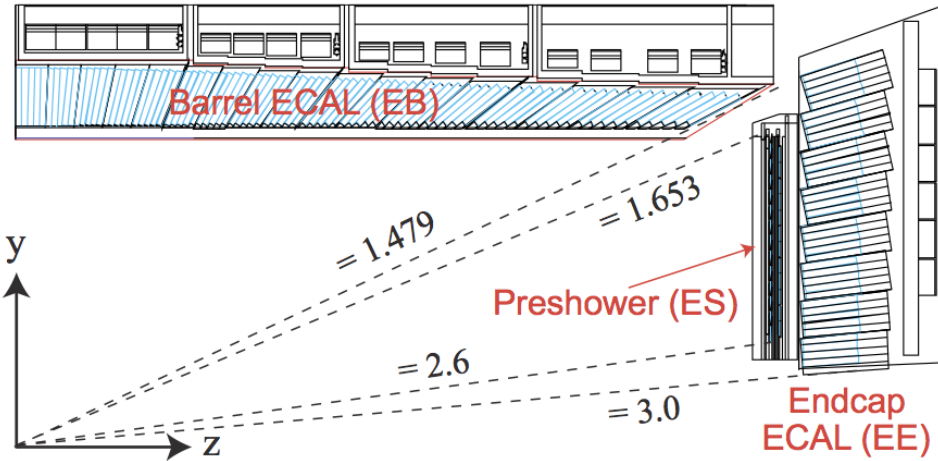


Figure 3.4: Illustration of the CMS ECAL showing the arrangement of the lead tungstate crystals in the EB and EE. The ES is also shown and is located in front of the EE [55].

3.2.4. Hadronic Calorimeter

Beyond the ECAL lies the Hadronic CALorimeter (HCAL) which is responsible for the accurate measurement of hadronic showers, crucial for analyses involving jets or missing energy signatures. The HCAL is a sampling calorimeter which consists of alternating layers of brass absorber and plastic scintillator. The exception being in the hadron forward ($3.0 < |\eta| < 5.0$) region where steel absorbers and quartz fibre scintillators are used because of their increased radiation tolerance. Hadron showers are initiated in the absorber layers inducing scintillation in the plastic scintillator tiles. These scintillation photons are converted by wavelength shifting fibres for read-out by hybrid photodiodes.

907

The HCAL's size is constrained to a compact size by the presence of the solenoid, requiring the placement of an additional outer calorimeter on the outside of the solenoid to increase the sampling depth of the HCAL. A schematic of the HCAL can be seen in Figure 3.5.

912

The HCAL covers the range $|\eta| < 5$ and consists of four sub-detectors: the Hadron Barrel (HB) $|\eta| < 1.3$, the Hadron Outer (HO), the Hadron Endcaps (HE) $1.3 < |\eta| < 3.0$ and the Hadron Forward (HF). The HB, contained between the outer edge of the ECAL and the inner edge of the solenoid is formed of 36 azimuthal wedges which are split

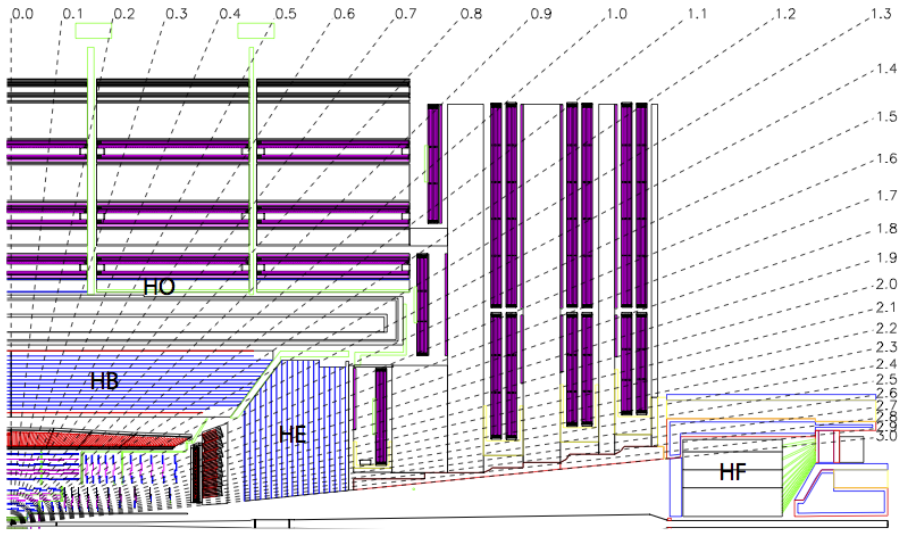


Figure 3.5: Schematic of the hadron calorimeters in the r-z plane, showing the locations of the **HCAL** components and the **HF**. [50].

917 between two half-barrel segments. Each wedge is segmented into four azimuthal angle
 918 (ϕ) sectors, and each half-barrel is further segmented into 16 η towers. The electronic
 919 readout chain, channels the light from the active scintillator layers from one ϕ -segment
 920 and all η -towers of a half-barrel to a Hybrid Photo Diode (**HPD**).

921 The relatively short number of interaction lengths (λ_l , the distance a hadron will travel
 922 through the absorber material before it has lost $\frac{1}{e}$ of its energy) within the **HB**, the lowest
 923 being $\lambda_l = 5.82$ at $|\eta| = 0$, facilitates the need for the ‘tail catching’ **HO** to increase the
 924 sampling depth in the central barrel rapidity region $|\eta| < 1.3$ to 11 interaction lengths.
 925 Significant fractions of the hadrons energy will also be deposited in the **ECAL** as it passes
 926 through the detector. Therefore, measurements of hadron energies in the central regions
 927 $|\eta| < 3.0$ use both the **ECAL** and **HCAL** to reconstruct the true energy from showering
 928 hadrons.

929 3.2.5. Muon Systems

930 Muons being too massive to radiate away energy via Bremsstrahlung, interact little in
 931 the calorimeters and mostly pass through the detector until they reach the system of
 932 muon detectors which forms the outer most part of the **CMS** detector.

933 Outside of the superconducting solenoid are four muon detection layers interleaved with
934 the iron return yokes, which measure the muons energy via ionisation of gas within
935 detector elements. Three types of gaseous chambers are used. The Drift Tube (**DT**),
936 Cathode Stripe Chamber (**CSC**), and Resistive Plate Chamber (**RPC**) systems provide
937 efficient detection of muons with pseudo-rapidity $|\eta| < 2.4$. The best reconstruction
938 performance is obtained when the muon chamber is combined with the inner tracking
939 information to determine muon trajectories and their momenta [56].

940

941 3.3. Event Reconstruction and Object Definition

942 The goal of event reconstruction is to take the raw information recorded by the detector
943 and to compute from it higher-level quantities which can be used at an analysis level.
944 These typically correspond to an individual particle’s energy and momenta, groups of
945 particles which shower in a narrow cone, and the overall global energy and momentum
946 balance of the event. The reconstruction of these objects are described in great detail in
947 [57], while covered below are brief descriptions of those which are most relevant to the
948 analysis detailed in Chapter 4.

949 3.3.1. Jets

950 Quarks and gluons are produced copiously at the LHC in the hard scattering of partons.
951 As these quarks and gluons fragment, they hadronize and decay into a group of strongly
952 interactive particles and their decay products. These streams of particles travel in the
953 same direction, as they have been “boosted” by the momentum of the primary hadron.
954 These collections of decay products are reconstructed and identified together as a “jet”.

955 At **CMS** jets are reconstructed from energy deposits in the detector via the anti-kt
956 algorithm [58] with size parameter $\Delta R = 0.5$. The anti-kt jet algorithm clusters jets by
957 defining a distance between hard (high p_T) and soft (low p_T) particles such that soft
958 particles are preferentially clustered with hard particles before being clustered between
959 themselves. This produces jets which are robust to soft particle radiation from the pile-up
960 conditions produced by the **LHC**.

961 There are two main types of jet reconstruction used at **CMS**, Calorimeter (Calo) and
962 Particle Flow (PF) jets [59]. Calorimeter jets are reconstructed using both the **ECAL**
963 and **HCAL** cells, combined into calorimeter towers. These calorimeter towers consist of
964 geometrically matched **HCAL** cells and **ECAL** crystals. Electronics noise is suppressed by
965 applying a threshold to the calorimeter cells, with pile-up effects reduced by a requirement
966 placed on the tower energy [60]. Calorimeter jets are the jets used within the analysis
967 presented in this thesis.

968 PF jets are formed from combining information from all of the **CMS** sub-detectors systems
969 to determine which final state particles are present in the event. Generally, any particle
970 is expected to produce some combination of a track in the silicon tracker, a deposit in
971 the calorimeters, or a track in the muon system. The PF jet momentum and spatial
972 resolutions are greatly improved with respect to calorimeter jets, as the use of the tracking
973 detectors and of the high granularity of **ECAL** allows resolution and measurement of
974 charged hadrons and photons inside a jet, which together constitute $\sim 85\%$ of the jet
975 energy [61].

976 The jets reconstructed by the clustering algorithm in **CMS** typically have an energy
977 that differs to the ‘true’ energy measured by a perfect detector. This stems from the
978 non-linear and nonuniform response of the calorimeters as well as other residual effects
979 including pile-up and underlying events. Therefore, additional corrections are applied to
980 recover a uniform relative response as a function of pseudo-rapidity. These are applied
981 as separate sub corrections [62].

- 982 • A pile-up correction is first applied to the jet. It subtracts the average extra energy
983 deposited in the jet that comes from other vertices present in the event and is
984 therefore not part of the hard jet itself.
- 985 • p_T and η dependant corrections derived from Monte Carlo simulations are used to
986 account for the non-uniform response of the detector.
- 987 • p_T and η residual corrections are applied to data only to correct for difference
988 between data and Monte Carlo. The residual is derived from QCD di-jet samples
989 and the p_T residual from $\gamma+$ jet and $Z+$ jets samples in data.

990 3.3.2. B-tagging

991 The decays of b quarks are suppressed by small CKM matrix elements. As a result, the
 992 lifetimes of b-flavoured hadrons, produced in the fragmentation of b quarks, are relatively
 993 long; \mathcal{O} 1ps. The identification of jets originating from b quarks is very important for
 994 searches for new physics and for measurements of SM processes.

995

996 Many different algorithms developed by CMS select b-quark jets based on variables such
 997 as; the impact parameters of the charged-particle tracks, the properties of reconstructed
 998 decay vertices, and the presence or absence of a lepton, or combinations thereof.

999 One of the most efficient of which is the Combined Secondary Vertex (CSV) algorithm
 1000 [63]. This operates based on secondary vertex and track-based lifetime information,
 1001 benchmarked in ‘Loose’, ‘Medium’ and ‘Tight’ working points, of which the medium
 1002 point is the tagger used within the α_T search presented in Section (4.1). All figures
 1003 within this sub-section, demonstrating the performance of this b-tagging algorithm are
 1004 taken from [64].

1005 Within the CSV tagger, a likelihood-based discriminator distinguishes between jets from
 1006 b-quarks, and those from charm or light quarks and gluons, shown in Figure 3.6. The
 1007 minimum thresholds on the discriminator for each working point correspond to the
 1008 mis-identification probability for light-parton jets of 10%, 1%, and 0.1%, respectively, in
 1009 jets with an average p_T of about 80 GeV.

1010 The b-tagging performance is evaluated to measure the b-jet tagging efficiency ϵ_b , and the
 1011 misidentification probability of charm ϵ_c and light-parton jets ϵ_s . The tagging efficiencies
 1012 for each of these three jet flavours are compared between data and MC simulation, from
 1013 which a series of p_T and $|\eta|$ dependant jet corrections are determined,

$$SF_{b,c,s} = \frac{\epsilon_{b,c,s}^{data}}{\epsilon_{b,c,s}^{MC}}. \quad (3.2)$$

1014 These are collectively named ‘Btag Scale Factors’ and allow MC simulation to accu-
 1015 rately reflect the running conditions and performance of the tagging algorithm in data.
 1016 Understanding of the b-tagging efficiency is essential in order to minimise systematic

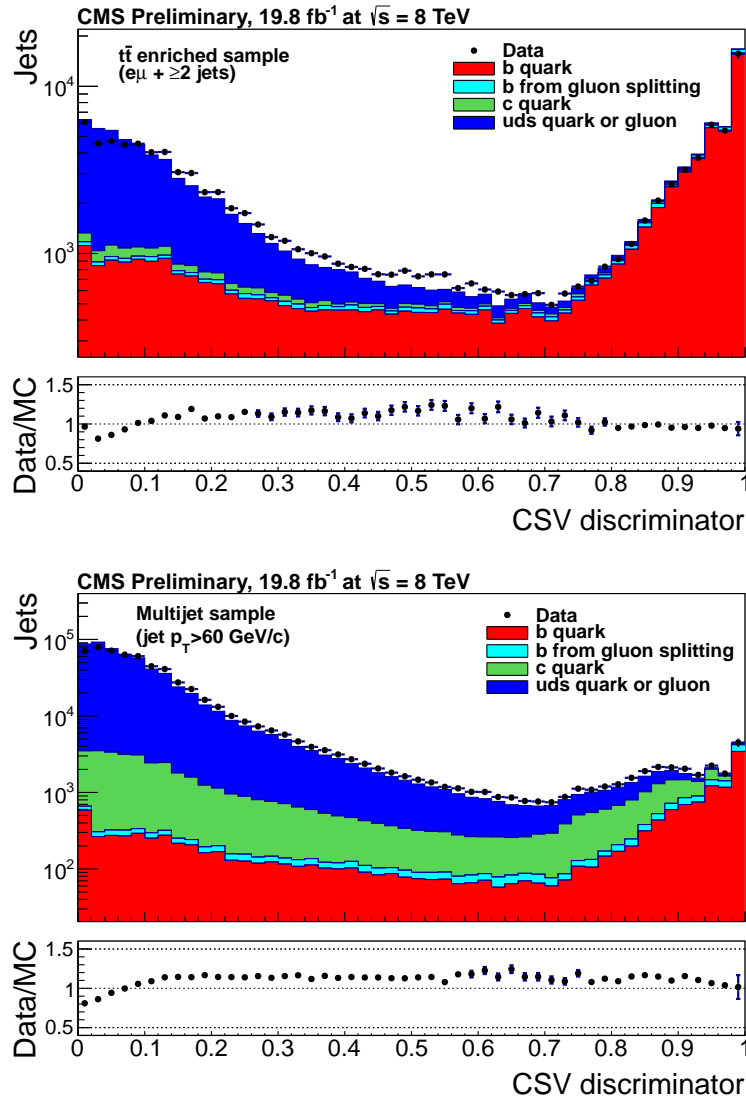


Figure 3.6: CSV algorithm discriminator values in enriched $t\bar{t}$ (top) and inclusive multi-jet samples (bottom) for b,c and light flavoured jets. The discriminator value used for each working points are determined from the misidentification probability for light-parton jets to be tagged as a b-jet, which are given as 0.244 (10%), 0.679 (1%) and 0.898 (0.1%) for the L, M and T working points respectively.

¹⁰¹⁷ uncertainties in physics analyses that employ b-tagging.

¹⁰¹⁸

¹⁰¹⁹ The b-tagging efficiency is measured in data using several methods applied to multi-jet
¹⁰²⁰ events, primarily based on a sample of jets enriched in heavy flavour content. One method
¹⁰²¹ requires the collection of events with a poorly isolated muon within a cone $\Delta R < 0.4$
¹⁰²² around the jet axis. Due to the semi-leptonic branching fraction of b hadrons being

significantly larger than that for other hadrons, these jets are more likely to arise from b quarks than from another flavour. The resultant momentum component of the muon, transverse to the jet axis, is larger in b-hadron decays than from light or charm flavoured jets.

Additionally, the performance of the tagger can also be benchmarked in $t\bar{t}$ events, where the top quark is expected to decay to a W boson and a b quark about 99.8% of the time [1]. Further selection criteria is applied to these events to further enrich the b quark content of these events. The methods to identify b-jets in data are discussed in great detail at [65]. The jet flavours within simulation are determined using truth level information and are compared to data to determine the appropriate correction scale factors (SF_b). These are displayed for the CSVM tagger in Figure 3.7.

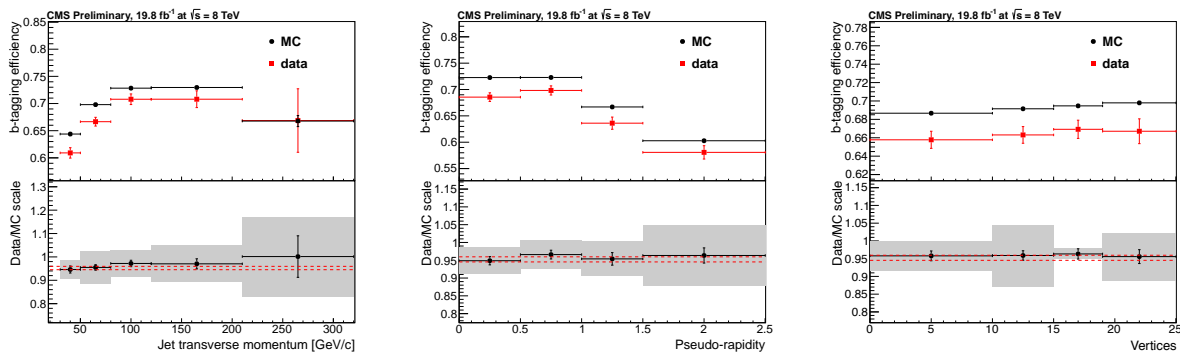


Figure 3.7: Measured in $t\bar{t} \rightarrow$ di-lepton events using the CSVM tagger: (upper panels) b-tagging efficiencies and (lower panels) data/MC scale factor SF_b as a function of (left) jet p_T , (middle) jet $|\eta|$ and (right) number of primary vertices. In the lower panels, the grey filled areas represent the total statistical and systematic uncertainties, whereas the dotted lines are the average SF_b values within statistical uncertainties.

The measurement of the misidentification probability for light-parton jets relies on the inversion of tagging algorithms, selecting non-b jets using the same variables and techniques used for benchmarking the b-tagging efficiency. The scale factors (SF_s) to be applied to correct simulation to data are shown in Figure 3.8 for the CSVM tagger.

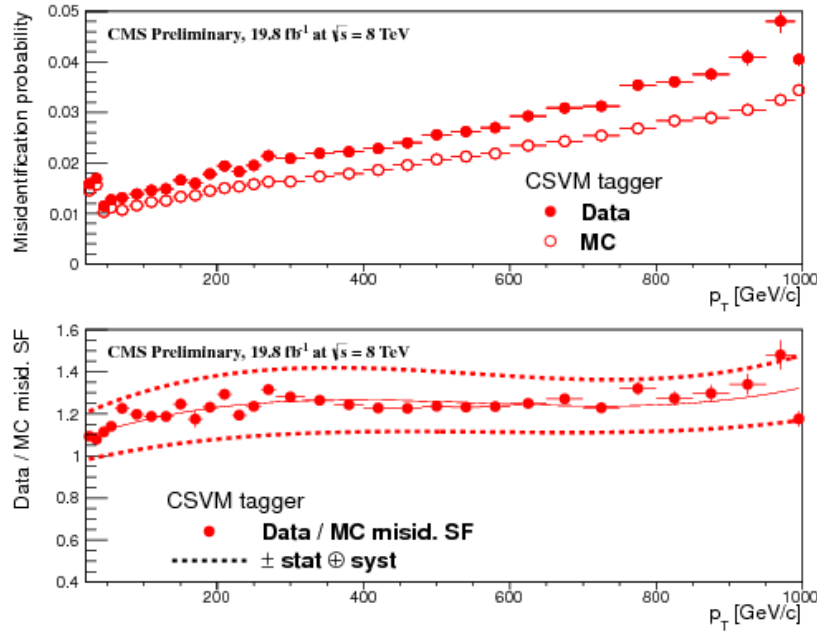


Figure 3.8: For the CSVM tagging criterion: (top) misidentification probability in data (filled circles) and simulation (open circles); (bottom) scale factor for the misidentification probability. The last p_T bin in each plot includes all jets with $p_T > 1000$ GeV. The solid curve is the result of a polynomial fit to the data points. The dashed curves represent the overall statistical and systematic uncertainties on the measurements.

1038 3.4. Triggering System

1039 With bunch crossings separated by just 50 ns, the rate at which data from all collisions
 1040 would have to be written out and processed would be unfeasible. A two-tiered triggering
 1041 system is applied at CMS in order to cope with the high collision rate of protons. The
 1042 CMS trigger is designed to use limited information from each event to determine whether
 1043 to record the event, reducing the rate of data taking to manageable levels whilst ensuring
 1044 a high efficiency of interesting physics object events are selected.

1045 The L1 is a pipelined, dead-timeless system based on custom-built electronics [66], and is
 1046 a combination of several sub systems which is shown pictorially in Figure 3.9. The L1
 1047 system is covered in more detail within the following section, along with a description
 1048 of the service work undertaken by the author to benchmark the performance of the L1
 1049 calorimeter trigger during the 2012 8 TeV run period.

1050 The Higher Level Trigger (HLT) is a large farm of commercial computers [67]. The HLT
 1051 processes events with software reconstruction algorithms that are more detailed, giving
 1052 performance more similar to the reconstruction used offline. The HLT reduces the event

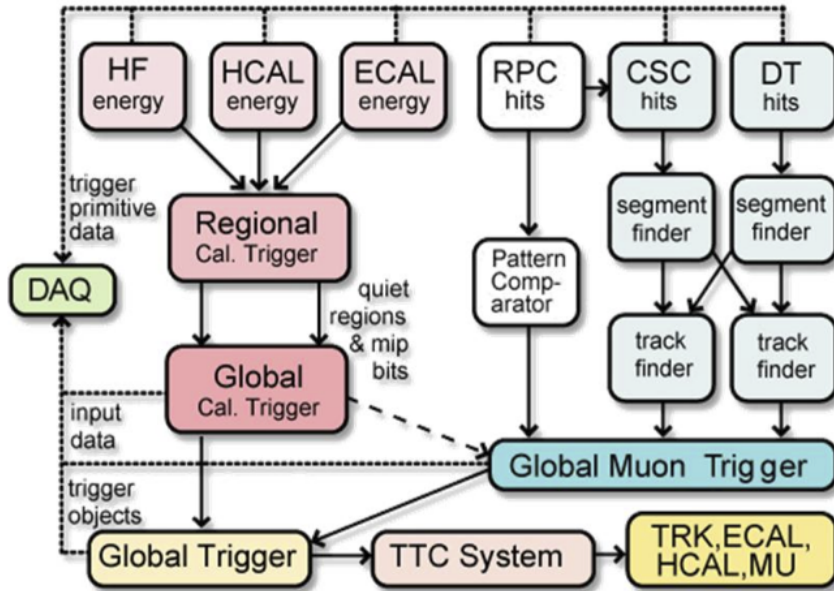


Figure 3.9: The CMS L1 Trigger system.

1053 rate written to disk by a factor of ~ 500 ($\sim 200\text{Hz}$). The recorded events are transferred
 1054 from CMS to the CERN computing centre, where event reconstruction is performed, and
 1055 then distributed to CMS computing sites around the globe for storage and analysis.

1056 3.4.1. The Level-1 Trigger

1057 The L1 trigger reduces the rate of events collected from 40 MHz to $\sim 100\text{ kHz}$ using
 1058 information from just the calorimeters and muon chambers, but not the tracker. This
 1059 is due to requirement that data from each and every bunch crossing be analysed with
 1060 no dead time, drastically reducing time available to process and reconstruct objects in
 1061 making a trigger decision. This facilitates the need for a pipelined processing architecture,
 1062 and so a tree system of triggers is used to decide whether to pass on an event to the HLT
 1063 for further reconstruction.

1064 Calorimeter and muon event information is processed separately by the Regional Calorime-
 1065 ter Trigger (RCT) and Regional Muon Trigger (RMT) systems respectively.

1066 Within the RCT, energy deposits from trigger towers in the ECAL and HCAL calorimeters
 1067 are summed into coarser calorimeter regions and sent to the Global Calorimeter Trigger
 1068 (GCT) for jet clustering.

1069 Given that electron and photon are much narrower objects than jets, the **RCT** is used
1070 to identify these candidates but makes no attempt to distinguish between them at this
1071 stage given the lack of tracking information. They are first identified by ensuring the
1072 energy deposits within the central trigger tower and its surrounding cells are above a
1073 certain programmable threshold. To ensure the object is not a hadron, the ratio of **HCAL**
1074 to **ECAL** in the central tower is calculated and checked to be below 5%. Additional
1075 algorithms are employed to ascertain whether the e/γ object is isolated/non-isolated.

1076 In the L1 **GCT**, coarse measurements of the energy deposited in the electromagnetic and
1077 hadronic calorimeters are combined, and by using sophisticated algorithms the following
1078 tasks are performed:

- 1079 • isolated and non-isolated electromagnetic objects are sorted (e and γ), with the four
1080 highest ranked (equivalent to highest transverse energy E_T) objects of each type
1081 passed onto the Global Trigger (**GT**),
- 1082 • energy sums from the calorimeters supplied by the **RCT** are used in performing
1083 jet clustering (described in the following section). The clustered jets are then
1084 sub-divided into categories depending on their pseudo-rapidity and the result of
1085 τ identification, being classified as either central, forward, or tau (τ). After being
1086 sorted by rank, the four highest of each category are passed to the **GT** for use in
1087 trigger decisions,
- 1088 • total transverse energy (E_T), the scalar sum of the energy deposits measured by
1089 L1, and missing transverse energy (\cancel{E}_T), defined as the negative vector sum of the
1090 transverse energy deposits measured at L1 are calculated,
- 1091 • total transverse jet energy (H_T), the scalar sum of the energy of all L1 clustered jet
1092 objects, and missing transverse jet energy (\cancel{H}_T), defined as the negative vector sum
1093 of the energy from L1 clustered jet objects are calculated and passed to the **GT**.

1094 In addition, quantities suitable for triggering minimum bias events, forward physics and
1095 beam background events are determined. Relevant muon isolation information is also
1096 passed on to the Global MuonTrigger (**GMT**) to be used in decisions involving the muon
1097 triggers, where it is combined with information from across the three muon sub-systems.
1098 The resultant final accept/reject decision at **L1** is then performed by the **GT**, based on
1099 the objects received from the **GCT** and **GMT** (e/γ , μ , jets, E_T , \cancel{E}_T , H_T , \cancel{H}_T).

1100 The L1 trigger is therefore of upmost importance to the functioning of the detector.
1101 Without a high-performing, efficient trigger and a good understanding of its performance

at ever increasing instantaneous luminosities, the data collected would be useless. Whilst it would be possible to maintain trigger efficiency by increasing the triggering thresholds for different jet or energy sum quantities, this is far from ideal. This could result in the failure to be sensitive to a wide range of new physics signatures, including many types of compressed spectra **SUSY** models where the mass splitting between squarks/gluinos and the **LSP** is small.

One such method introduced to help maintain low triggering thresholds, was via the introduction of a jet seed threshold into the L1 jet clustering algorithm. Observations of how the L1 trigger performance is affected by both the jet seed threshold, and changing **LHC** running conditions over the 2012 run period is presented in the following Sections (3.4.2 - 3.4.6).

3.4.2. The L1 Trigger Jet Algorithm

The L1 jet algorithm clusters jets using the transverse energy sums computed by the calorimeter trigger regions. Each region consists of 4×4 trigger tower windows which within the **CMS** barrel spans a region of $\Delta\eta \times \Delta\phi = 0.087 \times 0.087$ in pseudorapidity-azimuth. The jet trigger uses a 3×3 calorimeter region (144 trigger towers) sliding window technique, as shown on the left of Figure 3.10.

To increase the speed at which jets are clustered, 18 jet finders operate simultaneously over the whole detector. In order to reduce the total data duplicated and shared between these jet finders, the **GCT** employs a pre-clustering algorithm which then only share information with neighbouring regions when clustered jets are found.

A jet candidate is created when the sum of the **HCAL** and **ECAL** energies of the central calorimeter region has an energy deposit larger than all of its neighbouring regions $E_{T\text{ central}} > E_{T\text{ surround}}$. During the 2012 run period, a minimum threshold of 5 GeV was imposed on the central seeding region to suppress noise from non-collimated pile-up jets. This threshold is applied on the raw, uncorrected energy of the calorimeter regions and affects all clustered L1 jets. The effect of such a change to the jet algorithm on the triggering performance of L1 quantities is shown in Section (3.4.4).

The L1 jets are characterised by the E_T , summed over the 3×3 calorimeter regions, which corresponds to 12×12 trigger towers in barrel and endcap, or 3×3 larger **HF** towers in the **HF**. The ϕ size of the jet window is the same everywhere, whilst the η

¹¹³³ binning gets somewhat larger at high η due to calorimeter and trigger tower segmentation.
¹¹³⁴ The jets are labelled by the (η, ϕ) indices of the central calorimeter region.
¹¹³⁵ The **GCT** also determines whether or not a τ -veto bit has been set for each calorimeter
¹¹³⁶ region. This depends on whether the energy depositions in up to 4 contiguous trigger
¹¹³⁷ towers are below a programmable fraction of the regional E_T , see Figure 3.10 (right).
¹¹³⁸ These topologies are due to the hadronic decay modes of the τ containing one or three
¹¹³⁹ isolated pions. Any jet candidate that has energy deposits spread throughout the trigger
¹¹⁴⁰ towers in a calorimeter region is likely not from one or three isolated pions and the τ -veto
¹¹⁴¹ bit is set.
¹¹⁴² Jets with $3.0 < |\eta| < 5.0$ are classified as forward jets, whereas those with $|\eta| < 3.0$ are
¹¹⁴³ classified as either a central or τ -jet depending on the outcome of the setting of the τ -veto
¹¹⁴⁴ bits. The four highest energy central, forward and τ -jets in the calorimeter are further
¹¹⁴⁵ passed through Look Up Table (**LUT**)s, which apply a programmable η -dependent jet
¹¹⁴⁶ energy scale correction. Finally these jet objects are passed to the **GT** to make L1 trigger
¹¹⁴⁷ decisions.

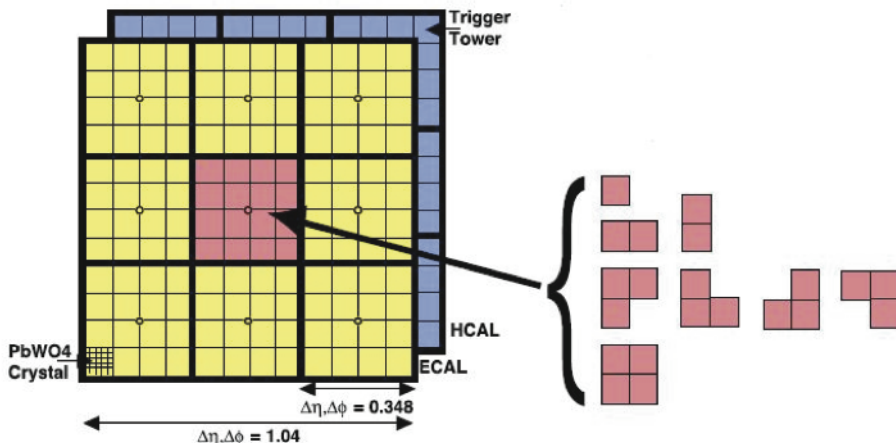


Figure 3.10: Illustration of the Level-1 jet finding algorithm. Each cell represents a trigger tower, which is the sum of the transverse energy contributions from both calorimeter systems. The τ -jet veto patterns for the central calorimeter region are displayed on the right.

¹¹⁴⁸ The performance of the L1 jets is evaluated with respect to offline jets, which are taken
¹¹⁴⁹ from the standard Calo jet and the PF jet reconstruction algorithms of **CMS**. Jets are
¹¹⁵⁰ corrected for pile-up and detector effects as described in Section (3.3.1). A moderate
¹¹⁵¹ level of noise rejection is applied to the offline jets by selecting jets passing the “loose”

1152 identification criteria for both Calo and PF. These jet criteria are listed in Appendix
1153 ([A.1](#)).

1154 3.4.3. Measuring L1 Jet Trigger Efficiencies

1155 The L1 jet efficiency is defined as the fraction of leading offline jets which were matched
1156 with a L1 τ - or central jet above a certain trigger threshold, divided by all events in the
1157 sample with at least a single offline jet above threshold.

1158 The efficiency is determined by matching the L1 and reconstructed offline jets spatially in
1159 $\eta - \phi$ space. The ΔR separation between the highest offline reconstructed jet ($E_T > 10$
1160 GeV and $|\eta| < 3$) and each L1 jet in the event is calculated. A match is made to the L1
1161 jet with the minimum ΔR to the reconstructed jet on the condition that it also satisfies
1162 $\Delta R < 0.5$.

1163 The matching efficiency for this procedure is found to be close to 100% above an offline
1164 jet threshold of 30(45) GeV for the run 2012B(C) data taking period (see [Appendix B.1](#)).

1165 Each efficiency curve is fitted with a function which is the cumulative distribution function
1166 of an Exponentially Modified Gaussian ([EMG](#)) distribution:

$$\text{1167 } f(x; \mu, \sigma, \lambda) = \frac{\lambda}{2} \cdot e^{\frac{\lambda}{2}(2\mu + \lambda\sigma^2 - 2x)} \cdot \text{erfc} \left(\frac{\mu + \lambda\sigma^2 - x}{\sqrt{2}\sigma} \right) \quad (3.3)$$

where erfc is the complementary error function defined as:

$$\text{erfc}(x) = 1 - \text{erf}(x) = \frac{2}{\sqrt{\pi}} \int_x^\infty e^{-t^2} dt.$$

1168 In this functional form, the parameter μ determines the point of 50% of the plateau
1169 efficiency, and the σ gives the resolution. This parametrisation is used to benchmark
1170 the efficiency at the plateau, the turn-on points and resolution for each L1 Jet trigger.
1171 The choice of function is purely empirical. Previous studies used the error function
1172 alone, which described the data well at high threshold values but could not describe the
1173 efficiencies well at lower thresholds [[68](#)].

1174 The efficiency turn-on curves for various L1 jet thresholds are evaluated as a function of
1175 the offline reconstructed jet E_T for central jets with $|\eta| < 3$. These are measured using
1176 single isolated μ triggers which have high statistics, and are orthogonal and therefore

Trigger	Calo		PF	
	μ	σ	μ	σ
L1_SingleJet16	21.09 ± 0.03	7.01 ± 0.02	22.17 ± 0.04	7.83 ± 0.03
L1_SingleJet36	41.15 ± 0.05	5.11 ± 0.02	39.16 ± 0.06	8.04 ± 0.03
L1_SingleJet92	95.36 ± 0.13	5.62 ± 0.03	90.85 ± 0.19	11.30 ± 0.10

Table 3.1: Results of a cumulative EMG function fit to the turn-on curves for L1 single jet triggers in run 2012 Run Period C, measured in an isolated μ data sample. The turn-on point, μ , and resolution, σ , of the L1 jet triggers are measured with respect to offline Calo Jets (left) and PF Jets (right).

unbiased to the hadronic triggers under study. Events are selected with some loose detector based isolation requirements to make sure the muon does not overlap with a jet, causing a discrepancy in the measurement of the calorimetric energy.

The efficiency is calculated with respect to offline Calo and PF Jets in Figure 3.11. Table 3.1 shows the values of these parameters, calculated for three example L1 single jet triggers taken from 2012 8 TeV data.

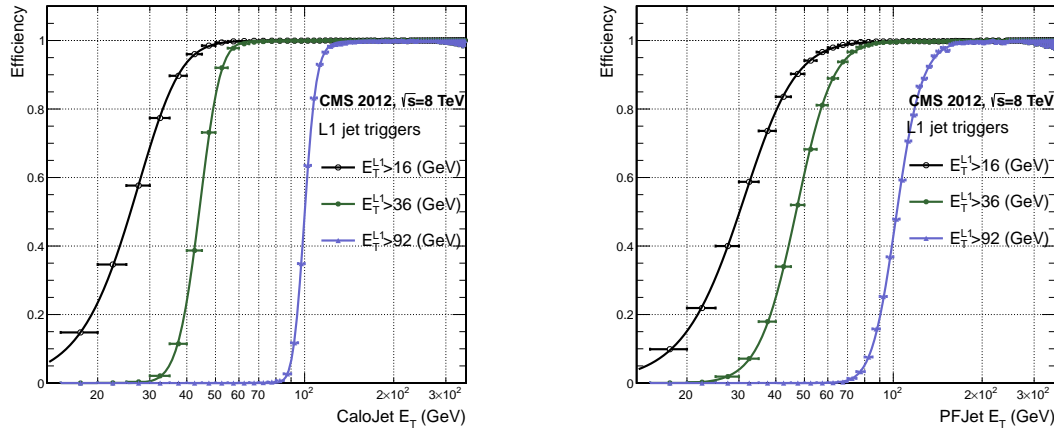


Figure 3.11: L1 jet efficiency turn-on curves as a function of the offline CaloJet E_T (left) and PFJet E_T (right), measured in 2012 Run Period C data and collected with an isolated single μ data sample.

The results from the L1 single jet triggers shows good performance for both Calo and PF jets. A better resolution is observed for Calo jets with respect to L1 jet quantities. This effect is due to Calo jet reconstruction using the same detector subsystems as for L1 jets. In contrast the PF jet reconstruction algorithm additionally utilises tracker and muon information, resulting in a poorer resolution when directly compared to L1 jet objects.

₁₁₈₈ **3.4.4. Effects of the L1 Jet Seed**

₁₁₈₉ Between run period B and C of the 2012 data taking period, a jet seed threshold
₁₁₉₀ was introduced into the L1 jet clustering algorithm. There was previously no direct
₁₁₉₁ requirement made on the energy deposited in the central region.

₁₁₉₂ The introduction of a jet seed threshold required that the central region have an uncor-
₁₁₉₃ rected energy deposit of $E_T \geq 5$ GeV. This value was motivated by studies of the effect
₁₁₉₄ that different jet seed thresholds had upon the trigger cross-sections and efficiencies of
₁₁₉₅ various H_T , single jet and multi-jet triggers. It was found that the 5 GeV threshold gave
₁₁₉₆ large reductions in trigger cross-sections particularly in the case of multi-jet and H_T
₁₁₉₇ triggers, whilst having a small impact on the measured efficiencies of these triggers [69].

₁₁₉₈ Its main purpose was to counteract the effects of high pile up running conditions which
₁₁₉₉ create a large number of soft non-collimated jets, that are then added to the jets from
₁₂₀₀ the primary interaction or other soft jets from other secondary interactions [70]. This in
₁₂₀₁ turn causes a large increase in trigger rate, due to the increase in the likelihood that the
₁₂₀₂ event causes the L1 trigger to fire.

₁₂₀₃ The effect of the introduction of this jet seed threshold between these two run periods is
₁₂₀₄ benchmarked through a comparison of the efficiency of the L1 jet triggers with respect
₁₂₀₅ to offline Calo jets and is shown in Figure 3.12.

₁₂₀₆ The L1 H_T trigger efficiency is also benchmarked at two values, which is shown in Figure
₁₂₀₇ 3.13. The L1 H_T sum is compared against the offline H_T constructed from Calo jets
₁₂₀₈ with $E_T \geq 40$ GeV. This requirement is imposed to account for the relative difference
₁₂₀₉ between uncorrected jet energy deposits within the GCT used to calculate the L1 H_T
₁₂₁₀ sum, and those same deposits after full object reconstruction has occurred.

₁₂₁₁ To negate any effects from different pile-up conditions in the run periods, the efficiencies
₁₂₁₂ are measured in events which contain between 15 and 20 primary vertices, as defined in
₁₂₁₃ Appendix (A.2).

₁₂₁₄ It can be seen that the performance of the $E_T > 36, 92$ single jet triggers are almost
₁₂₁₅ identical, with the jet seed having no measurable effect on these triggers as shown in
₁₂₁₆ Table 3.2.

₁₂₁₇ In the case of the H_T triggers, without the jet seed threshold a large increase in the
₁₂₁₈ trigger cross-section during high luminosity collisions will occur. The low energy threshold
₁₂₁₉ requirement for a jet to be clustered and added to the L1 H_T sum, will allow many

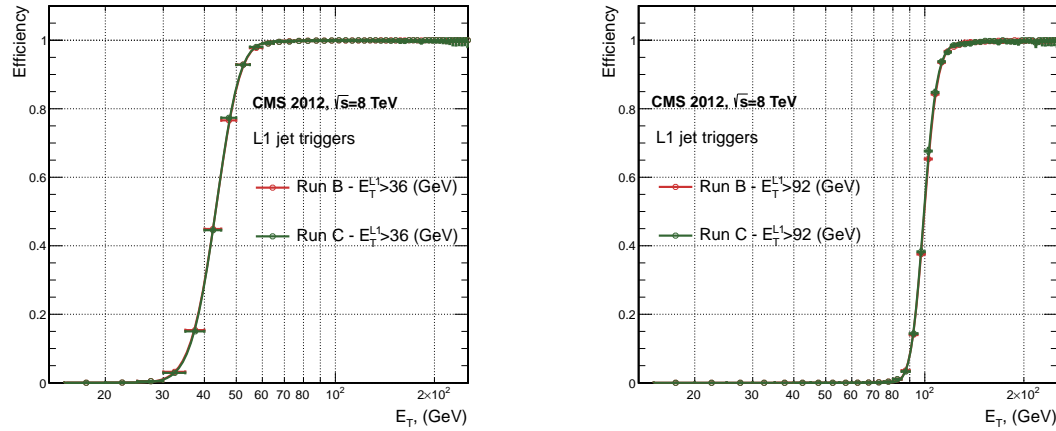


Figure 3.12: L1 jet efficiency turn-on curves as a function of the offline CaloJet E_T , measured for the L1 SingleJet 36 and 92 trigger in 2012 run period B and C collected with an isolated single μ sample.

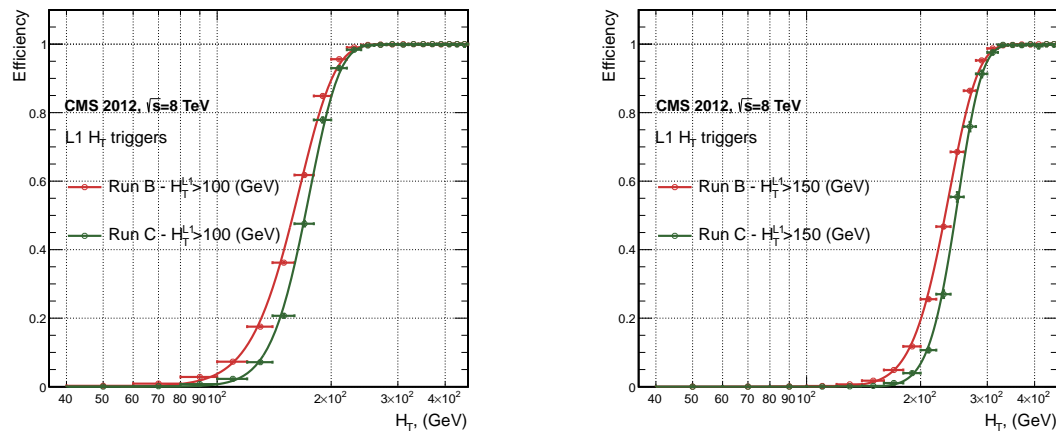


Figure 3.13: L1 H_T efficiency turn-on curves as a function of the offline CaloJet H_T , measured for the L1 H_T 100 and 150 trigger during the run 2012 B and C, collected using an isolated single μ triggered sample.

Trigger	2012B			2012C		
	μ	σ		μ	σ	
L1_SingleJet36	40.29 ± 0.04	5.34 ± 0.02		40.29 ± 0.11	5.21 ± 0.05	
L1_SingleJet92	94.99 ± 0.09	5.93 ± 0.06		94.82 ± 0.29	5.74 ± 0.18	

Table 3.2: Results of a cumulative **EMG** function fit to the turn-on curves for L1 single jet triggers in the 2012 run period B and C, preselected on an isolated muon trigger. The turn-on point μ and resolution σ of the L1 jet triggers are measured with respect to offline Calo Jets in run B (left) and run C (right).

soft jets from other secondary interactions to enter the calculation. The introduction of the jet seed threshold prevents the clustering of many of these diffuse low E_T pile-up jets, thus lowering the L1 GCT H_T calculation. Resultantly, different behaviours for the trigger turn-ons after the introduction of the jet seed threshold are expected for these triggers.

The mean, μ , values are measured to sit at higher H_T for both benchmarked H_T triggers, whilst a better resolution is also observed after the introduction of the jet seed threshold. These values can be found within Table 3.3.

Trigger	2012B		2012C	
	μ	σ	μ	σ
L1 HT-100	157.5 ± 0.08	32.9 ± 0.08	169.8 ± 0.08	28.7 ± 0.03
L1 H1-150	230.9 ± 0.02	37.3 ± 0.01	246.4 ± 0.16	31.8 ± 0.05

Table 3.3: Results of a cumulative EMG function fit to the turn-on curves for H_T in run 2012 B and C, preselected on an isolated single μ trigger. The turn-on point μ , resolution σ of the L1 H_T triggers are measured with respect to offline H_T , formed from CaloJets with a $E_T \geq 40$ in run period B (left) and C (right).

Despite this slight increase in the turn-on point of the H_T triggers, a large reduction in the trigger cross-section is achieved for all H_T triggers. As an example, the expected trigger cross-section for the L1HTT150 trigger as a function of instantaneous luminosity can be seen in Figure 3.14.

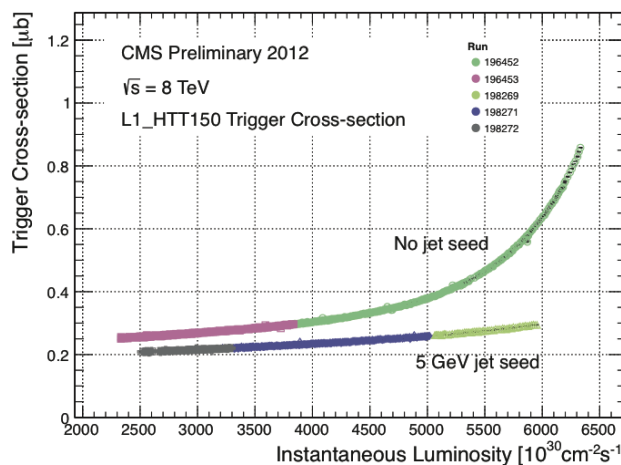


Figure 3.14: Trigger cross section for the L1HTT150 trigger path. Showing that a 5 GeV jet seed threshold dramatically reduces the dependance of cross section on the instantaneous luminosity for L1 H_T triggers [71].

1232 3.4.5. Robustness of L1 Jet Performance against Pile-up

1233 The performance of the L1 single jet triggers is evaluated in different pile-up conditions
1234 to determine any dependence on pile-up. Three different pile-up categories of 0-10,
1235 10-20 and >20 vertices are defined, reflecting the low, medium and high pile-up running
1236 conditions at CMS in 2012.

1237 The L1 triggers are benchmarked relative to Calo and PF jets in the run period where
1238 the jet seed threshold *is* applied, for the L1 single jet thresholds of 16, 36 and 92 GeV,
1239 shown in Figure 3.15. The results of fitting an EMG function to these efficiency turn-on
1240 curves are given in Table 3.4 and Table 3.5 for Calo and PF jets respectively.

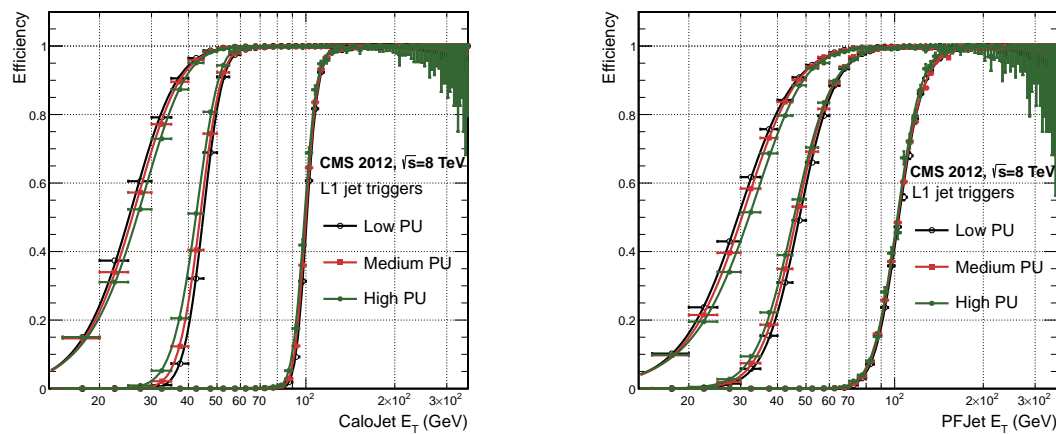


Figure 3.15: L1 jet efficiency turn-on curves as a function of the leading offline E_T Calo (left) and PF (right) jet, for low, medium and high pile-up conditions.

Vertices	0-10		11-20		> 20	
	μ	σ	μ	σ	μ	σ
L1_SingleJet16	19.9 ± 0.1	6.1 ± 0.3	20.8 ± 0.1	6.5 ± 0.1	22.3 ± 0.2	7.5 ± 0.1
L1_SingleJet36	41.8 ± 0.1	4.6 ± 0.1	40.9 ± 0.1	5.1 ± 0.1	40.6 ± 0.6	5.9 ± 0.2
L1_SingleJet92	95.9 ± 0.2	5.4 ± 0.1	95.2 ± 0.2	5.6 ± 0.1	94.5 ± 0.6	6.2 ± 0.3

Table 3.4: Results of a cumulative EMG function fit to the efficiency turn-on curves for L1 single jet triggers in the 2012 run period C, measured from isolated μ triggered data. The turn-on point, μ , and resolution, σ , of the L1 jet triggers are measured with respect to offline Calo jets in low (left), medium (middle) and high (right) pile-up conditions.

1241 No significant drop in efficiency is observed in the presence of a high number of primary
1242 vertices. The increase in hadronic activity in higher pile-up conditions, combined with
1243 the absence of pile-up subtraction for L1 jets, results in the expected observation of

Vertices	0-10		11-20		> 20	
	μ	σ	μ	σ	μ	σ
L1_SingleJet16	21.1 \pm 0.1	7.16 \pm 0.05	22.34 \pm 0.1	7.9 \pm 0.1	24.6 \pm 0.2	9.5 \pm 0.1
L1_SingleJet36	39.6 \pm 0.1	7.4 \pm 0.1	38.4 \pm 0.1	7.4 \pm 0.1	37.1 \pm 0.2	7.5 \pm 0.1
L1_SingleJet92	91.6 \pm 0.3	11.3 \pm 0.2	91.4 \pm 0.3	11.2 \pm 0.1	90.0 \pm 0.9	12.1 \pm 0.4

Table 3.5: Results of a cumulative EMG function fit to the efficiency turn-on curves for Level-1 single jet triggers in the 2012 run period C, measured from isolated μ triggered data. The turn-on point, μ , and resolution, σ , of the L1 jet triggers are measured with respect to offline PF jets in low (left), medium (middle) and high (right) pile-up conditions.

₁₂₄₄ a decrease in the μ value of the efficiency turn-ons as a function of pile-up. Similarly,
₁₂₄₅ the resolution, σ , of the turn-ons are found to gradually grow due to the larger pile-up
₁₂₄₆ corrections being applied to the offline reconstructed jets.

₁₂₄₇ These features are further emphasised when shown as a function of

$$\frac{(L1 E_T - \text{Offline } E_T)}{\text{Offline } E_T} \quad (3.4)$$

₁₂₄₈ in bins of matched leading offline jet E_T . The results of these individual fits categorised
₁₂₄₉ as a function of matched leading offline jet E_T can be found in Appendix (B.2), where
₁₂₅₀ each of the distributions are fitted with an EMG function as defined in Equation (3.3).

₁₂₅₁ The μ , σ and λ values extracted for the low, medium and high pile-up conditions are
₁₂₅₂ shown for Calo and PF jets in Figure 3.16 and Figure 3.17 respectively. The central
₁₂₅₃ value of $\frac{(L1 E_T - \text{Offline } E_T)}{\text{Offline } E_T}$ is observed, as expected, to increase as a function of jet E_T ,
₁₂₅₄ whilst the resolution also improves as a function of increasing offline jet E_T for all pile-up
₁₂₅₅ categories.

₁₂₅₆ When comparisons are made between the individual pile-up scenarios, it can be seen
₁₂₅₇ that in the presence of higher pile-up, μ is seen to shift to larger values and a poorer
₁₂₅₈ resolution, σ , observed. These differences between the different pile-up scenarios, can
₁₂₅₉ once again be attributed to an increasing number of soft pile-up jets that add to the
₁₂₆₀ transverse energy of the lead jet from the primary interaction within each successive
₁₂₆₁ category.

₁₂₆₂ The resolution of other L1 jet based energy sum quantities, H_T and H_T parameterised
₁₂₆₃ as in Equation (3.4), can be found in Appendix (B.3).

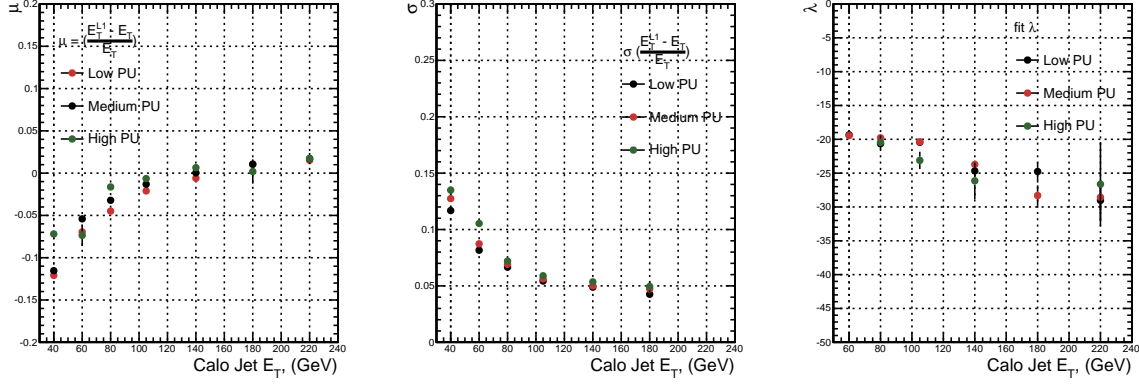


Figure 3.16: Fit values from an EMG function fitted to the resolution plots of leading Calo jet E_T measured as a function of $\frac{(\text{L1 } E_T - \text{Offline } E_T)}{\text{Offline } E_T}$ for low, medium and high pile-up conditions. The plots show the mean μ (left), resolution σ (middle) of the Gaussian as well as the decay term λ (right) of the exponential.

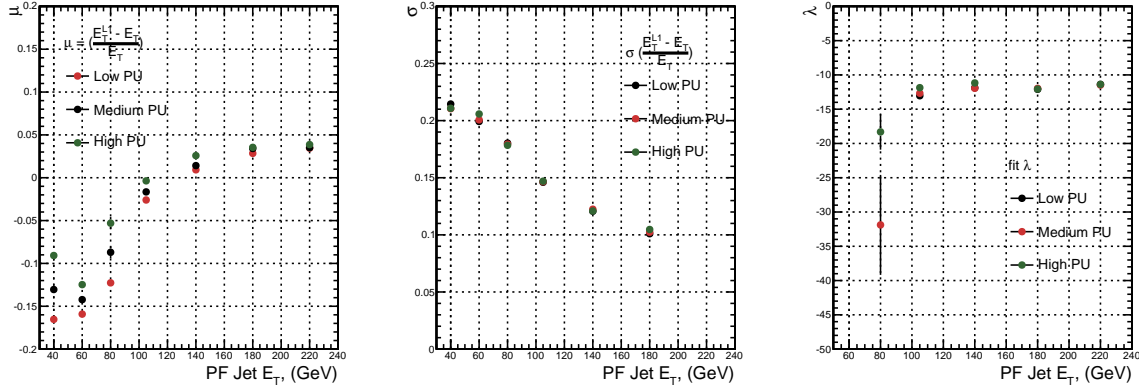


Figure 3.17: Fit values from an EMG function fitted to the resolution plots of leading PF jet E_T measured as a function of $\frac{(\text{L1 } E_T - \text{Offline } E_T)}{\text{Offline } E_T}$ for low and medium pile-up conditions. The plots show the mean μ (left), resolution σ (middle) of the Gaussian, as well as the decay term λ (right) of the exponential.

1264 3.4.6. Summary

1265 The performance of the CMS Level-1 Trigger has been studied and evaluated for jets
 1266 and energy sum quantities using data collected during the 2012 LHC 8 TeV run. These
 1267 studies include the effect of the introduction of a 5 GeV jet seed threshold into the jet
 1268 clustering algorithm, the purpose of which is to mitigate the effects of pile-up on the
 1269 rate of L1 triggers, whilst not adversely affecting the efficiency of these triggers. No

₁₂₇₀ significant change in performance is observed with this change and good performance is
₁₂₇₁ observed for a range of L1 quantities.

Chapter 4.

¹²⁷² SUSY Searches in Hadronic Final States ¹²⁷³

- ¹²⁷⁴ In this chapter a model independent search for **SUSY**, in hadronic final states with \cancel{E}_T
¹²⁷⁵ using the α_T variable is introduced and described in detail. The results presented are
¹²⁷⁶ based on a data sample of pp collisions collected in 2012 at $\sqrt{s} = 8$ TeV, corresponding
¹²⁷⁷ to an integrated luminosity of $11.7 \pm 0.5 \text{ fb}^{-1}$ [5].
- ¹²⁷⁸ The kinematic variable α_T is motivated as a variable to provide strong rejection of the
¹²⁷⁹ overwhelming QCD multi-jet background, which is prevalent to jets + \cancel{E}_T final states at
¹²⁸⁰ the **LHC**. This is achieved whilst maintaining sensitivity to a range of possible **SUSY**
¹²⁸¹ signals and is described in Section (4.1). The search and trigger strategy in addition to
¹²⁸² the event reconstruction and selection are outlined within Sections (4.2 - 4.3).
- ¹²⁸³ The method in which the **SM** background is estimated using data driven control samples
¹²⁸⁴ and an analytical technique to improve statistical precision at higher b-tag multiplicities
¹²⁸⁵ is detailed within Section (4.5). Included in this section is a discussion on the impact of
¹²⁸⁶ b-tagging and mis-tagging scale factors between data and simulation on any background
¹²⁸⁷ predictions. Improved precision in estimating background yields at large number of
¹²⁸⁸ b-tagged jets, is important in the context of sensitivity to natural **SUSY** models, first
¹²⁸⁹ outlined in Section (2.4.1).
- ¹²⁹⁰ A description of the formulation of appropriate systematic uncertainties to be applied
¹²⁹¹ to the background predictions to account for theoretical uncertainties, limitations in
¹²⁹² the modelling of event kinematics and instrumental effects is covered in Section (4.6).
¹²⁹³ Similarly the systematic determination for the **SMS** signal samples used to interpret the
¹²⁹⁴ physics reach of the analysis are examined in Section (4.7).

- 1295 Finally the statistical likelihood model to test the compatibility of the data with a **SMS**
 1296 only hypothesis, and to interpret the observations within the context of **SMS** models is
 1297 described in Section (4.8). The experimental reach of the analysis discussed within this
 1298 thesis is interpreted in two classes of **SMS** models, both introduced in Section (2.4.1).
 1299 The **SMS** models considered in this analysis are summarised in Table 4.1. For each model,
 1300 the **LSP** is assumed to be the lightest neutralino.
 1301 Within the table are also defined reference points, parameterised in terms of parent
 1302 gluino/squark and **LSP** sparticle masses, m_{parent} and m_{LSP} , respectively. These are
 1303 used within the following two chapters to demonstrate potential signal yields within the
 1304 hadronic search region of the analysis. The masses of each signal topology are chosen to
 1305 reflect parameter space which is within the expected sensitivity reach of the search.

Model	Production/decay mode	Reference model	
		m_{parent}	m_{LSP}
G1 (T1)	$pp \rightarrow \tilde{g}\tilde{g}^* \rightarrow q\bar{q}\tilde{\chi}_1^0 q\bar{q}\tilde{\chi}_1^0$	700	300
G2 (T1bbbb)	$pp \rightarrow \tilde{g}\tilde{g}^* \rightarrow b\bar{b}\tilde{\chi}_1^0 b\bar{b}\tilde{\chi}_1^0$	900	500
G3 (T1tttt)	$pp \rightarrow \tilde{g}\tilde{g}^* \rightarrow t\bar{t}\tilde{\chi}_1^0 t\bar{t}\tilde{\chi}_1^0$	850	250
D1 (T2)	$pp \rightarrow \tilde{q}\tilde{q}^* \rightarrow q\bar{q}\tilde{\chi}_1^0 q\bar{q}\tilde{\chi}_1^0$	600	250
D2 (T2bb)	$pp \rightarrow \tilde{b}\tilde{b}^* \rightarrow b\bar{b}\tilde{\chi}_1^0 b\bar{b}\tilde{\chi}_1^0$	500	150
D3 (T2tt)	$pp \rightarrow \tilde{t}\tilde{t}^* \rightarrow t\bar{t}\tilde{\chi}_1^0 t\bar{t}\tilde{\chi}_1^0$	400	0

Table 4.1: A summary of the **SMS** models interpreted in this analysis, involving both direct (D) and gluino-induced (G) production of squarks and their decays. Reference models are also defined in terms of parent and **LSP** sparticle mass.

1306 4.1. An Introduction to the α_T Search

- 1307 A proton-proton collision resulting in the production and decay of supersymmetric
 1308 particles, would manifest as a final state containing energetic jets and \cancel{E}_T in the hadronic
 1309 channel. The search focuses on topologies where new heavy supersymmetric, R-parity
 1310 conserving particles are pair-produced in pp collisions. These particles decaying to a
 1311 **LSP** escape the detector undetected, leading to significant missing energy and missing
 1312 hadronic transverse energy,

$$H_T = \left| \sum_{i=1}^n \vec{p_T}^{jet_i} \right|. \quad (4.1)$$

- ₁₃₁₃ This is defined as the vector sum of the transverse energies of jets selected in an event.
₁₃₁₄ Energetic jets produced in the decay of these supersymmetric particles also can produce
₁₃₁₅ significant visible transverse energy,

$$H_T = \sum_{i=1}^n E_T^{jet_i}, \quad (4.2)$$

- ₁₃₁₆ defined as the scalar sum of the transverse energies of jets selected in an event.
₁₃₁₇ A search within this channel is greatly complicated in a hadron collider environment;
₁₃₁₈ where the overwhelming background comes from inherently balanced multi-jet (“QCD”)
₁₃₁₉ events, which are produced with an extremely large cross-section as demonstrated within
₁₃₂₀ Figure 4.1. \cancel{E}_T can appear in such events with a substantial mis-measurement, stochastic
₁₃₂₁ fluctuations of jet energy, or missed objects due to detector mis-calibration or noise
₁₃₂₂ effects.

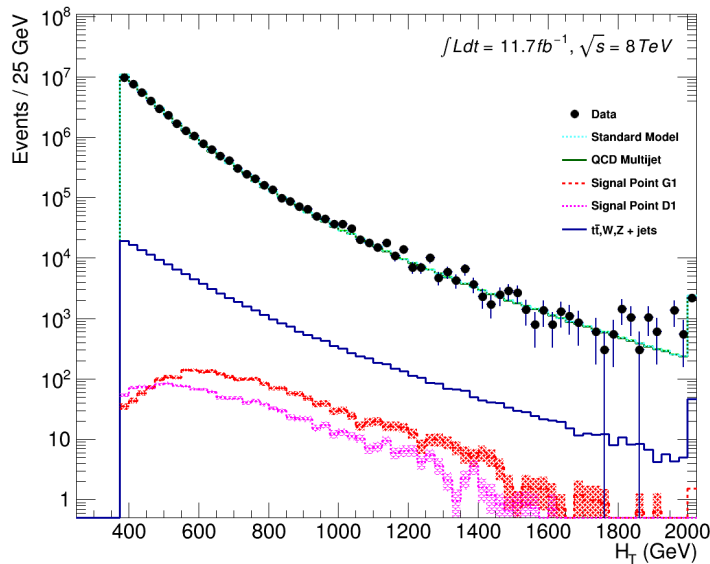


Figure 4.1: Reconstructed offline H_T distribution in the hadronic signal selection, from 11.7 fb^{-1} of data, in which no α_T requirement is made. Sample is collected from prescaled H_T triggers. Overlaid are expectations from MC simulation of EWK processes as well as two reference signal models (labelled G1 and D1 from Table 4.1).

- ₁₃₂₃ Additional SM background from EWK processes with genuine \cancel{E}_T from escaping neutrinos
₁₃₂₄ comprise the irreducible background within this search and come mainly from:

- $Z \rightarrow \nu\bar{\nu} + \text{jets}$,
 - $W \rightarrow l\nu + \text{jets}$ in which a lepton falls outside of detector acceptance, is not reconstructed, is mis-identified, or the lepton decays hadronically $\tau \rightarrow \text{had}$,
 - $t\bar{t}$ with at least one leptonically decaying W , which is missed in the detector as detailed above,
 - small background contributions from DY, single top and Diboson (WW,ZZ,WZ) processes.
- The search is designed to have a strong separation between events with genuine and “fake” \cancel{E}_T which is achieved primarily through the dimensionless kinematic variable, α_T [72][73].

4.1.1. The α_T Variable

For a perfectly measured di-jet QCD event, conservation laws dictate that both jets must be of equal magnitude and produced in opposite directions. However, in the case of di-jet events with genuine \cancel{E}_T (as detailed above), no such requirement is made of the two jets, as depicted in Figure 4.2.

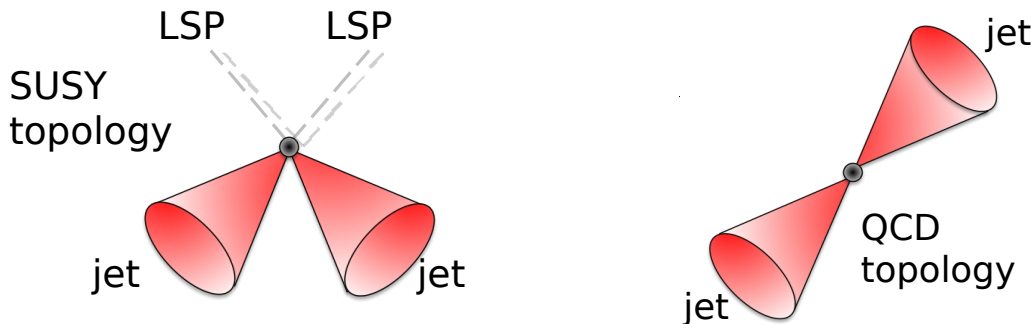


Figure 4.2: The event topologies of background QCD dijet events (right) and a generic SUSY signature with genuine \cancel{E}_T (left).

Exploiting this feature leads to the formulation of α_T (first inspired by [74]) in di-jet systems defined as,

$$\alpha_T = \frac{E_T^{j_2}}{M_T}, \quad (4.3)$$

1342 where $E_T^{j_2}$ is the transverse energy of the least energetic of the two jets and M_T defined
1343 as:

$$M_T = \sqrt{\left(\sum_{i=1}^2 E_T^{j_i}\right)^2 - \left(\sum_{i=1}^2 p_x^{j_i}\right)^2 - \left(\sum_{i=1}^2 p_y^{j_i}\right)^2} \equiv \sqrt{H_T^2 - \cancel{H}_T^2}. \quad (4.4)$$

1344 A perfectly balanced di-jet event i.e. $E_T^{j_1} = E_T^{j_2}$ would yield an α_T value of 0.5. In events
1345 with jets that are not ‘back-to-back’, for example when a W or Z recoils off a system of
1346 jets, α_T can achieve values in excess of 0.5. Most importantly, balanced multi-jet events
1347 in which jets *are* mis-measured, will generally result in an α_T of less than 0.5, thus giving
1348 the α_T variable discriminating power between these processes.

1349 α_T can be extended to apply to any arbitrary number of jets. This is undertaken by
1350 modelling a system of n jets as a di-jet system, through the formation of two pseudo-jets
1351 [75]. The two pseudo-jets are built by merging the jets present, and are chosen to be as
1352 balanced as possible, i.e the $\Delta H_T \equiv |E_T^{pj_1} - E_T^{pj_2}|$ is minimised between the two pseudo
1353 jets. Using Equation (4.4), α_T can be rewritten as,

$$\alpha_T = \frac{1}{2} \frac{H_T - \Delta H_T}{\sqrt{H_T^2 - \cancel{H}_T^2}} = \frac{1}{2} \frac{1 - \Delta H_T/H_T}{\sqrt{1 - (\cancel{H}_T/H_T)^2}}. \quad (4.5)$$

1354 The distribution of α_T for the two jet categories used within this analysis, $2 \leq n_{jet} \leq 3$
1355 and $n_{jet} \geq 4$ jets, is shown in the Figure 4.3. It can be seen that the distributions peak
1356 at an α_T value of 0.5, before falling away sharply and being free of a simulated multi-jet
1357 background at larger α_T values. These distributions serve to demonstrate the ability
1358 of the α_T variable to discriminate between multi-jet events and EWK processes with
1359 genuine \cancel{E}_T in the final state.

1360 The α_T requirement used within the search is chosen to be $\alpha_T > 0.55$ to ensure that
1361 the QCD multi-jet background is negligible even in the presence of moderate jet mis-

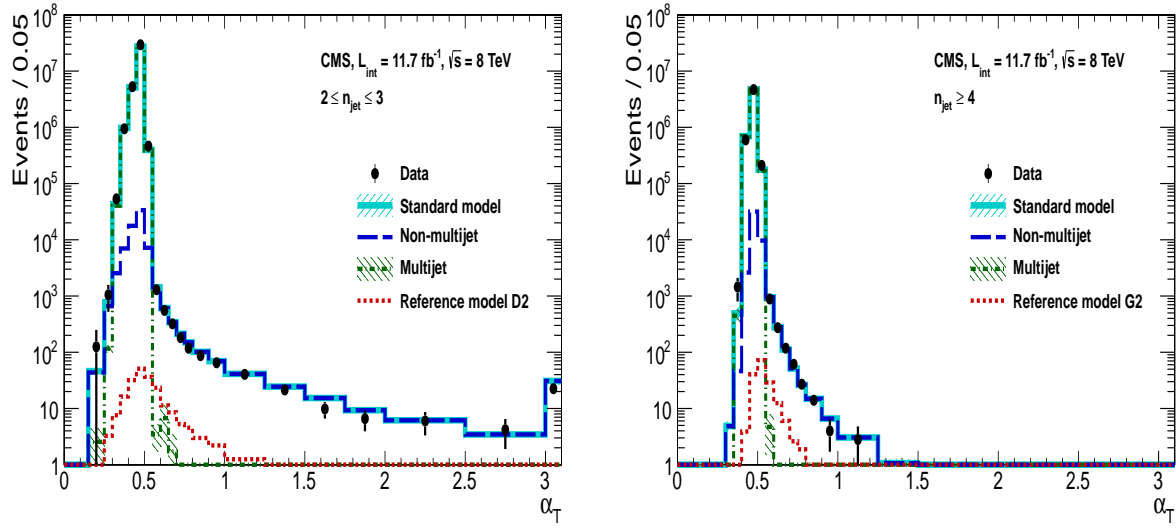


Figure 4.3: The α_T distributions for the low 2-3 (left) and high ≥ 4 (right) jet multiplicities after a full analysis selection and $H_T > 375$ requirement. Data is collected using both prescaled H_T triggers and dedicated α_T triggers for below and above $\alpha_T = 0.55$ respectively. Expected yields as given by simulation are also shown for multi-jet events (green dash-dotted line), EWK backgrounds with genuine \cancel{E}_T (blue long-dashed line), the sum of all SM processes (cyan solid line) and the reference signal model D2 (left, red dotted line) or G2 (right, red dotted line).

measurement. There still remains other effects which can cause multi-jet events to artificially have a large α_T value, which are discussed in detail in Section (4.2.2).

4.2. Search Strategy

The aim of the analysis presented in this thesis is to identify an excess of events in data over the SM background expectation in multi-jet final states and significant \cancel{E}_T . The essential suppression of the dominant multi-jet background for such a search is addressed by the α_T variable, described in the previous section. For estimation of the remaining EWK backgrounds, three independent data control samples are used to predict the different processes that compose the background :

- $\mu + \text{jets}$ control sample to determine $W + \text{jets}$, $t\bar{t}$ and single top backgrounds,
- $\gamma + \text{jets}$ control sample to determine the irreducible $Z \rightarrow \nu\bar{\nu} + \text{jets}$ background,
- $\mu\mu + \text{jets}$ control sample to also determine the irreducible $Z \rightarrow \nu\bar{\nu} + \text{jets}$ background.

1374 These control samples are chosen to be rich in specific **EWK** processes, free of QCD
1375 multi-jet events and to also be kinematically similar to the hadronic signal region that
1376 they are estimating the backgrounds of, see Section (4.2.3). The redundancy of using the
1377 $\gamma + \text{jets}$ and $\mu\mu + \text{jets}$ sample to predict the same background within the signal region,
1378 brings an opportunity to reliably crosscheck and validate the background estimation
1379 method, and is utilised in both the determination of background estimation systematics
1380 (Section(4.6)) and in the maximum likelihood fit (Section(4.8)).

1381 To remain inclusive to a large range of possible **SUSY** models, the signal region is split into
1382 the following categories to allow for increased sensitivity to different **SUSY** topologies:

1383 **Sensitivity to a range of **SUSY** mass splittings**

1384 The hadronic signal region is defined by $H_T > 275$, divided into eight bins in H_T .
1385 – Two bins of width 50 GeV in the range $275 < H_T < 375$ GeV,
1386 – five bins of width 100 GeV in the range $375 < H_T < 875$ GeV,
1387 – and a final open bin, $H_T > 875$ GeV.

1388 The choice of the lowest H_T bin in the analysis is driven primarily by trigger
1389 constraints. The mass difference between the **LSP** and the particle that it decays
1390 from is an important factor in the amount of hadronic activity in the event.

1391 A large mass splitting will lead to hard high p_T jets which contribute to the H_T sum.
1392 From Figure 4.1 it can be seen that the **SM** background falls sharply at high H_T
1393 values, therefore many H_T categories will lead to easier identification of such signals.
1394 Conversely, smaller mass splittings lead to softer jet p_T 's which will subsequently
1395 fall into the lower H_T range.

1396 **Sensitivity to production method of **SUSY** particles**

1397 The production mechanism of any potential **SUSY** signal can lead to different event
1398 topologies. One such way to discriminate between gluino ($g\tilde{g}$ - “high multiplicity”),
1399 and direct squark ($q\tilde{q}$ - “low multiplicity”) induced production of **SUSY** particles is
1400 realised through the number of reconstructed jets in the final state.

1401 The analysis is thus split into two jet categories: $2 \leq n_{\text{jet}} \leq 3$ jets, $n_{\text{jet}} \geq 4$ jets to
1402 give sensitivity to both of these mechanisms.

1403 **Sensitivity to “Natural **SUSY**” via tagging jets from b-quarks**

Jets originating from bottom quarks (b-jets) are identified through vertices that are displaced with respect to the primary interaction. The algorithm used to tag b-jets is the Combined Secondary Vertex Medium Working Point (**CSVM**) tagger, described within Section (3.3.2). A cut is placed on the discriminator variable of > 0.679 , leading to a gluon/light-quark mis-tag rate of approximately 1% and a jet p_T dependant b-tagging efficiency of 60-70% [76].

Natural **SUSY** models would be characterised through final-state signatures rich in bottom quarks. A search relying on methods to identify jets originating from bottom quarks through b-tagging, will significantly improve the sensitivity to this class of signature. This gain in sensitivity stems from a vast reduction in the vector boson + jet backgrounds (W, Z) at higher b-tag jet multiplicities, which typically have no b-flavoured quarks in their decays.

Therefore, events are categorised according to the number of b-tagged jets reconstructed in each event, in the following: $n_b^{\text{reco}} = 0, = 1, = 2, = 3, \geq 4$ b-tag categories. In the highest ≥ 4 b-tag category due to a limited number of expected signal and background events, just three H_T bins are employed: 275-325 GeV, 325-375 GeV, ≥ 375 GeV.

This characterisation is identically mirrored in all control samples, with the information from all samples and b-tag categories used simultaneously in the likelihood model, see Section (4.8).

The combination of the H_T , jet multiplicity and b-tag categorisation of the signal region as described above, results in 67 different bins in which the analysis is interpreted in. A visualisation of the analysis categorisation is depicted in Figure 4.4.

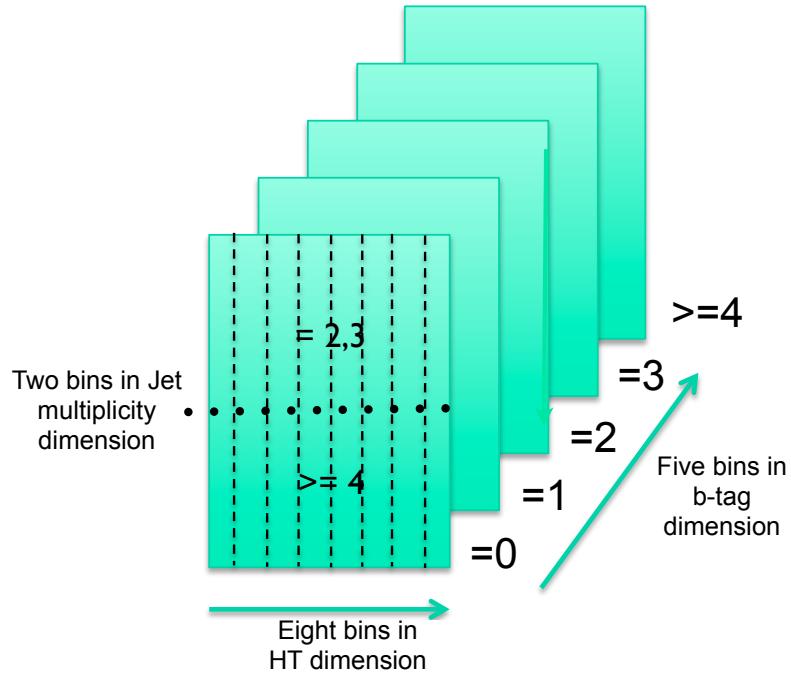


Figure 4.4: Pictorial depiction of the analysis strategy employed by the α_T search to increase sensitivity to a wide spectra of SUSY models.

¹⁴²⁷ 4.2.1. Physics Objects

¹⁴²⁸ The physics objects used in the analysis are defined below, and follow the recommendation
¹⁴²⁹ of the various CMS Physics Object Groups (POGs).

¹⁴³⁰ • Jets

¹⁴³¹ The jets used in this analysis are CaloJets, reconstructed as described in Section
¹⁴³² (3.3.1) using the anti- k_T jet clustering algorithm.

¹⁴³³ To ensure the jet object falls within the calorimeter systems a pseudo-rapidity
¹⁴³⁴ requirement of $|\eta| < 3$ is applied. Each jet must pass a “loose” identification criteria
¹⁴³⁵ to reject jets resulting from unphysical energy, the criteria of which are detailed in
¹⁴³⁶ Table A.1 [77].

¹⁴³⁷ • Muons

¹⁴³⁸ Muons are selected in the $\mu + \text{jets}$ and $\mu\mu + \text{jets}$ control samples, and vetoed in
¹⁴³⁹ the signal region. The same cut based identification criteria is applied to muons in
¹⁴⁴⁰ both search regions and is summarised in Table 4.2 [78].

Variable	Definition
Is Global Muon	Muon contains both a hit in the muon chamber and a matched track in the inner tracking system.
$\chi^2 < 10$	χ^2 of global muon track fit. Used to suppress hadronic punch-through and muons from decays in flight.
Muon chamber hits > 0	At least one muon chamber hit included in global muon track fit.
Muon station hits > 1	Muon segment hits in at least two muon stations, which suppresses hadronic punch-through and accidental track-to-segment matches.
$d_{xy} < 0.2\text{mm}$	The tracker track transverse impact parameter w.r.t the primary vertex. Suppresses cosmic muons and muons from decays in flight.
$d_z < 0.5\text{mm}$	The longitudinal distance of the tracker track w.r.t the primary vertex. Loose selection requirement to further suppress cosmic muons, muons from decays in flight and tracks from pileup.
Pixel hits > 0	Suppresses muons from decays in flight by requiring at least one pixel hit in the tracker.
Track layer hits > 5	Number of tracker layers with hits, to guarantee a good p_T measurement. Also suppresses muons from decays in flight.
PF Iso < 0.12	Isolation based upon the sum of the charged and neutral hadrons and photon objects within a ΔR 0.4 cone of the muon object, corrected for pile up effects on the isolation sum.

Table 4.2: Muon identification criteria used within the analysis for selection/veto purposes in the muon control/signal selections.

¹⁴⁴¹ Additionally muons are required to be within the acceptance of the muon tracking
¹⁴⁴² systems. For the muon control samples, trigger requirements necessitate a $|\eta| <$
¹⁴⁴³ 2.1 for the selection of muons. In the signal region where muons are vetoed, these
¹⁴⁴⁴ conditions are relaxed to $|\eta| < 2.5$ and a minimum threshold of $p_T > 10 \text{ GeV}$ is
¹⁴⁴⁵ required of muon objects.

• Photons

¹⁴⁴⁷ Photons are selected within the $\gamma + \text{jets}$ control sample and vetoed in all other
¹⁴⁴⁸ selections. Photons are identified in both cases according to the cut based criteria
¹⁴⁴⁹ listed in Table 4.3 [79].

Variable	Definition
$H/E < 0.05$	The ratio of hadronic energy in the HCAL tower directly behind the ECAL super-cluster and the ECAL super-cluster itself.
$\sigma_{in\eta} < 0.011$	The log energy weighted width (σ), of the extent of the shower in the η dimension.

Continued on next page

R9 < 1.0	The ratio of the energy of the 3×3 crystal core of the super-cluster compared to the total energy stored in the 5×5 super-cluster.
Combined Isolation < 6 GeV	The photons are required to be isolated with no electromagnetic or hadronic activity within a radius $\Delta R = 0.3$ of the photon object. A combination of the pileup subtracted [80], ECAL , HCAL and tracking isolation sums are used to determine the combined total isolation value.

Table 4.3: Photon identification criteria used within the analysis for selection/veto purposes in the $\gamma +$ jets control/signal selections.

1450

1451 Photon objects are also required to have a minimum momentum of $p_T > 25$ GeV.

1452 **• Electrons**

1453 Electron identification is defined for veto purposes. They are selected according to
1454 the following cut-based criteria listed in Table 4.4, utilising PF-based isolation.

Variable	Barrel	EndCap	Definition
$\Delta\eta_{In}$	<0.007	<0.009	$\Delta\eta$ between SuperCluster position and the coordinate of the associated track at the interaction vertex, assuming no radiation.
$\Delta\phi_{In}$	<0.15	<0.10	$\Delta\phi$ between SuperCluster position and track direction at interaction vertex extrapolated to ECAL assuming no radiation.
$\sigma_{in\eta\eta}$	<0.01	<0.03	Cluster shape covariance, measure the η dispersion of the electrons electromagnetic shower over the ECAL supercluster.
H/E	<0.12	<0.10	The ratio of hadronic energy in the HCAL tower directly behind the ECAL super-cluster and the ECAL super-cluster itself.
d0 (vtx)	<0.02	<0.02	The tracker track transverse impact parameter w.r.t the primary vertex.
dZ (vtx)	<0.20	<0.20	The longitudinal distance of the tracker track w.r.t the primary vertex.
$ (\frac{1}{E_{ECAL}} - \frac{1}{p_{track}}) $	<0.05	<0.05	Comparison of energy at supercluster $1/E_{ECAL}$ and that of the track momentum at the vertex $1/p_{track}$. Causes suppression of fake electrons at low p_T .
PF Iso	<0.15	<0.15	Combined PF isolation of charged hadrons, photons, neutral hadrons within a $\Delta R < 0.3$ cone size. Isolation sum is corrected for pileup using effective area corrections for neutral particles.

Table 4.4: Electron identification criteria used within the analysis for veto purposes.

1455 Electrons are required to be identified at $|\eta| < 2.5$, with a minimum $p_T > 10 \text{ GeV}$
1456 threshold to ensure that the electrons fall within the tracking system of the detector.

1457 • **Noise and \cancel{E}_T Filters**

1458 A series of noise filters are applied to veto events which contain spurious non-physical
1459 jets that are not picked up by the jet id, and events which give large unphysical \cancel{E}_T
1460 values. These filters are listed within Table 4.5.

Noise Filters	Variable	Definition
CSC tight beam halo filter		As proton beams circle the LHC , proton interactions with the residual gas particles or the beam collimators can occur, producing showers of secondary particles which can interact with the CMS detector.
HBHE noise filter with isolated noise rejection		Anomalous noise in the HCAL not due to electronics noise, but rather due to instrumentation issues associated with the HPD 's and Readout Boxes (RBXs).
HCAL laser filter		The HCAL uses laser pulses for monitoring the detector response. Some laser pulses have accidentally been fired in the physics orbit, and ended up polluting events recorded for physics analysis.
ECAL dead cell trigger primitive (TP) filter		EB and EE have single noisy crystals which are masked in reconstruction. Use the Trigger Primitive (TP) information to assess how much energy was lost in masked cells.
Bad EE Supercrystal filter		Two supercrystals in EE are found to occasionally produce high amplitude anomalous pulses in several channels at once, causing a large \cancel{E}_T spike.
ECAL Laser correction filter		A laser calibration multiplicative factor is applied to correct for transparency loss in each crystal during irradiation. A small number of crystals receive unphysically large values of this correction and become very energetic, resulting in \cancel{E}_T .

Table 4.5: Noise filters that are applied to remove spurious and non-physical \cancel{E}_T signatures within the **CMS** detector.

1461 **4.2.2. Event Selection**

1462 The selection criteria for events within the analysis are detailed below. A set of common
1463 cuts are applied to both signal (maximise acceptance to a range of **SUSY** signatures), and
1464 control samples (retain similar jet kinematics for background predictions), with additional
1465 selection cuts applied to each control sample to enrich the sample in a particular **EWK**
1466 processes, see Section (4.2.3).

- ¹⁴⁶⁷ The jets considered in the analysis are required to have a transverse momentum $p_T > 50$
¹⁴⁶⁸ GeV, with a minimum of two jets required in the event. The highest E_T jet is required
¹⁴⁶⁹ to lie within the central tracker acceptance $|\eta| < 2.5$, and the two leading p_T jets must
¹⁴⁷⁰ each have $p_T > 100$ GeV. Any event which has a jet with $p_T > 50$ GeV that either fails
¹⁴⁷¹ the “loose” identification criteria described in Section(4.2.1) or has $|\eta| > 3.0$, is rejected.
¹⁴⁷² Similarly events in which an electron, muon or photon fails object identification but
¹⁴⁷³ passes η and p_T restrictions, are identified as an “odd” lepton/photon and the event is
¹⁴⁷⁴ vetoed.
- ¹⁴⁷⁵ At low H_T , the jet p_T threshold requirements required to be considered as part of the
¹⁴⁷⁶ analysis and enter the H_T sum are scaled downwards. These are scaled down in order
¹⁴⁷⁷ to extend phase space at low H_T , preserving similar jet multiplicities and background
¹⁴⁷⁸ admixture seen at higher H_T , as listed in Table 4.6.

H_T bin	minimum jet p_T	second leading jet p_T
$275 < H_T < 325$	36.7	73.3
$325 < H_T < 375$	43.3	86.6
$375 < H_T$	50.0	100.0

Table 4.6: Jet thresholds used in the three H_T regions of the analysis.

- ¹⁴⁷⁹ Within the signal region, to suppress SM processes with genuine \cancel{E}_T from neutrinos,
¹⁴⁸⁰ events containing isolated electrons or muons are vetoed. Furthermore to ensure a pure
¹⁴⁸¹ multi-jet topology, events are vetoed if an isolated photon is found with $p_T > 25$ GeV.
¹⁴⁸² An α_T requirement of > 0.55 is required to reduce the QCD multi-jet background to
¹⁴⁸³ a negligible amount. Finally, additional cleaning cuts are applied to protect against
¹⁴⁸⁴ pathological deficiencies such as reconstruction failures or severe energy mis-measurements
¹⁴⁸⁵ due to detector inefficiencies:

- Significant H_T can arise in events with no real \cancel{E}_T due to multiple jets falling below the p_T threshold for selecting jets. This in turn leads to events which can then incorrectly pass the α_T requirements of the analysis. This effect can be negated by requiring that the missing transverse momentum reconstructed from jets alone does not greatly exceed the missing transverse momentum reconstructed from all of the detector’s calorimeter towers,

$$R_{miss} = H_T / \cancel{E}_T < 1.25.$$

- 1486 • Fake \cancel{E}_T and \cancel{H}_T can arise due to significant jet mis-measurements caused by a small
 1487 number of non-functioning **ECAL** regions. These regions absorb electromagnetic
 1488 showers which are subsequently not added to the jet energy sum. To circumvent
 1489 this problem the following procedure is employed: For each jet in the event, the
 1490 angular separation

$$\Delta\phi_j^* \equiv \Delta\phi(\vec{p_j} - \sum_{i \neq j} \vec{p_i}), \quad (4.6)$$

1491 is calculated where that jet is itself removed from the event. Here $\Delta\phi^*$ is a measure
 1492 of how aligned the \cancel{H}_T of an event is with a jet. A small value (i.e. the \cancel{H}_T vector
 1493 lies along the jet axis) is indicative of an inherently balanced event in which a jet has
 1494 been mis-measured. For every jet in an event with $\Delta\phi^* < 0.5$, if the ΔR distance
 1495 between the selected jet and the closest dead **ECAL** region is also < 0.3 , then the
 1496 event is rejected. Similarly events are rejected if the jet points within $\Delta R < 0.3$ of
 1497 the **ECAL** barrel-endcap gap at $|\eta| = 1.5$.

1498 Some of the key distributions of the analysis are compared to simulated **SM** processes,
 1499 shown in Figure 4.5. The simulated samples are normalised to a luminosity of 11.7 fb^{-1} ,
 1500 with no requirement placed upon the number of b-tagged jets or number of jets in the
 1501 distributions shown. In the case of this inclusive selection, the dominant backgrounds
 1502 in the signal regions are, $Z \rightarrow \nu\bar{\nu}$ and $W + \text{jet}$ processes, with a smaller $t\bar{t}$ background
 1503 accompanied by other residual backgrounds.

1504 The distributions shown are presented for purely illustrative purposes, with the simulation
 1505 not used in absolute terms for the estimation of background processes within the signal
 1506 region, see Sections (4.2.3, 4.5). However it is nevertheless important to demonstrate
 1507 that good agreement exists between the modelling of key variables in simulation and
 1508 data.

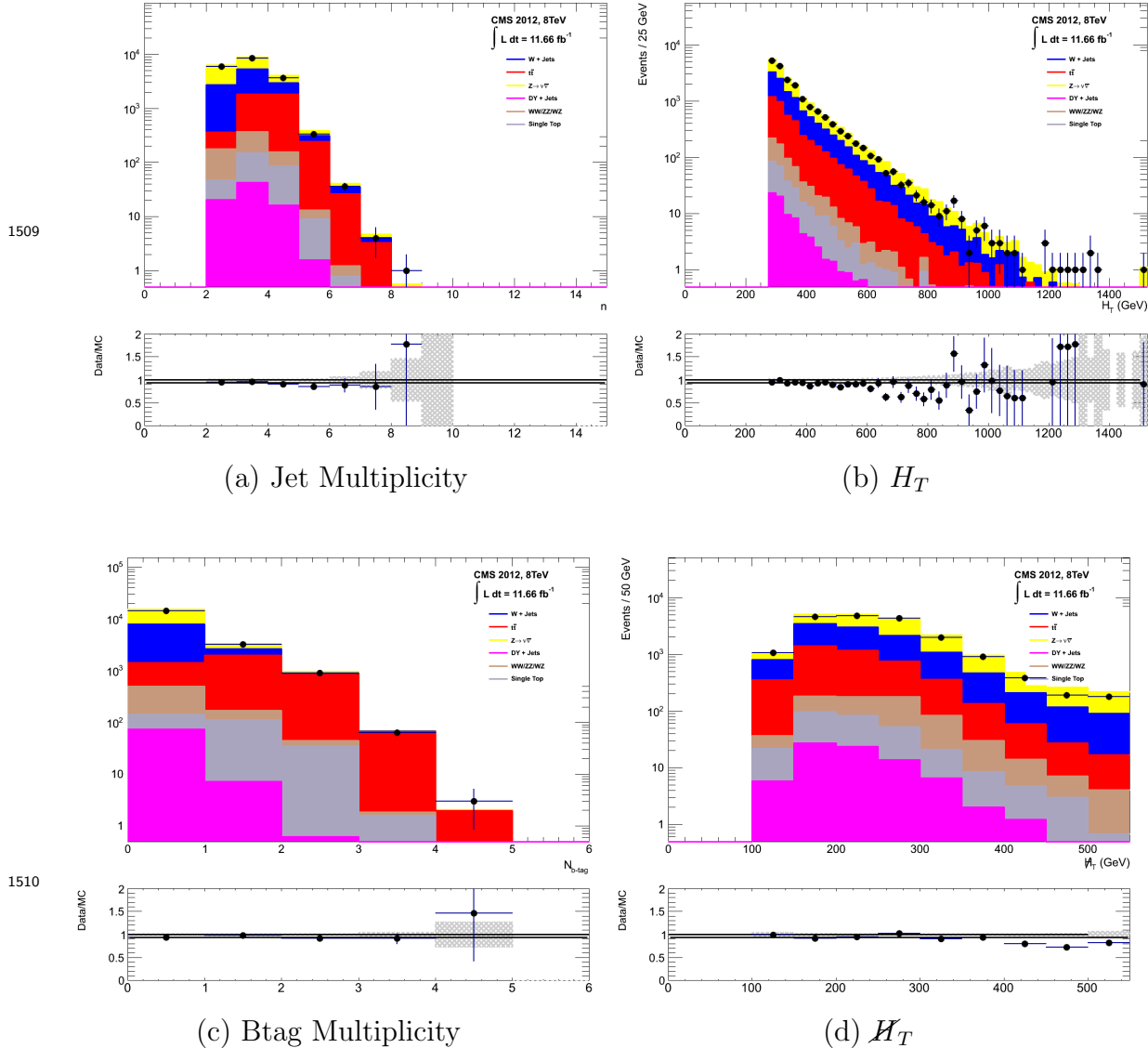


Figure 4.5: Data/MC comparisons of key variables for the hadronic signal region, following the application of the hadronic selection criteria and the requirements of $H_T > 275$ GeV and $\alpha_T > 0.55$. Bands represent the uncertainties due to the statistical size of the MC samples. No requirement is made upon the number of b-tagged jets or jet multiplicity in these distributions.

4.2.3. Control Sample Definition and Background Estimation

The method used to estimate the background contributions in the hadronic signal region relies on the use of a Transfer Factor (TF). This is determined from MC simulation in both the control, N_{MC}^{control} , and signal, N_{MC}^{signal} , region to transform the observed yield

1515 measured in data for a control sample, $N_{\text{obs}}^{\text{control}}$, into a background prediction, $N_{\text{pred}}^{\text{signal}}$, via
1516 Equation (4.7),

$$N_{\text{pred}}^{\text{signal}} = \frac{N_{\text{MC}}^{\text{signal}}}{N_{\text{MC}}^{\text{control}}} \times N_{\text{obs}}^{\text{control}}. \quad (4.7)$$

1517 All simulation samples are normalised to the luminosity of the data samples of the
1518 relevant selection they are being applied to. Through this method, “vanilla” predictions
1519 for the **SM** background in the signal region can be made by considering separately the
1520 sum of the prediction from the combination of either the $\mu + \text{jets}$ and $\gamma + \text{jets}$, or $\mu +$
1521 jets and $\mu\mu + \text{jets}$ samples.

1522 It must be noted that the final background estimation from which results are interpreted,
1523 is calculated via a fitting procedure defined formally by the likelihood model described
1524 in Section (4.8).

1525 The sum of the expected yields from all simulated processes listed in Section (4.1), enter
1526 the denominator, $N_{\text{MC}}^{\text{control}}$, of the **TF** defined in Equation (4.7) for each control sample.
1527 However, only the specific processes being estimated by the control sample enter the
1528 numerator, $N_{\text{MC}}^{\text{signal}}$.

1529 For the $\mu + \text{jets}$ sample the processes entering the numerator are,

$$N_{\text{MC}}^{\text{signal}}(H_T, n_{\text{jet}}) = N_W + N_{t\bar{t}} + N_{DY} + N_t + N_{di-boson}, \quad (4.8)$$

1530 whilst for both the $\mu\mu + \text{jets}$ and $\gamma + \text{jets}$ samples the only simulated processes used in
1531 the numerator is,

$$N_{\text{MC}}^{\text{signal}}(H_T, n_{\text{jet}}) = N_{Z \rightarrow \nu\bar{\nu}}. \quad (4.9)$$

1532 The control samples and the **EWK** processes they are specifically tuned to select are
1533 defined below, with distributions of key variables for each of the control samples shown
1534 for illustrative purposes in Figures 4.6, 4.7 and 4.8. No requirement is placed upon the

number of b-tagged jets or jet multiplicity in the distributions shown. The distributions highlight the background compositions of each control sample, where in general, good agreement is observed between data and simulation, giving confidence that the samples are well understood. The contribution from QCD multi-jet events is expected to be negligible:

The $\mu +$ jets control sample

Events from $W +$ jets and $t\bar{t}$ processes enter into the hadronic signal sample due to unidentified leptons from acceptance effects or reconstruction inefficiencies and hadronic tau decays. These leptons originate from the decay of high p_T W bosons.

The control sample specifically identify $W \rightarrow \mu\nu$ decays within a similar phase-space of the signal region, where the muon is subsequently ignored in the calculation of event level variables, i.e. H_T , \mathcal{H}_T , α_T .

All kinematic jet-based selection criteria are identical to those applied in the hadronic search region (with the exception of an α_T , requirement discussed below) detailed in Section (4.2.2), with the same H_T , jet multiplicity and b-jet multiplicity categorisation described previously. Furthermore, the following selection criteria are also required:

- Muons originating from W boson decays are selected by requiring one tightly isolated muon defined in Table 4.2, with a $p_T > 30$ GeV and $|\eta| < 2.1$. Both of these thresholds arise from trigger restrictions.
- The transverse mass of the W candidate must satisfy $M_T(\mu, \cancel{E}_T) > 30$ GeV (to suppress QCD multi-jet events).
- Events which contain a jet overlapping with a muon $\Delta R(\mu, \text{jet}) < 0.5$ are vetoed to remove events from muons produced as part of a jet’s hadronisation process.
- Events containing a second muon candidate which has failed id, but passing p_T and $|\eta|$ requirements, are checked to have an invariant mass that satisfies $|M_{\mu\mu} - m_Z| > 25$, thus removing $Z \rightarrow \mu\mu$ contamination.

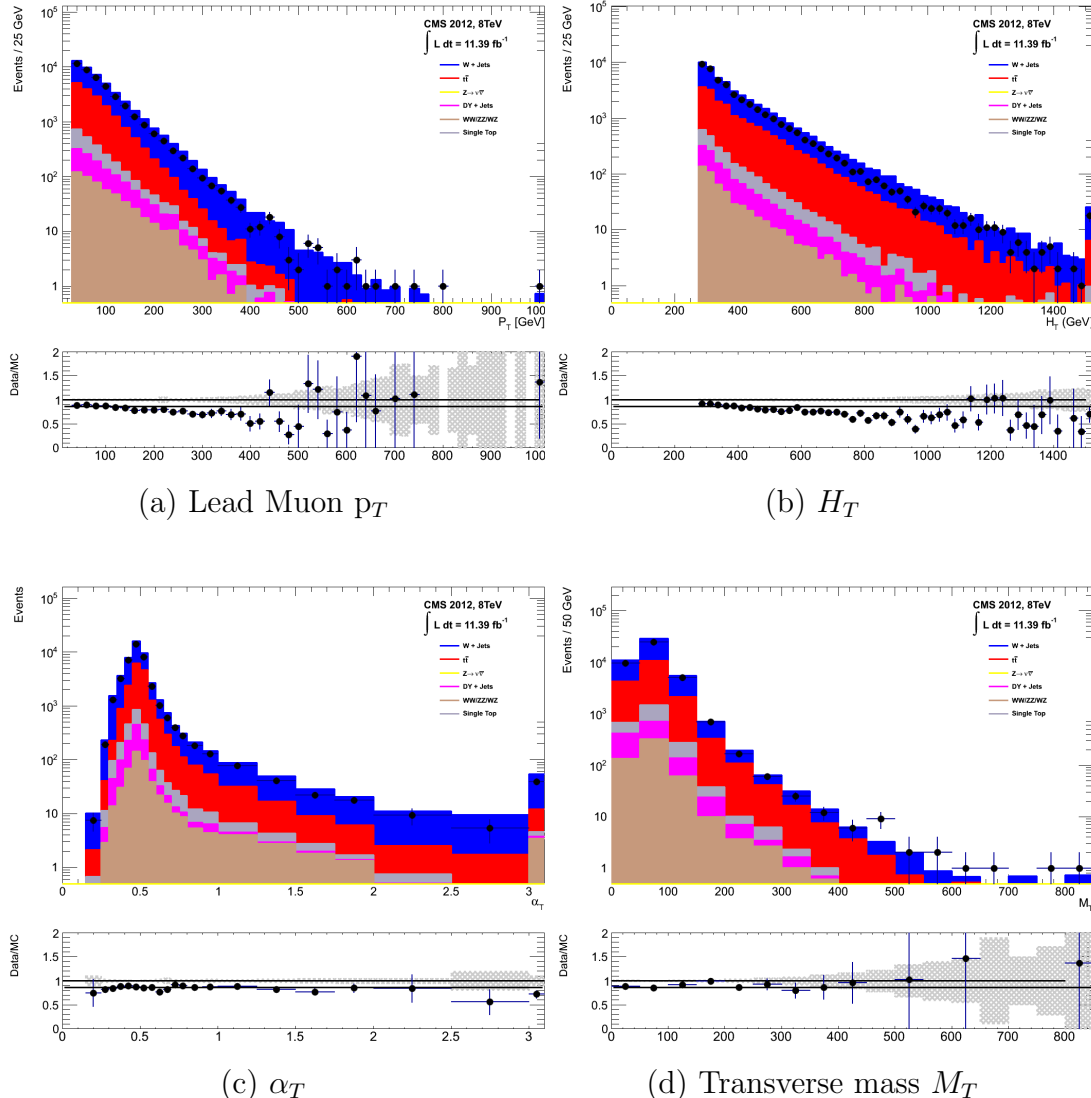


Figure 4.6: Data/MC comparisons of key variables for the $\mu +$ jets selection, following the application of selection criteria and the requirements that $H_T > 275$ GeV. Bands represent the uncertainties due to the statistical size of the MC samples. No requirement is made upon the number of b-tagged jets or jet multiplicity in these distributions.

The $\mu\mu$ + jets control sample

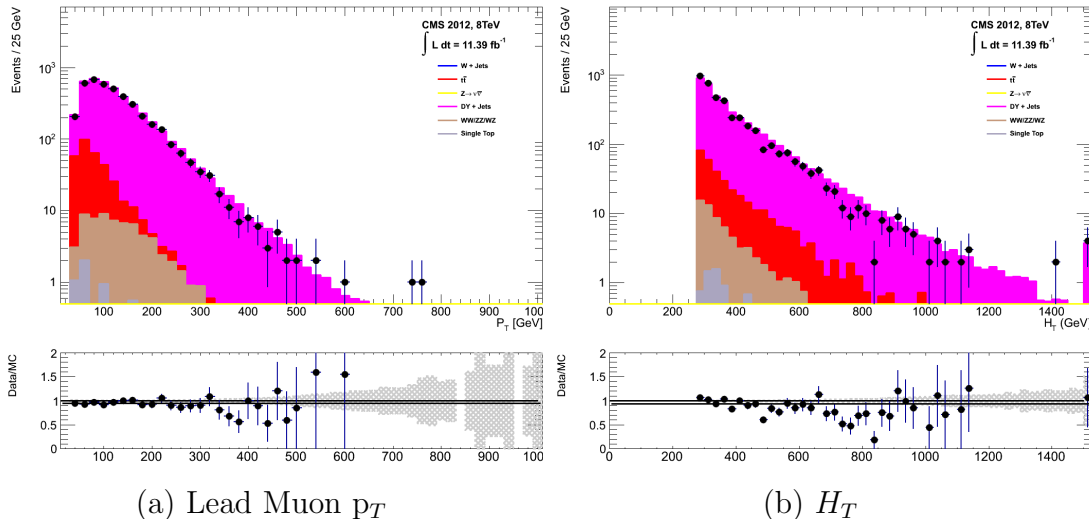
An irreducible $Z \rightarrow \nu\bar{\nu} + \text{jets}$ background enters into the signal region from genuine E_T from the escaping neutrinos. This background is estimated using two control samples, the first of which is the $Z \rightarrow \mu\bar{\mu} + \text{jets}$ process, which posses identical kinematic properties, but with different acceptance and branching ratio [1].

The same acceptance requirements as the $\mu + \text{jets}$ selection for muons is applied, as defined in Table 4.2. Muons in the event are ignored for the purpose of the

calculation of event level variables. In addition to kinematic jet-based selection criteria (with the exception of an α_T requirement, discussed below) and event categorisation, which are identical to the hadronic search region, the following selection criteria are also specified:

- Muons originating from a Z boson decay are selected, requiring exactly two tightly isolated muons. Due to trigger requirements the leading muon is required to have $p_T > 30$ GeV and $|\eta| < 2.1$. The requirement of the p_T on the second muon is relaxed to 10 GeV.
- Events are vetoed if containing a jet overlapping with a muon $\Delta R(\mu, \text{jet}) < 0.5$.
- In order to specifically select two muons both originating from a single Z boson decay, the invariant mass of the two muons must satisfy $|M_{\mu\mu} - m_Z| < 25$.

The $\mu\mu + \text{jets}$ sample is able to make predictions in the signal region of the two lowest H_T bins, providing coverage where the $\gamma + \text{jets}$ sample is unable to, due to trigger requirements. In higher H_T bins, the higher event statistics of the $\gamma + \text{jets}$ sample is also used in determining the $Z \rightarrow \nu\bar{\nu}$ estimation.



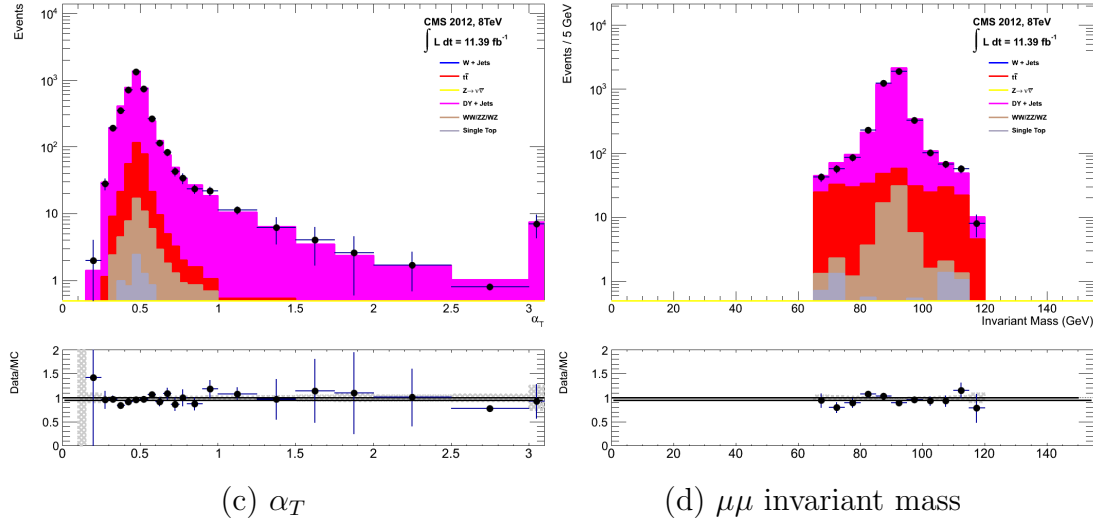


Figure 4.7: Data/MC comparisons of key variables for the $\mu\mu + \text{jets}$ selection, following the application of selection criteria and the requirements that $H_T > 275$ GeV. Bands represent the uncertainties due to the statistical size of the MC samples. No requirement is made upon the number of b-tagged jets or jet multiplicity in these distributions.

The $\gamma + \text{jets}$ control sample

The $Z \rightarrow \nu\bar{\nu} + \text{jets}$ background is also estimated from a $\gamma + \text{jets}$ control sample. When the E_T of the photon is greater than the mass of the Z , it possesses a larger cross-section and has kinematic properties similar to those of $Z \rightarrow \nu\bar{\nu}$ events if the photon is ignored [81].

Within the control channel, the photon is ignored for the purpose of the calculation of event level variables, and identical selection criteria to the hadronic signal region are applied. In addition the follow requirements are also made:

- Exactly one photon is selected, satisfying identification criteria as detailed in Table 4.3, with a minimum $p_T > 165$ GeV to satisfy trigger thresholds and $|\eta| < 1.45$ to ensure the photon remains in the barrel of the detector.
- A selection criteria of $\Delta R(\gamma, \text{jet}) < 1.0$, between the photon and all jets is applied to ensure the acceptance of only well isolated $\gamma + \text{jets}$ events.
- Given that the photon is ignored, this control sample can only be applied in the H_T region > 375 GeV, due to the trigger thresholds on the minimum p_T of the photon, and the H_T requirement of an $\alpha_T > 0.55$ cut from Equation (4.5). This

is maintained in this control sample due to contamination from QCD processes in the absence of an α_T cut.

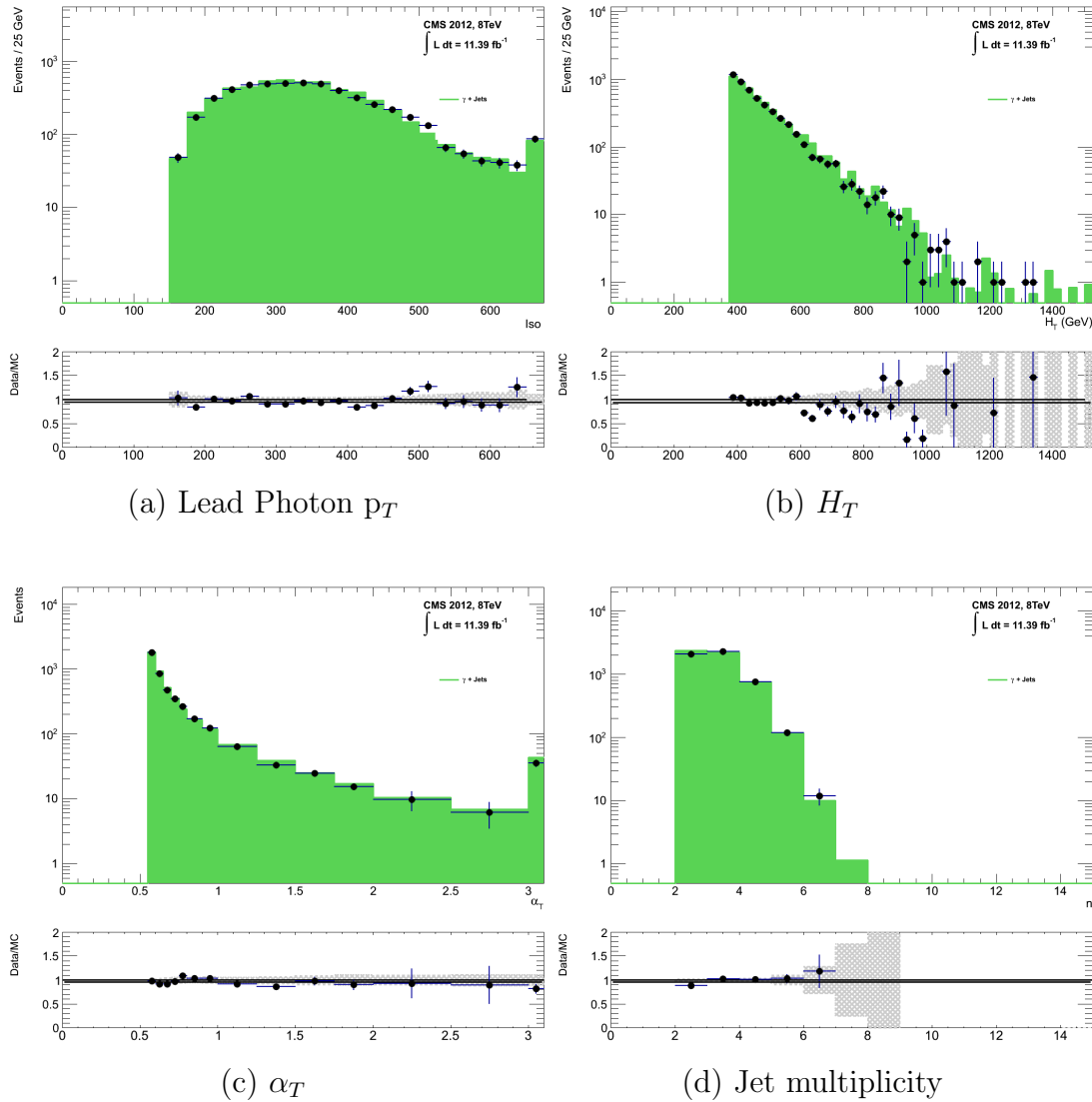


Figure 4.8: Data/MC comparisons of key variables for the $\gamma + \text{jets}$ selection, following the application of selection criteria and the requirements that $H_T > 375 \text{ GeV}$ and $\alpha_T > 0.55$. Bands represent the uncertainties due to the statistical size of the MC samples. No requirement is made upon the number of b-tagged jets or jet multiplicity in these distributions.

The selection criteria of the three control samples are defined to ensure background composition and event kinematics mirror closely the signal region. This is done in order to minimise the reliance on simulation to model correctly the backgrounds and event kinematics in the control and signal samples.

1612 However in the case of the $\mu + \text{jets}$ and $\mu\mu + \text{jets}$ samples, the α_T requirement is relaxed
1613 in the selection criteria of these samples. This is made possible as contamination from
1614 QCD multi-jet events is suppressed to a negligible level by the other kinematic selection
1615 criteria within the two control samples, selecting pure EWK processes. Thus in this way,
1616 the acceptance of the two muon control samples can be significantly increased, which
1617 simultaneously improves their statistical and predictive power and also dilutes the effect
1618 of any potential signal contamination.

1619 The modelling of the α_T variable is probed through a dedicated set of closure tests,
1620 described in Section (4.6), which demonstrate that the different α_T acceptances for
1621 the control and signal samples have no significant systematic bias on the background
1622 predictions.

1623 4.2.4. Estimating the QCD Multi-jet Background

1624 A negligible background from QCD multi-jet events within the hadronic signal region is
1625 expected due to a combination of selection requirements, and additional applied cleaning
1626 filters. However a conservative approach is still adopted and the likelihood model, see
1627 Section (4.8.2), is given the freedom to accommodate any potential QCD multi-jet
1628 contamination.

1629 Any potential contamination can be identified through the variable R_{α_T} , defined as the
1630 ratio of events above and below the α_T threshold value used in the analysis. This is
1631 modelled by a H_T dependant falling exponential function which takes the form,

$$R_{\alpha_T}(H_T) = A_{\text{QCD}} \exp^{-k_{\text{QCD}} H_T}, \quad (4.10)$$

1632 where the parameters A_{QCD} and k_{QCD} are the normalisation and exponential decay
1633 constants, respectively.

1634 For QCD multi-jet event topologies, this exponential behaviour as a function of H_T is
1635 expected for several reasons. The improvement of jet energy resolution at higher H_T
1636 due to higher p_T jets leads to a narrower peaked α_T distribution, causing R_{α_T} to fall.
1637 Similarly at higher H_T values > 375 GeV, the jet multiplicity rises slowly with H_T . As
1638 shown in Figure 4.3, at higher jet multiplicities the result of the combinatorics used in

1639 the determination of α_T lead to more conservative α_T values, also resulting in a narrower
1640 distribution.

1641 The value of the decay constant k_{QCD} is constrained via measurements within data
1642 sidebands to the signal region. This is also done to validate the falling exponential
1643 assumption for QCD multi-jet topologies. The sidebands are enriched in QCD multi-jet
1644 background and defined as regions where either α_T is relaxed or that the R_{miss} cut is
1645 inverted. Figure 4.9 depicts the definition of these data sidebands used to constrain the
1646 value of k_{QCD} .

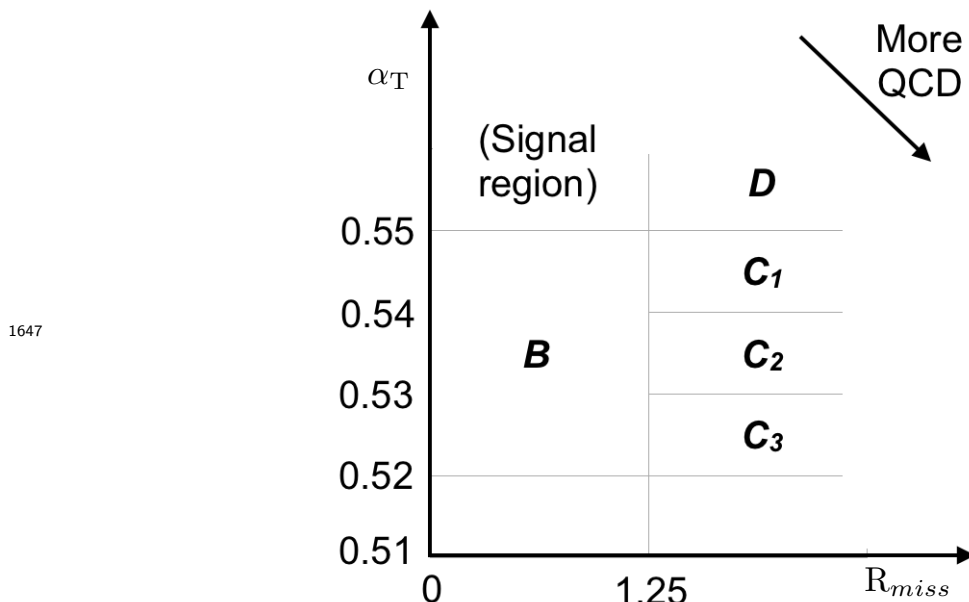


Figure 4.9: QCD sideband regions, used for determination of k_{QCD} .

1648 The fit results used to determine the value of k_{QCD} are shown in Appendix (C.1), for
1649 which the best fit parameter value obtained from sideband region B is determined to be
1650 $k_{\text{QCD}} = 2.96 \pm 0.64 \times 10^{-2} \text{ GeV}^{-1}$.

1651 The best fit values of the remaining three C sideband regions are used to estimate
1652 the systematic uncertainty on the central value obtained from sideband region B. The
1653 variation of these measured values is used to determine the error on the determined
1654 central value, and is calculated to be $1.31 \pm 0.26 \times 10^{-2} \text{ GeV}^{-1}$. This relative error of \sim
1655 20% gives an estimate of the systematic uncertainty of the measurement to be applied to
1656 k_{QCD} .

1657 Finally the same procedure is performed for sideband region D as an independent
1658 crosscheck, to establish that the value of k_{QCD} extracted from a lower α_T slice, can be

1659 applied to the signal region $\alpha_T > 0.55$. The likelihood fit is performed across all H_T
1660 bins within the QCD enriched region with no constraint applied to k_{QCD} . The resulting
1661 best fit value for k_{QCD} shows good agreement between that and the weighted mean,
1662 determined from the three C sideband regions. This demonstrates that the assumption
1663 of using the central value determined from sideband region B, to provide an unbiased
1664 estimator for k_{QCD} in the signal region ($\alpha_T > 0.55$) is valid.

1665 Table 4.7 summarises the best fit k_{QCD} values determined for each of the sideband regions
1666 to the signal region.

Sideband region	$k_{QCD} (\times 10^{-2} GeV^{-1})$	p -value
B	2.96 ± 0.64	0.24
C ₁	1.19 ± 0.45	0.93
C ₂	1.47 ± 0.37	0.42
C ₃	1.17 ± 0.55	0.98
C(weighted mean)	1.31 ± 0.26	-
D(likelihood fit)	1.31 ± 0.09	0.57

Table 4.7: Best fit values for the parameters k_{QCD} obtained from sideband regions B,C₁,C₂,C₃. The weighted mean is determined from the three measurements made within sideband region C. The maximum likelihood value of k_{QCD} given by the simultaneous fit using sideband region D. Quotes errors are statistical only.

1667 4.3. Trigger Strategy

1668 A cross trigger based on the H_T and α_T values of an event, is used with varying thresholds
1669 across H_T bins to record the events used in the hadronic signal region. The α_T legs of
1670 the HT_alphaT triggers used in the analysis, are chosen to suppress QCD multi-jet events
1671 and control trigger rate, whilst maintaining signal acceptance. To maintain an acceptable
1672 rate for these analysis triggers, only calorimeter information is used in the reconstruction
1673 of the H_T sum, leading to the necessity for Calo jets to be used within the analysis.

1674 A single object prescaled HT trigger is used to collect events for the hadronic control
1675 region, described above in Section (4.2.4).

1676 The performance of the α_T and H_T triggers used to collect data for the signal and
1677 hadronic control region is measured with respect to a reference sample collected using
1678 the muon system. This allows measurement of both the Level 1 seed and higher level

1679 triggers simultaneously, as the reference sample is collected independently of any jet
1680 requirements.

1681 The selection for the trigger efficiency measurement is identical to that described in
1682 Section (4.2.2), with the requirement of exactly one well identified muon with $p_T > 30$
1683 GeV. This muon is then subsequently ignored.

1684 The efficiencies measured for the HT_alphaT triggers in each individual H_T and α_T leg,
1685 is summarised in Table 4.8 for each H_T category of the analysis.

H_T range (GeV)	ϵ on H_T leg (%)	ϵ on α_T leg (%)
275-325	$87.7^{+1.9}_{-1.9}$	$82.8^{+1.0}_{-1.1}$
325-375	$90.6^{+2.9}_{-2.9}$	$95.9^{+0.7}_{-0.9}$
375-475	$95.7^{+0.1}_{-0.1}$	$98.5^{+0.5}_{-0.9}$
475- ∞	$100.0^{+0.0}_{-0.0}$	$100.0^{+0.0}_{-4.8}$

Table 4.8: Measured efficiencies of the H_T and α_T legs of the HT and HT_alphaT triggers in independent analysis bins. The product of the two legs gives the total efficiency of the trigger in a given offline H_T bin.

1686 Data for the control samples of the analysis, detailed in Section (4.2.3), are collected
1687 using a single object photon trigger for the $\gamma +$ jets sample, and a single object muon
1688 trigger for both the $\mu +$ jets and $\mu\mu +$ jets control samples.

1689 The photon trigger is measured to be fully efficient for the threshold $p_T^{\text{photon}} > 150$ GeV,
1690 whilst the single muon efficiency satisfying $p_T^{\text{muon}} > 30$ GeV is measured to have an
1691 efficiency of $(88 \pm 2)\%$ that is independent of H_T . In the case of the $\mu\mu +$ jets control
1692 sample, the efficiency is measured to be $(95 \pm 2)\%$ for the lowest H_T bin, rising (due to
1693 the average p_T of the second muon in the event increasing at larger H_T) to $(98 \pm 2)\%$ in
1694 the highest H_T category.

1695 4.4. Measuring Standard Model Process 1696 Normalisation Factors via H_T Sidebands

1697 The theoretical cross-sections of different SM processes at Next to Next Leading Order
1698 (NNLO) and the number of available simulated events generated for a particular process,
1699 is typically used to determine the appropriate normalisation for a simulation sample.
1700 However within the particular high- H_T and high- \mathcal{E}_T corners of kinematic phase space

1701 probed within this search, the theoretical cross sections for various processes are far less
1702 well understood.

1703 To mitigate the problem of theoretical uncertainties and arbitrary choices of cross
1704 sections, the normalisation of the simulation samples are determined through the use of
1705 data sidebands. The sidebands are used to calculate sample specific correction factors
1706 (k-factors), that are appropriate for the H_T - \cancel{E}_T phase space covered by this analysis.

1707 They are defined within the $\mu +$ jets and $\mu\mu +$ jets control sample, by the region $200 <$
1708 $H_T < 275$, using the same jet p_T thresholds as the adjacent first analysis bin. Individual
1709 EWK processes are isolated within each of these control samples via requirements on jet
1710 multiplicity and the requirement on b-tag multiplicity, summarised in Table 4.9. The
1711 purity of the samples are typically $> 90\%$ with any residual contamination subtracted
1712 prior to determination of the correction factors. The resultant k-factor for each process
1713 is determined by then taking ratio of the data yield over the expectation from simulation
1714 in the sideband. Subsequently these k-factors are then applied to the processes within
1715 the phase space of the analysis.

Process	Selection	Observation	MC expectation	k-factor
W + jets	$\mu +$ jets, $n_b=0$, $n_{jet} = 2,3$	26950	29993.2 ± 650.1	0.90 ± 0.02
$Z \rightarrow \mu\mu +$ jets	$\mu\mu +$ jets, $n_b=0$, $n_{jet} = 2,3$	3141	3402.0 ± 43.9	0.92 ± 0.02
$t\bar{t}$	$\mu +$ jets, $n_b=2$, $n_{jet} = \geq 4$	2190	1967.8 ± 25.1	1.11 ± 0.02

Table 4.9: k-factors calculated for different EWK processes. All k-factors are derived relative to theoretical cross-sections calculated in NNLO. The k-factors measured for the $Z \rightarrow \mu\mu +$ jets processes, are also applied to the $Z \rightarrow \nu\bar{\nu} +$ jets and $\gamma +$ jets simulation samples.

1716 It is worth pointing out that these correction factors have a negligible effect when
1717 providing a background estimation for the signal region. The TFs used in the analysis
1718 are found to be unaffected by application of these k-factors due to the similarity in the
1719 background composition of the control and signal regions. However when systematic
1720 uncertainties are determined in Section (4.6), the closure tests performed are sensitive
1721 to these corrections when extrapolations between different n_b^{reco} and n_{jet} categories are
1722 performed.

1723 4.5. Determining Monte Carlo Simulation Yields 1724 with Higher Statistical Precision

1725 Reconstructing events from **EWK** processes with many b-tagged jets (≥ 3), n_b^{reco} , is largely
1726 driven by the mis-tagging of light jets within the event. This is clear when considering
1727 the main **EWK** backgrounds in the analysis, such as $t\bar{t} + \text{jets}$ events, which typically
1728 contain two b-flavoured jets from the decay of the top quarks, whilst $W + \text{jets}$ and
1729 $Z \rightarrow \mu\mu + \text{jets}$ events will typically contain no b-flavoured jets.

1730 When the expectation for the number of n_b^{reco} jets is taken directly from simulation, the
1731 statistical uncertainty at large reconstructed b-tagged jet multiplicities becomes relatively
1732 large. In order to reduce this uncertainty one approach is to use the information encoded
1733 throughout all events in the simulation sample, to measure each of the following four
1734 ingredients:

- 1735 1. the b-tagging efficiency in the event selection,
- 1736 2. the charm-tagging efficiency in the event selection,
- 1737 3. the mis-tagging rate in the event selection,
- 1738 4. the underlying flavour distribution of the jets in the events.

1739 Together they can be used to determine the n_b^{reco} distribution of the process being
1740 measured. This method allows the determination of higher b-tag multiplicities to a higher
1741 degree of accuracy, reducing the statistical uncertainties of the simulation yields which
1742 enter into the **TF**'s. For the discussion that follows, these predictions are determined on
1743 average (i.e not on an event-by-event basis), and will be known as the formula method.

1744 4.5.1. The Formula Method

1745 The assigning of jet flavours to reconstruction level jets in simulation is achieved via an
1746 algorithmic method defined as:

- 1747 • attempt to find the parton that most likely determines the properties of the jet and
1748 assign that flavour as the true flavour,
- 1749 • “final state” partons (after showering, radiation) are analysed (also within $\Delta R <$
1750 0.3 of reconstructed jet cone),

- 1751 • if there is a b/c flavoured parton within the jet cone: label the jet as a b/c flavoured
1752 jet,
- 1753 • otherwise: assign flavour of the hardest parton within the jet cone.

1754 This process is employed within each individual simulation sample and independently for
1755 each H_T - n_{jet} category in the analysis. The n_b^{reco} distribution can then be constructed in
1756 an analytical way using the formula:

$$N(n) = \sum_{n_b^{\text{gen}} + n_c^{\text{gen}} + n_q^{\text{gen}} = n_{\text{jet}}} \sum_{n_b^{\text{tag}} + n_c^{\text{tag}} + n_q^{\text{tag}} = n} N(n_b^{\text{gen}}, n_c^{\text{gen}}, n_q^{\text{gen}}) \times P(n_b^{\text{tag}}, n_b^{\text{gen}}, \epsilon) \times \\ P(n_c^{\text{tag}}, n_c^{\text{gen}}, \beta) \times P(n_q^{\text{tag}}, n_q^{\text{gen}}, m), \quad (4.11)$$

1757 with $N(n)$ representing the number of n b-tagged jets of a simulated **SM** process in a
1758 particular H_T - n_{jet} category.

1759 Let $N(n_b^{\text{gen}}, n_c^{\text{gen}}, n_q^{\text{gen}})$ represent the 3-dimensional underlying jet flavour distribution in
1760 simulation, with b underlying b-quarks, c underlying c-quarks and q underlying light
1761 quarks which are matched to reconstructed jets as detailed above. Light quarks defined
1762 as those which originate from a u , d , s , g and τ jets, which having similar mis-tagging
1763 rates are grouped together.

1764 The variables $n_{b/c/q}^{\text{tag}}$ signify the number of times that a particular jet flavour results in
1765 a tagged jet, of which the sum of the three terms must equal the number of n tagged
1766 jets being calculated. Similarly $n_{b/c/q}^{\text{gen}}$ represent the flavour admixture of the jets, which
1767 having been identified using the above technique as b, c or light flavoured jets, are
1768 required by definition that the sum of the three to fall within the n_{jet} category being
1769 analysed.

1770 Finally $P(n_b^{\text{tag}}, n_b^{\text{gen}}, \epsilon)$, $P(n_c^{\text{tag}}, n_c^{\text{gen}}, \beta)$ and $P(n_q^{\text{tag}}, n_q^{\text{gen}}, m)$ correspond to the binomial
1771 probabilities for the tagging of jet with a particular flavour to occur, based on its measured
1772 tagging efficiency (ϵ , β or m). This formula is applied to calculate the resultant n_b^{reco}
1773 distribution, within a H_T category for each process in turn.

1774 This approach ultimately results in a more precise n_b^{reco} distribution prediction, due to the
1775 utilisation of all events in simulation sample which pass selection in extracting the overall

1776 underlying n_b^{reco} distribution. This is particularly useful at higher n_b^{reco} multiplicities
1777 where a lack of events in simulation can lead to relatively large statistical uncertainties.

1778 4.5.2. Establishing Proof of Principle

1779 In order to validate the procedure, the predictions determined from the formula method
1780 summarised in Equation (4.11), are compared directly with those obtained directly from
1781 simulation. Resultantly no simulation to data correction factors are applied when making
1782 this comparison

1783 This sanity check for the $\mu +$ jets control sample is presented in Table 4.10, for all n_b^{reco}
1784 and H_T categories with no requirement placed upon the jet multiplicity of the events.

H_T Bin (GeV)	275–325	325–375	375–475	475–575
Formula $n_b = 0$	12632.66 ± 195.48	6696.08 ± 82.59	6368.96 ± 75.34	2906.27 ± 39.65
Vanilla $n_b = 0$	12612.95 ± 198.68	6687.97 ± 83.78	6359.27 ± 76.50	2898.27 ± 36.89
Formula $n_b = 1$	4068.09 ± 45.71	2272.76 ± 26.14	2181.32 ± 25.07	1089.14 ± 13.82
Vanilla $n_b = 1$	4067.73 ± 60.30	2268.02 ± 30.20	2180.69 ± 28.73	1094.37 ± 24.14
Formula $n_b = 2$	1963.71 ± 22.44	1087.55 ± 13.57	1055.57 ± 13.25	554.96 ± 7.95
Vanilla $n_b = 2$	1984.53 ± 26.19	1094.43 ± 16.67	1068.96 ± 16.36	558.14 ± 10.51
Formula $n_b = 3$	146.94 ± 2.07	79.97 ± 1.37	78.05 ± 1.35	49.84 ± 1.03
Vanilla $n_b = 3$	149.52 ± 4.84	85.98 ± 3.64	74.45 ± 3.29	49.54 ± 2.68
Formula $n_b \geq 4$	2.26 ± 0.12	1.29 ± 0.10	5.32 ± 0.20	-
Vanilla $n_b \geq 4$	1.84 ± 0.50	1.02 ± 0.39	4.86 ± 0.83	-
H_T Bin (GeV)	575–675	675–775	775–875	>875
Formula $n_b = 0$	1315.68 ± 19.49	640.49 ± 11.90	327.81 ± 7.91	424.27 ± 9.27
Vanilla $n_b = 0$	1315.23 ± 20.20	641.96 ± 12.48	329.09 ± 8.36	424.02 ± 9.73
Formula $n_b = 1$	490.41 ± 7.45	226.95 ± 4.42	109.91 ± 2.84	129.97 ± 3.07
Vanilla $n_b = 1$	490.52 ± 9.92	222.22 ± 6.21	107.46 ± 4.15	129.64 ± 4.64
Formula $n_b = 2$	256.75 ± 4.58	113.45 ± 2.70	52.10 ± 1.69	59.29 ± 1.78
Vanilla $n_b = 2$	253.43 ± 6.52	117.17 ± 4.27	52.70 ± 2.80	59.45 ± 3.00
Formula $n_b = 3$	25.66 ± 0.69	12.48 ± 0.46	5.52 ± 0.31	6.83 ± 0.33
Vanilla $n_b = 3$	29.18 ± 2.06	11.77 ± 1.26	6.18 ± 0.95	7.53 ± 1.05

Table 4.10: Comparing yields in simulation within the $\mu +$ jets selection determined from the formula method described in Equation (4.11), and that taken directly from simulation. The numbers are normalised to 11.4fb^{-1} . No simulation to data corrections are applied.

1785 It can be seen as expected, that there is good consistency between the results determined
 1786 via the formula method and ‘raw’ simulation yields. Similarly the power of this approach
 1787 can be seen in the reduction of this statistical error in the prediction across all H_T and
 1788 n_b^{reco} categories. In particular the statistical uncertainty is reduced by several factors in
 1789 the highest $n_b^{reco} \geq 4$ category.

1790 4.5.3. Correcting Measured Efficiencies in Simulation to Data

1791 As detailed in Section (3.3.2), it is necessary for certain p_T and η dependant corrections,
 1792 to be applied to both the b-tagging efficiency and mis-tagging rates in order to correct
 1793 the efficiencies from simulation to the efficiencies measured in data. These correction
 1794 factors are considered when determining the simulation yields for each selection, which
 1795 are used to construct the TFs of the analysis. The magnitude of this correction are
 1796 measured individually for each H_T category and are shown in Figure 4.10.

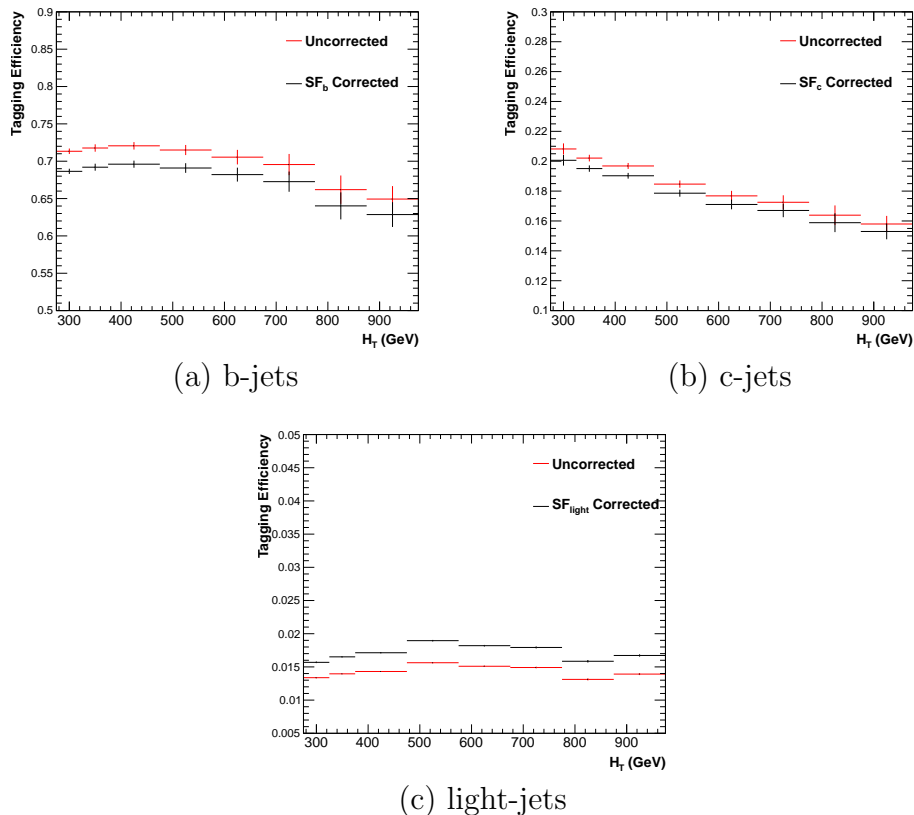


Figure 4.10: Tagging efficiencies of (a) b-jets, (b) c-jets, and (c) light-jets as a function all jets within each H_T category. Efficiencies measured directly from simulation (black) and with data to simulation $SF_{b,c,light}$ correction factors (red) are applied.

1797 Each of the correction factors for the b, c and light flavoured jets come with an associated
1798 systematic uncertainty. The uncertainties across different jet p_T and η categories, are
1799 considered as fully correlated. When computing the magnitude of the effect of this
1800 systematic uncertainty on the **TFs** of the analysis, the measured tagging efficiencies for
1801 each jet flavour are scaled up/down simultaneously within each H_T and n_{jet} category by
1802 the systematic uncertainty of the $SF_{b, c, \text{light}}$ scale factors.

1803 Varying the scale factor corrections by their systematic uncertainty will change the
1804 absolute yields within each n_b^{reco} bin of all selections. However, ultimately it is the change
1805 in the **TFs** which influences the final background prediction from each of the control
1806 samples. The magnitude of the absolute change in each **TF**, constructed from when the
1807 $\mu + \text{jets}$ control sample is used to predict the entire hadronic signal region background,
1808 is shown in Table 4.11.

n_b^{reco}	275–325	325–375	375–475	475–575
= 0	$0.557^{+0.001}_{-0.001} \pm 0.012$	$0.495^{+0.001}_{-0.001} \pm 0.009$	$0.383^{+0.001}_{-0.001} \pm 0.005$	$0.307^{+0.001}_{-0.002} \pm 0.006$
= 1	$0.374^{+0.006}_{-0.006} \pm 0.006$	$0.320^{+0.006}_{-0.005} \pm 0.005$	$0.251^{+0.005}_{-0.005} \pm 0.004$	$0.185^{+0.003}_{-0.003} \pm 0.004$
= 2	$0.226^{+0.002}_{-0.002} \pm 0.004$	$0.201^{+0.001}_{-0.002} \pm 0.004$	$0.159^{+0.001}_{-0.001} \pm 0.004$	$0.134^{+0.000}_{-0.001} \pm 0.004$
= 3	$0.221^{+0.002}_{-0.002} \pm 0.005$	$0.208^{+0.002}_{-0.001} \pm 0.007$	$0.164^{+0.001}_{-0.000} \pm 0.006$	$0.144^{+0.001}_{-0.001} \pm 0.007$
≥ 4	$0.222^{+0.004}_{-0.005} \pm 0.015$	$0.248^{+0.003}_{-0.003} \pm 0.035$	$0.123^{+0.002}_{-0.003} \pm 0.009$	-
	575–675	675–775	775–875	≥ 875
= 0	$0.263^{+0.001}_{-0.002} \pm 0.006$	$0.215^{+0.000}_{-0.001} \pm 0.007$	$0.171^{+0.000}_{-0.001} \pm 0.009$	$0.111^{+0.000}_{-0.001} \pm 0.006$
= 1	$0.154^{+0.003}_{-0.003} \pm 0.005$	$0.138^{+0.003}_{-0.004} \pm 0.006$	$0.121^{+0.005}_{-0.005} \pm 0.007$	$0.091^{+0.002}_{-0.002} \pm 0.006$
= 2	$0.104^{+0.000}_{-0.001} \pm 0.005$	$0.079^{+0.001}_{-0.001} \pm 0.006$	$0.063^{+0.001}_{-0.002} \pm 0.007$	$0.071^{+0.000}_{-0.000} \pm 0.008$
= 3	$0.116^{+0.001}_{-0.001} \pm 0.009$	$0.069^{+0.001}_{-0.001} \pm 0.007$	$0.079^{+0.001}_{-0.001} \pm 0.017$	$0.095^{+0.003}_{-0.002} \pm 0.020$

Table 4.11: The absolute change in the **TFs** used to predict the entire signal region **SM** background, using the $\mu + \text{jets}$ control sample when the systematic uncertainties of the data to simulation scale factors are varied by $\pm 1\sigma$. The impact of the change is shown for each H_T and n_b^{reco} category with no requirement made on the jet multiplicity of the events. (Also quoted are the statistical uncertainties)

1809 It can be seen that the **TFs** are found to be relatively insensitive to the systematic
1810 uncertainty of the b-tag scale factors (showing typically less than $\sim 2\%$ change). This
1811 can be accounted for by the similar composition of the signal and control sample
1812 backgrounds, such that any change in the underlying n_b^{reco} distribution will be reflected
1813 in both signal and control regions and cancel out in the **TF**.

1814 Any overall systematic effect on the overall background prediction of the analysis from
1815 these b-tag scale factor uncertainties is incorporated within the data driven systematics
1816 introduced in the following section.

1817 4.6. Systematic Uncertainties on Transfer Factors

1818 Since the TFs used to establish the background prediction are obtained from simulation,
1819 an appropriate systematic uncertainty is assigned to account for theoretical uncertainties
1820 [82] and limitations in the simulation modelling of event kinematics and instrumental
1821 effects.

1822 The magnitudes of these systematic uncertainties are established through a data driven
1823 method, in which the three independent control samples of the analysis ($\mu + \text{jets}$, $\mu\mu$
1824 + jets, $\gamma + \text{jets}$) are used to in a series of closure tests. The yields from one of these
1825 control samples, along with the corresponding TF obtained from simulation, are used to
1826 predict the expected yields in another control sample. This procedure therefore utilised
1827 the same method used in determining a background prediction for the signal region as
1828 already established in Section (4.2.3).

1829 The level of agreement between the predicted and observed yields is expressed as the
1830 ratio

$$\frac{(N_{\text{obs}} - N_{\text{pred}})}{N_{\text{pred}}}, \quad (4.12)$$

1831 while considering only the statistical uncertainties on the prediction, N_{pred} , and the
1832 observation, N_{obs} . No systematic uncertainty is assigned to the prediction, and resultantly
1833 the level of closure is defined by the statistical significance of a deviation from the ratio
1834 from zero.

1835 This ratio is measured for each H_T category in the analysis, allowing these closure tests to
1836 be sensitive to both the presence of any significant biases or any possible H_T dependence
1837 to the level of closure.

1838 Eight sets of closure tests are defined between the three data control samples, conducted
1839 independently between the two jet multiplicity ($2 \leq n_{\text{jet}} \leq 3$, $n_{\text{jet}} \geq 4$) categories. Each

1840 of these tests are specifically chosen to probe each of the different key ingredients of the
1841 simulation modelling that can affect the background prediction.

1842 Each of the different modelling components and the relevant closure tests are described
1843 below:

1844 **α_T modelling**

1845 The modelling of the α_T distribution in genuine E_T events is probed with the μ
1846 + jets control sample. This test is important to verify the approach of removing
1847 the $\alpha_T > 0.55$ requirement from the $\mu +$ jets and $\mu\mu +$ jets samples to increase
1848 the precision of the background prediction. The test uses the $\mu +$ jets sample
1849 without an α_T cut to make a prediction into the $\mu +$ jets sample defined with the
1850 requirement $\alpha_T > 0.55$.

1851 **Background admixture**

1852 The sensitivity of the translation factors to the relative admixture of events from
1853 $W +$ jets and $t\bar{t}$ processes is probed by two closure tests.

1854 Within the $\mu +$ jets sample, a W boson enriched sub-sample ($n_b = 0$) is used
1855 to predict yields in a $t\bar{t}$ enriched sub-sample ($n_b = 1$). Similarly, the $t\bar{t}$ enriched
1856 sub-sample ($n_b = 1$) is also used to predict yields for a further enriched $t\bar{t}$ sub-sample
1857 ($n_b = 2$), further probing the modelling of the n_b^{reco} distribution.

1858 Similarly a further closure test probes the relative contribution of $Z +$ jets to $W +$ jets
1859 and $t\bar{t}$ events, through the use of the $\mu +$ jets sample to predict yields for the $\mu\mu +$
1860 jets control sample. This closure test, also at some level probes the muon trigger
1861 and reconstruction efficiencies, given that exactly one or two muons are required by
1862 the different selections.

1863 These tests represent an extremely conservative approach as the admixture of the
1864 two backgrounds remains similar when a prediction is made between the control
1865 samples and the signal region. This is contrary to the closure tests defined above
1866 which make predictions between two very different admixtures of $W +$ jets and $t\bar{t}$
1867 events.

1868 **Consistency check between $Z \rightarrow \nu\bar{\nu}$ predictions**

1869 This is an important consistency check between the $\mu\mu +$ jets and $\gamma +$ jets, which
1870 are both used in the prediction of the $Z \rightarrow \nu\bar{\nu}$ in the signal region. This is conducted

1871 by using the $\gamma + \text{jets}$ sample to predict yields for the $\mu\mu + \text{jets}$ control sample.
 1872 Using $\gamma + \text{jets}$ processes as a method to predict $Z + \text{jet}$ processes is subject to
 1873 theory uncertainties [83], which can be probed by this data driven closure test within
 1874 a $Z \rightarrow \mu\mu$ control sample.

1875 **Modelling of jet multiplicity**

1876 The simulation modelling of the jet multiplicity within each control sample is
 1877 important due to the exclusive jet multiplicity categorisation within the analysis.
 1878 This is probed via the use of each of the three control samples to independently
 1879 predict from the lower jet multiplicity category $2 \leq n_{\text{jet}} \leq 3$, to the high jet category
 1880 $n_{\text{jet}} \geq 4$.

1881 For the case of the $\mu + \text{jets}$ and $\mu\mu + \text{jets}$ control samples, this test also serves as a
 1882 further probe of the admixture between $W + \text{jets}/Z + \text{jets}$ and $t\bar{t}$.

1883 To test for the assumption that no H_T dependencies exist within the background pre-
 1884 dictions of the analysis, the first five closure tests defined above are used, with zeroeth
 1885 and first order polynomial fits applied to each test individually. This is summarised in
 1886 Table 4.12 and Table 4.13 which show the results for both the $2 \leq n_{\text{jet}} \leq 3$ and ≥ 4 jet
 1887 multiplicity bins respectively.

Closure test	Symbol	Constant fit		Linear fit	
		Best fit value	p-value	Slope (10^{-4})	p-value
$\alpha_T < 0.55 \rightarrow \alpha_T > 0.55 (\mu + \text{jets})$	Circle	-0.06 ± 0.02	0.93	-1.3 ± 2.2	0.91
0 b-jets \rightarrow 1 b-jet ($\mu + \text{jets}$)	Square	0.07 ± 0.02	0.98	-1.6 ± 1.6	1.00
1 b-jets \rightarrow 2 b-jet ($\mu + \text{jets}$)	Triangle	-0.07 ± 0.03	0.76	-2.7 ± 3.0	0.76
$\mu + \text{jets} \rightarrow \mu\mu + \text{jets}$	Cross	0.10 ± 0.03	0.58	-1.1 ± 2.3	0.49
$\mu\mu + \text{jets} \rightarrow \gamma + \text{jets}$	Star	-0.06 ± 0.04	0.31	4.2 ± 4.3	0.29

Table 4.12: A summary of the results obtained from zeroeth order polynomial (i.e. a constant) and linear fits to five sets of closure tests performed in the $2 \geq n_{\text{jet}} \geq 3$ category. The two columns show the best fit value for the slope obtained when performing a constant (left) and linear (right) fit and the p-value for that fit.

1888 Table 4.14 shows the same fits applied to the three closure tests that probe the modelling
 1889 between the two n_{jet} categories. The best fit value and its uncertainty is listed for each
 1890 set of closure tests in all three tables, along with the p-value of the constant and linear
 1891 fits applied.

1892 The best fit value for the constant parameter is indicative of the level of closure, averaged
 1893 across the full H_T range of the analysis, and the p-value an indicator of any significant
 1894 dependence on H_T within the closure tests. The best fit values of all the tests are either

Closure test	Symbol	Constant fit		Linear fit	
		Best fit value	p-value	Slope (10^{-4})	p-value
$\alpha_T < 0.55 \rightarrow \alpha_T > 0.55 (\mu + \text{jets})$	Circle	-0.05 ± 0.03	0.21	3.0 ± 2.9	0.21
$0 \text{ b-jets} \rightarrow 1 \text{ b-jet} (\mu + \text{jets})$	Square	-0.03 ± 0.03	0.55	-1.0 ± 1.9	0.47
$1 \text{ b-jets} \rightarrow 2 \text{ b-jet} (\mu + \text{jets})$	Triangle	-0.02 ± 0.03	0.39	1.1 ± 2.2	0.31
$\mu + \text{jets} \rightarrow \mu\mu + \text{jets}$	Cross	0.08 ± 0.07	0.08	4.8 ± 4.3	0.07
$\mu\mu + \text{jets} \rightarrow \gamma + \text{jets}$	Star	-0.03 ± 0.10	0.72	-4.0 ± 7.0	0.64

Table 4.13: A summary of the results obtained from zeroeth order polynomial (i.e. a constant) and linear fits to five sets of closure tests performed in the $n_{\text{jet}} \geq 4$ category. The two columns show the best fit value for the slope obtained when performing a constant (left) and linear (right) fit and the p-value for that fit.

Closure test	Symbol	Constant fit		Linear fit	
		Best fit value	p-value	Slope (10^{-4})	p-value
$\mu + \text{jets}$	Inverted triangle	-0.03 ± 0.02	0.02	0.0 ± 1.0	0.01
$\mu + \text{jets}$ (outlier removed)	Inverted triangle	-0.04 ± 0.01	0.42	-1.4 ± 1.1	0.49
$\gamma + \text{jets}$	Diamond	0.12 ± 0.05	0.79	6.0 ± 4.7	0.94
$\mu\mu + \text{jets}$	Asterisk	-0.04 ± 0.07	0.20	4.9 ± 4.4	0.20

Table 4.14: A summary of the results obtained from zeroeth order polynomial (i.e. a constant) and linear fits to three sets of closure tests performed between the $2 \leq n_{\text{jet}} \leq 3$ and $n_{\text{jet}} \geq 4$ categories. The two columns show the best fit value for the slope obtained when performing a constant (left) and linear (right) fit and the p-value for that fit.

1895 statistically compatible with zero bias (i.e. less than 2σ from zero) or at the level of 10%

1896 or less, with the exception of one closure test discussed below.

1897 Within Table 4.14, there exists one test that does not satisfy the above statement, which
 1898 is the $2 \leq n_{\text{jet}} \leq 3 \rightarrow n_{\text{jet}} \geq 4$ test using the $\mu + \text{jets}$ control sample. The low p-value
 1899 can be largely attributed to an outlier between $675 < H_T < 775$ GeV, rather than any
 1900 significant trend in H_T . Removing this single outlier from the constant fit performed,
 1901 gives a best fit value of -0.04 ± 0.01 , $\chi^2 / \text{d.o.f} = 6.07/6$. and a p-value of 0.42. These
 1902 modified fit results are also included in Table 4.14.

1903 Additionally, it is found that the best fit values for the slope terms of the linear fits in
 1904 all three tables are of the order 10^{-4} , which corresponds to a percent level change per
 1905 100 GeV. However in all cases, the best fit values are fully compatible with zero (within
 1906 1σ) once again with the exception detailed above, indicating that the level of closure is
 1907 indeed H_T independent.

4.6.1. Determining Systematic Uncertainties from Closure**Tests**

Once it has been established that no significant bias or trend exists within the closure tests, systematic uncertainties are determined. The statistical precision of the closure tests is considered a suitable benchmark for determining the systematic uncertainties that are assigned to the TFs, which are propagated through to the likelihood fit.

The systematic uncertainty band is split into five separate regions of H_T . Within each region the square root of the sample variance, σ^2 , is taken over the eight closure tests to determine the systematic uncertainties to be applied within that region.

Using this procedure the systematic uncertainties for each region are calculated and are shown in Table 4.15, with the systematic uncertainty to be used in the likelihood model conservatively rounded up to the nearest decile and applied across all n_b^{reco} categories.

H_T band (GeV)	$2 \leq n_{\text{jet}} \leq 3$	$n_{\text{jet}} \geq 4$
$275 < H_T < 325$	10%	10%
$325 < H_T < 375$	10%	10%
$375 < H_T < 575$	10%	10%
$575 < H_T < 775$	20%	20%
$H_T > 775$	20%	30%

Table 4.15: Calculated systematic uncertainties for the five H_T regions, determined from the closure tests. Uncertainties shown for both jet multiplicity categories. Values used within the likelihood model are conservatively rounded up to the nearest decile.

Figure 4.11 shows the sets of closure tests overlaid on top of grey bands that represent the H_T dependent systematic uncertainties. These systematic uncertainties are assumed to be fully uncorrelated between the different n_b multiplicity categories and across the five H_T regions. This can be considered a more conservative approach given that some correlations between adjacent H_T categories could be expected due to comparable kinematics.

These closure tests represent a conservative estimate of the systematic uncertainty in making a background prediction for the signal region. This is due to significant differences in the background composition and event kinematics between the two sub-samples used in the closure tests. This is not the case when a signal region prediction is made, due to the two sub-samples both having a comparable background admixture and similar kinematics owing to the fact that the TFs are always constructed using the same (n_{jet} , n_b^{reco} , H_T) category.

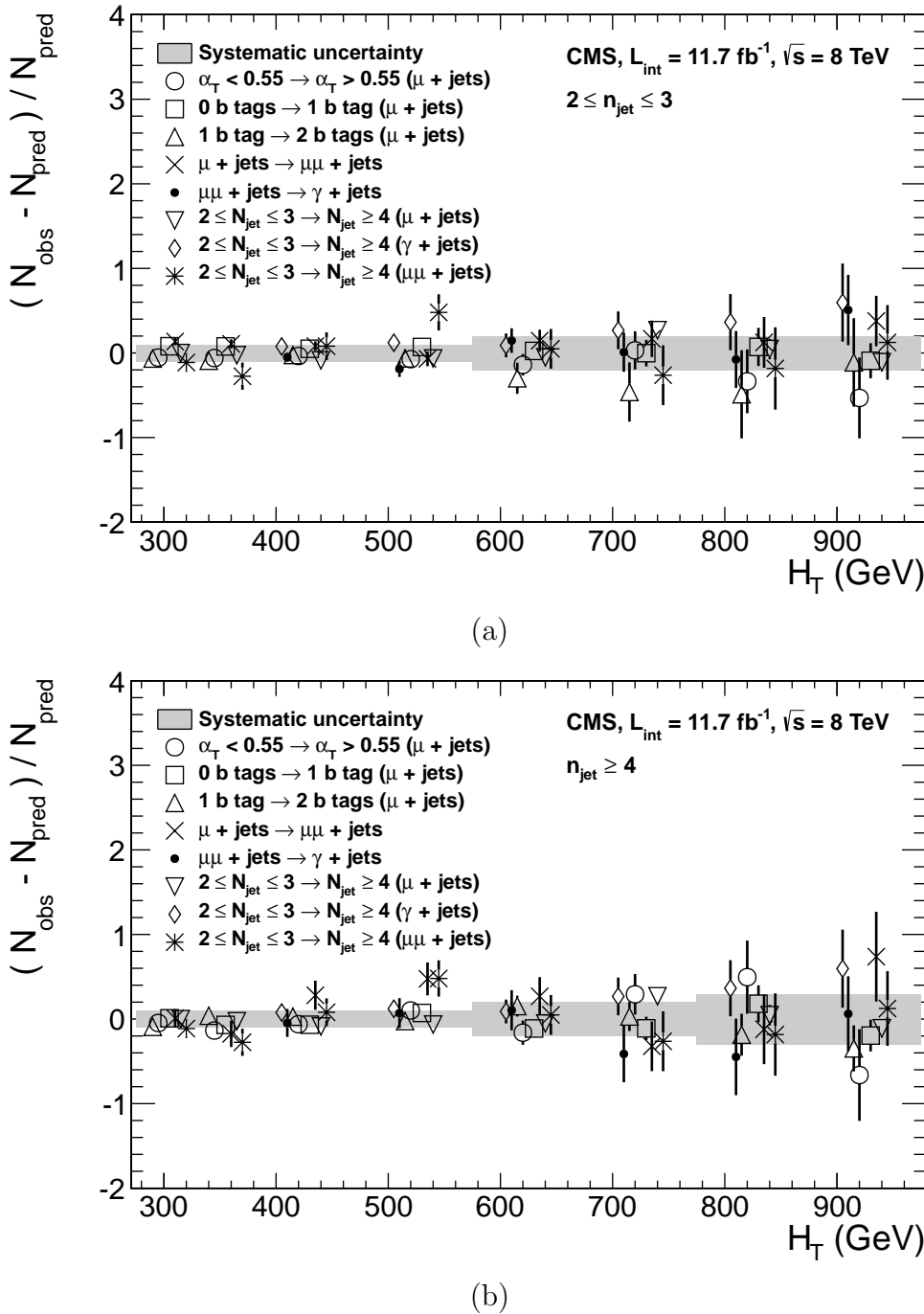


Figure 4.11: Sets of closure tests (open symbols) overlaid on top of the systematic uncertainty used for each of the five H_T regions (shaded bands) and for the two different jet multiplicity categories: (a) $2 \leq n_{\text{jet}} \leq 3$ and (b) $n_{\text{jet}} \geq 4$.

1932 This point is emphasised when we examine the sensitivity of the TFs to a change in the
 1933 admixture of $W + \text{jets}$ and $t\bar{t}$ with the control and signal samples. This is accomplished
 1934 by varying the cross-sections of the $W + \text{jets}$ and $t\bar{t}$ by +20% and -20%, respectively.

1935 Figures C.2 and C.3 within Appendix C, show the effect upon the closure tests for both
1936 jet multiplicity categories. Given these variations in cross-sections, the level of closure is
1937 found to be significantly worse, with biases as large as $\sim 30\%$, most apparent in the
1938 lowest H_T bins. However, the TFs used to extrapolate from control to signal are seen to
1939 change only at the percent level by this large change in cross-section, shown in Table C.1.
1940 Given the robust behaviour of the translation factors with respect to large (and opposite)
1941 variations in the $W + \text{jets}$ and $t\bar{t}$ cross-sections, one can assume with confidence that
1942 any bias in the translation factors is adequately (and conservatively) covered by the
1943 systematic uncertainties used in the analysis.

1944 4.7. Simplified Models, Efficiencies and Systematic 1945 Uncertainties

1946 The results of the analysis are interpreted using various SMS signal models, which as
1947 already introduced in Section (2.4.1) offer a natural starting point for quantifying and
1948 characterising SUSY signals, and a means to identify the boundaries of search sensitivity
1949 for different mass splittings, kinematic ranges, and final states.
1950 Each model is parameterised in a two dimensional parameter space, $(m_{\tilde{q}/\tilde{g}}, m_{\text{LSP}})$, from
1951 which upper limits on the production cross-sections of the various SMS models can be
1952 set.
1953 Each signal sample is generated at Leading Order (LO) with Pythia [84], and cross-
1954 sections calculated for Next to Leading Order (NLO) and Next to Leading Logarithmic
1955 Order (NLL) [85], with events simulated using the Fastsim framework. This framework
1956 represents a simplified simulation of the CMS detector, but allows for faster production
1957 of various signal topologies with different mass parameters.
1958 A series of correction factors are applied to account for differences between Fastsim [86]
1959 and Fullsim [87] simulation, which can affect the resultant n_b^{reco} distribution and which
1960 are detailed in Section (4.7.2).

1961 4.7.1. Signal Efficiency

1962 The analysis selection efficiency, ϵ , is measured for each mass point of the interpreted
 1963 model. This serves as a measure of the sensitivity of the signal selection for that particular
 1964 sparticle, LSP mass and final state topology. The signal yield is then given by

$$1965 \quad Y(m_{\tilde{q}/\tilde{g}}, m_{LSP}) = \epsilon \times \sigma \times \mathcal{L}, \quad (4.13)$$

1965 where σ represents the model's cross-section and \mathcal{L} the luminosity. An upper limit on σ
 1966 taken from theory can then allow for the setting of limits in terms of the particle mass.

1967 Figure 4.12 shows the expected signal efficiency of the signal selection for the T1 and
 1968 T2 SMS models interpreted in this analysis. The efficiency maps are produced with the
 1969 requirement $H_T > 275$ GeV (i.e. no H_T categorisation) and requirements on n_{jet} and
 1970 n_b^{reco} are the most sensitive to the model in question.

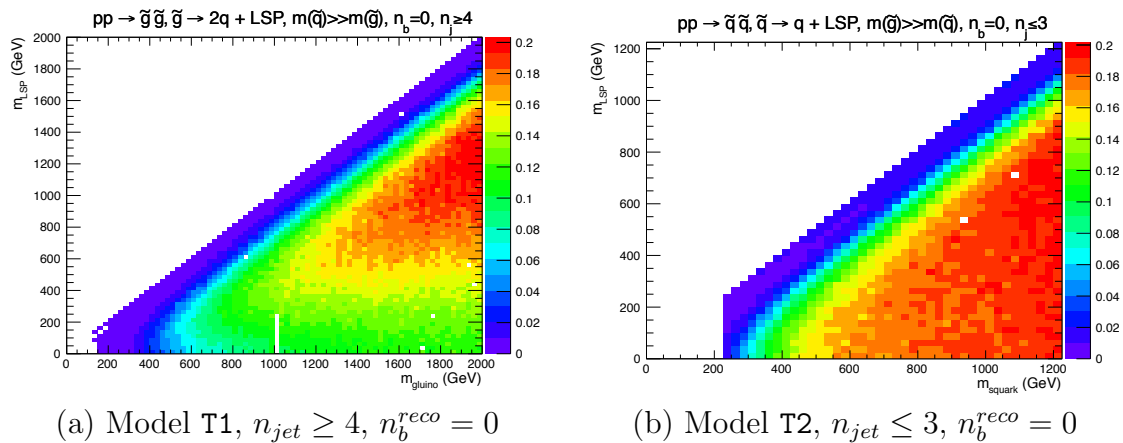


Figure 4.12: Signal efficiencies for the SMS models (a) T1 ($\tilde{g}\tilde{g}^* \rightarrow q\bar{q}\tilde{\chi}_1^0 q\bar{q}\tilde{\chi}_1^0$) and (b) T2 ($\tilde{q}\tilde{q}^* \rightarrow q\tilde{\chi}_1^0 q\tilde{\chi}_1^0$) when requiring $n_{jet} \geq 4$ and ≤ 3 respectively, and $n_b^{reco} = 0$.

1971 The same procedure is conducted in the analysis control samples. It is found in the $\mu +$
 1972 jets control samples, that the signal-to-background ratios for the expected signal yields in
 1973 each of the SMS models are many time smaller than in the hadronic signal region. The
 1974 relative contamination for the $\mu\mu +$ jets sample is smaller still due to the requirement of
 1975 a second muon. The relative contamination for the $\gamma +$ jets sample is expected to be
 1976 zero for the models under consideration. These small, relative levels of contamination
 1977 are accounted for in the fitting procedure, as described in Section (4.8.4).

4.7.2. Applying B-tagging Scale Factor Corrections in Signal Samples

- High-statistic **FastSim** signal simulation samples are unavailable for each signal point, which means that a different procedure to the formula method described in Section (4.5) is employed. Furthermore, the use of the **FastSim** framework in the reconstruction introduces an extra set of scale-factor corrections, to be applied simultaneously with those correcting **FullSim** to the data.
- For these signal models, an event-by-event re-weighting procedure is applied. This applied weight depends on both the flavour content and the b-tagging status of the reconstruction level jets in the event.
- The re-weighting procedure can be described by first considering a single jet within a signal event. The flavour of the jet is determined using the method described in Section (4.5.1).
- Maps of the tagging efficiencies, parameterised as a function of jet p_T and η are produced from **FullSim** simulation samples for each of the b, c and light jet flavours. These efficiencies are calculated from simulation events which pass the hadronic signal selection. The p_T and η binning of each map is chosen to match the correction maps of **FullSim** to data defined in [76].
- The actual tagging efficiency of the **FastSim** jet, $\epsilon_{\text{FastSim}}(p_T, \eta, f)$, differs from that measured in **FullSim**, $\epsilon_{MC}(p_T, \eta, f)$, as detailed above and is related via an additional correction factor,

$$\epsilon_{\text{FastSim}}(p_T, \eta, f) = \frac{\epsilon_{MC}(p_T, \eta, f)}{SF_{\text{Fast} \rightarrow \text{Full}}(p_T, \eta, f)}. \quad (4.14)$$

- $SF_{\text{Fast} \rightarrow \text{Full}}(p_T, \eta, f)$ represents a set of p_T and η dependant corrections, that are specific for each **SMS** model. These corrections are calculated from the ratio of tagging rates between a **FullSim** $t\bar{t}$ sample, and a selection of mass points from each **FastSim** **SMS** model, again measured individually for b, c and light-flavoured jets.
- The tagging efficiencies measured in data [76], $\epsilon_{Data}(p_T, \eta, f)$, can then be related to $\epsilon_{\text{FastSim}}(p_T, \eta, f)$ by the equation,

$$\begin{aligned}
\epsilon_{Data}(p_T, \eta, f) &= \epsilon_{MC}(p_T, \eta, f) \times SF_{MC \rightarrow Data}(p_T, \eta, f) \\
&= \epsilon_{FastSim}(p_T, \eta, f) \times \underbrace{SF_{Fast \rightarrow Full}(p_T, \eta, f) \times SF_{MC \rightarrow Data}(p_T, \eta, f)}_{SF_{Fast} \rightarrow Data}.
\end{aligned} \tag{4.15}$$

2005 For each jet, the weight of the event is re-weighted according to whether the jet fires the
2006 tagger. In the instance that the jet *is* tagged, the event weight will be modified by,

$$\text{weight} = SF_{Fast \rightarrow Data} \times \text{weight}, \tag{4.16}$$

2007 and in the case that the jet does *not* fire the tagger,

$$\text{weight} = \frac{1 - \epsilon_{Data}(p_T, \eta, f)}{1 - \epsilon_{FastSim}(p_T, \eta, f)} \times \text{weight}. \tag{4.17}$$

2008 This procedure is applied to all events that pass the selection criteria, thus correcting
2009 the **FastSim** n_b^{reco} distribution to data.

2010 4.7.3. Experimental Uncertainties

2011 The systematic uncertainty on the expected signal acceptance \times analysis efficiency is
2012 determined independently for the each **SMS** model considered. These systematics stem
2013 from uncertainties on the parton distribution functions, the luminosity measurement, jet
2014 energy scale, b-tag scale factor measurements and the efficiencies of various selection
2015 criteria used in the signal selection, including the H_T / E_T , dead **ECAL** cleaning filter
2016 and lepton / photon event vetoes.

2017 Rather than trying to estimate the level of systematic that is applicable point-by-point
2018 in a model space, general behaviours are considered; and instead constant systematics
2019 are estimated in two regions of the **SMS** models parameter space.

2020 These two regions are defined as, near (small mass splittings) and far (large mass
2021 splittings) from the mass degenerate diagonal, where the far region is bounded by the
2022 condition

$$m_{\tilde{q}/\tilde{g}} - m_{LSP} > 350 GeV \quad m_{\tilde{q}/\tilde{g}} > 475 GeV.$$

2023 The total systematics in each region are evaluated in the following ways:

2024 **Jet energy scale:** The relative change in the signal efficiency is gauged by varying
2025 the energy of all jets in an event up or down according to a p_T and η dependent jet
2026 energy scale uncertainty. Within the two systematic regions, the resulting systematic
2027 uncertainties for each **SMS** model are determined by taking the value of the 68th
2028 percentile for the distributions of the relative change in the signal efficiency.

2029 **Luminosity measurement:** The uncertainty on the measurement of the luminosity
2030 collected propagates through to an uncertainty on the signal event yield when
2031 considering any new physics model, which is currently 4.4% [88].

2032 **Parton density function :** Each signal sample is produced using the CTEQ6L1
2033 parton density function. The effect on the signal acceptance when re-weighting to
2034 the central value of three different parton distribution functions, CT10, MSTW08
2035 and NNPDF2.1 are examined [89]. It is found that the change of the signal efficiency
2036 in different **SMS** models, due to the alternate PDF sets are typically a few percent,
2037 and approaches 10% at higher squark/gluon and **LSP** masses.

2038 **$\mathcal{H}_T/\mathcal{E}_T$ cleaning filter:** The ratio of the efficiencies of the cleaning filter are
2039 compared in simulation and data after application of the $\mu +$ jets control sample
2040 selection. No α_T requirement or further event cleaning filters are applied. The
2041 ratio of the efficiencies observed in data and simulation for a cut value of $\mathcal{H}_T/\mathcal{E}_T <$
2042 1.25 and the two jet multiplicity categories, $2 \leq n_{jet} \leq 3$ and $n_{jet} \geq 4$ are $1.028 \pm$
2043 0.007 and 1.038 ± 0.015 respectively. These deviations are taken to represent the
2044 systematic uncertainty on the simulation modelling of this variable.

2045 **Dead ECAL cleaning filter:** The ratio of the efficiencies observed in data and
2046 simulation for this filter in the two jet multiplicity categories, $2 \leq n_{jet} \leq 3$ and
2047 $n_{jet} \geq 4$, are 0.961 ± 0.008 and 0.961 ± 0.009 , respectively. These deviations

2048 from unity are taken to represent the systematic uncertainties in the modelling in
2049 simulation of this filter.

2050 **Lepton and photon vetoes:** The uncertainty on the efficiency of the lepton and
2051 photon vetoes is determined by considering truth information. The efficiency of
2052 the vetoes is measured after applying relevant object filters with identical logic,
2053 but based on truth instead of reconstructed objects. Where the efficiency is found
2054 to not be 100%, it is taken to represent the fraction of signal events that are
2055 incorrectly vetoed. This deviation is taken directly as the systematic uncertainty on
2056 the efficiency. The systematic uncertainty is only non-zero for models which contain
2057 third-generation quarks in the final state, where the uncertainties are at the order
2058 of 1% level.

2059 **B-tag scale factor uncertainties:** The relative change in the signal efficiency
2060 is observed when relevant flavour, p_T and η dependant b-tag correction factors,
2061 are varied up or down by their systematic uncertainty. Within the two systematic
2062 regions, the resulting systematic uncertainties for each **SMS** model are determined
2063 by taking the value of the 68th percentile for the distributions of the relative change
2064 in the signal efficiency, over all mass points.

2065 Tables 4.16 and 4.17 summarise all the aforementioned systematic uncertainties on the
2066 signal efficiencies for each individual **SMS** model interpreted in the analysis. In the case
2067 of the **T1tttt** model, in which pair produced gluinos decay to $t\bar{t}$ pairs and the **LSP**,
2068 the near region of **SMS** space is not considered, and so no systematic uncertainties are
2069 included.

2070 In both of the defined regions it is found that the systematic uncertainties are relatively
2071 flat justifying the approach taken. The systematic uncertainties applied to the region
2072 near to the diagonal fall in the range 13-15%; similarly, for the region far from the
2073 diagonal the determined uncertainties are in the range of 12-23%. These uncertainties
2074 are all propagated through to the limit calculation.

Model	Luminosity	p.d.f	JES	H_T/\bar{E}_T	Dead ECAL	Lepton Veto	b-tagging	Total
T1	4.4	10.0	5.6	3.8	4.1	n/a	3.1	13.9
T2	4.4	10.0	4.1	2.8	4.1	n/a	2.4	12.9
T2tt	4.4	10.0	6.5	3.8	4.1	0.8	0.8	13.9
T2bb	4.4	10.0	4.8	2.8	4.1	0.3	2.2	13.1
T1tttt	n/a	n/a	n/a	n/a	n/a	n/a	n/a	n/a
T1bbbb	4.4	10.0	7.3	3.8	4.1	0.5	2.7	14.5

Table 4.16: Estimates of systematic uncertainties on the signal efficiency (%) for various **SMS** models when considering points in the region near to the diagonal (i.e. small mass splitting and compressed spectra). The uncertainties are added in quadrature to obtain the total.

Model	Luminosity	p.d.f	JES	H_T/\bar{E}_T	Dead ECAL	Lepton Veto	b-tagging	Total
T1	4.4	10.0	0.8	3.8	4.1	n/a	6.6	14.0
T2	4.4	10.0	1.1	2.8	4.1	n/a	5.8	13.4
T2tt	4.4	10.0	3.5	3.8	4.1	0.6	1.6	12.9
T2bb	4.4	10.0	0.9	2.8	4.1	0.3	2.7	12.3
T1tttt	4.4	10.0	0.5	3.8	4.1	1.4	19.4	23.0
T1bbbb	4.4	10.0	1.5	3.8	4.1	0.4	10.1	16.0

Table 4.17: Estimates of systematic uncertainties on the signal efficiency (%) for various **SMS** models when considering points in the region far from the diagonal (i.e. large mass splitting). The uncertainties are added in quadrature to obtain the total.

2075 4.8. Statistical Interpretation

2076 For a given category of events satisfying requirements on both n_{jet} and n_b^{reco} , a likelihood
 2077 model of the observations in multiple data samples is used to gauge agreement between
 2078 the observed yields in the hadronic signal region, and the predicted yields obtained from
 2079 the control samples. In addition to checking whether the predictions are compatible
 2080 with a **SM** only hypothesis, the likelihood model is also used to test for the presence
 2081 of a variety of signal models. The statistical framework outlined within this section is
 2082 presented in greater detail within [90].

2083 4.8.1. Hadronic Sample

2084 Let N be the number of bins on H_T , with n^i the number of events observed satisfying
 2085 all selection requirements in each H_T bin i. The likelihood of the observations can then
 2086 be written:

$$L_{had} = \prod_i \text{Pois}(n^i | b^i + s^i), \quad (4.18)$$

2087 where b^i represents the expected SM background

$$b^i = EWK_i + QCD_i, \quad (4.19)$$

2088 and s^i the expected number of signal events from the different SMS models interpreted.
2089 Pois refers to the Poisson distribution of these values and is defined as:

$$\text{Pois}(\chi|\lambda) = \frac{\lambda^\chi \exp^{-\lambda}}{k!}. \quad (4.20)$$

2090 4.8.2. H_T Evolution Model

2091 The hypothesis, that for a process the α_T ratio falls exponentially (see Section (4.2.4))
2092 in H_T is defined by Equation (4.10), where k_{QCD} is constrained by measurements in a
2093 signal sideband region.

2094 The expected QCD background, QCD^i , within a bin i is then modelled as,

$$QCD^i = m^i A_{QCD} e^{-k_{QCD} \langle H_T \rangle}, \quad (4.21)$$

2095 where m_i represent the number of events observed with $\alpha_T \leq 0.55$ in each H_T bin i , and
2096 $\langle H_T \rangle$ represent the mean H_T of each bin. Expressed as functions of just the zeroth bin,
2097 QCD^0 , and k_{QCD} , the QCD expectation is given by

$$QCD^i = QCD^0 \left(\frac{m^i}{m^0} \right) e^{-k_{QCD} (\langle H_T \rangle^i - \langle H_T \rangle^0)}. \quad (4.22)$$

²⁰⁹⁸ 4.8.3. EWK Control Samples

²⁰⁹⁹ The EWK background estimation within each bin, i , is broken into two components, the
²¹⁰⁰ expected yield from $Z \rightarrow \nu\bar{\nu}$ and $t\bar{t}$ -W (plus other residual backgrounds) events. This is
²¹⁰¹ written as, Z_{inv}^i and $t\bar{t}W^i$, and it follows that

$$EWK^i = Z_{inv}^i + t\bar{t}W^i. \quad (4.23)$$

²¹⁰² This can be further expressed as

$$Z_{inv}^i \equiv f_{Zinv}^i \times EWK^i, \quad (4.24)$$

$$t\bar{t}W^i \equiv (1 - f_{Zinv}^i) \times EWK^i, \quad (4.25)$$

²¹⁰³ where f_{Zinv}^i represents the expected yield from $Z \rightarrow \nu\bar{\nu}$ in bin i divided by the expected
²¹⁰⁴ EWK background EWK^i . This fraction is modelled as a linear component

$$f_{Zinv}^i = f_{Zinv}^0 + \frac{\langle H_T \rangle^i - \langle H_T \rangle^0}{\langle H_T \rangle^{N-1} - \langle H_T \rangle^0} (f_{Zinv}^{N-1} - f_{Zinv}^i), \quad (4.26)$$

²¹⁰⁵ where N again represents the number of H_T bins, and f_{Zinv}^i and f_{Zinv}^{N-1} are float parameters
²¹⁰⁶ whose final values are limited between zero and one.

²¹⁰⁷ Within each H_T bin there are three background measurements for the different control
²¹⁰⁸ samples, n_γ^i , n_μ^i and $n_{\mu\mu}^i$, representing the event yields from the $\gamma +$ jets, $\mu +$ jets and
²¹⁰⁹ $\mu\mu +$ jets control samples respectively. Each of these have a corresponding yield in
²¹¹⁰ simulation, MC_γ^i , MC_μ^i and $MC_{\mu\mu}^i$. Within the hadronic signal region there are also
²¹¹¹ corresponding simulated yields for $Z \rightarrow \nu\bar{\nu}$ (MC_{Zinv}^i) and $t\bar{t} + W$ ($MC_{t\bar{t}+W}^i$), which are
²¹¹² used to define

$$r_\gamma^i = \frac{MC_\gamma^i}{MC_{Zinv}^i}; \quad r_{\mu\mu}^i = \frac{MC_{\mu\mu}^i}{MC_{Zinv}^i}; \quad r_\mu^i = \frac{MC_\mu^i}{MC_{t\bar{t}+W}^i} \quad (4.27)$$

2113 where r_p^i represents the inverse of the TFs used to extrapolate the yield of each background
2114 process.

2115 The likelihoods regarding the three measured yields n_γ^i , $n_{\mu\mu}^i$, n_μ^i can then be fully expressed
2116 as

$$L_\gamma = \prod_i \text{Pois}(n_\gamma^i | \rho_{\gamma Z}^j \cdot r_\gamma^i \cdot Z_{inv}^i), \quad (4.28)$$

$$L_{\mu\mu} = \prod_i \text{Pois}(n_{\mu\mu}^i | \rho_{\mu\mu Z}^j \cdot r_{\mu\mu}^i \cdot Z_{inv}^i), \quad (4.29)$$

$$L_\mu = \prod_i \text{Pois}(n_\mu^i | \rho_{\mu Y}^j \cdot r_\mu^i \cdot Y^i + s_\mu^i), \quad (4.30)$$

$$(4.31)$$

2117 which contain an additional term s_μ^i , which represents the signal contamination in the
2118 $\mu + \text{jets}$ sample. The parameters $\rho_{\gamma Z}^j$, $\rho_{\mu\mu}^j$ and ρ_μ^j represent “correction factors” that
2119 accommodate the data driven systematic uncertainties derived from the control samples
2120 in Section (4.12).

2121 Each of these equations are used to estimate the maximum likelihood value for relevant
2122 background in the signal region given the observations n_p^i in each of the control samples
2123 (see Section (4.2.3)).

2124 The measurements in each of the control samples and the hadronic signal region, along
2125 with the ratios r_γ^i , $r_{\mu\mu}^i$, and r_μ^i , are all considered simultaneously through the relationships
2126 defined by Equations (4.19),(4.24) and (4.25).

2127 In addition to the Poisson product, an additional log-normal term is introduced to
2128 accommodate the systematic uncertainties given by,

$$L_{EWK \ syst} = \prod_j \text{Logn}(1.0 | \rho_{\mu W}^j, \sigma_{\mu W}^j) \times \text{Logn}(1.0 | \rho_{\mu\mu Z}^j, \sigma_{\mu\mu Z}^j) \times \text{Logn}(1.0 | \rho_{\gamma Z}^j, \sigma_{\gamma Z}^j). \quad (4.32)$$

2129 The parameters ρ^j , ρ^j and ρ^j represent “correction factors” that accommodate the
2130 systematic uncertainties associated with the control sample based background constraints.

2131 The quantities $\sigma_{\gamma Z}^j$, $\sigma_{\mu\mu Z}^j$ and $\sigma_{\mu W}^j$ represent the relative systematic uncertainties for the
2132 control sample constraints. Logn represents the log-normal distribution [91],

$$\text{Logn}(x \mid \mu, \sigma_{rel}) = \frac{1}{x\sqrt{2\pi}\ln k} \exp\left(\frac{\ln^2(\frac{x}{\mu})}{2\ln^2 k}\right); \quad k = 1 + \sigma_{rel}. \quad (4.33)$$

2133 Five parameters per control sample are used to span the eight H_T categories, with just
2134 one used for the three H_T in the $n_b^{reco} \geq 4$ category. These parameters span the same
2135 H_T ranges described in Section (4.6) and is shown in Table 4.18.

H_T bin (i)	0	1	2	3	4	5	6	7
syst. parameter (j)	0	1	2	2	3	3	4	4

H_T bin (i)	0	1	2
syst. parameter (j)	0	0	0

Table 4.18: The systematic parameters used in H_T bins. Left: categories with eight bins; right: category with three bins.

2136 Alternatively, in the higher n_b^{reco} categories ($n_b^{reco} \geq 2$), only the single muon sample is
2137 used to constrain the total EWK background. This is due to a lack of statistics in the
2138 $\mu\mu + \text{jets}$ and $\gamma + \text{jets}$ at these n_b^{reco} multiplicities. Therefore the likelihood functions
2139 for the control samples are reduced and simply represented by

$$L'_\mu = \prod_i \text{Pois}(n_\mu^i | \rho_{\mu Y}^j \cdot r_\mu'^i \cdot EWK^i + s_\mu^i), \quad (4.34)$$

2140 where

$$r_\mu'^i = \frac{MC_\mu^i}{MC_{t\bar{t}+W}^i + MC_{Zinv}^i}. \quad (4.35)$$

2141 4.8.4. Contributions from Signal

2142 The cross-section for each model is represented by x , while l represents the total recorded
2143 luminosity considered by the analysis in the signal region. Let ϵ_{had}^i and ϵ_μ^i represent the
2144 analysis selection efficiency for that particular signal model in H_T bin i of the hadronic
2145 and $\mu + \text{jets}$ control sample respectively. Letting δ represent the relative uncertainty on

- 2146 the signal yield, assumed to be fully correlated across all bins, and ρ_{sig} the “correction
2147 factor” to the signal yield which accommodates this uncertainty. f represents an unknown
2148 multiplicative factor on the signal cross section, for which an allowed interval is computed.
2149 The expected signal yield s^i is thus given by

$$s^i \equiv f \rho_{sig} x l \epsilon_{had}^i \quad (4.36)$$

- 2150 and signal contamination with the $\mu +$ jets control sample by

$$s_\mu^i \equiv f \rho_{sig} x l \epsilon_\mu^i. \quad (4.37)$$

- 2151 The systematic uncertainty on the signal is additionally incorporated by the term

$$L_{\text{sig}} = \text{Logn}(1.0 | \rho_{sig}, \delta). \quad (4.38)$$

- 2152 A discussion of the **SMS** signal models through which the analysis is interpreted can be
2153 found in the following chapter.

2154 4.8.5. Total Likelihood

- 2155 The total likelihood function for a given signal category $k(n_b^{\text{reco}}, n_{jet})$ is then given by
2156 the product of the likelihood functions introduced within the previous sections:

$$\begin{aligned} L_{\text{Tot}}^k &= L_{had}^k \times L_\mu^k \times L_\gamma^k \times L_{\mu\mu}^k \times L_{EWKsyst}^k \times L_{QCD}^k & (0 \leq n_b^{\text{reco}} \leq 1), \\ L_{\text{Tot}}^k &= L_{had}^k \times L'_\mu^k \times L_{\mu\text{syst}}^k \times L_{QCD}^k & (n_b^{\text{reco}} \geq 2). \end{aligned} \quad (4.39)$$

- 2157 In categories containing eight H_T bins and utilising the three control samples ($\mu +$ jets,
2158 $\mu\mu +$ jets, $\gamma +$ jets), there are 25 nuisance parameters. When just one control sample

2159 is used to estimate the **EWK** background, this is reduced to 15 nuisance parameters.

2160 In the $n_b^{\text{reco}} \geq 4$ category where only three H_T bins are used, there are just 6 nuisance

2161 parameters. This information is summarised within Table 4.19.

Nuisance parameter	Total
$(EWK^i)_{i:0-7(2)}$	8 (3)
$f_{Z^{\text{inv}}}^0$	1*
$f_{Z^{\text{inv}}}^7$	1*
QCD^0	1
k_{QCD}	1
$(\rho_{\gamma Z}^j)_{j:2-4}$	3 *
$(\rho_{\mu\mu Z}^j)_{j:0-4}$	5 *
$(\rho_{\mu W}^j)_{j:0-4(0)}$	5 (1)

Table 4.19: Nuisance parameters used within the different hadronic signal bins of the analysis. Parameters denoted by a * are not considered in the case of a single control sample being used to predict the **EWK** background. Numbers within brackets highlight the number of nuisance parameters in the case of three H_T bins being used.

2162 When considering **SUSY** signal models within the likelihood, the additional L_{sig} term
2163 is included and therefore when multiple categories are fitted simultaneously the total
2164 likelihood is then represented by

$$L_{\text{Tot}}^{\text{signal}} = L_{\text{sig}} \times \prod_k L_{\text{Tot}}^k. \quad (4.40)$$

Chapter 5.

²¹⁶⁵ Results and Interpretation

²¹⁶⁶ Using the statistical framework outlined in the previous chapter, results are shown for
²¹⁶⁷ the compatibility of the collected data with a **SM**-only hypothesis in Section (5.1). The
²¹⁶⁸ data is further interpreted within the context of various **SMS** models within Section (5.2).

²¹⁶⁹ 5.1. Compatibility with the Standard Model ²¹⁷⁰ Hypothesis

²¹⁷¹ The **SM** background only hypothesis is tested by removing any signal contributions
²¹⁷² within the signal and control samples, and the likelihood function defined in Equation
²¹⁷³ (4.39) maximised over all parameters using Rootfit [92] and MINUIT [93]. The results of
²¹⁷⁴ the search consist of the observed yields in the hadronic signal sample, and the $\mu + \text{jets}$,
²¹⁷⁵ $\mu\mu + \text{jets}$ and $\gamma + \text{jets}$ control samples.

²¹⁷⁶ These observed yields along with the expectations and uncertainties given by the simulta-
²¹⁷⁷ neous fit for the hadronic signal region are given in Table 5.2. The results obtained from
²¹⁷⁸ the simultaneous fits, including that of the three control samples, are shown in Figure
²¹⁷⁹ 5.1-5.8, as summarised in Table 5.1.

²¹⁸⁰ The figures show a comparison between the observed yields and the **SM** expectations
²¹⁸¹ across all H_T bins, and in all n_{jet} and n_b^{reco} multiplicity categories. In all categories the
²¹⁸² samples are well described by the **SM** only hypothesis. In particular no significant excess
²¹⁸³ is observed above **SM** expectation within the hadronic signal region.

n_{jet}	n_b^{reco}	Control samples fitted	Figure
2-3	0	$\mu + \text{jets}$, $\mu\mu + \text{jets}$, $\gamma + \text{jets}$	5.1
2-3	1	$\mu + \text{jets}$, $\mu\mu + \text{jets}$, $\gamma + \text{jets}$	5.2
2-3	2	$\mu + \text{jets}$	5.3
≥ 4	0	$\mu + \text{jets}$, $\mu\mu + \text{jets}$, $\gamma + \text{jets}$	5.4
≥ 4	1	$\mu + \text{jets}$, $\mu\mu + \text{jets}$, $\gamma + \text{jets}$	5.5
≥ 4	2	$\mu + \text{jets}$	5.6
≥ 4	3	$\mu + \text{jets}$	5.7
≥ 4	4	$\mu + \text{jets}$	5.8

Table 5.1: Summary of control samples used by each fit results, and the Figures in which they are displayed.

Cat	n_b^{reco}	n_{jet}	H_T bin (GeV)							
			275-325	325-375	375-475	474-575	575-675	675-775	775-875	875- ∞
SM Data	0	≤ 3	6235^{+100}_{-67} 6232	2900^{+60}_{-54} 2904	1955^{+34}_{-39} 1965	558^{+14}_{-15} 552	186^{+11}_{-10} 177	$51.3^{+3.4}_{-3.8}$ 58	$21.2^{+2.3}_{-2.2}$ 16	$16.1^{+1.7}_{-1.7}$ 25
		≥ 4	1010^{+34}_{-24} 1009	447^{+19}_{-16} 452	390^{+19}_{-15} 375	250^{+12}_{-11} 274	111^{+9}_{-7} 113	$53.3^{+4.3}_{-4.3}$ 56	$18.5^{+2.4}_{-2.4}$ 16	$19.4^{+2.5}_{-2.7}$ 27
SM Data	1	≤ 3	1162^{+37}_{-29} 1164	481^{+18}_{-19} 473	341^{+15}_{-16} 329	$86.7^{+4.2}_{-5.6}$ 95	$24.8^{+2.8}_{-2.7}$ 23	$7.2^{+1.1}_{-1.0}$ 8	$3.3^{+0.7}_{-0.7}$ 4	$2.1^{+0.5}_{-0.5}$ 1
		≥ 4	521^{+25}_{-17} 515	232^{+15}_{-12} 236	188^{+12}_{-11} 204	106^{+6}_{-6} 92	$42.1^{+4.1}_{-4.4}$ 51	$17.9^{+2.2}_{-2.0}$ 13	$9.8^{+1.5}_{-1.4}$ 13	$6.8^{+1.2}_{-1.1}$ 6
SM Data	2	≤ 3	224^{+15}_{-14} 222	$98.2^{+8.4}_{-6.4}$ 107	$59.0^{+5.2}_{-6.0}$ 58	$12.8^{+1.6}_{-1.6}$ 12	$3.0^{+0.9}_{-0.7}$ 5	$0.5^{+0.2}_{-0.2}$ 1	$0.1^{+0.1}_{-0.1}$ 0	$0.1^{+0.1}_{-0.1}$ 0
		≥ 4	208^{+17}_{-9} 204	103^{+9}_{-7} 107	$85.9^{+7.2}_{-6.9}$ 84	$51.7^{+4.6}_{-4.7}$ 59	$19.9^{+3.4}_{-3.0}$ 24	$6.8^{+1.2}_{-1.3}$ 5	$1.7^{+0.7}_{-0.4}$ 1	$1.3^{+0.4}_{-0.3}$ 2
SM Data	3	≥ 4	$25.3^{+5.0}_{-4.2}$ 25	$11.7^{+1.7}_{-1.8}$ 13	$6.7^{+1.4}_{-1.2}$ 4	$3.9^{+0.8}_{-0.8}$ 2	$2.3^{+0.6}_{-0.6}$ 2	$1.2^{+0.3}_{-0.4}$ 3	$0.3^{+0.2}_{-0.1}$ 0	$0.1^{+0.1}_{-0.1}$ 0
		≥ 4	$0.9^{+0.4}_{-0.7}$ 1	$0.3^{+0.2}_{-0.2}$ 0				$0.6^{+0.3}_{-0.3}$ 2		

Table 5.2: Comparison of the measured yields in each H_T , n_{jet} and n_b^{reco} jet multiplicity bins for the hadronic sample with the **SM** expectations and combined statistical and systematic uncertainties given by the simultaneous fit.

²¹⁸⁴ Given the lack of an excess in data hinting at a possible supersymmetric signature within
²¹⁸⁵ the data, interpretations are made on the production masses and cross-section of a range
²¹⁸⁶ of **SUSY** decay topologies within the following section.

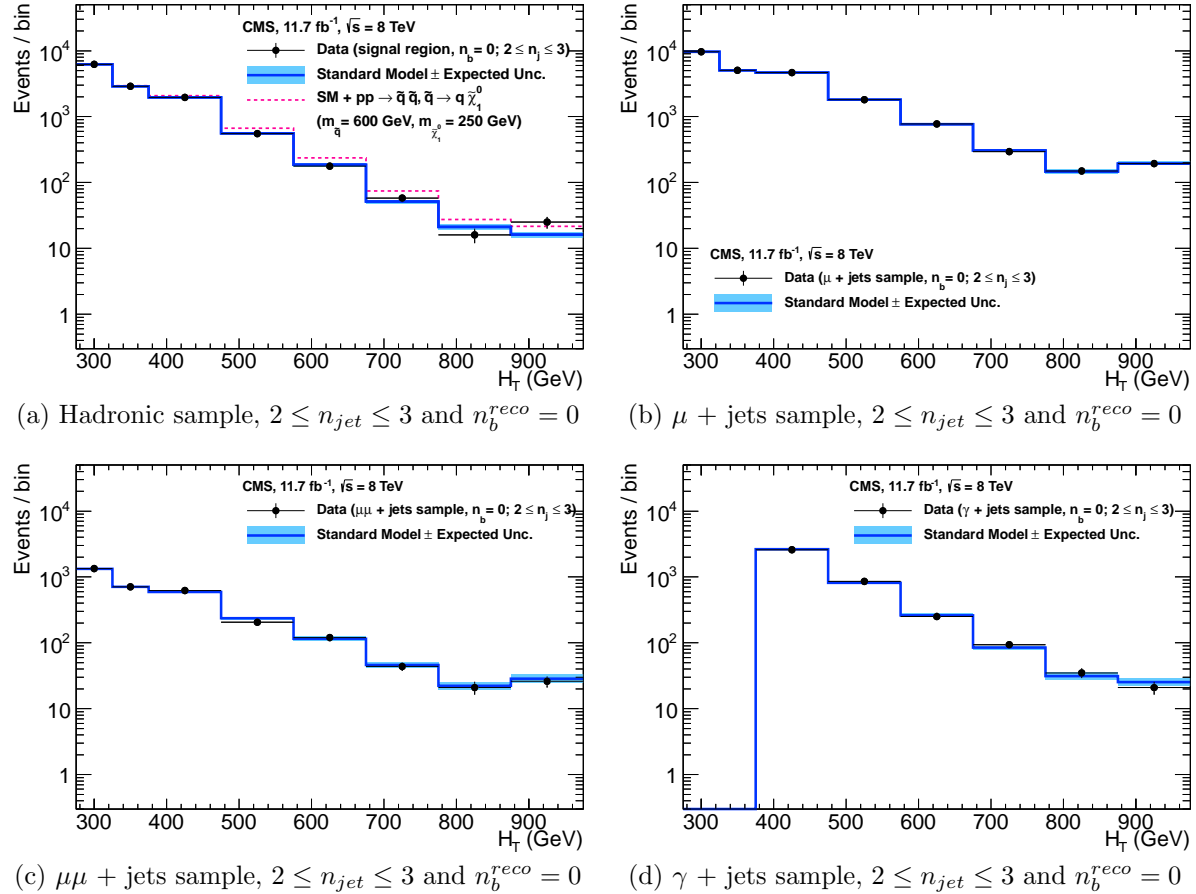


Figure 5.1: Comparison of the observed yields and SM expectations given by the simultaneous fit in bins of H_T for the (a) hadronic, (b) $\mu +$ jets, (c) $\mu\mu +$ jets and (d) $\gamma +$ jets samples when requiring $n_b^{reco} = 0$ and $n_{jet} \leq 3$. The observed event yields in data (black dots) and the expectations and their uncertainties for all SM processes (blue line with light blue bands) are shown. An example signal expectation (red solid line) for the D1 SMS signal point from Table 4.1 is superimposed on the SM background expectation.

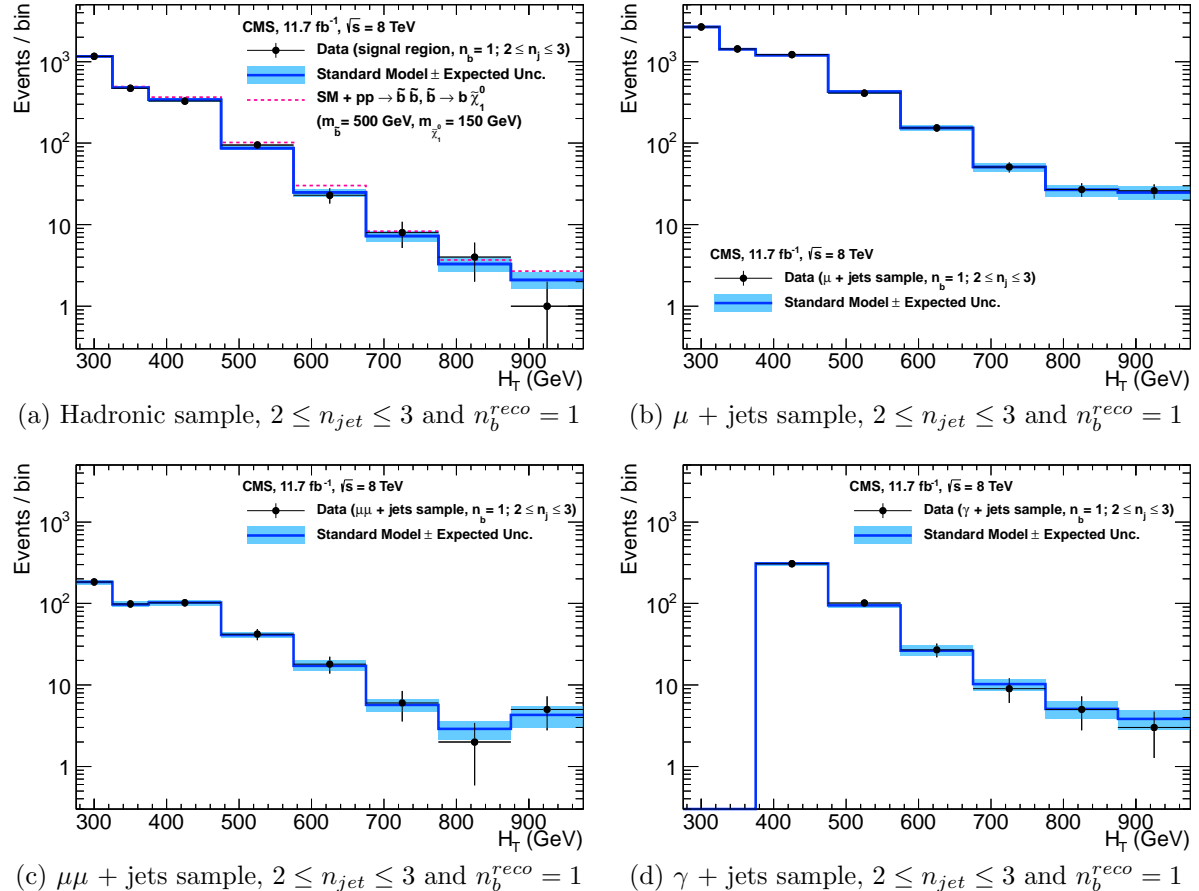


Figure 5.2: Comparison of the observed yields and SM expectations given by the simultaneous fit in bins of H_T for the (a) hadronic, (b) $\mu +$ jets, (c) $\mu\mu +$ jets and (d) $\gamma +$ jets samples when requiring $n_b^{reco} = 1$ and $n_{jet} \leq 3$. The observed event yields in data (black dots) and the expectations and their uncertainties for all SM processes (blue line with light blue bands) are shown. An example signal expectation (red solid line) for the D2 SMS signal point from Table 4.1 is superimposed on the SM background expectation.

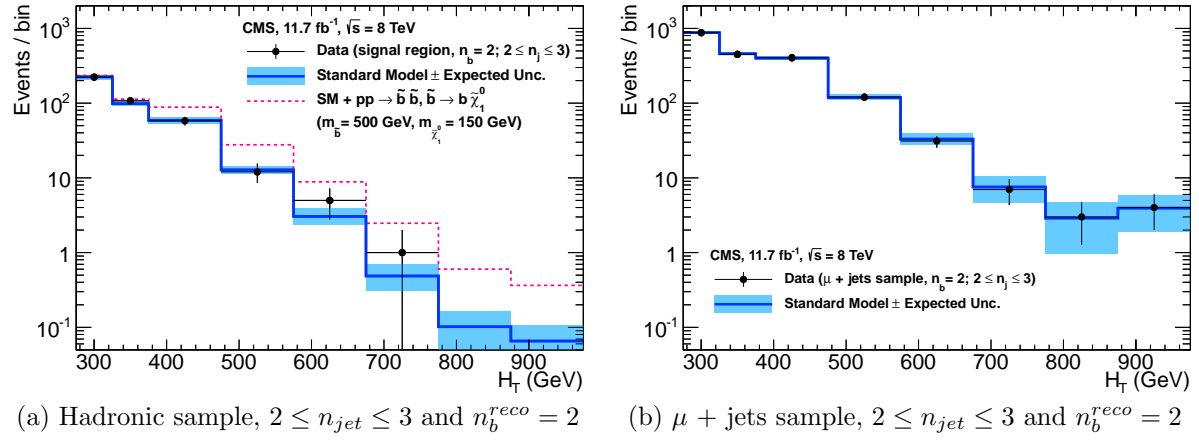


Figure 5.3: Comparison of the observed yields and SM expectations given by the simultaneous fit in bins of H_T for the (a) hadronic, (b) $\mu +$ jets, (c) $\mu\mu +$ jets and (d) $\gamma +$ jets samples when requiring $n_b^{reco} = 2$ and $n_{jet} \leq 3$. The observed event yields in data (black dots) and the expectations and their uncertainties for all SM processes (blue line with light blue bands) are shown. An example signal expectation (red solid line) for the D2 SMS signal point from Table 4.1 is superimposed on the SM background expectation.

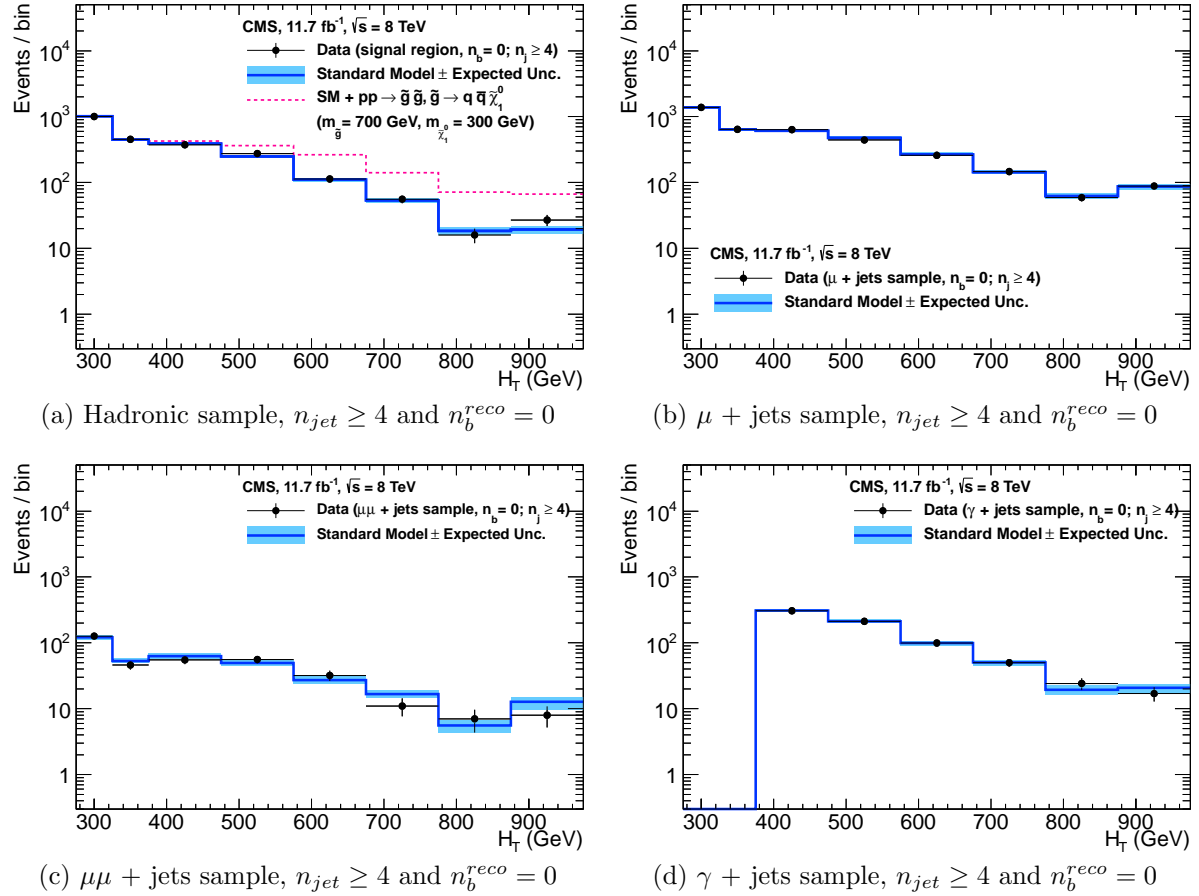


Figure 5.4: Comparison of the observed yields and SM expectations given by the simultaneous fit in bins of H_T for the (a) hadronic, (b) $\mu +$ jets, (c) $\mu\mu +$ jets and (d) $\gamma +$ jets samples when requiring $n_b^{reco} = 0$ and $n_{jet} \geq 4$. The observed event yields in data (black dots) and the expectations and their uncertainties for all SM processes (blue line with light blue bands) are shown. An example signal expectation (red solid line) for the D2 SMS signal point from Table 4.1 is superimposed on the SM background expectation.

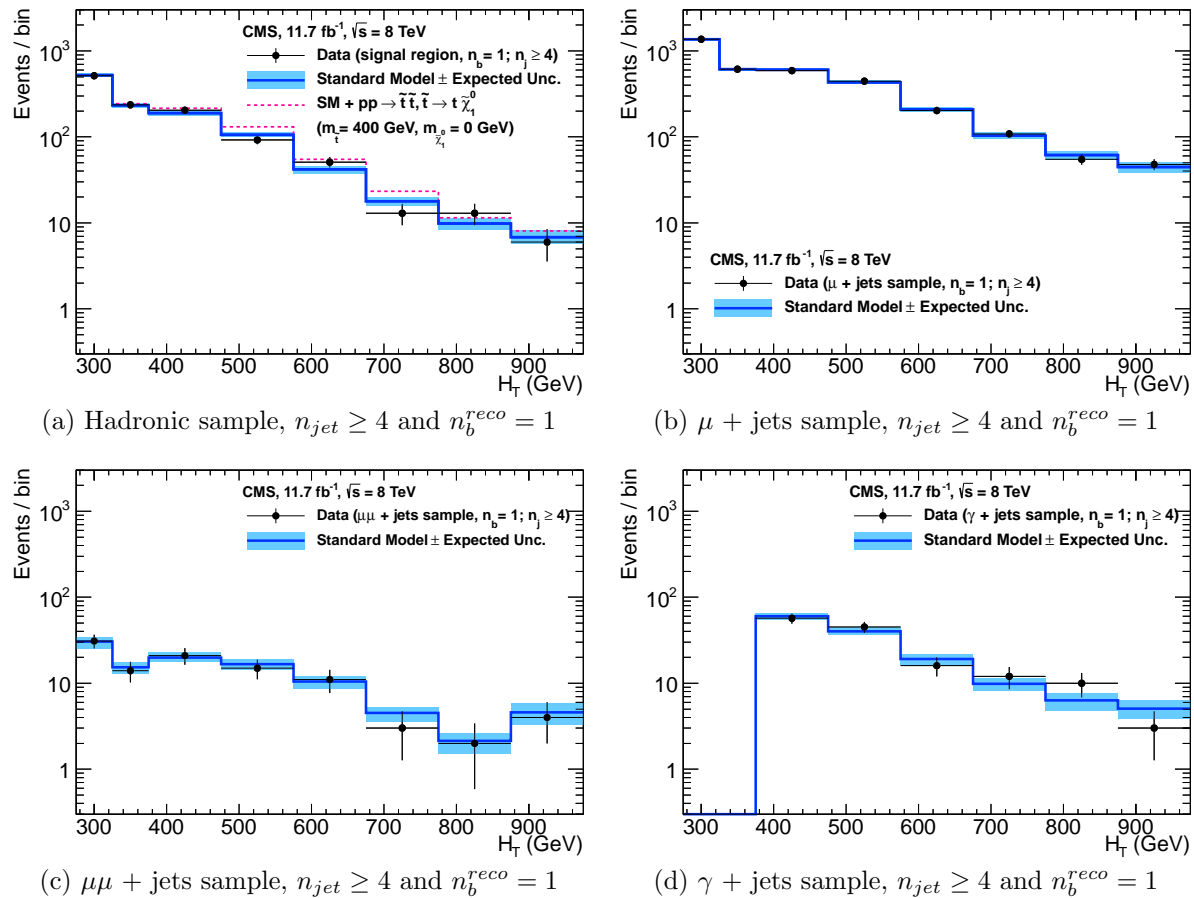


Figure 5.5: Comparison of the observed yields and SM expectations given by the simultaneous fit in bins of H_T for the (a) hadronic, (b) $\mu +$ jets, (c) $\mu\mu +$ jets and (d) $\gamma +$ jets samples when requiring $n_b^{reco} = 1$ and $n_{jet} \geq 4$. The observed event yields in data (black dots) and the expectations and their uncertainties for all SM processes (blue line with light blue bands) are shown.

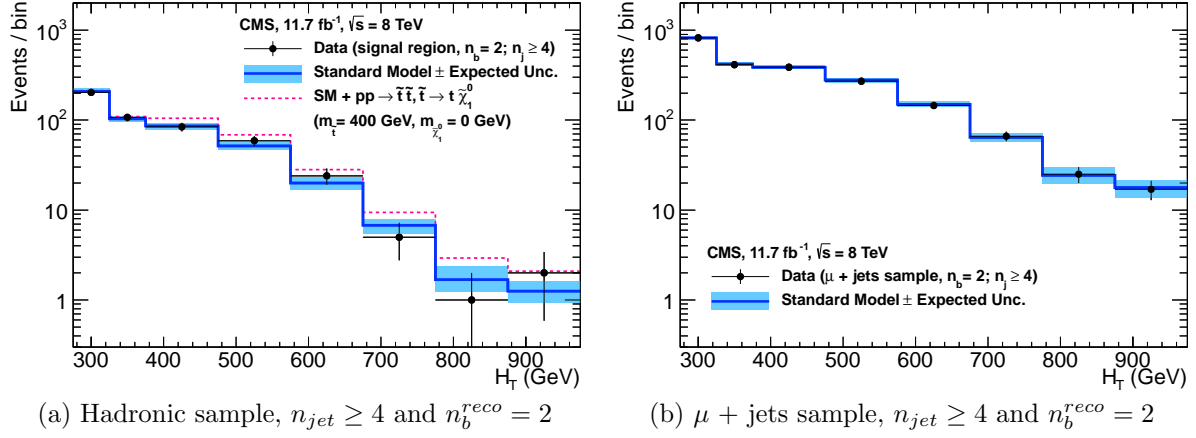


Figure 5.6: Comparison of the observed yields and SM expectations given by the simultaneous fit in bins of H_T for the (a) hadronic, (b) $\mu +$ jets, (c) $\mu\mu +$ jets and (d) $\gamma +$ jets samples when requiring $n_b^{reco} = 2$ and $n_{jet} \geq 4$. The observed event yields in data (black dots) and the expectations and their uncertainties for all SM processes (blue line with light blue bands) are shown. An example signal expectation (red solid line) for the D3 SMS signal point from Table 4.1 is superimposed on the SM background expectation.

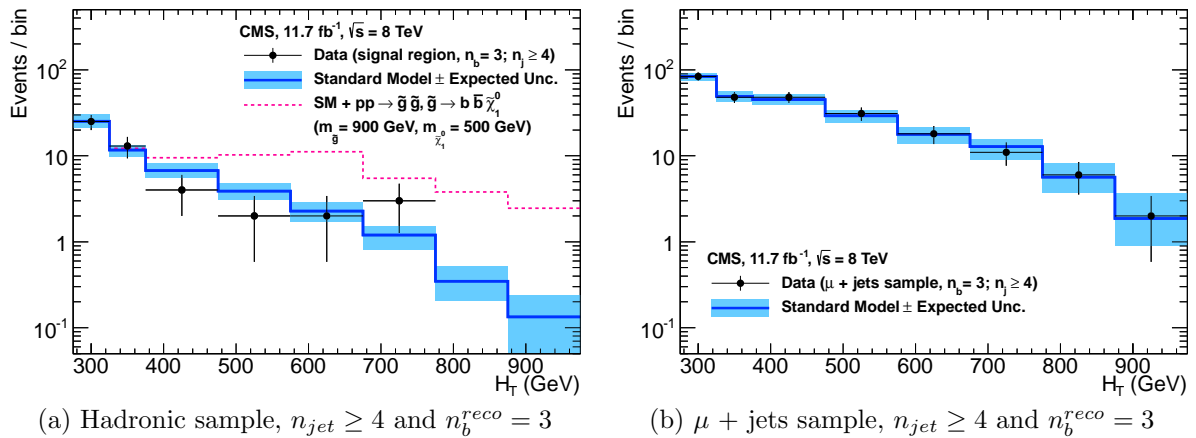


Figure 5.7: Comparison of the observed yields and SM expectations given by the simultaneous fit in bins of H_T for the (a) hadronic, (b) $\mu +$ jets, (c) $\mu\mu +$ jets and (d) $\gamma +$ jets samples when requiring $n_b^{reco} = 3$ and $n_{jet} \geq 4$. The observed event yields in data (black dots) and the expectations and their uncertainties for all SM processes (blue line with light blue bands) are shown. An example signal expectation (red solid line) for the G2 SMS signal point from Table 4.1 is superimposed on the SM background expectation.

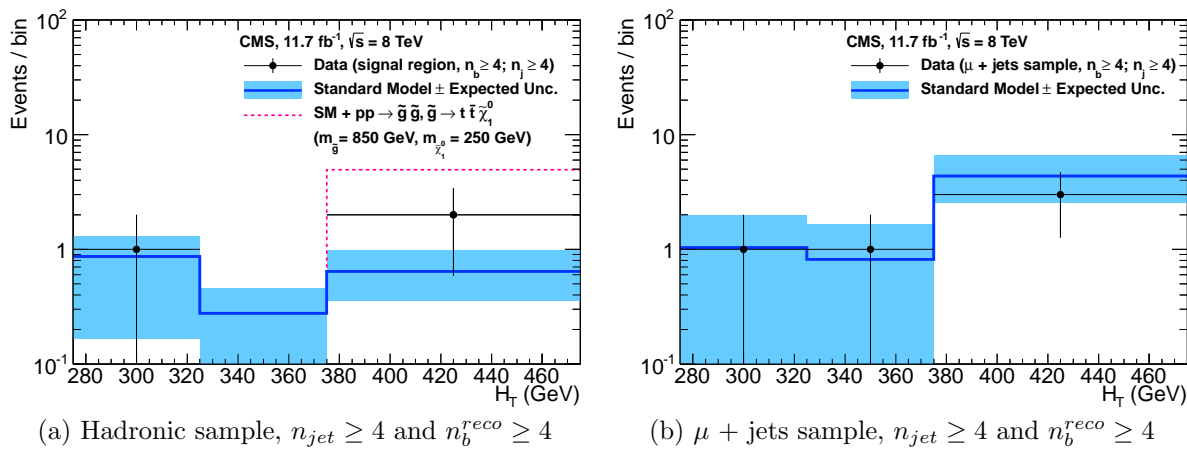


Figure 5.8: Comparison of the observed yields and SM expectations given by the simultaneous fit in bins of H_T for the (a) hadronic, (b) $\mu +$ jets, (c) $\mu\mu +$ jets and (d) $\gamma +$ jets samples when requiring $n_b^{reco} \geq 4$ and $n_{jet} \geq 4$. The observed event yields in data (black dots) and the expectations and their uncertainties for all SM processes (blue line with light blue bands) are shown. An example signal expectation (red solid line) for the G3 SMS signal point from Table 4.1 is superimposed on the SM background expectation.

²¹⁸⁷ **5.2. SUSY**

²¹⁸⁸ Limits are set in the parameter space of a set of **SMS** models that characterise both
²¹⁸⁹ natural **SUSY** third generation squark production, and compressed spectra where the
²¹⁹⁰ mass splitting between the particle and **LSP** is small, leading to soft final state jets.
²¹⁹¹ However as detailed in Section (2.4.1), the individual models are not representative of a
²¹⁹² real physical **SUSY** model as only one decay process is considered. Instead these models
²¹⁹³ represent a way to test for signs of specific signatures indicating new physics.

²¹⁹⁴ **5.2.1. The CL_s Method**

²¹⁹⁵ The CLs method [94][95][96] is used to compute the limits for signal models, with the
²¹⁹⁶ one-sided profile likelihood ratio as the test statistic [97].

The test statistic is defined as

$$q(\mu) = \begin{cases} -2\log\lambda(\mu) & \text{when } \mu \geq \hat{\mu}, \\ 0 & \text{otherwise.} \end{cases} \quad (5.1)$$

²¹⁹⁷ where

$$\lambda(\mu) = \frac{L(\mu, \theta_\mu)}{L(\hat{\mu}, \hat{\theta})} \quad (5.2)$$

²¹⁹⁸ represents the profile likelihood ratio, in which $\mu \equiv f$ from Section (4.8.4), is the
²¹⁹⁹ parameter characterising the signal strength. $\hat{\mu}$ is defined as the maximum likelihood
²²⁰⁰ value, $\hat{\theta}$ the set of maximum likelihood values of the nuisance parameters and θ_μ the set
²²⁰¹ of maximum values of the nuisance parameters for a given value of μ .

²²⁰² When $\mu \equiv f = 1$, the signal model is considered at its nominal production cross section.
²²⁰³ The distribution of q_μ is built up via the generation of pseudo experiments in order to
²²⁰⁴ obtain two distributions for the background (B) and signal plus background (S+B) cases.

²²⁰⁵ The compatibility of a signal model with observations in data is determined by the
²²⁰⁶ parameter CL_s ,

$$\text{CL}_S = \frac{\text{CL}_{S+B}}{\text{CL}_B}, \quad (5.3)$$

with CL_B and CL_{S+B} defined as one minus the quantiles of the observed value in the data of the two distributions. A model is considered to be excluded at 95% confidence level when $\text{CL}_s \leq 0.05$ [98].

5.2.2. Interpretation in Simplified Signal Models

Different n_{jet} and n_b^{reco} bins are used in the interpretation of different **SMS** models. The choice of categories used, are made such that the signal to background ratio will be maximised for the model in question, increasing sensitivity to that particular type of final state signature. The production and decay modes of the **SMS** models under consideration are summarised in Table 5.3, with limit plots of the experimental reach in these models shown in Figure 5.10.

The models T1 and T2 are used to characterise the pair production of gluinos and first or second generation squarks respectively. The low number of third generation quarks produced from this decay topology makes choosing to interpret within the $n_b^{\text{reco}} = 0$ category beneficial to improving sensitivity to these models. In the case of the T2 model, two sets of exclusion contours are shown. These correspond to the production of eight first- and second-generation (left-/right-handed) squarks with degenerate masses and the case of just a single light squark with all other squarks decoupled at much higher masses.

Conversely the T2bb, T1tttt, and T1bbbb **SMS** models describe various production and decay mechanisms in the context of third-generation squarks. In this situation considering higher n_b^{reco} categories bring significant improvements to the sensitivity to these types of final state signature.

Finally the choice of jet category is made dependant upon the production mechanism, where gluino induced and direct squark production results in a large or small number of final state jets respectively.

Experimental uncertainties on the **SM** background predictions (10 – 30%, described in Section (4.6.1)), the luminosity measurement (4.4%), and the total acceptance times

Model	Production/decay	n_{jet}	n_b^{reco}	Process	Limit	$m_{\tilde{q}/\tilde{g}}^{\text{best}}$ (GeV)	$m_{\text{LSP}}^{\text{best}}$ (GeV)
T1	$pp \rightarrow \tilde{g}\tilde{g}^* \rightarrow q\bar{q}\tilde{\chi}_1^0 q\bar{q}\tilde{\chi}_1^0$	≥ 4	0	5.9(a)	5.10(a)	~ 950	~ 450
T2	$pp \rightarrow \tilde{q}\tilde{q}^* \rightarrow q\tilde{\chi}_1^0 q\tilde{\chi}_1^0$	≤ 3	0	5.9(b)	5.10(b)	~ 775	~ 325
T2bb	$pp \rightarrow \tilde{b}\tilde{b}^* \rightarrow b\tilde{\chi}_1^0 \bar{b}\tilde{\chi}_1^0$	≤ 3	1,2	5.9(c)	5.10(c)	~ 600	~ 200
T1tttt	$pp \rightarrow \tilde{g}\tilde{g}^* \rightarrow t\bar{t}\tilde{\chi}_1^0 t\bar{t}\tilde{\chi}_1^0$	≥ 4	2,3, ≥ 4	5.9(d)	5.10(d)	~ 975	~ 325
T1bbbb	$pp \rightarrow \tilde{g}\tilde{g}^* \rightarrow b\bar{b}\tilde{\chi}_1^0 b\bar{b}\tilde{\chi}_1^0$	≥ 4	2,3, ≥ 4	5.9(e)	5.10(e)	~ 1125	~ 650

Table 5.3: A table representing the **SMS** models interpreted within the analysis. The model name and production and decay chain is specified in the first two columns. Each **SMS** model is interpreted in specific n_{jet} and n_b^{reco} categories which are detailed in the third and fourth columns. The last two columns indicate the search sensitivity for each model, representing the largest $m_{\tilde{q}/\tilde{g}}$ mass beyond which no limit can be set for this particular decay topology. The quoted values are conservatively determined from the observed exclusion based on the theoretical production cross section minus 1σ uncertainty.

efficiency of the selection for the considered signal model (12 –18%, from Section (4.7)) are included in the calculation of the limit.

Signal efficiency in the kinematic region defined by $0 < m_{\tilde{q}/\tilde{g}} < 175$ GeV or $m_{\tilde{q}/\tilde{g}} < 300$ GeV is strongly affected by the presence of Initial State Radiation (**ISR**). This is a region in which direct (i.e. non-**ISR** induced) production is kinematically forbidden due to the $H_T > 275$ GeV requirement, therefore a large percentage of signal acceptance is due to the effect of **ISR** jets. Given the large associated uncertainties, no interpretation is provided for this kinematic region.

The estimates on mass limits shown in Table 5.3, are determined conservatively from the observed exclusion based on the theoretical production cross section, minus 1σ uncertainty. The most stringent mass limits on pair-produced sparticles are obtained at low **LSP** masses and larger squark and gluino masses due to the high p_T jets and consequently high H_T of such signal topologies. The limits are seen to weaken for compressed spectra points closer to the diagonal, where the signal populates the lower H_T bins in which more background resides. For all of the considered models, there is an **LSP** mass beyond which no limit can be set, which can be observed from the figures referenced in the table.

Two small upwards fluctuations are observed within the data, and are seen at high H_T within the $n_b^{reco} = 0$ category and at mid- H_T in the $n_b^{reco} = 1, 2$ categories, see Table 5.2. As each of these fluctuations occur within at least one of the analysis categories that each **SMS** model interpretation is made, the observed exclusions within all **SMS** models are generally found to be weaker than the expected limits in the region of 1-2 standard

2254 deviations. In isolation these fluctuations are not significant and additional data would
2255 be necessary to make any further conclusions.

2256 Despite these fluctuations, the range of parameter space that can be excluded has been
2257 extended with respect to analysis based upon the $\sqrt{s} = 7$ TeV dataset [99], by up to
2258 225 and 150 GeV for $m_{\tilde{q}(\tilde{g})}^{\text{best}}$ and m_{LSP}^{best} respectively. The parameter space for light third
2259 generation squarks, the main tenet of natural SUSY models, is increasingly squeezed for
2260 larger mass splitting, with exclusions in the region of 1 TeV in these topologies.

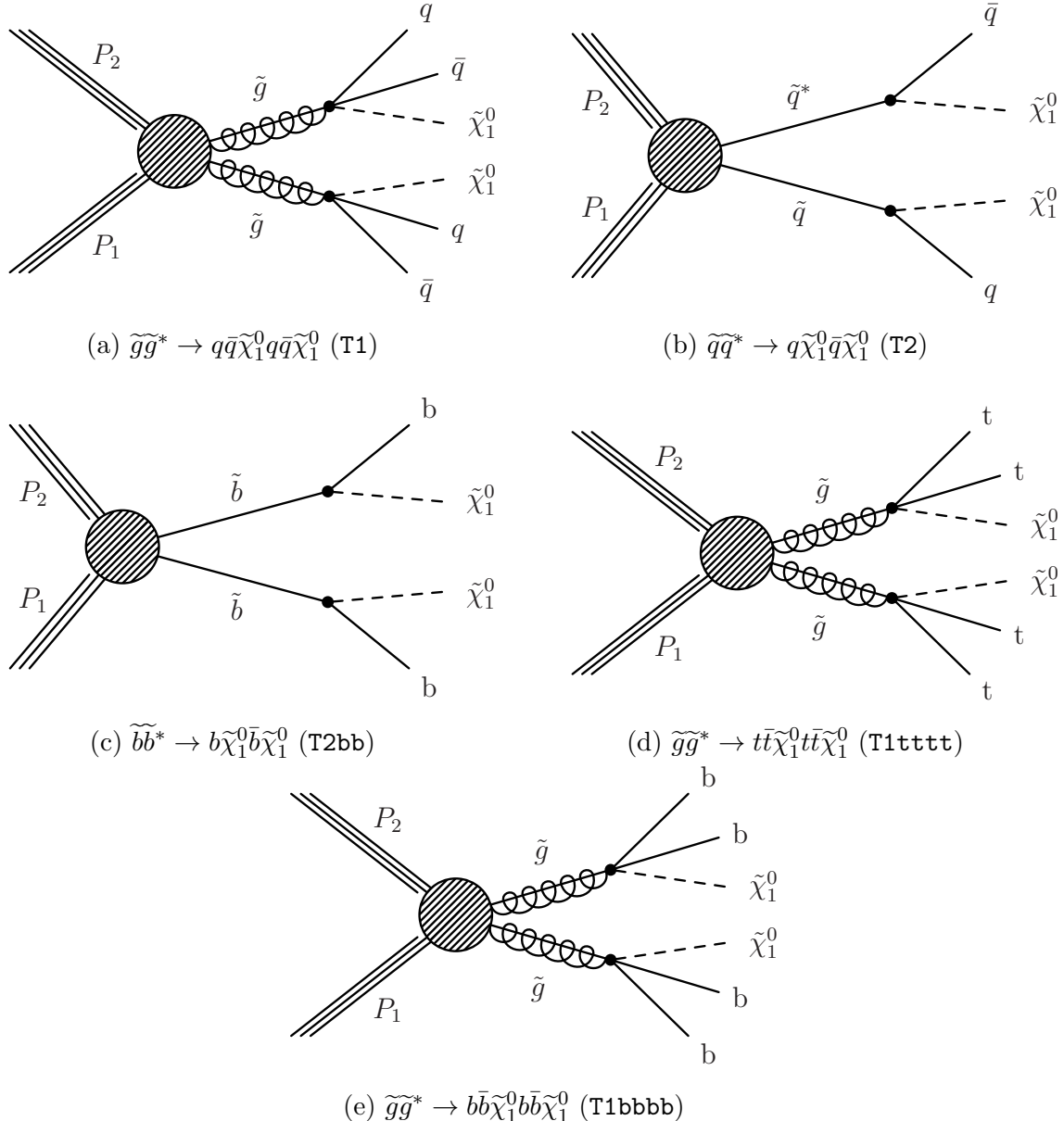


Figure 5.9: Production and decay modes for the various SMS models interpreted within the analysis.

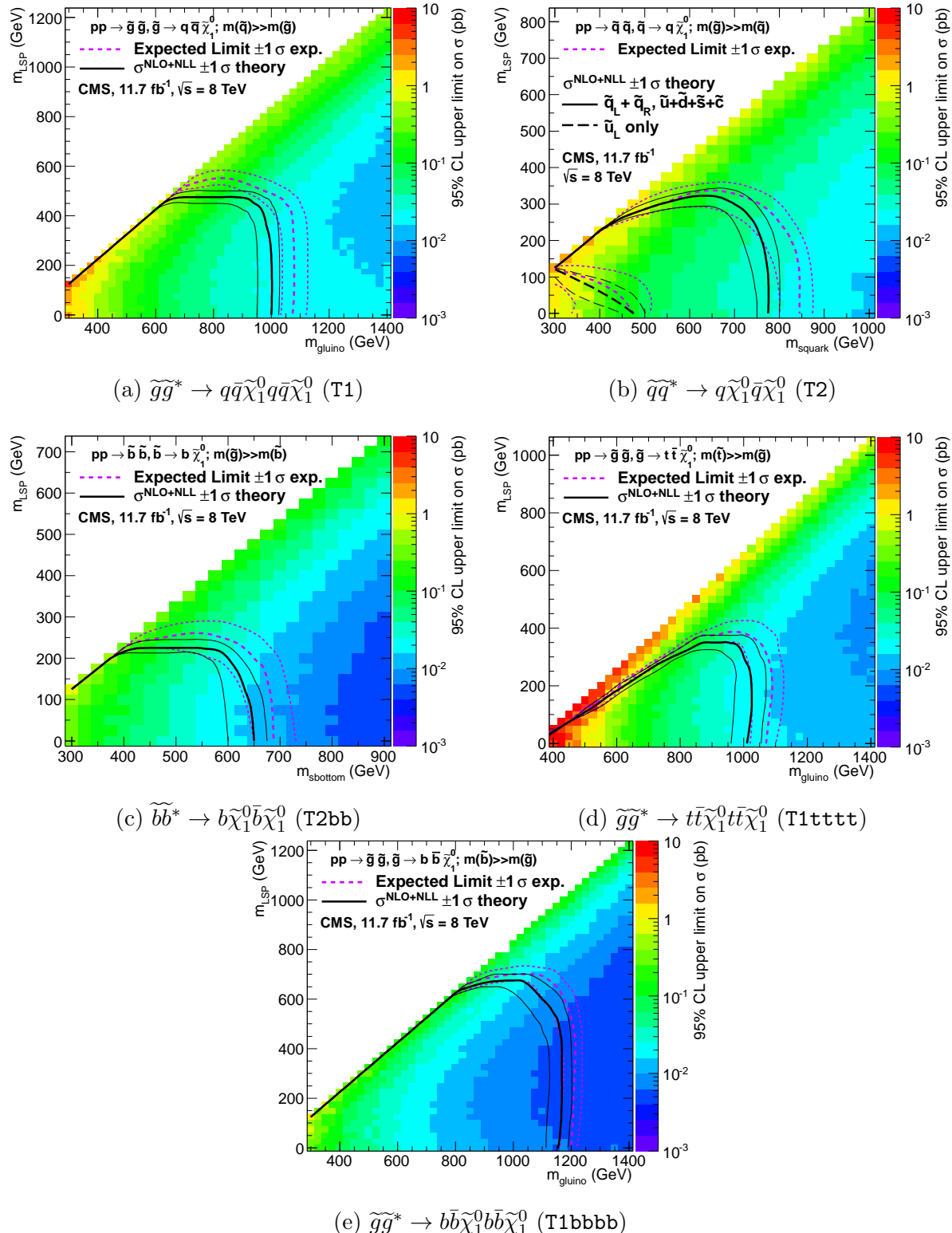


Figure 5.10: Upper limit of cross section at 95% CL as a function of $m_{\tilde{q}/\tilde{g}}$ and m_{LSP} for various SMS models. The solid thick black line indicates the observed exclusion region assuming NLO and NLL SUSY production cross section. The analysis selection efficiency is measured for each interpreted model, with the signal yield per point given by $\epsilon \times \sigma$. The thin black lines represent the observed excluded region when varying the cross section by its theoretical uncertainty. The dashed purple lines indicate the median (thick line) 1σ (thin lines) expected exclusion regions.

Chapter 6.

²²⁶¹ SUSY Searches with B-tag

²²⁶² Templates

²²⁶³ Within this chapter a complementary technique is discussed as a means to predict
²²⁶⁴ the distribution of three and four reconstructed b-quark jets in an event sample. The
²²⁶⁵ recent discovery of the Higgs boson has made third-generation “Natural SUSY” models
²²⁶⁶ attractive, given that light top and bottom squarks are a candidate to stabilise divergent
²²⁶⁷ loop corrections to the Higgs boson mass. In the case where the gluino is also light and
²²⁶⁸ then subsequently decays to third generation sparticle pairs, many events with a large
²²⁶⁹ number of final state b flavoured jets can arise.

²²⁷⁰ The method employs a templated fit to estimate the SM background at high b-tag
²²⁷¹ multiplicities (3-4), from a fit conducted in a low reconstructed b-jets (0-2) control
²²⁷² region of an event sample. This approach can hypothetically be applied to generic
²²⁷³ supersymmetric searches, to gain sensitivity to signals which contain a higher number of
²²⁷⁴ b-tagged jets than the search’s irreducible SM backgrounds.

²²⁷⁵ As a proof-of-concept, the procedure is applied to the SM enriched $\mu + \text{jets}$ control
²²⁷⁶ sample of the α_T search detailed in Chapter 4, and validated in both data and simulation.
²²⁷⁷ This method is then further utilised to provide an independent crosscheck of the SM
²²⁷⁸ background estimations determined by the α_T search within its hadronic signal region,
²²⁷⁹ at high b-tag multiplicities.

²²⁸⁰ To highlight the relative insensitivity of the choice of b-tagging algorithm working point in
²²⁸¹ the effectiveness of the procedure, results are presented using the CSV tagger (introduced
²²⁸² in Section (3.3.2)) for the “Loose”, “Medium” and “Tight” working points.

2283 6.1. Concept

2284 The dominant **SM** backgrounds of most **SUSY** searches are typically $t\bar{t}$ + jets, W + jets,
2285 $Z \rightarrow \nu\bar{\nu}$ + jets or other rare processes with neutrinos in the final state. These processes
2286 are characterised by typically having zero or two underlying b-quarks per event as shown
2287 in Table 6.1. This ultimately means that the resultant shape of the n_b^{reco} distribution for
2288 these two types of event topologies will differ greatly due to varying tagging rates of the
2289 different jet flavours present in the final state.

2290 Similarly, a third generation gluino mediated **SUSY** signal, such at the **T1tttt** and
2291 **T1bbbb** models described in the previous chapter, will typically have four underlying
2292 b-quarks in its final state. Therefore the resultant shape of the n_b^{reco} distribution from
2293 such a signal will be further skewed towards a higher number of b-tagged jets. As **SM**
2294 processes with a similarly large number of underlying b-quarks are rare, a signal indicative
2295 of natural **SUSY** can potentially be easily identified, via an observed excess of $n_b^{\text{reco}} = 3$,
 ≥ 4 events over **SM** expectations.

Typical underlying b-quark content	Process
= 0	$W \rightarrow l\nu$ + jets $Z \rightarrow \nu\bar{\nu}$ + jets $Z/\gamma^* \rightarrow \mu\mu$ + jets
= 1	$t + \text{jets}$
= 2	$t\bar{t} + \text{jets}$

Table 6.1: Typical underlying b-quark content of different **SM** processes which are common to many **SUSY** searches.

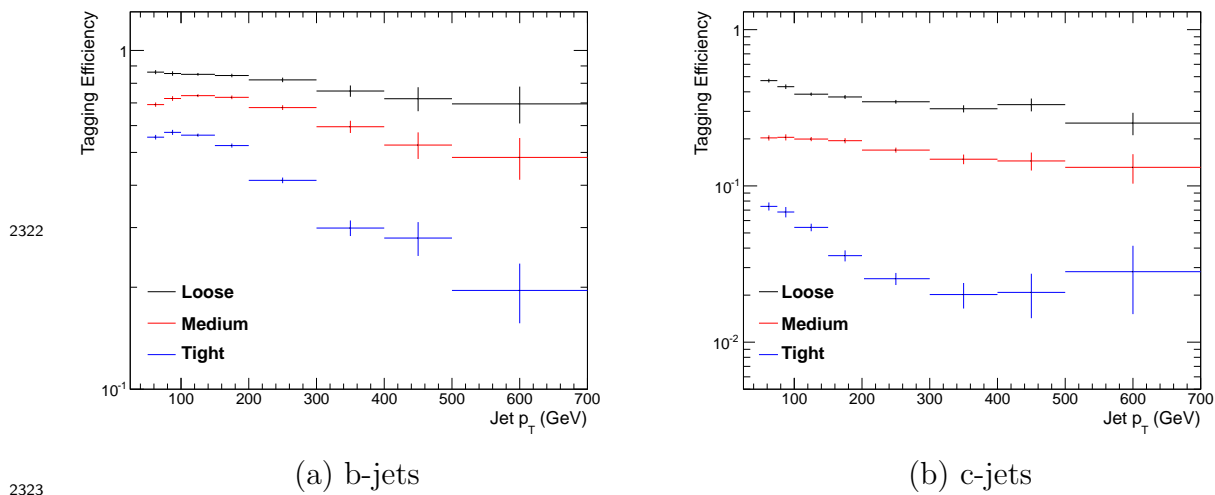
2296

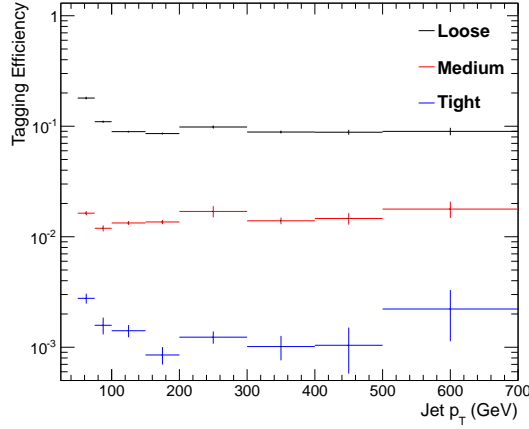
2297 This compatibility of the n_b^{reco} distribution in data can be tested via the parameterisation
2298 of the **SM** backgrounds in terms of these two most common underlying b-quark topologies
2299 within different search categories of a supersymmetric search.

2300 Two templates, representing processes which have an underlying b-quark content of
2301 zero or two are defined as Z0 and Z2 respectively (single top processes are a negligible
2302 background, $< 1\%$, within the α_T search to which this method is applied in the following
2303 section, and are thus incorporated within the Z2 template). These template shapes are
2304 then used to extrapolate a **SM** background prediction for high n_b^{reco} multiplicities from
2305 the fitting of these two template shapes to a low n_b^{reco} control region (0-2) under the
2306 assumption of negligible signal contamination.

2307 The simplest way to determine the shapes of the n_b^{reco} distributions for both templates
 2308 would be, after the application of the relevant event selection, to take the underlying n_b^{reco}
 2309 distribution directly from simulation. However as discussed within Section (4.5), there
 2310 are large statistical uncertainties for high n_b^{reco} multiplicities, the very region in which we
 2311 wish to use the templates to estimate the background in. This is particularly prominent
 2312 for the Z0 templates, which contain few b-flavoured final state jets and depend largely
 2313 of the mis-tagging of all the remaining light-flavoured jets in the event. Therefore to
 2314 improve the statistical precision of the template at larger b-tag multiplicities, the formula
 2315 method first introduced in Section (4.5.1) is utilised to generate the template shapes.

2316 It must also be taken into consideration that the template shapes of each analysis category
 2317 are dependant upon the jet-flavour content and b-tagging rate within the phase space
 2318 of interest, with the tagging probabilities of a jet being a function of the jet p_T , the
 2319 pseudo-rapidity $|\eta|$, and jet-flavour. This can be observed in Figure 6.1, where the
 2320 b-tagging / c-quark mis-tagging / light mis-tagging efficiency for the three working points
 2321 of the CSV tagger are shown as a function of jet p_T .





(c) light-jets

Figure 6.1: The b-tagging (a), c-quark mis-tagging (b), and light-quark mis-tagging rate (c) as a function of jet p_T , measured in simulation after the application of α_T analysis $\mu + \text{jets}$ control sample selection, in the region $H_T > 375$. Efficiencies are measured for the three **CSV** working points.

2324 Therefore before the template shapes can be generated by the formula method, the
 2325 relevant jet p_T and η corrections are applied to correct the measured b-tagging rate in
 2326 simulation to that of data, as specified in Section (4.5.3). These corrections propagate
 2327 through to the average determined b-tagging rates for each jet flavour, consequently
 2328 affecting the final Z_0 and Z_2 n_b^{reco} template shapes determined within each analysis
 2329 category (H_T and n_{jet} in the case of the α_T search).

2330 The templates, once generated from simulation via the formula method are then fitted to
 2331 data in a low n_b^{reco} control region (0-2), by allowing the normalisation constants θ_{Z_0} and
 2332 θ_{Z_2} of the two templates to float. The fits are performed independently within each of the
 2333 defined analysis category to remove any dependence on the modelling of jet multiplicity
 2334 between simulation and data. Best fit values of θ_{Z_0} and θ_{Z_2} are used, along with the
 2335 fixed shape of each template, to extrapolate a **SM** background estimation within the
 2336 high n_b^{reco} signal region (3,4) as shown in Figure 6.2.

2337 Any large excess in data is an indication that the n_b^{reco} distribution is not adequately
 2338 described by the **SM** backgrounds encapsulated by the templates. This could mean there
 2339 are additional **SM** backgrounds that fall within the selection of the analysis that need to
 2340 be considered, or that there is signal present within the data. This method relies solely
 2341 on fitting to the shape of the n_b^{reco} distribution, and can in principle, be applied to any

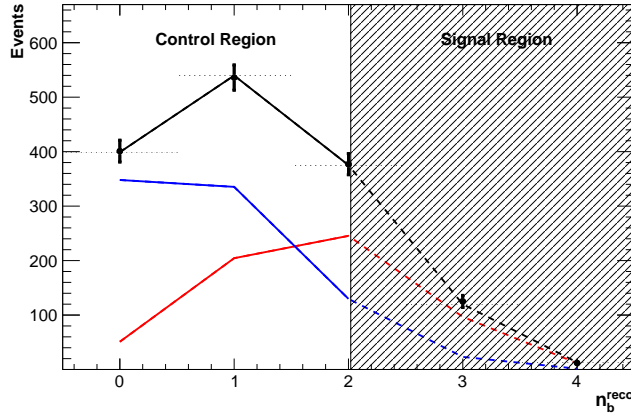


Figure 6.2: An example of a template fit with the defined Z_0 (blue) and Z_2 (red) templates to data within the low n_b^{reco} control region (left). The shape of the two templates are fixed but the normalisations θ_{Z_0} and θ_{Z_2} are allowed to vary. The best fit values are then applied to extrapolate a combined background prediction from the shaded signal region (right), represented by the dashed black line.

2342 analysis where the signal hypothesis has a larger underlying b-quark spectra than the
2343 **SM** backgrounds.

2344 However, in the scenario where a **SUSY** signal sits at a low number of underlying b-quarks,
2345 the template would be unable to discriminate between this signal and background during
2346 the fit in the control region. This will be the case unless the jet p_T distribution of the
2347 signal and background were drastically different, in which case there would anyway,
2348 be many more sensitive and practical ways to establish the presence of a signal in the
2349 data than this method. Indeed the template method is only really applicable to the
2350 hypothesis that any signal resides at high n_b^{reco} and that the control region $0 \leq n_b^{\text{reco}} \leq 2$
2351 has negligible signal contamination.

2352 6.2. Application to the α_T Search

2353 As detailed in the previous chapter, the α_T analysis is a search for **SUSY** particles
2354 in all-hadronic final states, utilising the kinematic variable α_T to suppress QCD to a
2355 negligible level. **SM** enriched control samples are used to estimate the background within
2356 an all-hadronic signal region.

2357 The selection for the $\mu + \text{jets}$ control samples defined in Section (4.2.3) is used to
2358 demonstrate the template fitting procedure both conceptually in simulation, and also

when applied in data. This is chosen, as such a selection is dominated by events stemming from the SM processes with little or no signal contamination from potential new physics. Contributions from rare SM processes with a higher underlying b-quark content (e.g. $t\bar{t}b\bar{b}$) are similarly suppressed. For these reasons, there is a degree of confidence that the procedure should adequately describe the observations in data when extrapolated to the signal region.

As a departure from the α_T search strategy described in the previous section, events are categorised according to jet multiplicity categories of 3, 4 and ≥ 5 reconstructed jets per event (di-jet events are not included as there is no contribution to the high n_b^{reco} region (3,4)), in order to reduce the kinematic range of the jet p_T 's within each category. Furthermore the analysis is split into just three H_T regions, for the purpose of increasing statistics within the control region,

- 275-325 GeV
- 325-375 GeV
- > 375 GeV

contrary to the eight used within the α_T analysis. Templates for both underlying b-quark content hypotheses are then generated for the nine defined event categories.

6.2.1. Proof of Principle in Simulation

This template procedure must be first demonstrated to work within simulated events free from any potential signal contamination before it can be applied to data. By combining the relevant ingredients necessary to employ the formula method, n_b^{reco} shape templates are generated individually for each n_{jet} and H_T category using one half of the available simulated events for each SM process. The two generated templates are then fit in the low n_b^{reco} (0-2) control region, to the n_b^{reco} distribution taken directly from the other half of the simulated event samples.

The simulation samples in the analysis are split in this way to allow for statistically independent fits to be performed. The aim of this procedure is to check that the template fit can accurately extrapolate the n_b^{reco} distribution within the defined signal region from two independent but kinematically identical samples. Additionally, as the half of the simulated events used to mimic data is taken directly from simulation, good closure between the initial fits within the control region and extrapolation to the signal region

2390 will also serve as a validation of the formula method in accurately describing the n_b^{reco}
2391 distribution itself. In this case, as the template shapes are being fitted to simulation, it
2392 is *not* necessary to apply the relevant corrections of the b-tagging rates between data
2393 and simulation.

2394 Within Figure 6.3, the results of this fitting procedure are shown for each CSV working
2395 point. Results are presented for the $n_{jet} \geq 5$ category, using the $\mu +$ jets control sample
2396 selection in the inclusive $H_T > 375$ GeV analysis bin. The grey bands represent the
2397 statistical uncertainty on the template shapes. Additional fits are shown for other n_{jet}
2398 categories and can be found within Appendix D.1.

2399 Furthermore the extrapolated fit predictions within the high n_b^{reco} signal region, are
2400 summarised for all H_T bins and working points in Table 6.2.

H_T		275-325	325-375	>375
Loose working point				
Simulation	$n_b = 3$	793.0 ± 14.8	387.9 ± 10.2	794.1 ± 14.34
Template		820.4 ± 26.7	376.3 ± 11.9	780.1 ± 15.1
Simulation	$n_b = 4$	68.2 ± 3.9	27.6 ± 2.7	91.3 ± 4.9
Template		72.5 ± 4.7	28.3 ± 2.34	84.4 ± 3.8
Medium working point				
Simulation	$n_b = 3$	133.7 ± 5.7	74.5 ± 4.5	164.2 ± 6.4
Template		132.8 ± 4.8	74.5 ± 3.9	159.9 ± 5.7
Simulation	$n_b = 4$	1.6 ± 0.6	0.6 ± 0.4	3.4 ± 0.9
Template		1.8 ± 0.2	1.1 ± 0.2	4.1 ± 0.4
Tight working point				
Simulation	$n_b = 3$	26.9 ± 2.6	13.9 ± 1.9	31.8 ± 2.9
Template		24.7 ± 1.5	13.8 ± 1.2	28.1 ± 1.5
Simulation	$n_b = 4$	0.5 ± 0.4	-	-
Template		0.1 ± 0.1	0.1 ± 0.1	0.2 ± 0.1

Table 6.2: Summary of the fit predictions in the n_b^{reco} signal region after combination of the $n_{jet} = 3, = 4, \geq 5$ categories compared against yields taken directly from simulation. The fit predictions are extrapolated from a $n_b^{reco} = 0, 1, 2$ control region and simulation yields are normalised to an integrated luminosity of 10 fb^{-1} . The uncertainties quoted on the template yields are purely statistical.

2401 The pull distributions for all the fits performed can be found in Appendix D.2, and are
2402 compatible with a mean of zero and standard deviation of one, showing no obvious bias
2403 to the fitting procedure. Each of the fits performed show good compatibility between
2404 the template shapes and data from simulation within the defined control region, with
2405 additional good overall agreement also observed for extrapolation to the signal region as
2406 shown in Table 6.2. This validates both the formula method used in the generation of

2407 the template shapes as well as the method of predicting the **SM** background in the high
 2408 n_b^{reco} signal region.

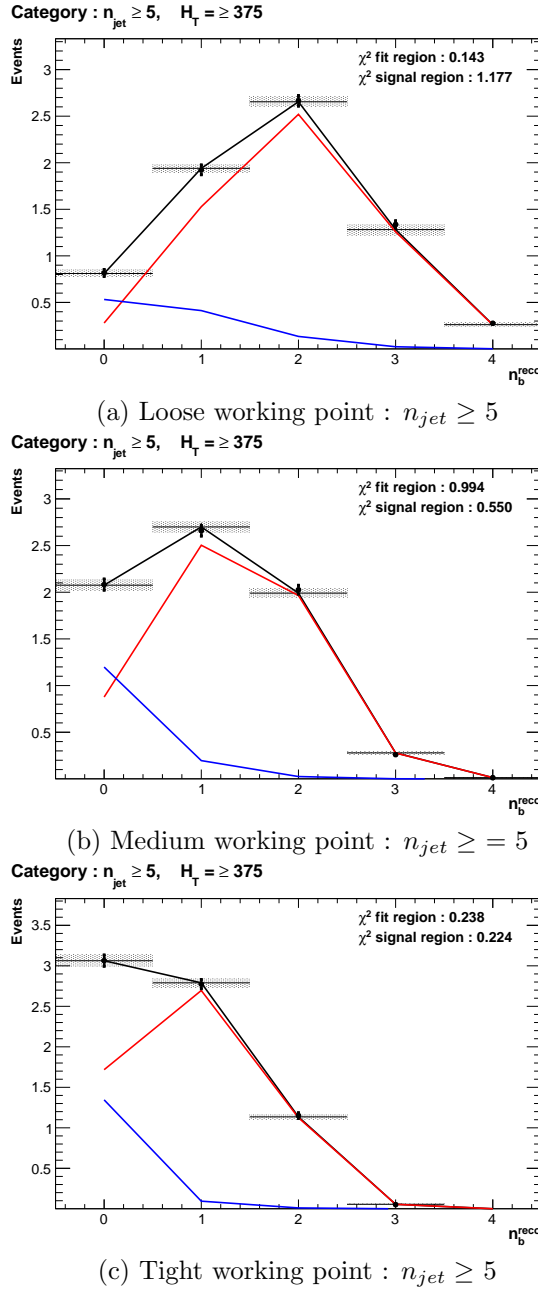


Figure 6.3: The results of fitting the $Z = 0$ and $Z = 2$ templates in the $n_b^{reco} = 0, 1, 2$ control region to yields from simulation in the $\mu + \text{jets}$ control sample for the $H_T > 375 \text{ GeV}$, $n_{jet} \geq 5$ category for all **CSV** working points. The blue template represents $Z = 0$, while the red template represents $Z = 2$. Grey bands represent the statistical uncertainty of the fit. The χ^2 parameter displayed represents the goodness of fit to the low n_b^{reco} (0-2) control region.

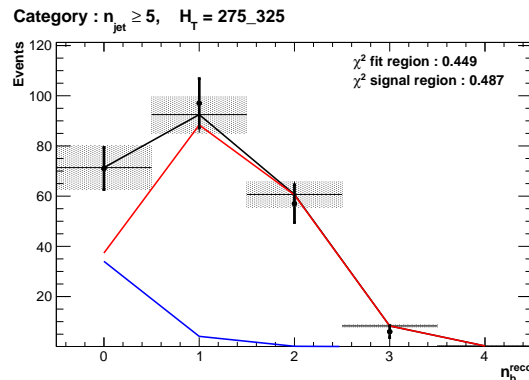
2409 The application of this method to the same selection in a data control sample is now
2410 used to demonstrate necessary control over the efficiency and mis-tagging rates when
2411 b-tagging scale factors are applied, and to test the assumption of no signal contamination
2412 with the $\mu +$ jets control sample.

2413 6.2.2. Results in a Data Control Sample

2414 The procedure is now applied to the 2012 8 TeV dataset in the $\mu +$ jets control sample, to
2415 establish the validity of this method in data. The relevant data to simulation b-tagging
2416 scale factors are applied to produce corrected values of the efficiency and mis-tagging
2417 rates within each analysis category [76].

2418 Figure 6.4 shows the results of the templates derived from simulation to each of the three
2419 defined H_T bins, in the $n_{jet} \geq 5$ category for the medium working point CSV tagger (the
2420 same working point used within the α_T analysis). Grey bands represent the statistical
2421 uncertainty of the fit combined in quadrature with the systematic uncertainties of varying
2422 the data to simulation scale factors up and down by their b-tag scale factor systematic
2423 uncertainties. Additional fit results for other jet multiplicities are found in Appendix
2424 D.3.

2425



2426

(a) $n_{jet} \geq 5$, $275 < H_T < 325$

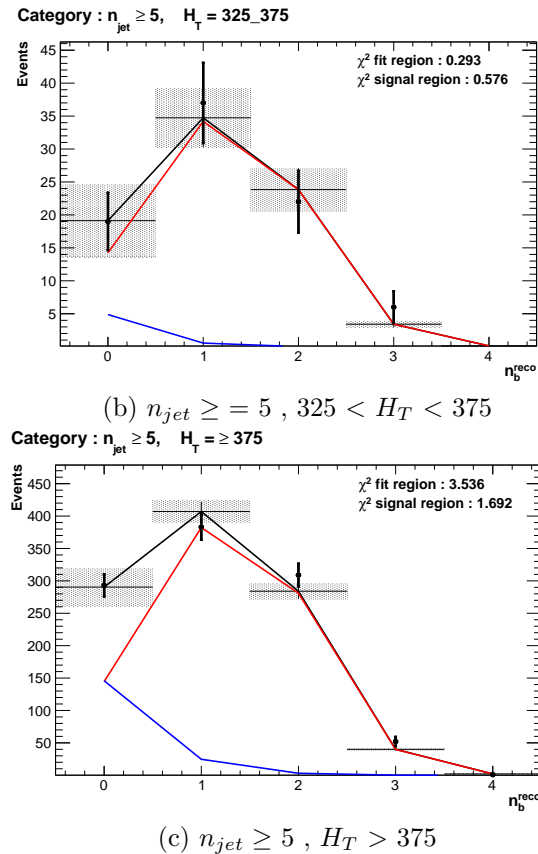


Figure 6.4: The results of fitting the $Z = 0$ and $Z = 2$ templates in the $n_b^{reco} = 0, 1, 2$ control region to data from the $\mu + \text{jets}$ control sample, for the **CSV** medium working point, with a jet multiplicity $n_{jet} \geq 5$, in all three H_T categories. The blue template represents $Z = 0$, while the red template represents $Z = 2$. The χ^2 parameter displayed represents the goodness of fit to the low n_b^{reco} (0-2) control region.

2427 The numerical results and extrapolation to the $n_b^{reco} = 3, 4$ bins for all H_T and working
 2428 points, is shown in Table 6.3.

2429 When this method is applied to the $\mu + \text{jets}$ control sample, it is expected that good
 2430 agreement would be observed between the template predictions and observation in the
 2431 absence of signal contamination. The good compatibility for all working points as shown
 2432 in the table, demonstrate that this is the case and that the method is able to accurately
 2433 predict the background yields. However the assumption of negligible signal contamination
 2434 can no longer made when applied to the hadronic signal region of the α_T search, where
 2435 agreement between estimated backgrounds and observations in data is now not necessarily
 2436 expected.

H_T		275-325	325-375	>375
Loose working point				
Data	$n_b = 3$	838	394	717
Template		861.8 ± 38.1	372.1 ± 18.4	673.2 ± 34.5
Data	$n_b = 4$	81	43	81
Template		78.5 ± 5.8	27.6 ± 2.6	78.6 ± 3.3
Medium working point				
Data	$n_b = 3$	137	79	152
Template		131.2 ± 4.3	75.1 ± 2.9	137.8 ± 5.7
Data	$n_b = 4$	1	1	3
Template		1.8 ± 0.1	0.9 ± 0.1	3.1 ± 0.2
Tight working point				
Data	$n_b = 3$	24	15	25
Template		23.0 ± 0.9	12.9 ± 0.6	20.3 ± 1.1
Data	$n_b = 4$	0	0	1
Template		0.1 ± 0.1	0.1 ± 0.1	0.2 ± 0.1

Table 6.3: Summary of the fit predictions in the n_b^{reco} signal region of the $\mu +$ jets control sample, after combination of the $n_{jet} = 3, = 4, \geq 5$ categories. The predictions are extrapolated from a $n_b^{reco} = 0, 1, 2$ control region using 11.4 fb^{-1} of $\sqrt{s} = 8\text{TeV}$ data. The uncertainties quoted on the template yields are purely statistical.

2437 6.2.3. Application to the α_T Hadronic Search Region

2438 As an accompaniment to the background estimation methods outlined in the α_T search,
 2439 the b-tag template method offers a complementary way of testing the **SM** only background
 2440 hypothesis within the hadronic signal region of the search. In the presence of a natural
 2441 **SUSY** signature mediated by a light gluino and containing four underlying \tilde{b} or \tilde{t} squarks,
 2442 which subsequently decay to t or b quarks, the number of reconstructed $n_b^{reco} = 3, \geq 4$
 2443 events will be enhanced.

2444 Figure 6.5 shows the the results of the template shapes derived from simulation and
 2445 fitted to data for each of the three **CSV** working points, in the $n_{jet} \geq 5, H_T > 375$
 2446 GeV category. Grey bands represent the statistical uncertainty of the fit combined in
 2447 quadrature with the systematic uncertainties of varying the data to simulation scale
 2448 factors up and down by their measured systematic uncertainties. Additional fit results
 2449 for other jet multiplicities are found in Appendix D.4.

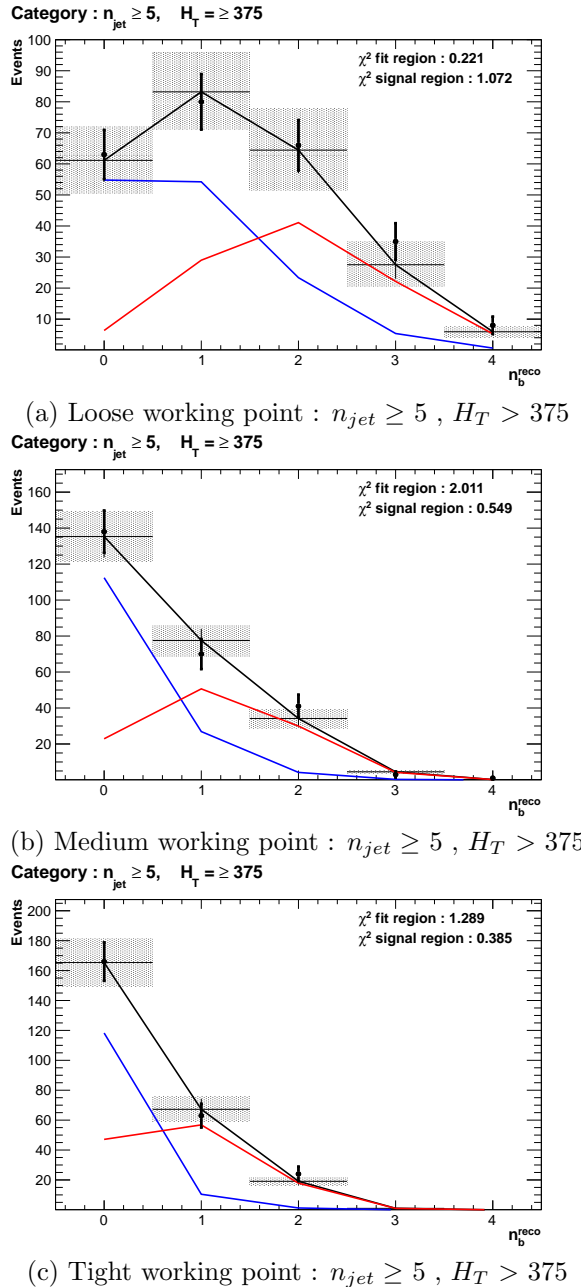


Figure 6.5: The results of fitting the $Z = 0$ and $Z = 2$ templates in the $n_b^{reco} = 0, 1, 2$ control region to data from the hadronic signal selection, in the $n_{jet} \geq 5$ and $H_T > 375$ category for all CSV working points. The blue template represents $Z = 0$, while the red template represents $Z = 2$. The χ^2 parameter displayed represents the goodness of fit to the low n_b^{reco} (0-2) control region.

The numerical results and extrapolation to the $n_b^{reco} = 3, 4$ bins for all H_T and working points are shown in Table 6.4. Also included within the table are total SM background predictions determined by the maximum likelihood fit in both jet multiplicity categories

2453 of the α_T analysis for the **CSVM** tagger, as introduced in Section (4.8). No excess of
2454 data is found for any of the three **CSV** working points. Predictions within the signal
2455 region from this method are also found to be compatible with the background predictions
2456 determined by the α_T simultaneous fit as already shown in Table 5.2.

H_T		275-325	325-375	>375
Loose working point				
Data		198	85	126
Template	$n_b = 3$	207.1 ± 33.3	103.4 ± 10.9	124.98 ± 16.2
Data		15	9	16
Template	$n_b = 4$	15.9 ± 3.7	8.05 ± 1.2	13.1 ± 2.2
Medium working point				
Data		32	16	15
Template	$n_b = 3$	26.4 ± 1.7	12.7 ± 1.2	19.9 ± 2.8
α_T ML Fit		$29.8_{-4.4}^{+5.2}$	$14.0_{-2.0}^{+1.8}$	$16.5_{-1.4}^{+1.4}$
Data		1	0	2
Template	$n_b = 4$	0.3 ± 0.2	0.3 ± 0.1	0.5 ± 0.2
α_T ML Fit		$0.9_{-0.7}^{+0.4}$	$0.3_{-0.2}^{+0.2}$	$0.6_{-0.3}^{+0.3}$
Tight working point				
Data		5	2	0
Template	$n_b = 3$	4.03 ± 0.3	2.4 ± 0.3	3.1 ± 0.3
Data		1	0	0
Template	$n_b = 4$	0.1 ± 0.1	0.1 ± 0.1	0.0 ± 0.1

Table 6.4: Summary of the fit predictions in the n_b^{reco} signal region of the α_T hadronic signal selection, after combination of the $n_{jet} = 3, = 4, \geq 5$ categories. The predictions are extrapolated from a $n_b^{reco} = 0, 1, 2$ control region using 11.7 fb^{-1} of $\sqrt{s} = 8\text{TeV}$ data. The uncertainties quoted on the template yields are purely statistical.

2457 6.3. Summary

2458 A **SUSY** signature such as one from gluino-induced third-generation squark production,
2459 would result in a final state with an underlying b-quark content greater than two. In
2460 order to be able to discriminate such signatures from the **SM** background, templates are
2461 generated based on a parameterisation of **SM** processes, where the underlying b-quarks
2462 per event is typically zero or two. These templates are then fit to data in a low n_b^{reco}
2463 (0-2) control region in order to extrapolate a prediction within a high n_b^{reco} (3-4) signal
2464 region. This approach is built upon the assumptions that the defined control region is
2465 almost entirely free of any possible signal contamination from either a third generation
2466 **SUSY** signal, or other possible signal topologies with a small number of b quarks in the
2467 final state.

2468 The method was demonstrated both in simulation and also in data, using the **SM**
2469 enriched $\mu + \text{jets}$ selection from the α_T search. This was conducted to prove conceptually
2470 and experimentally that the method is valid and that there is adequate control over
2471 the efficiency and mis-tagging rates in data for all working points of the **CSV** tagger.
2472 Additionally this method was further applied to the α_T analysis signal region, where
2473 good agreement is observed between the predictions from the template extrapolations,
2474 observations in data and the background estimation method of the α_T analysis.

Chapter 7.

²⁴⁷⁵ Conclusions

²⁴⁷⁶ A search for supersymmetry is presented based on a data sample of pp collisions collected
²⁴⁷⁷ at $\sqrt{s} = 8$ TeV, corresponding to an integrated luminosity of 11.7 ± 0.5 fb⁻¹. Final
²⁴⁷⁸ states with two or more jets and significant \cancel{E}_T , a typical final state topology of R-parity
²⁴⁷⁹ conserving SUSY models have been analysed. The α_T variable is utilised as the main
²⁴⁸⁰ discriminator between balanced multi-jet backgrounds and those with real missing energy.

²⁴⁸¹ Additionally a measurement of the performance of the Level-1 trigger for jets and
²⁴⁸² energy sum quantities is also presented. These studies quantify any change in Level-1
²⁴⁸³ performance after the introduction of a 5 GeV jet seed threshold into the jet clustering
²⁴⁸⁴ algorithm. This change is introduced to facilitate a reduction in the rate at which jets
²⁴⁸⁵ are formed at Level-1 from pile-up jets which are not of interest to physics analyses. This
²⁴⁸⁶ change is necessary to ensure that trigger thresholds can be maintained at lower values,
²⁴⁸⁷ in the presence of an increasing number of pile-up interactions per bunch crossing over
²⁴⁸⁸ the 2012 run period. No significant change in single jet trigger efficiencies is observed
²⁴⁸⁹ and good performance is observed for a range of Level-1 energy sum quantities.

²⁴⁹⁰ Within the SUSY search presented in this analysis, Standard Model backgrounds are
²⁴⁹¹ estimated from a simultaneous binned likelihood fit to a hadronic signal selection, as
²⁴⁹² well as three Standard Model enriched control samples. The search is split into H_T , n_b^{reco}
²⁴⁹³ and n_{jet} categories to increase the sensitivity to a range of possible supersymmetric final
²⁴⁹⁴ states. Systematic errors due to theory, detector effects and simulation deficiencies are
²⁴⁹⁵ quantified through the use of data driven closure tests and accounted for in the final
²⁴⁹⁶ interpretation, where observations in data are found to be compatible with a SM only
²⁴⁹⁷ hypothesis.

2498 In the absence of a signal like excess, the analysis is further interpreted in a set of **SMS**
2499 models. In the considered models with gluino pair production and for small **LSP** masses,
2500 exclusion limits of the gluino mass are set in the range 950-1125 GeV. For **SMS** models
2501 with direct squark pair production, first or second generation squarks are excluded up to
2502 around 775 GeV and bottom squarks are excluded up to masses of 600 GeV, again for
2503 small **LSP** masses. In the context of ‘natural’ **SUSY** models, with many reconstructed
2504 b-jets in the final state, limits are set in the range of 975-1125 GeV again for large mass
2505 splittings between the parent squarks and the **LSP**.

2506 A complementary approach, that uses a template fit method to estimate the b-tagged
2507 jet distribution of **SM** processes within a supersymmetric search is introduced and then
2508 validated in simulation and data. The approach can be used to identify any excess in
2509 data arising from third generation supersymmetric signatures, and is utilised within this
2510 thesis as a crosscheck of the α_T background estimation in a high number of reconstructed
2511 b-tagged jets. It is found to give a **SM** background estimation that is in good agreement
2512 with both the α_T search and a **SM** only hypothesis. As light third generation squarks
2513 are an important feature of ‘natural’ **SUSY** models if they are to ultimately be the
2514 solution to the fine tuning problem [100], the limits imposed through interpretations of
2515 the **T1bbbb** and **T1tttt** **SMS** models within the α_T search, put pressure on such theories,
2516 by squeezing the parameter space in which light third generation squarks can reside.

2517

Appendix A.

²⁵¹⁸ Miscellaneous

²⁵¹⁹ A.1. Jet Identification Criteria

²⁵²⁰ For Calo jets the following identification criteria were applied:

Loose CaloJet Id	
Variable	Definition
$f_{HPD} < 0.98$	Fraction of jet energy contributed from “hottest” HPD , which rejects HCAL noise.
$f_{EM} > 0.01$	Noise from the HCAL is further suppressed by requiring a minimal electromagnetic component to the jet f_{EM} .
$N_{hits}^{90} \geq 2$	Jets that have $> 90\%$ of its energy from a single channel are rejected, to serve as a safety net that catches jets arising from undiagnosed noisy channels.

Table A.1: Criteria for a reconstructed jet to pass the loose calorimeter jet id.

²⁵²¹ For PF jets the following identification criteria were applied:

Loose PF jet Id	
Variable	Definition
<code>nfhJet < 0.99</code>	Fraction of jet composed of neutral hadrons. HCAL noise tends to populate high values of neutral hadron fraction.
<code>nemfJet < 0.99</code>	Fraction of jet composed of neutral electromagnetic energy. ECAL noise tends to populate high values of neutral EM fraction.
<code>nmultiJet > 1</code>	Number of constituents that jet is composed from.
<code>chfJet > 0</code>	Fraction of jet composed of charged hadrons.
<code>cmultiJet > 0</code>	Number of charged particles that compose jet.
<code>cemfJet < 0.99</code>	Fraction of jet composed of charged electromagnetic energy.

Table A.2: Criteria for a reconstructed jet to pass the loose PF jet id.

2522 **A.2. Primary Vertices**

2523 The pile-up per event is defined by the number of 'good' reconstructed primary vertices
 2524 in the event, with each vertex satisfying the following requirements:

Good primary vertex requirement	
Variable	Definition
$N_{dof} > 4$	The number of degree of freedom, from the vertex fit to compute the best estimate of the vertex parameters.
$ \Delta z_{vtx} < 24\text{cm}$	The distance, $ \Delta z_{vtx} $, to the position of the closest HLT primary vertex.
$\rho < 2\text{cm}$	The perpendicular distance of track position to the beam spot.

Table A.3: Criteria for a vertex in an event to be classified as a 'good' reconstructed primary vertex.

Appendix B.

²⁵²⁵ L1 Jets

²⁵²⁶ B.1. Jet Matching Efficiencies

²⁵²⁷ The single jet turn-on curves are derived from events independent of whether the leading
²⁵²⁸ jet in an event is matched to a Level 1 jet using ΔR matching detailed in Section (3.4.3)
²⁵²⁹ or not. These turn-ons are produced from events which are not triggered on jet quantities
²⁵³⁰ and therefore it is not guaranteed that the lead jet of an event will be seeded by a Level
²⁵³¹ 1 jet. Figure B.1 shows the particular matching efficiency of a lead jet to a L1 jet.

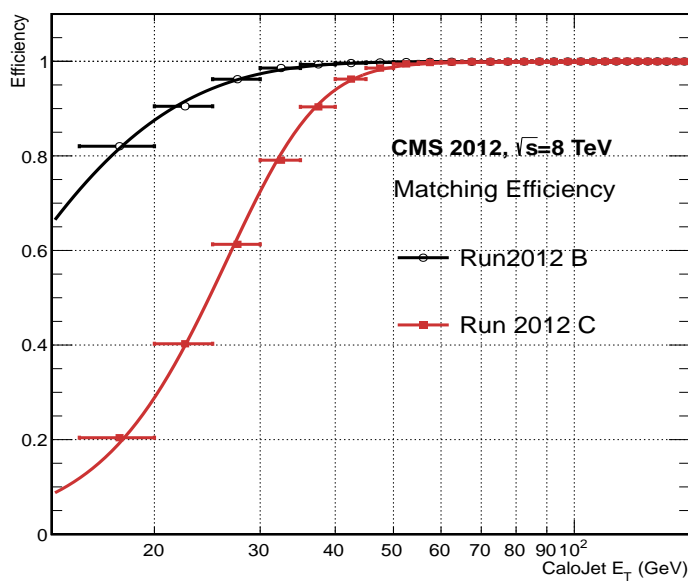


Figure B.1: Leading jet matching efficiency as a function of the offline CaloJet E_T , measured in an isolated muon triggered dataset in the 2012B and 2012C run periods.

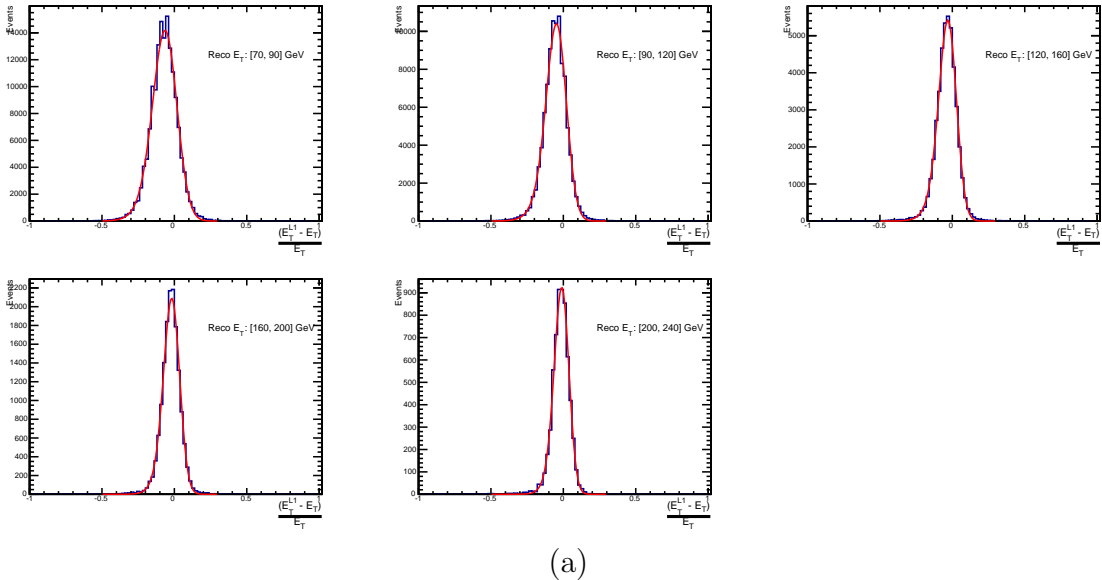
Run Period	μ	σ
2012B	6.62 ± 0.01	0.79 ± 0.03
2012C	19.51 ± 0.03	7.14 ± 0.02

Table B.1: Results of a cumulative EMG function fit to the turn-on curves for the matching efficiency of the leading jet in an event to a Level-1 jet in run 2012C and 2012B data, measured in an isolated muon triggered sample. The turn-on point, μ , and resolution, σ , are measured with respect to offline Calo Jet E_T .

2532 It can be seen that the turn-on occurs at a lower E_T during the 2012B run period. The
 2533 seed threshold requirement of a 5 GeV jet seed in run 2012C result in more events in
 2534 which even the lead offline jet does not have an associated L1 jet. This can be attributed
 2535 to events with soft non-collimated jets in which the energy deposits are not centralised
 2536 in a calorimeter region. However, for larger jet E_T thresholds typical of those used by
 2537 physics analyses, 100% efficiency is observed, and therefore this effect has no impact to
 2538 overall physics performance.

2539 A fit of an **EMG** function to the matching efficiencies find mean, μ , values of 6.62 GeV
 2540 and 19.51 GeV for Run 2012B and 2012C respectively and is shown in Table B.1.

2541 B.2. Leading Jet Energy Resolution



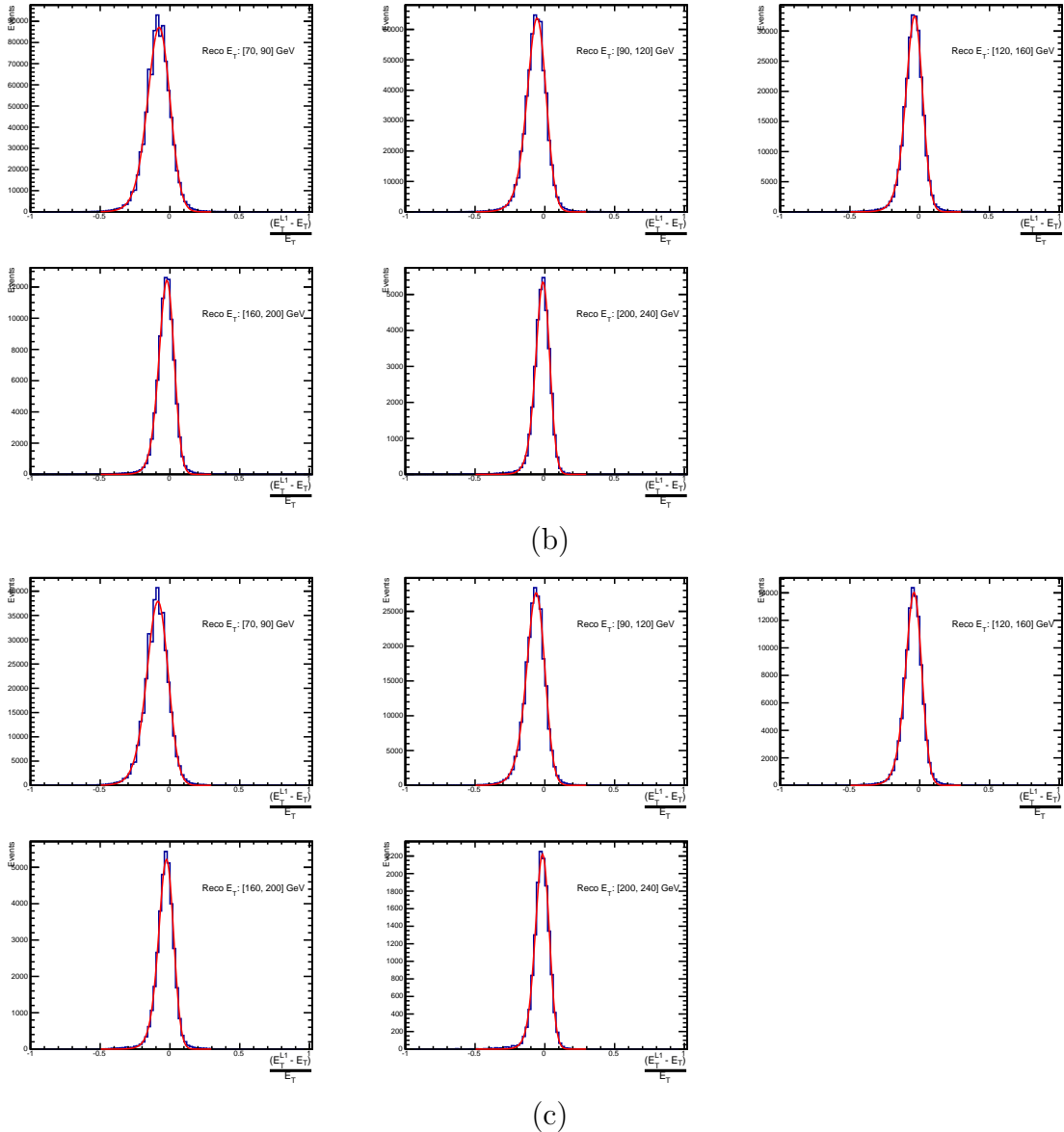
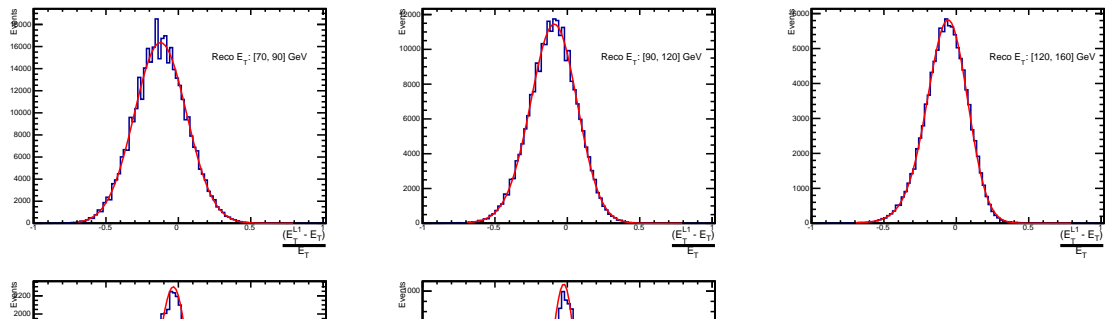
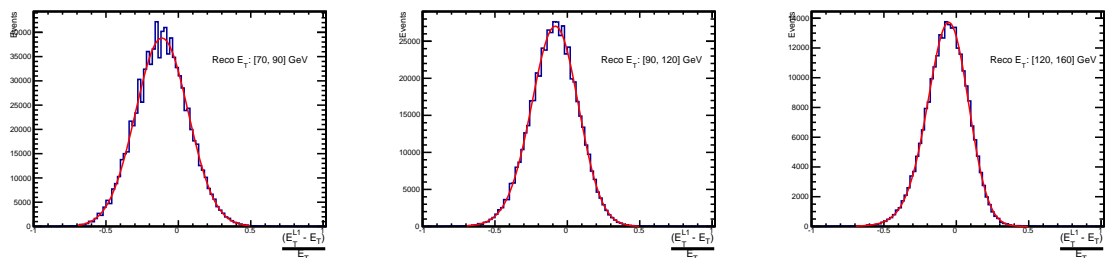


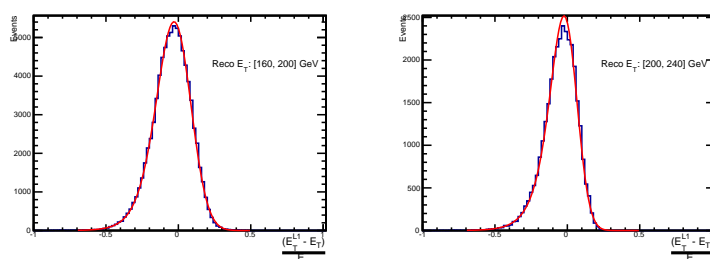
Figure B.2: Resolution plots of the leading offline jet Calo E_T measured as a function of $\frac{(L1 E_T - \text{Offline } E_T)}{\text{Offline } E_T}$ for (a) low, (b) medium, and (c) high pile-up conditions as defined in Section (3.4.4).

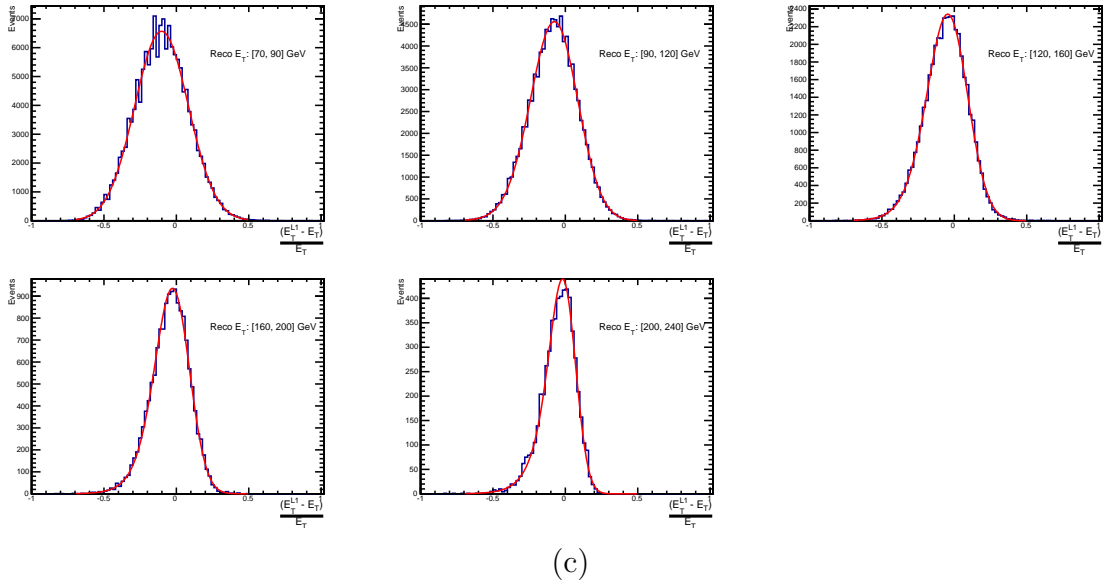


(a)



(b)





(c)

Figure B.3: Resolution plots of the leading offline jet PF E_T measured as a function of $\frac{(L1 E_T - \text{Offline } E_T)}{\text{Offline } E_T}$ for (a) low, (b) medium, and (c) high pile-up conditions as defined in Section (3.4.4).

2542 B.3. Resolution for Energy Sum Quantities

2543 The following plots show the resolution parameters for energy sum quantities as a function
 2544 of the quantity (q) itself. In this case, the μ , σ and λ fit values to an **EMG** function
 2545 defined by Equation (3.3) for each of the individual $\frac{(L1 q - \text{Offline } q)}{\text{Offline } q}$ distributions, in bins
 2546 of the quantity (q) is displayed.

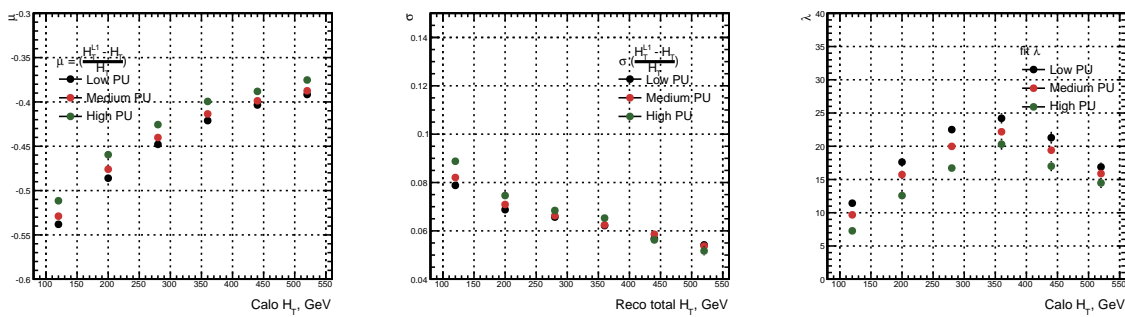


Figure B.4: H_T resolution parameters in bins of Calo H_T measured for the defined low, medium and high pile-up conditions. Shown are the mean μ (left), resolution σ (middle) and λ (right) fit values to an **EMG** function for the $\frac{(L1 H_T - H_T)}{H_T}$ distributions.

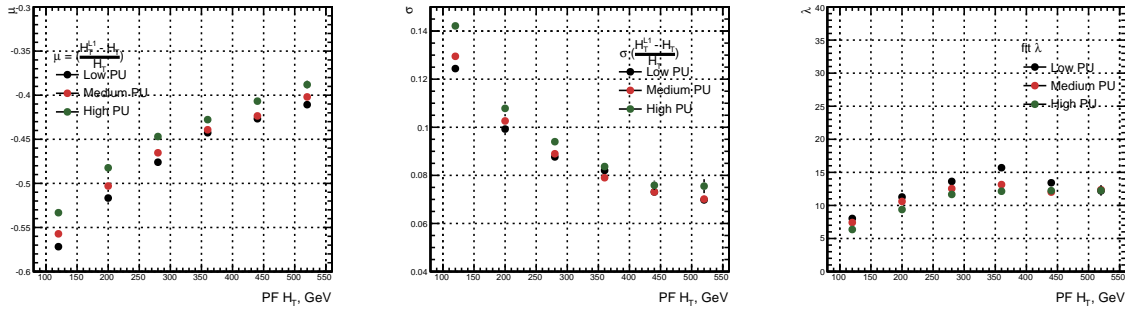


Figure B.5: H_T resolution parameters in bins of $PF H_T$ measured for the defined low, medium and high pile-up conditions. Shown are the mean μ (left), resolution σ (middle) and λ (right) fit values to an EMG function for the $\frac{(L1H_T - H_T)}{H_T}$ distributions.

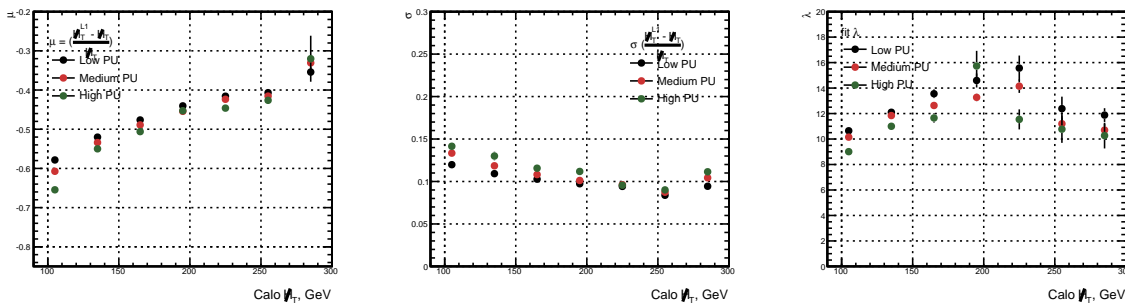


Figure B.6: H_T resolution parameters in bins of $Calo H_T$ measured for the defined low, medium and high pile-up conditions. Shown are the mean μ (left), resolution σ (middle) and λ (right) fit values to an EMG function for the $\frac{(L1H_T - H_T)}{H_T}$ distributions.

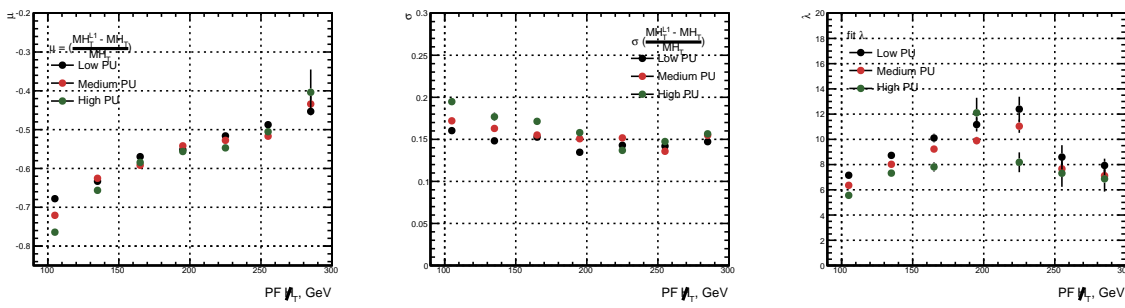


Figure B.7: H_T resolution parameters in bins of $PF H_T$ measured for the defined low, medium and high pile-up conditions. Shown are the mean μ (left), resolution σ (middle) and λ (right) fit values to an EMG function for the $\frac{(L1H_T - H_T)}{H_T}$ distributions.

Appendix C.

²⁵⁴⁷ Additional Material on Background ²⁵⁴⁸ Estimation Methods

²⁵⁴⁹ C.1. Determination of k_{QCD}

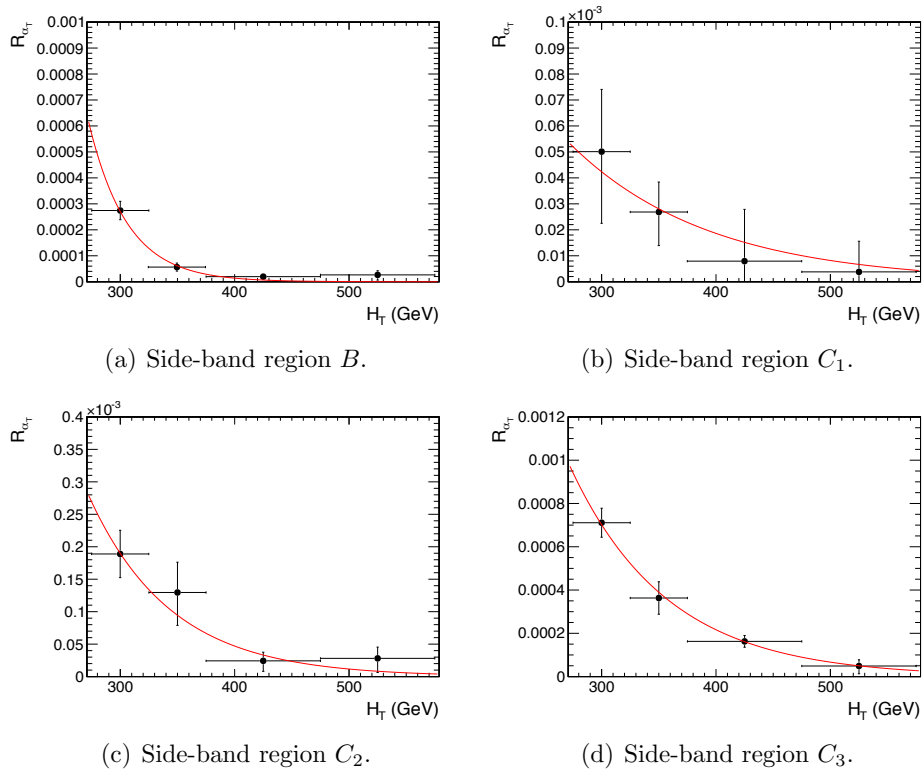


Figure C.1: $R_{\alpha_T}(H_T)$ and exponential fits for each of the data sideband regions. Fit is conducted between the H_T region $275 < H_T < 575$.

2551 **C.2. Effect of Varying Background Cross-sections on**
 2552 **Closure Tests**

2553 Closure tests with cross section variations of +20% and -20% applied to $W + \text{jets}$ and $t\bar{t}$
 2554 processes respectively.

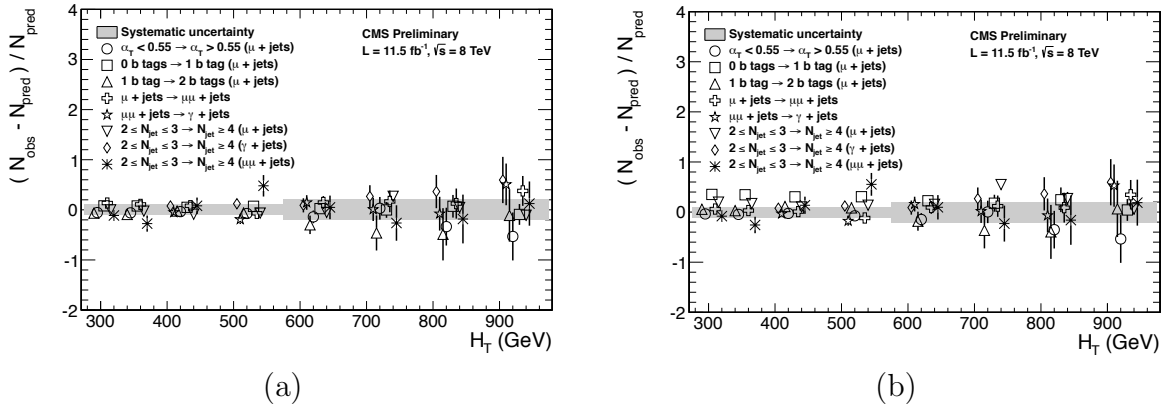


Figure C.2: Sets of closure tests (open symbols) overlaid on top of the systematic uncertainty used for each of the five H_T regions (shaded bands) in the $2 \leq n_{jet} \leq 3$ jet multiplicity category for nominal and varied cross-sections; (a) Nominal and (b) Varied $\pm 20\%$.

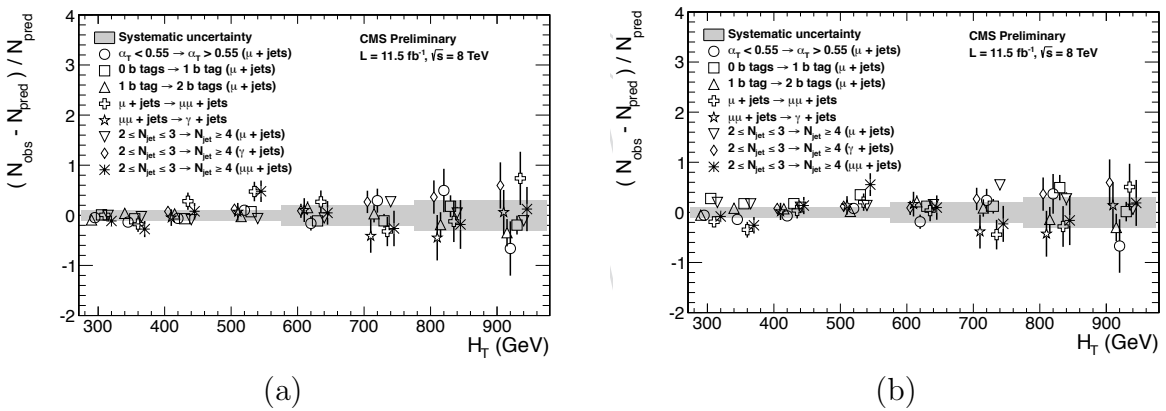


Figure C.3: Sets of closure tests (open symbols) overlaid on top of the systematic uncertainty used for each of the five H_T regions (shaded bands) in the $n_{jet} \geq 4$ jet multiplicity category for nominal and varied cross-sections; (a) Nominal (b) Varied $\pm 20\%$.

		H_T (GeV)			
n_b^{reco}	Cross Section	275–325	325–375	375–475	475–575
0	Nominal	0.303 \pm 0.010	0.258 \pm 0.007	0.192 \pm 0.003	0.148 \pm 0.004
	Varied	0.300 \pm 0.010	0.256 \pm 0.007	0.191 \pm 0.003	0.147 \pm 0.004
1	Nominal	0.294 \pm 0.005	0.246 \pm 0.004	0.189 \pm 0.003	0.139 \pm 0.003
	Varied	0.295 \pm 0.006	0.248 \pm 0.004	0.191 \pm 0.003	0.140 \pm 0.003
2	Nominal	0.208 \pm 0.003	0.183 \pm 0.004	0.145 \pm 0.003	0.123 \pm 0.004
	Varied	0.211 \pm 0.004	0.185 \pm 0.004	0.147 \pm 0.003	0.124 \pm 0.004
3	Nominal	0.214 \pm 0.005	0.202 \pm 0.007	0.159 \pm 0.006	0.140 \pm 0.007
	Varied	0.215 \pm 0.005	0.203 \pm 0.007	0.159 \pm 0.006	0.140 \pm 0.007
≥ 4	Nominal	0.220 \pm 0.015	0.245 \pm 0.035	0.119 \pm 0.009	-
	Varied	0.220 \pm 0.015	0.245 \pm 0.035	0.119 \pm 0.009	-
n_b^{reco}	Cross Section	575–675	675–775	775–875	875– ∞
0	Nominal	0.119 \pm 0.004	0.098 \pm 0.005	0.077 \pm 0.006	0.049 \pm 0.005
	Varied	0.120 \pm 0.005	0.098 \pm 0.006	0.077 \pm 0.007	0.049 \pm 0.005
1	Nominal	0.115 \pm 0.004	0.093 \pm 0.005	0.075 \pm 0.007	0.063 \pm 0.006
	Varied	0.116 \pm 0.004	0.098 \pm 0.005	0.081 \pm 0.007	0.065 \pm 0.006
2	Nominal	0.096 \pm 0.005	0.070 \pm 0.006	0.051 \pm 0.007	0.063 \pm 0.008
	Varied	0.098 \pm 0.005	0.073 \pm 0.006	0.053 \pm 0.007	0.064 \pm 0.008
3	Nominal	0.114 \pm 0.009	0.065 \pm 0.007	0.070 \pm 0.017	0.092 \pm 0.020
	Varied	0.114 \pm 0.009	0.066 \pm 0.007	0.070 \pm 0.016	0.093 \pm 0.020

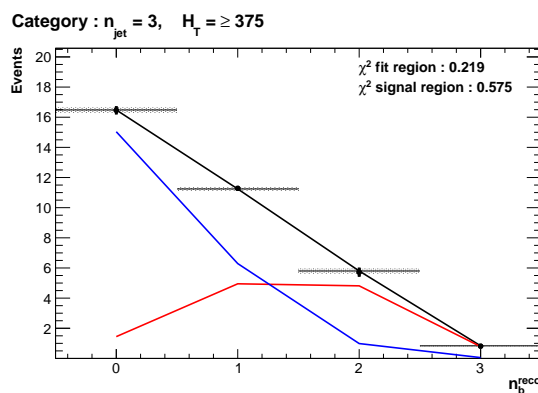
Table C.1: Translation factors constructed from the $\mu +$ jets control sample and signal selection MC, to predict yields for the $W +$ jets and $t\bar{t}$ back-grounds in the signal region with (a) NNLO cross sections corrected by k-factors determined from a data sideband see Section (4.4), marked as Nominal, and (b) the same cross sections but with those for $W +$ jets and $t\bar{t}$ varied up and down by 20%, respectively, marked as Varied. No requirement is placed on the jet multiplicity of events within this table.

Appendix D.

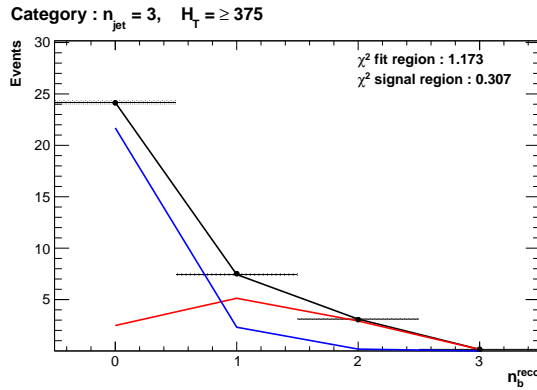
2555 Additional Material For B-tag 2556 Template Method

2557 D.1. Templates Fits in Simulation

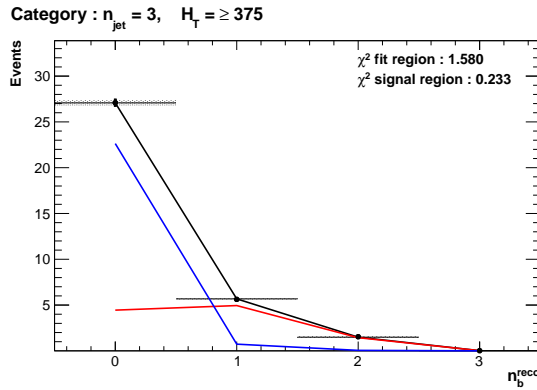
2558 The result of template fits for the three CSV working points in the $n_{jet} = 3, H_T > 375$
2559 category:



(a) Loose working point $n_{jet} = 3$



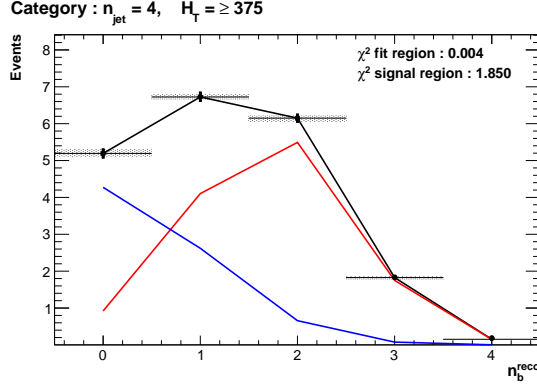
(b) Medium working point $n_{jet} = 3$



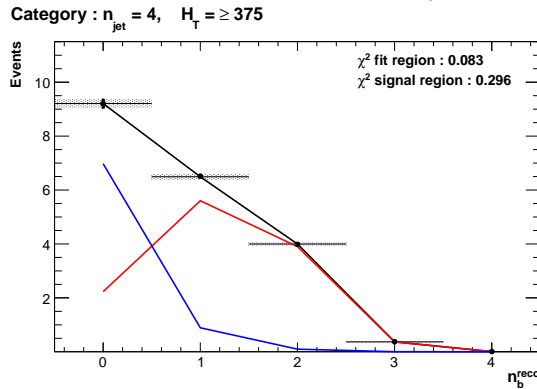
(c) Tight working point $n_{jet} = 3$

Figure D.1: The results of fitting the $Z = 0$ and $Z = 2$ templates in the $n_b^{reco} = 0, 1, 2$ control region to yields from simulation in the $\mu +$ jets control sample for the $H_T > 375$ GeV, $n_{jet} = 3$ category. The blue template represents $Z = 0$, while the red template represents $Z = 2$. Grey bands represent the statistical uncertainty of the fit. The χ^2 parameter displayed represents the goodness of fit to the low n_b^{reco} (0-2) control region.

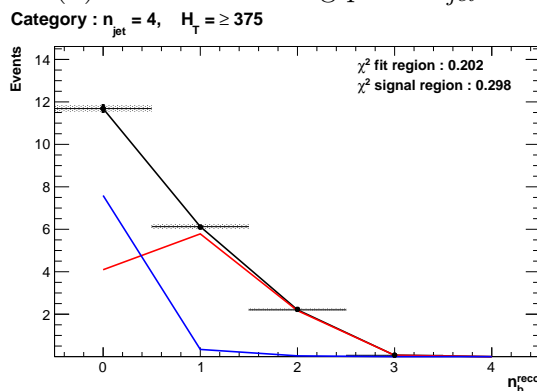
2560 Template fits for the three **CSV** working points in the $n_{jet} = 4$, $H_T > 375$ category:



(a) Loose working point $n_{jet} = 4$



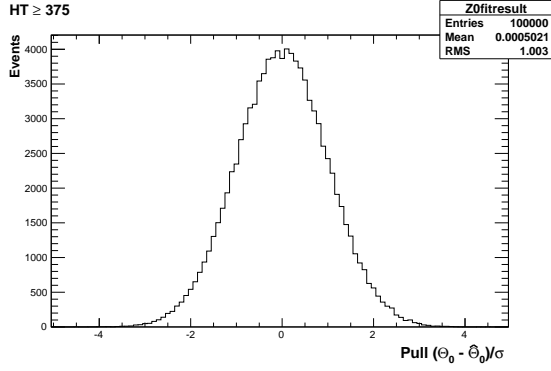
(b) Medium working point $n_{jet} = 4$



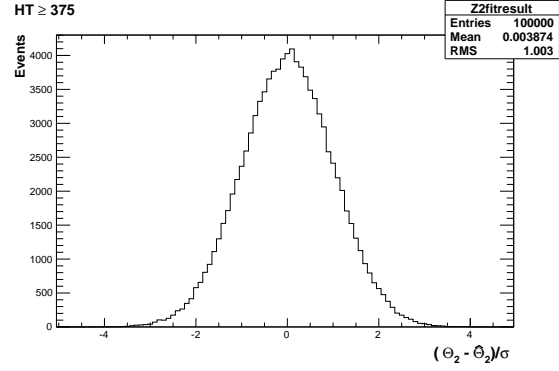
(c) Tight working point $n_{jet} = 4$

Figure D.2: The results of fitting the $Z = 0$ and $Z = 2$ templates in the $n_b^{reco} = 0, 1, 2$ control region to yields from simulation in the $\mu +$ jets control sample for the $H_T > 375$ GeV, $n_{jet} = 4$ category. The blue template represents $Z = 0$, while the red template represents $Z = 2$. Grey bands represent the statistical uncertainty of the fit. The χ^2 parameter displayed represents the goodness of fit to the low n_b^{reco} (0-2) control region.

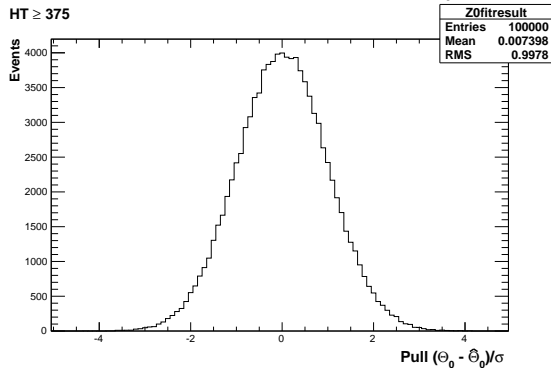
2561 D.2. Pull Distributions for Template Fits



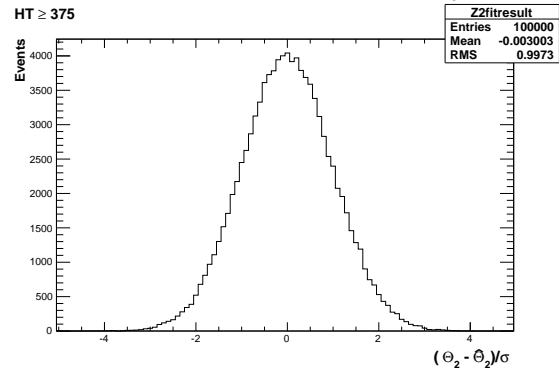
(a) Z0 Template, $H_T > 375$, $n_{jet} = 3$



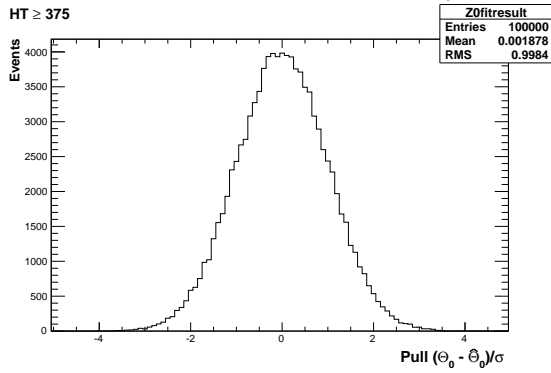
(b) Z2 Template, $H_T > 375$, $n_{jet} = 3$



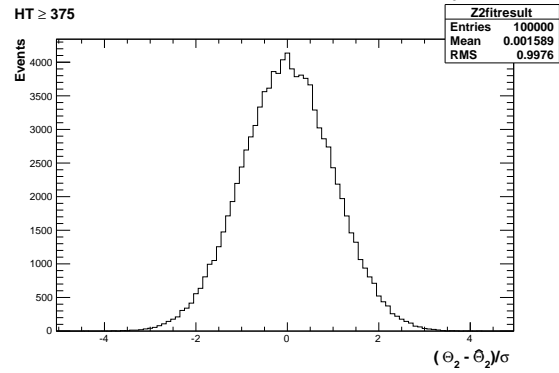
(a) Z0 Template, $H_T > 375$, $n_{jet} = 4$



(b) Z2 Template, $H_T > 375$, $n_{jet} = 4$



(a) Z0 Template, $H_T > 375$, $n_{jet} \geq 5$



(b) Z2 Template, $H_T > 375$, $n_{jet} \geq 5$

Figure D.3: Pull distributions of the normalisation parameter of each template, $\frac{(\theta - \hat{\theta})}{\sigma}$. Distributions are constructed from 10^4 pseudo-experiments generated by a gaussian distribution with width σ , centred on the nominal template value of each point within the low n_b^{reco} control region. Distributions are shown for both Z0 and Z2 templates for the medium CSV working point.

2562 **D.3. Templates Fits in Data Control Sample**

2563 Template fits for the three H_T bins, in the $n_{jet} = 3$, medium **CSV** working point:

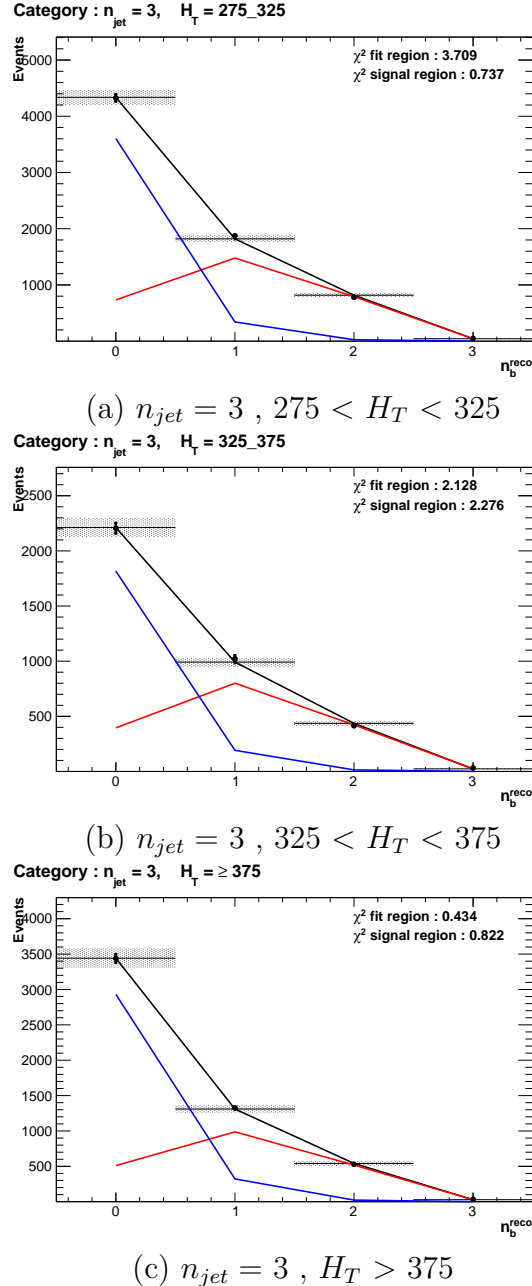


Figure D.4: The results of fitting the $Z = 0$ and $Z = 2$ templates in the $n_b^{reco} = 0, 1, 2$ control region to data from the $\mu +$ jets control sample, for the **CSV** medium working point, with a jet multiplicity $n_{jet} = 3$, in all three H_T categories. The χ^2 parameter displayed represents the goodness of fit to the low n_b^{reco} (0-2) control region.

2564 Template fits for the three H_T bins, in the $n_{jet} = 4$, medium CSV working point:

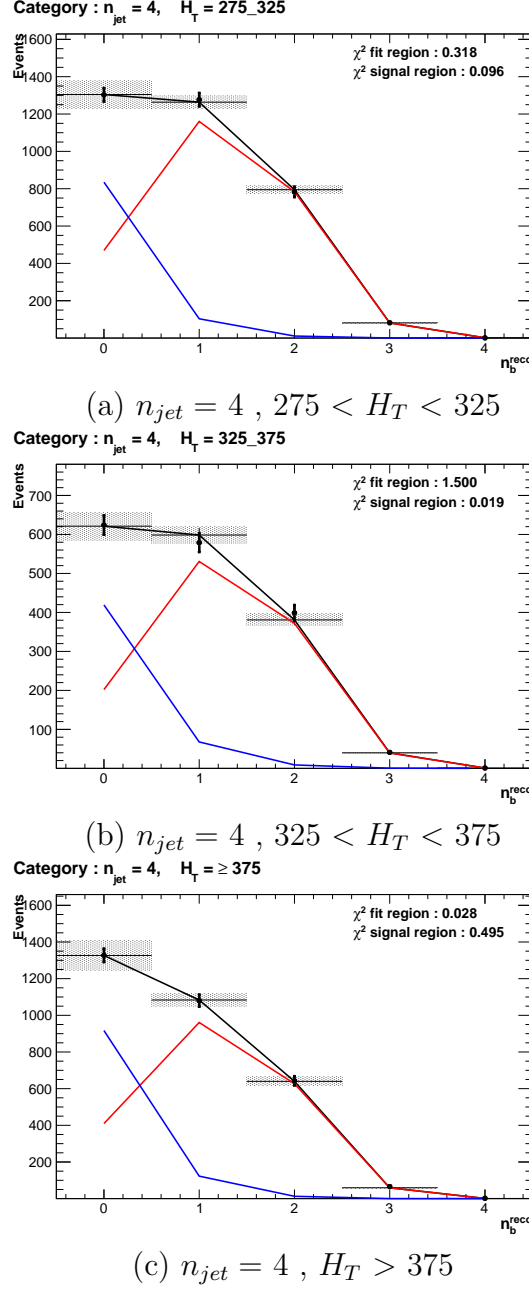


Figure D.5: The results of fitting the $Z = 0$ and $Z = 2$ templates in the $n_b^{reco} = 0, 1, 2$ control region to data from the $\mu +$ jets control sample, for the CSV medium working point, with a jet multiplicity $n_{jet} = 4$, in all three H_T categories. The blue template represents $Z = 0$, while the red template represents $Z = 2$. The χ^2 parameter displayed represents the goodness of fit to the low n_b^{reco} (0-2) control region.

2565 **D.4. Templates Fits in Data Signal Region**

2566 Template fits for the three **CSV** working points, in the $n_{jet} = 3, H_T > 375$ category :

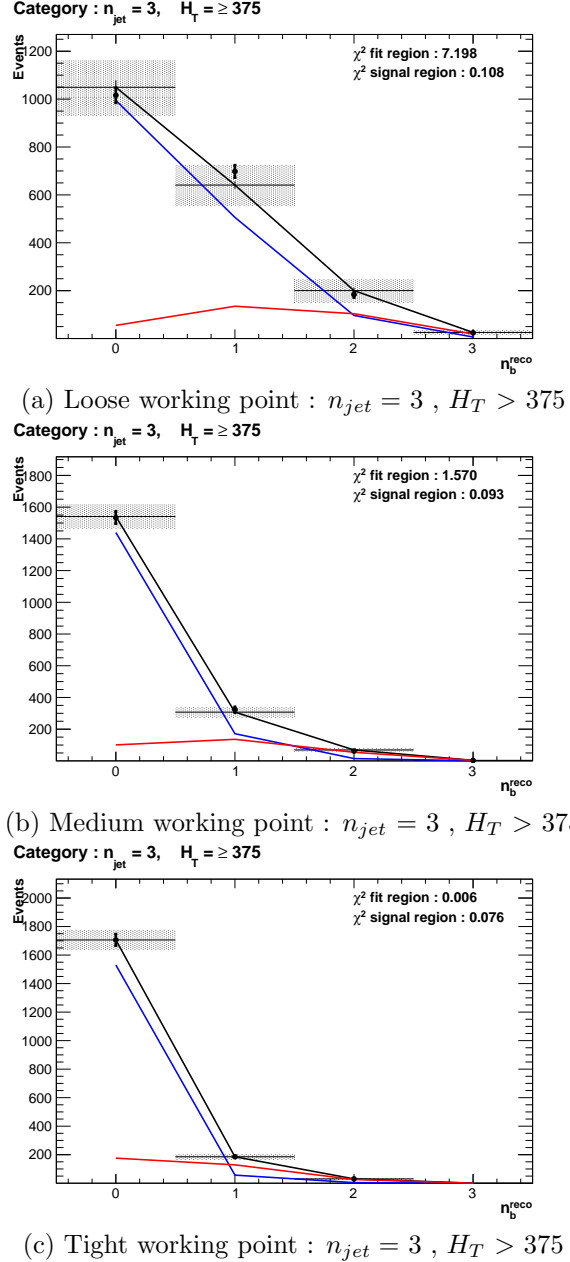


Figure D.6: The results of fitting the $Z = 0$ and $Z = 2$ templates in the $n_b^{reco} = 0, 1, 2$ control region to data from the hadronic signal selection, in the $n_{jet} = 3$ and $H_T > 375$ category for all **CSV** working points. The blue template represents $Z = 0$, while the red template represents $Z = 2$. The χ^2 parameter displayed represents the goodness of fit to the low n_b^{reco} (0-2) control region.

2567 Template fits for the three **CSV** working points, in the $n_{jet} = 4, H_T > 375$ category :

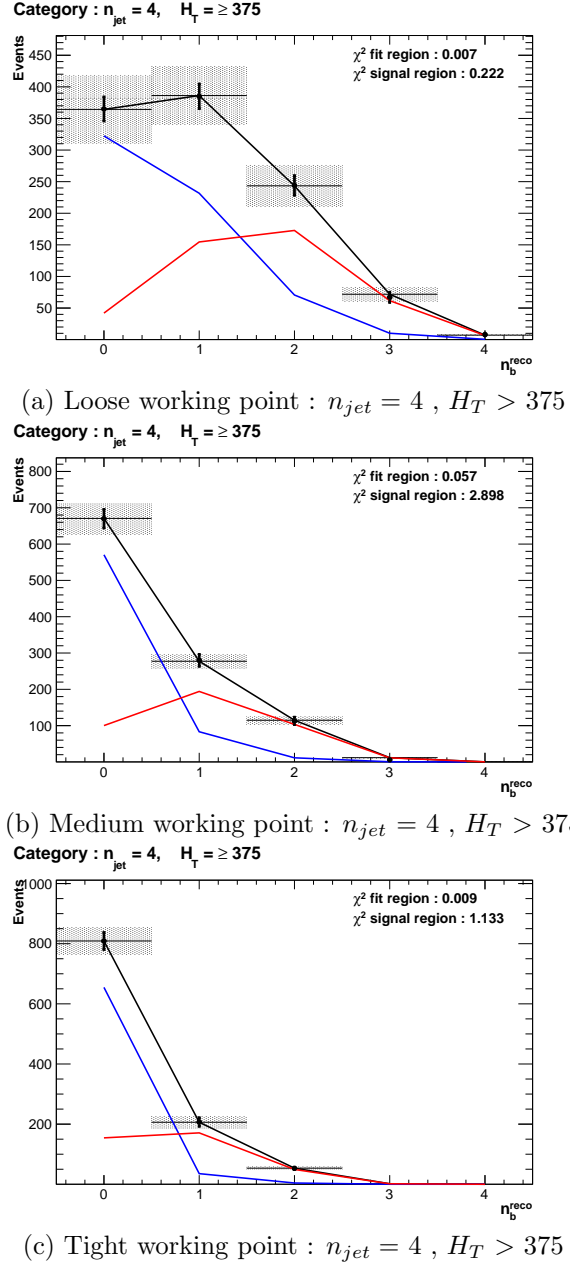


Figure D.7: The results of fitting the $Z = 0$ and $Z = 2$ templates in the $n_b^{reco} = 0, 1, 2$ control region to data from the hadronic signal selection, in the $n_{jet} = 4$ and $H_T > 375$ category for all CSV working points. The blue template represents $Z = 0$, while the red template represents $Z = 2$. The χ^2 parameter displayed represents the goodness of fit to the low n_b^{reco} (0-2) control region.

2569 Bibliography

- 2570 [1] Particle Data Group Collaboration, “Review of Particle Physics (RPP)”,
2571 *Phys.Rev.* **D86** (2012) 010001, [doi:10.1103/PhysRevD.86.010001](https://doi.org/10.1103/PhysRevD.86.010001).
- 2572 [2] G. H. et al., “Nine-year Wilkinson Microwave Anisotropy Probe (WMAP)
2573 Observations: Cosmological Parameter Results”, *The Astrophysical Journal
Supplement Series* **208** (2013), no. 2,.
- 2575 [3] ATLAS Collaboration Collaboration, “Observation of a new particle in the search
2576 for the Standard Model Higgs boson with the ATLAS detector at the LHC”,
2577 *Phys.Lett.* **B716** (2012) 1–29, [doi:10.1016/j.physletb.2012.08.020](https://doi.org/10.1016/j.physletb.2012.08.020),
2578 [arXiv:1207.7214](https://arxiv.org/abs/1207.7214).
- 2579 [4] CMS Collaboration, “Observation of a new boson at a mass of 125 GeV with the
2580 CMS experiment at the LHC”, *Phys.Lett.* **B716** (2012) 30–61,
2581 [doi:10.1016/j.physletb.2012.08.021](https://doi.org/10.1016/j.physletb.2012.08.021), [arXiv:1207.7235](https://arxiv.org/abs/1207.7235).
- 2582 [5] CMS Collaboration, “Search for supersymmetry in hadronic final states with
2583 missing transverse energy using the variables AlphaT and b-quark multiplicity in
2584 pp collisions at 8 TeV”, *Eur.Phys.J.* **C73** (2013) 2568,
2585 [doi:10.1140/epjc/s10052-013-2568-6](https://doi.org/10.1140/epjc/s10052-013-2568-6), [arXiv:1303.2985](https://arxiv.org/abs/1303.2985).
- 2586 [6] S. Weinberg, “A Model of Leptons”, *Phys. Rev. Lett.* **19** (Nov, 1967)
2587 [doi:10.1103/PhysRevLett.19.1264](https://doi.org/10.1103/PhysRevLett.19.1264).
- 2588 [7] S. Glashow, “Partial Symmetries of Weak Interactions”, *Nucl.Phys.* **22** (1961)
2589 [doi:10.1016/0029-5582\(61\)90469-2](https://doi.org/10.1016/0029-5582(61)90469-2).
- 2590 [8] A. Salam, “Weak and Electromagnetic Interactions”, *Conf.Proc.* **C680519**
2591 (1968).
- 2592 [9] G. Hooft, “Renormalizable Lagrangians for massive Yang-Mills fields”, *Nuclear
Physics B* **35** (1971)

- 2594 [doi:
http://dx.doi.org/10.1016/0550-3213\(71\)90139-8](http://dx.doi.org/10.1016/0550-3213(71)90139-8).
- 2595 [10] Gargamelle Neutrino Collaboration Collaboration, “Observation of Neutrino Like
2596 Interactions Without Muon Or Electron in the Gargamelle Neutrino Experiment”,
2597 *Phys.Lett.* **B46** (1973) 138–140, [doi:
10.1016/0370-2693\(73\)90499-1](http://dx.doi.org/10.1016/0370-2693(73)90499-1).
- 2598 [11] UA1 Collaboration Collaboration, “Experimental Observation of Lepton Pairs of
2599 Invariant Mass Around 95-GeV at the CERN SPS Collider”, *Phys.Lett.* **B126**
2600 (1983) 398–410, [doi:
10.1016/0370-2693\(83\)90188-0](http://dx.doi.org/10.1016/0370-2693(83)90188-0).
- 2601 [12] UA2 Collaboration Collaboration, “Observation of Single Isolated Electrons of
2602 High Transverse Momentum in Events with Missing Transverse Energy at the
2603 CERN $\bar{p}p$ Collider”, *Phys.Lett.* **B122** (1983)
2604 [doi:
10.1016/0370-2693\(83\)91605-2](http://dx.doi.org/10.1016/0370-2693(83)91605-2).
- 2605 [13] E. Noether, “Invariante Variationsprobleme”, *Nachrichten von der Gesellschaft
2606 der Wissenschaften zu Göttingen, Mathematisch-Physikalische Klasse* **1918** (1918).
- 2607 [14] F. Halzen and A. D. Martin, “Quarks and Leptons”. 1985.
- 2608 [15] “Introduction to Elementary Particles”. Wiley-VCH, 2nd edition, October, 2008.
- 2609 [16] C. S. Wu et al., “Experimental Test of Parity Conservation in Beta Decay”,
2610 *Physical Review* **105** (February, 1957) [doi:
10.1103/PhysRev.105.1413](http://dx.doi.org/10.1103/PhysRev.105.1413).
- 2611 [17] P. Higgs, “Broken symmetries, massless particles and gauge fields”, *Physics
2612 Letters* **12** (1964), no. 2,
2613 [doi:
http://dx.doi.org/10.1016/0031-9163\(64\)91136-9](http://dx.doi.org/10.1016/0031-9163(64)91136-9).
- 2614 [18] F. Englert and R. Brout, “Broken Symmetry and the Mass of Gauge Vector
2615 Mesons”, *Phys. Rev. Lett.* **13** (Aug, 1964) [doi:
10.1103/PhysRevLett.13.321](http://dx.doi.org/10.1103/PhysRevLett.13.321).
- 2616 [19] P. W. Higgs, “Broken Symmetries and the Masses of Gauge Bosons”, *Phys. Rev.
2617 Lett.* **13** (Oct, 1964) [doi:
10.1103/PhysRevLett.13.508](http://dx.doi.org/10.1103/PhysRevLett.13.508).
- 2618 [20] G. S. Guralnik, “Global Conservation Laws and Massless Particles”, *Phys. Rev.
2619 Lett.* **13** (Nov, 1964) [doi:
10.1103/PhysRevLett.13.585](http://dx.doi.org/10.1103/PhysRevLett.13.585).
- 2620 [21] S. Weinberg, “A Model of Leptons”, *Phys. Rev. Lett.* **19** (Nov, 1967) 1264–1266,
2621 [doi:
10.1103/PhysRevLett.19.1264](http://dx.doi.org/10.1103/PhysRevLett.19.1264).
- 2622 [22] H. Yukawa, “On the Interaction of Elementary Particles. I”, *Progress of
2623 Theoretical Physics Supplement* **1** (1955) [doi:
10.1143/PTPS.1.1](http://dx.doi.org/10.1143/PTPS.1.1).

- [23] (Super-Kamiokande Collaboration) Collaboration, “Evidence for Oscillation of Atmospheric Neutrinos”, *Phys. Rev. Lett.* **81** (Aug, 1998) [doi:10.1103/PhysRevLett.81.1562](https://doi.org/10.1103/PhysRevLett.81.1562).
- [24] R. Becker-Szendy et al., “A Search for muon-neutrino oscillations with the IMB detector”, *Phys.Rev.Lett.* **69** (1992) [doi:10.1103/PhysRevLett.69.1010](https://doi.org/10.1103/PhysRevLett.69.1010).
- [25] S. P. Martin, “A Supersymmetry primer”, [arXiv:hep-ph/9709356](https://arxiv.org/abs/hep-ph/9709356).
- [26] H. Nilles, “Supersymmetry, Supergravity and Particle Physics”. Physics reports. North-Holland Physics Publ., 1984.
- [27] H. E. Haber and G. L. Kane, “The Search for Supersymmetry: Probing Physics Beyond the Standard Model”, *Phys.Rept.* **117** (1985) [doi:10.1016/0370-1573\(85\)90051-1](https://doi.org/10.1016/0370-1573(85)90051-1).
- [28] E. Witten, “Dynamical Breaking of Supersymmetry”, *Nucl.Phys.* **B188** (1981) [doi:10.1016/0550-3213\(81\)90006-7](https://doi.org/10.1016/0550-3213(81)90006-7).
- [29] J. Wess and B. Zumino, “Supergauge transformations in four dimensions”, *Nuclear Physics B* **70** (1974), no. 1, [doi:http://dx.doi.org/10.1016/0550-3213\(74\)90355-1](http://dx.doi.org/10.1016/0550-3213(74)90355-1).
- [30] H. Muller-Kirsten and A. Wiedemann, “Introduction to Supersymmetry”. World Scientific lecture notes in physics. World Scientific, 2010.
- [31] I. Aitchison, “Supersymmetry in Particle Physics: An Elementary Introduction”. Cambridge University Press, 2007.
- [32] K. A. Intriligator and N. Seiberg, “Lectures on Supersymmetry Breaking”, *Class.Quant.Grav.* **24** (2007) [arXiv:hep-ph/0702069](https://arxiv.org/abs/hep-ph/0702069).
- [33] Y. Shadmi, “Supersymmetry breaking”, [arXiv:hep-th/0601076](https://arxiv.org/abs/hep-th/0601076).
- [34] C. Burgess et al., “Warped Supersymmetry Breaking”, *JHEP* **0804** (2008) [doi:10.1088/1126-6708/2008/04/053](https://doi.org/10.1088/1126-6708/2008/04/053), [arXiv:hep-th/0610255](https://arxiv.org/abs/hep-th/0610255).
- [35] H. Murayama, “Supersymmetry breaking made easy, viable, and generic”, [arXiv:0709.3041](https://arxiv.org/abs/0709.3041).
- [36] H. Baer and X. Tata, “Weak Scale Supersymmetry: From Superfields to Scattering Events”. Cambridge University Press, 2006.

- 2653 [37] S. P. Martin, “Implications of supersymmetric models with natural R-parity
2654 conservation”, [doi:10.1103/PhysRevD.54.2340](https://doi.org/10.1103/PhysRevD.54.2340), [arXiv:hep-ph/9602349](https://arxiv.org/abs/hep-ph/9602349).
- 2655 [38] G. L. Kane, C. F. Kolda, L. Roszkowski, and J. D. Wells, “Study of constrained
2656 minimal supersymmetry”, *Phys.Rev.* **D49** (1994)
2657 [doi:10.1103/PhysRevD.49.6173](https://doi.org/10.1103/PhysRevD.49.6173), [arXiv:hep-ph/9312272](https://arxiv.org/abs/hep-ph/9312272).
- 2658 [39] C. Strege et al., “Updated global fits of the cMSSM including the latest LHC
2659 SUSY and Higgs searches and XENON100 data”, *JCAP* **1203** (2012)
2660 [doi:10.1088/1475-7516/2012/03/030](https://doi.org/10.1088/1475-7516/2012/03/030), [arXiv:1112.4192](https://arxiv.org/abs/1112.4192).
- 2661 [40] M. Citron et al., “The End of the CMSSM Coannihilation Strip is Nigh”,
2662 *Phys.Rev.* **D87** (2013) [doi:10.1103/PhysRevD.87.036012](https://doi.org/10.1103/PhysRevD.87.036012), [arXiv:1212.2886](https://arxiv.org/abs/1212.2886).
- 2663 [41] D. Ghosh, M. Guchait, S. Raychaudhuri, and D. Sengupta, “How Constrained is
2664 the cMSSM?”, *Phys.Rev.* **D86** (2012) [doi:10.1103/PhysRevD.86.055007](https://doi.org/10.1103/PhysRevD.86.055007),
2665 [arXiv:1205.2283](https://arxiv.org/abs/1205.2283).
- 2666 [42] LHC New Physics Working Group Collaboration, “Simplified Models for LHC
2667 New Physics Searches”, *J.Phys.* **G39** (2012) 105005,
2668 [doi:10.1088/0954-3899/39/10/105005](https://doi.org/10.1088/0954-3899/39/10/105005), [arXiv:1105.2838](https://arxiv.org/abs/1105.2838).
- 2669 [43] J. Alwall, P. Schuster, and N. Toro, “Simplified Models for a First
2670 Characterization of New Physics at the LHC”, *Phys.Rev.* **D79** (2009) 075020,
2671 [doi:10.1103/PhysRevD.79.075020](https://doi.org/10.1103/PhysRevD.79.075020), [arXiv:0810.3921](https://arxiv.org/abs/0810.3921).
- 2672 [44] CMS Collaboration, “Interpretation of Searches for Supersymmetry with
2673 simplified Models”, *Phys.Rev.* **D88** (2013) 052017,
2674 [doi:10.1103/PhysRevD.88.052017](https://doi.org/10.1103/PhysRevD.88.052017), [arXiv:1301.2175](https://arxiv.org/abs/1301.2175).
- 2675 [45] J. Hisano, K. Kurosawa, and Y. Nomura, “Natural effective supersymmetry”,
2676 *Nucl.Phys.* **B584** (2000) 3–45, [doi:10.1016/S0550-3213\(00\)00343-6](https://doi.org/10.1016/S0550-3213(00)00343-6),
2677 [arXiv:hep-ph/0002286](https://arxiv.org/abs/hep-ph/0002286).
- 2678 [46] M. Papucci, J. T. Ruderman, and A. Weiler, “Natural SUSY Endures”, *JHEP*
2679 **1209** (2012) 035, [doi:10.1007/JHEP09\(2012\)035](https://doi.org/10.1007/JHEP09(2012)035), [arXiv:1110.6926](https://arxiv.org/abs/1110.6926).
- 2680 [47] B. Allanach and B. Gripaios, “Hide and Seek With Natural Supersymmetry at the
2681 LHC”, *JHEP* **1205** (2012) 062, [doi:10.1007/JHEP05\(2012\)062](https://doi.org/10.1007/JHEP05(2012)062),
2682 [arXiv:1202.6616](https://arxiv.org/abs/1202.6616).
- 2683 [48] ALICE Collaboration, “The ALICE experiment at the CERN LHC”, *JINST* **3**

- 2684 (2008) S08002, [doi:10.1088/1748-0221/3/08/S08002](https://doi.org/10.1088/1748-0221/3/08/S08002).
- 2685 [49] ATLAS Collaboration, “The ATLAS Experiment at the CERN Large Hadron
2686 Collider”, *JINST* **3** (2008) [doi:10.1088/1748-0221/3/08/S08003](https://doi.org/10.1088/1748-0221/3/08/S08003).
- 2687 [50] CMS Collaboration, “The CMS experiment at the CERN LHC”, *JINST* **0803**
2688 (2008) S08004,
2689 [doi:10.1088/1748-0221/3/08/S08004](https://doi.org/10.1088/1748-0221/3/08/S08004), [10.1088/1748-0221/3/08/S08004](https://doi.org/10.1088/1748-0221/3/08/S08004).
- 2690 [51] LHCb Collaboration, “The LHCb Detector at the LHC”, *JINST* **3** (2008)
2691 S08005, [doi:10.1088/1748-0221/3/08/S08005](https://doi.org/10.1088/1748-0221/3/08/S08005).
- 2692 [52] J.-L. Caron, “LHC Layout. Schema general du LHC.”, (Sep, 1997).
- 2693 [53] CMS Collaboration, “CMS Luminosity - Public Results”, , (2011).
2694 <http://twiki.cern.ch/twiki/bin/view/CMSPublic/LumiPublicResults>.
- 2695 [54] CERN, “CMS Compact Muon Solenoid.”, (Feb, 2010).
2696 <http://public.web.cern.ch/public/Objects/LHC/CMSnc.jpg>.
- 2697 [55] “The CMS Electromagnetic Calorimeter Project: Technical Design Report”.
2698 Technical Design Report CMS. CERN, Geneva, 1997.
- 2699 [56] “The CMS Muon Project: Technical Design Report”. Technical Design Report
2700 CMS. CERN, Geneva, 1997.
- 2701 [57] CMS Collaboration, “The CMS Physics Technical Design Report, Volume 1”,
2702 *CERN/LHCC 2006-001* (2006).
- 2703 [58] M. Cacciari, G. P. Salam, and G. Soyez, “The anti- k_t jet clustering algorithm”,
2704 *Journal of High Energy Physics* **2008** (2008), no. 04, 063.
- 2705 [59] “Jet Performance in pp Collisions at 7 TeV”, CMS-PAS-JME-10-003, CERN,
2706 Geneva, (2010).
- 2707 [60] X. Janssen, “Underlying event and jet reconstruction in CMS”, CMS-CR-2011-012,
2708 CERN, Geneva, (Jan, 2011).
- 2709 [61] CMS Collaboration, “Determination of jet energy calibration and transverse
2710 momentum resolution in CMS”, *Journal of Instrumentation* **6** (2011), no. 11.,
- 2711 [62] R. Eusebi, “Jet energy corrections and uncertainties in CMS: reducing their impact
2712 on physics measurements”, *Journal of Physics: Conference Series* **404** (2012).

- 2713 [63] CMS Collaboration, “Algorithms for b Jet identification in CMS”,
2714 CMS-PAS-BTV-09-001, CERN, 2009. Geneva, (Jul, 2009).
- 2715 [64] CMS Collaboration, “Performance of b-tagging at $\sqrt{s} = 8$ TeV in multijet, $t\bar{t}$ and
2716 boosted topology events”, CMS-PAS-BTV-13-001, CERN, Geneva, (2013).
- 2717 [65] CMS Collaboration, “Identification of b-quark jets with the CMS experiment”,
2718 *Journal of Instrumentation* **8** (2013), no. 04.,
- 2719 [66] CMS Collaboration, “CMS. The TriDAS Project. Technical design report, Vol. 1:
2720 The trigger systems”,,
- 2721 [67] CMS Collaboration, “CMS: The TriDAS Project. Technical design report, Vol. 2:
2722 Data acquisition and high-level trigger”,.
- 2723 [68] CMS Collaboration, “ Calibration and Performance of the Jets and Energy Sums
2724 in the Level-1 Trigger”, CMS IN 2013/006 (2013), CERN, Geneva, (2013).
- 2725 [69] B. L. Shorney-Mathias, , and A. Tapper, “Search for supersymmetry in pp
2726 collisions with all-hadronic final states using the α_T variable with the CMS
2727 detector at the LHC”. PhD thesis, Imperial Coll., London, 2014. Presented 2013.
- 2728 [70] CMS Collaboration, “ Study of Level-1 Trigger Jet Performance in High Pile-up
2729 Running Conditions”,.
- 2730 [71] J. J. Brooke, “Performance of the CMS Level-1 Trigger”, CMS-CR-2012-322,
2731 CERN, Geneva, (Nov, 2012).
- 2732 [72] CMS Collaboration, “Search for supersymmetry in final states with missing
2733 transverse energy and 0, 1, 2, or at least 3 b-quark jets in 7 TeV pp collisions
2734 using the variable alphaT”, *JHEP* **1301** (2013) 077,
2735 [doi:10.1007/JHEP01\(2013\)077](https://doi.org/10.1007/JHEP01(2013)077), [arXiv:1210.8115](https://arxiv.org/abs/1210.8115).
- 2736 [73] CMS Collaboration, “SUSY searches with dijet events”, CMS-PAS-SUS-08-005,
2737 (2008).
- 2738 [74] L. Randall and D. Tucker-Smith, “Dijet Searches for Supersymmetry at the Large
2739 Hadron Collider”, *Phys. Rev. Lett.* **101** (Nov, 2008) 221803,
2740 [doi:10.1103/PhysRevLett.101.221803](https://doi.org/10.1103/PhysRevLett.101.221803).
- 2741 [75] CMS Collaboration, “Search strategy for exclusive multi-jet events from
2742 supersymmetry at CMS”, CMS-PAS-SUS-09-001, CERN, 2009. Geneva, (Jul,

- 2743 2009).
- 2744 [76] CMS Collaboration, “CMS Btag POG : CMS b-tagging performance database”, ,
2745 (2013). <https://twiki.cern.ch/twiki/bin/viewauth/CMS/BtagPOG>.
- 2746 [77] CMS Collaboration, “Calorimeter Jet Quality Criteria for the First CMS Collision
2747 Data”, CMS-PAS-JME-09-008, CERN, 2010. Geneva, (Apr, 2010).
- 2748 [78] The CMS Collaboration, “Performance of CMS muon reconstruction in pp
2749 collision events at 7 TeV”, *Journal of Instrumentation* **7** (October, 2012) 2P,
2750 [doi:10.1088/1748-0221/7/10/P10002](https://doi.org/10.1088/1748-0221/7/10/P10002), [arXiv:1206.4071](https://arxiv.org/abs/1206.4071).
- 2751 [79] CMS Collaboration, “Search for supersymmetry in events with photons and
2752 missing energy”, CMS-PAS-SUS-12-018, CERN, Geneva, (2012).
- 2753 [80] M. Cacciari and G. P. Salam, “Pileup subtraction using jet areas”, *Phys.Lett.*
2754 **B659** (2008) [doi:10.1016/j.physletb.2007.09.077](https://doi.org/10.1016/j.physletb.2007.09.077), [arXiv:0707.1378](https://arxiv.org/abs/0707.1378).
- 2755 [81] Z. Bern et al., “Driving missing data at next-to-leading order”, *Phys. Rev. D* **84**
2756 (Dec, 2011) 114002, [doi:10.1103/PhysRevD.84.114002](https://doi.org/10.1103/PhysRevD.84.114002).
- 2757 [82] Z. Bern et al., “Driving Missing Data at Next-to-Leading Order”, *Phys.Rev.*
2758 **D84** (2011) 114002, [doi:10.1103/PhysRevD.84.114002](https://doi.org/10.1103/PhysRevD.84.114002), [arXiv:1106.1423](https://arxiv.org/abs/1106.1423).
- 2759 [83] CMS Collaboration Collaboration, “Data-Driven Estimation of the Invisible Z
2760 Background to the SUSY MET Plus Jets Search”, CMS-PAS-SUS-08-002, CERN,
2761 2009. Geneva, (Jan, 2009).
- 2762 [84] T. Sjostrand, S. Mrenna, and P. Z. Skands, “PYTHIA 6.4 Physics and Manual”,
2763 *JHEP* **0605** (2006) 026, [doi:10.1088/1126-6708/2006/05/026](https://doi.org/10.1088/1126-6708/2006/05/026),
2764 [arXiv:hep-ph/0603175](https://arxiv.org/abs/hep-ph/0603175).
- 2765 [85] W. Beenakker, R. Hopker, M. Spira, and P. Zerwas, “Squark and gluino
2766 production at hadron colliders”, *Nucl.Phys.* **B492** (1997) 51–103,
2767 [doi:10.1016/S0550-3213\(97\)80027-2](https://doi.org/10.1016/S0550-3213(97)80027-2), [arXiv:hep-ph/9610490](https://arxiv.org/abs/hep-ph/9610490).
- 2768 [86] S. Abdullin et al., “The Fast Simulation of the CMS Detector at LHC”, *Journal*
2769 *of Physics: Conference Series* **331** (2011), no. 3.,
- 2770 [87] S. Banerjee, M. D. Hildreth, and the CMS Collaboration, “Validation and Tuning
2771 of the CMS Full Simulation”, *Journal of Physics: Conference Series* **331** (2011).
- 2772 [88] CMS Collaboration, “CMS Luminosity Based on Pixel Cluster Counting - Summer

- 2773 2012 Update”, CMS-PAS-LUM-12-001, CERN, Geneva, (2012).
- 2774 [89] M. Botje et al., “The PDF4LHC Working Group Interim Recommendations”,
2775 [arXiv:1101.0538](https://arxiv.org/abs/1101.0538).
- 2776 [90] E. M. Laird, “A Search for Squarks and Gluinos with the CMS Detector”,.
- 2777 [91] R. Cousins, “Probability Density Functions for Positive Nuisance Parameters”.
2778 2012. <http://www.physics.ucla.edu/cousins/stats/cousinslognormalprior.pdf>.
- 2779 [92] L. Moneta, K. Cranmer, G. Schott, and W. Verkerke, “The RooStats project”,
2780 2010. [arXiv:1009.1003](https://arxiv.org/abs/1009.1003).
- 2781 [93] F. James and M. Roos, “Minuit: A System for Function Minimization and
2782 Analysis of the Parameter Errors and Correlations”, *Comput.Phys.Commun.* **10**
2783 (1975) 343–367, [doi:10.1016/0010-4655\(75\)90039-9](https://doi.org/10.1016/0010-4655(75)90039-9).
- 2784 [94] A. L. Read, “Presentation of search results: the CL s technique”, *Journal of
2785 Physics G: Nuclear and Particle Physics* **28** (2002).
- 2786 [95] T. Junk, “Confidence level computation for combining searches with small
2787 statistics”, *Nuclear Instruments and Methods in Physics Research Section A* **434**
2788 (1999), no. 23, [doi:\[http://dx.doi.org/10.1016/S0168-9002\\(99\\)00498-2\]\(http://dx.doi.org/10.1016/S0168-9002\(99\)00498-2\)](http://dx.doi.org/10.1016/S0168-9002(99)00498-2).
- 2789 [96] A. L. Read, “Modified frequentist analysis of search results (the CL_s method)”,
2790 CERN-OPEN-2000-205, (2000).
- 2791 [97] G. Cowan, K. Cranmer, E. Gross, and O. Vitells, “Asymptotic formulae for
2792 likelihood-based tests of new physics”, *The European Physical Journal C* **71**
2793 (2011) [doi:10.1140/epjc/s10052-011-1554-0](https://doi.org/10.1140/epjc/s10052-011-1554-0).
- 2794 [98] G. Cowan, K. Cranmer, E. Gross, and O. Vitells, “Asymptotic formulae for
2795 likelihood-based tests of new physics”, *European Physical Journal C* **71**
2796 (February, 2011) [doi:10.1140/epjc/s10052-011-1554-0](https://doi.org/10.1140/epjc/s10052-011-1554-0), [arXiv:1007.1727](https://arxiv.org/abs/1007.1727).
- 2797 [99] CMS Collaboration Collaboration, “Search for supersymmetry in final states with
2798 missing transverse energy and 0, 1, 2, or at least 3 b-quark jets in 7 TeV pp
2799 collisions using the variable alphaT”, *JHEP* **1301** (2013) 077,
2800 [doi:10.1007/JHEP01\(2013\)077](https://doi.org/10.1007/JHEP01(2013)077), [arXiv:1210.8115](https://arxiv.org/abs/1210.8115).
- 2801 [100] E. Hardy, “Is Natural SUSY Natural?”, *JHEP* **1310** (2013) 133,
2802 [doi:10.1007/JHEP10\(2013\)133](https://doi.org/10.1007/JHEP10(2013)133), [arXiv:1306.1534](https://arxiv.org/abs/1306.1534).

2803 Acronyms

2804	ALICE	A Large Ion Collider Experiment
2805	ATLAS	A Toroidal LHC ApparatuS
2806	APD	Avalanche Photo-Diodes
2807	BSM	Beyond Standard Model
2808	CERN	European Organisation for Nuclear Research
2809	CMS	Compact Muon Solenoid
2810	CMSSM	Compressed Minimal SuperSymmetric Model
2811	CSC	Cathode Stripe Chamber
2812	CSV	Combined Secondary Vertex
2813	CSVM	Combined Secondary Vertex Medium Working Point
2814	DT	Drift Tube
2815	ECAL	Electromagnetic CALorimeter
2816	EB	Electromagnetic CALorimeter Barrel
2817	EE	Electromagnetic CALorimeter Endcap
2818	ES	Electromagnetic CALorimeter pre-Shower
2819	EMG	Exponentially Modified Gaussian
2820	EPJC	European Physical Journal C
2821	EWK	Electroweak Sector
2822	GCT	Global Calorimeter Trigger
2823	GMT	Global MuonTrigger
2824	GT	Global Trigger
2825	HB	Hadron Barrel
2826	HCAL	Hadronic CALorimeter

2827	HE	Hadron Endcaps
2828	HF	Hadron Forward
2829	HLT	Higher Level Trigger
2830	HO	Hadron Outer
2831	HPD	Hybrid Photo Diode
2832	ISR	Initial State Radiation
2833	LUT	Look Up Table
2834	L1	Level 1 Trigger
2835	LEP	Large Electron-Positron Collidior
2836	LHC	Large Hadron Collider
2837	LHCb	Large Hadron Collider Beauty
2838	LO	Leading Order
2839	LSP	Lightest Supersymmetric Partner
2840	NLL	Next to Leading Logorithmic Order
2841	NLO	Next to Leading Order
2842	NNLO	Next to Next Leading Order
2843	POGs	Physics Object Groups
2844	PS	Proton Synchrotron
2845	QED	Quantum Electro-Dynamics
2846	QCD	Quantum Chromo-Dynamics
2847	QFT	Quantum Field Theory
2848	RBXs	Readout Boxes
2849	RPC	Resistive Plate Chamber
2850	RCT	Regional Calorimeter Trigger
2851	RMT	Regional Muon Trigger

2852	SUSY	SUperSYmmetry
2853	SM	Standard Model
2854	SMS	Simplified Model Spectra
2855	SPS	Super Proton Synchrotron
2856	TF	Transfer Factor
2857	TP	Trigger Primative
2858	VEV	Vacuum Expectation Value
2859	VPT	Vacuum Photo-Triodes
2860	WIMP	Weakly Interacting Massive Particle